THESE

en vue de l'obtention du grade de Docteur, délivré par

l'ECOLE NORMALE SUPERIEURE DE LYON

Ecole Doctorale N°52
Physique et Astrophysique de Lyon

Discipline : Physique

Soutenue publiquement le 24/06/2024, par :

Lucien JEZEQUEL

Phase space approach to topological physics: Mode-shell correspondence and extensions to non-Hermitian and non-linear systems

Approche en espace des phases de la physique topologique : La correspondance mode-coquille et ses extensions aux systèmes non-Hermitiens et non-linéaires

---

Devant le jury composé de :

CAYSSOL, Jérome	Professeur des universités	Université de Bordeaux	Rapporteur
COOK, Ashley	Chercheuse	Max Planck Institute	Examinatrice
FLEURY, Romain	Professeur	EPFL	Examinateur
ZILBERBERG, Oded	Professeur	Konstanz University	Rapporteur
DELPLACE, Pierre	Chargé de recherche HDR	ENS de Lyon	Directeur de thèse

Laboratoire de Physique
de l'ENS de Lyon
46, allée d'Italie
69007 Lyon

École doctorale N°52
Physique et Astrophysique de Lyon
4 rue Enrico Fermi
69266 Villerbane

Remerciements

À la fin de cette troisième année, cette thèse arrive finalement à son terme. Au cours de ces trois années, j'ai eu le plaisir d'être entouré par de nombreuses personnes qui ont toutes influencé, à leur manière, cette thèse de multiples façons, et je souhaite exprimer ma profonde gratitude envers ceux qui ont rendu cette aventure possible.

Tout d'abord, je tiens à remercier chaleureusement mon directeur de thèse, Pierre Delplace, pour son encadrement exceptionnel, son écoute et son soutien dans les multiples projets qui ont constitué cette thèse. Ses conseils avisés, sa grande culture du domaine et sa pédagogie scientifique ont été des soutiens importants tout au long de la thèse.

Je souhaite aussi remercier les collègues et collaborateurs avec qui j'ai pu discuter de physique topologique durant cette thèse. Je suis reconnaissant des perspectives différentes qu'ils ont apportées et qui m'ont permis d'approfondir ma connaissance du domaine. Merci donc à Baptiste Bermon, David Carpentier, Thomas Espinasse, Romain Fleury, Marcelo Guzmán, Xinxin Guo, Guillaume Laibe, Armand Leclerc, Jaquelin Luneau, Nicolas Perez, Clément Tauber, Antoine Venaille et Zhe Zhang.

Mes remerciements vont également aux rapporteurs et membres de mon jury qui ont accepté de prendre le temps d'examiner cette thèse ainsi que pour leurs retours constructifs.

Un grand merci à l'équipe du laboratoire de Physique de l'ENS de Lyon, où j'ai eu la chance de mener mes recherches. L'atmosphère collaborative et les échanges fructueux avec mes collègues ont été essentiels pour le développement de cette thèse. Merci aussi à toutes les équipes administratives dont le soutien permet de se concentrer pleinement sur la recherche.

Merci en particulier à mes amis et collègues doctorants/postdocs/stagiaires, membres du TSWM ou du groupe de 11h45, pour leur soutien moral et leur amitié tout au long de ces années. Merci pour les moments partagés et les discussions informelles durant ces trois années. Merci donc à Baptiste, Youssef, Geoffroy, Yohann, Léo, Aubin, Alex, Jaquelin, Laszlo, Emile et Hubert.

Merci aussi, de manière générale, à tous les étudiants et membres des cercles ludistes qui m'ont accompagné durant ces années à l'ENS. Vous êtes trop nombreux pour être tous cités ici dans un temps raisonnable, mais vous avez égayé ces sept années d'amitiés fortes et de moments inoubliables, merci beaucoup pour cela.

Je souhaite exprimer ma profonde gratitude à mes parents et à ma famille, qui ont joué un rôle essentiel dans l'éveil de ma passion pour la physique. Nul doute que cela a participé à ma vocation de chercheur et à l'existence de cette thèse.

Enfin, je tiens à remercier Céline pour son soutien infaillible durant ces trois années. Ta patience et ta compréhension m'ont été précieuses, et je te suis infiniment reconnaissant pour tout.

À tous ceux qui, de près ou de loin, ont contribué à l'accomplissement de cette thèse, je vous adresse mes remerciements les plus sincères.

Contents

Introduction **1**

0.1 From topology to waves . . . 1
0.2 Bulk-edge correspondence and beyond . . . 3
0.3 Goals and outline . . . 6

I Mode-shell correspondence **11**

1 Mode-shell correspondence for chiral zero modes **13**

1.1 Overview of the mode-shell correspondence for chiral symmetric systems . . . 13
1.1.1 Chiral symmetry and chiral index . . . 14
1.1.2 Role and necessity of a smooth energy filter $f(E)$ . . . 16
1.1.3 Role and necessity of a phase space filter $\hat{\theta}_\Gamma$ . . . 17
1.1.4 Mode-shell correspondence . . . 19
1.1.5 winding numbers as semi-classical limits of the chiral invariant in phase space . . . 20
1.2 Mode-shell correspondences in $1D$ spaces . . . 23
1.2.1 The bulk-edge correspondence for $1D$ unbounded chiral lattices . . . 23
1.2.2 A dual bulk-boundary correspondence in wavenumber space for bounded continuous systems . . . 27
1.2.3 A mixed $x-k$ correspondence in phase space for unbounded continuous $1D$ systems . . . 31
1.2.4 Discrete approximations of continuous/unbounded topological models . . . 33
1.3 Higher dimensional chiral mode-shell correspondences . . . 36
1.3.1 Expression of the general chiral index . . . 36
1.3.2 Chiral Weak-insulators and flat-band topology . . . 39
1.3.3 Higher-order chiral insulators . . . 43
1.4 Conclusion . . . 48

2 Mode-shell correspondence for spectral-flow systems **49**

2.1 Spectral flow and mode-shell correspondence . . . 49
2.1.1 Spectral flow index . . . 49
2.1.2 Smooth formulation of the index . . . 50
2.1.3 Spectral flow and quantised conductance . . . 53
2.2 Mode-shell correspondence in $1D$ and $2D$ systems . . . 56
2.2.1 1D quantum channel . . . 56
2.3 2D cases . . . 58
2.3.1 2D lattice Chern insulator . . . 58
2.3.2 2D continuous case . . . 59
2.4 Higher dimensional construction . . . 61

2.4.1 Weak/stacked topology . . . 61
2.4.2 Higher-order topology . . . 62
2.5 Conclusion . . . 64

3 Mode-shell correspondence: $2D$-Dirac cones and $3D$-Weyl cones 65
3.1 Construction of modes invariants and their mode-shell correspondence . . . 65
3.2 Examples of models with Dirac and Weyl cones . . . 67
3.2.1 General remarks and constructions . . . 67
3.2.2 Single Dirac/Weyl cones . . . 68
3.2.3 Bulk Dirac/Weyl cones separated in wavenumber . . . 69
3.3 Dirac/Weyl cones confined in position . . . 70
3.4 Dirac/Weyl cones at edges of topological insulators . . . 72
3.5 Conclusion . . . 73

II Topological ascpects beyond Hermitian linear systems 75

4 Non-Hermitian topology 77
4.1 Why non-hermiticity in physics . . . 77
4.2 Hermiticity, non-Hermiticity and associated properties . . . 78
4.3 Line gap and point gap . . . 78
4.4 Sensitivity of the non-Hermitian spectrum . . . 79
4.5 Singular value decomposition . . . 81
4.6 Hermitian mapping and topological invariants . . . 81
4.7 Conclusion . . . 84

5 Non-linear topology 85
5.1 Non-linearity and deformation of zero-modes . . . 85
5.2 Generalised non-linear chiral symmetry . . . 88
5.3 Experimental realisation . . . 91
5.4 Conclusion . . . 92

Conclusion and perspectives 95

Bibliography 96

Appendices 109
A Smoothness/fast-decay Fourier duality . . . 109
B Wigner-Weyl transform . . . 110
B.1 The continuous version . . . 110
B.2 The discrete version . . . 112
C Higher order insulators with hard boundary: Partial semi-classical limit and numerical programs . . . 113
D Proof of the general mode-shell correspondence . . . 117
D.1 Chiral case . . . 117
D.2 Non chiral case . . . 118

Introduction

0.1 From topology to waves

This thesis lies at the intersection of two fields, the first one is topology which is a part of mathematics, the second one is the study of waves which is instead usually considered as a part of physics. Those fields may seem quite far from each other at first glance and therefore it is not obvious why their intersection is interesting. In this introduction, I would like to explain what are the key ideas that allowed such a rich intersection to exist.

One way to present topology is to say that it is a field of mathematics which studies the properties of objects that are stable by smooth deformation. Not all interesting properties are topological, but when it is the case, the corresponding property is more robust as, by definition, it should resist to small changes or errors on how the object is made. For example, one of the most basic topological property is probably the number of holes in a 2D surface (see figure 1.a). It is a property preserved when one deform the surface as a modeling clay. For example, a sphere has no hole, contrary to the donuts that has one and therefore, one cannot deform one into the other in a smooth way.

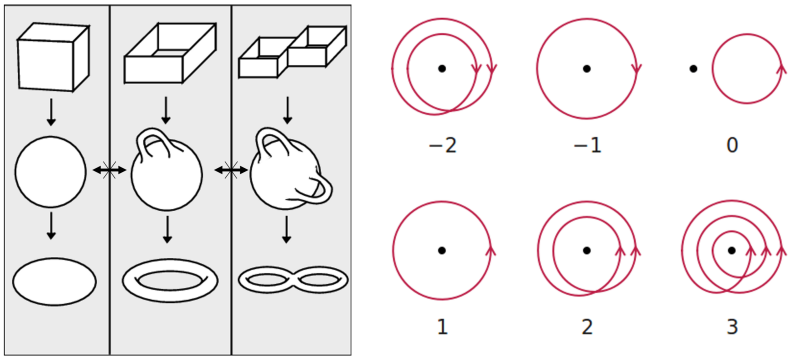

Figure 1: a) examples of surfaces classified by their number of holes. Surface from the same column can be smoothly deformed into one an other while surfaces from different columns cannot. b) Example of paths having a given winding number around a point. Reproduced from [1] and Jim Belk, public domain.

Another relatively simple topological property is the winding number of an oriented path around a point in 2D that is supposed to be impenetrable (see figure 1.b). If two paths do not wind the same number of times around the point, they cannot be smoothly deformed from one to the other without crossing the impenetrable point. Therefore such winding number is a topological invariant.

It is also possible to find applications of topology which are more closely related to physical applications. In particular, topology has been used, to identify topologically protected defects or configurations of continuous vector fields. For example, in ferromagnetic materials, the local magnetisation is a vector field whose norm is constrained to non-zero value but relatively free orientation. A topological defect can appear (see figure 2) which is a singularity where the local magnetisation either ceases to be a vector of non-zero amplitude or ceases to be continuous. Once a defect appears, it is impossible to remove it by local deformation. Therefore the defect is topologically protected. The protection comes from the fact that, if we follow a path that circles the singularity (red circle), then the local magnetisation in those defects has a non-trivial winding number. Such a property cannot be changed by local perturbation and constrains the existence of the singularity.

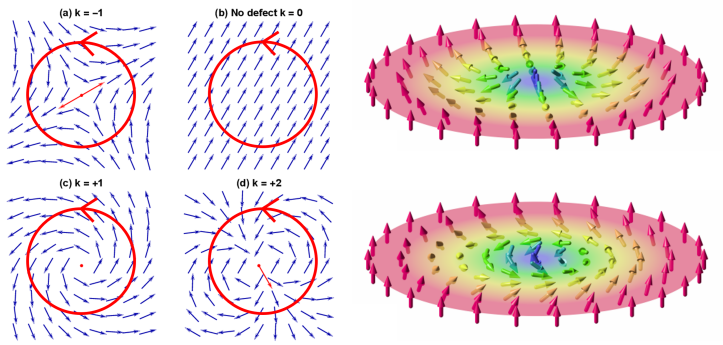

Figure 2: examples of configurations of local magnetisation with (left) a $2D$ magnetisation which has a topological defect (right) $3D$ magnetisation represented in two skyrmion configurations. Reproduced from [2] and Karin Everschor-Sitte and Matthias Sitte, public domain.

There are also configurations which have no discontinuity but are still topologically protected. The most famous one is probably the skyrmion [3] which also occurs in ferromagnetic material but when the local magnetisation vector is 3D instead of 2D. Such a configuration is protected by another topological invariant which is not a winding number but instead the degree of the magnetisation function in real space $\mathbb{R}^2 \to \mathbb{S}^2$ (compactified at infinity). Without going to much into the detail, the topological protection makes the skyrmion particularly stable in the ferromagnetic materials, and it cannot be removed without either creating a discontinuity, having a point of zero magnetisation or annihilating the skyrmion with another one of opposite degree. Therefore once skyrmions appear, they tend to survive quite a long time in dynamic and become interesting configurations to study.

Besides the analysis of the topological properties of vector fields, there is another topic that has proven particularly relevant in physics: the study of the topological properties of wave operators. Indeed wave operators are central objects in physics as they are the objects which govern the evolution of all wave equations. The Hamiltonians is for example the central operator at the heart of the Schrodinger wave equation.

$$i\partial_t |\psi\rangle = \hat{H} |\psi\rangle \tag{1}$$

However operators are not confined to the quantum world and also appear in classical wave equations. The pressure wave equation can for example be written has

$$\partial_t \begin{pmatrix} v \\ p \end{pmatrix} = - \begin{pmatrix} 0 & \frac{1}{\rho}\partial_x \\ \kappa\partial_x & 0 \end{pmatrix} \begin{pmatrix} v \\ p \end{pmatrix} = M \begin{pmatrix} v \\ p \end{pmatrix} \tag{2}$$

with ρ the density of the fluid, κ its bulk modulus and where v and p are the velocity and pressure fields. In this case, the differential operator M is the operator encoding the dynamics of the equation.

If one wants to study the topology of wave operators, the notion of constrain is often essential. This is due to the fact that, similarly to vector fields, operators are linear and, without constrain, can be smoothly deformed into one another through the path $t \to t\hat{H}_1 + (1-t)\hat{H}_2$ and the topology would be trivial. For vector fields like the local magnetisation, vectors are constrain to have a non zero amplitude and it is this constrain which allows the topology. In the context of operators, the constrain is instead typically the existence of a gap in the spectrum of the operator.

The spectrum of an Hermitian operator $\hat{H}$ are the values E for which there is an eigenvector $|\psi_E\rangle$ such that

$$H\,|\psi_E\rangle = E\,|\psi_E\rangle\,. \tag{3}$$

When $\hat{H}$ is Hermitian, the spectrum is real. We say that the operator $\hat{H}$ is gapped around an energy E_0 if there is an interval $E_0 - \Delta/2 < E < E_0 + \Delta/2$ where there is no eigenvalue of energy E, Δ is then called the size of the gap. If such an interval does not exist, we say that the operator is gapless in E_0. We will see, later in the thesis, that this picture get more complicated in the non-Hermitian case. But for now we keep it simple and stick to the Hermitian case.

It is often useful to be a little bit more precise and determine in which regions the operator is gapped and in which it is gapless. In particular we will be interested about the localisation of these regions in position x and in reciprocal/wavenumber space k with the union of the two forming the phase space (x, k). For that we will use the Wigner-Weyl transform which maps, in a one to one correspondence, operators $\hat{H}$, to matrix of smaller rank called "symbol" $H(x, k)$ and which are parameterised by the phase space coordinates (x, k).

$$H(x,k) = \int dx' \left\langle x + \frac{x'}{2} \right| \hat{H} \left| x - \frac{x'}{2} \right\rangle e^{-ikx'}. \tag{4}$$

In the particular case where the operator is invariant by translation in x, it coincides with the well known Fourier transform. Such a tool can be applied both for Hamiltonians or for density operator $\hat{\rho_\psi} = |\psi\rangle\langle\psi|$ which allows us to qualitatively understand where eigenenergies and eigenmodes are located in phase space. It will be a goal of the thesis to go further into the details, but for now, we can say that an Hamiltonian is gapped in a region of phase space if its symbol $H(x, k)$ is gapped in such a region or if the modes $|\psi\rangle$ which are gapless are negligible in such a region $\rho_\psi(x, k) \approx 0$. Conversly, he Hamiltonian will be called gapless if the condition is not verified.

We will see that most results in the field of wave/operator topology typically share the same structure. They impose a gap condition in certain regions of phase space, and show that there necessarily exists gapless regions elsewhere in phase space which are topologically protected. The best known of these results being the bulk-edge correspondence.

0.2 Bulk-edge correspondence and beyond

One of the most historically important applications of topology to wave systems is probably the quantum Hall effect. In 1980, Klaus von Klitzing discovered the extraordinary quantification of the transverse conductivity in 2D materials under strong magnetic fields [5]. This phenomenon was already measured at the time with a relative precision of 10^{-5}, and currently, it is measured with a precision between 10^{-9} and 10^{-10}. The explanation for this phenomenon was provided by David Thouless and his coworkers in 1982 [6]. In materials where the quantum Hall effect appears, an energy gap prevents electrons from propagating in the bulk. However, on the edge

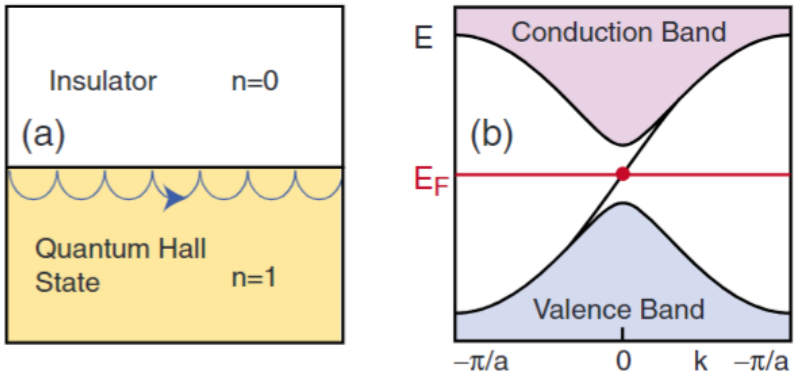

Figure 3: Schematic view of the Quantum Hall effect. In the bulk, all the modes are gapped on energy, while there is a mode confined at the edge which is unidirectional and gapless. Reproduced from [4].

of the material, low-energy excitation modes appear, with multiplicity equal to a topological invariant which is an integer depending only on the bulk properties of the material. Such a correspondence between a gapless topological property occurring at the edge and a topological property defined in the bulk, which is gapped, became known as the bulk-edge correspondence [7–9]. This result sparked an entire field at the boundary between physics and mathematics, which motivated this thesis.

Indeed, such a bulk-edge correspondence has been extended to many systems, well beyond the case of the quantum effect and beyond quantum matter to all wave systems. As initiated with photonic crystals [10–13], it followed that many experimental platforms, quantum and classical, emerged with the aim of engineering, probing, and manipulating robust boundary modes like for robust wave guiding [14] or quantum computing [15, 16].

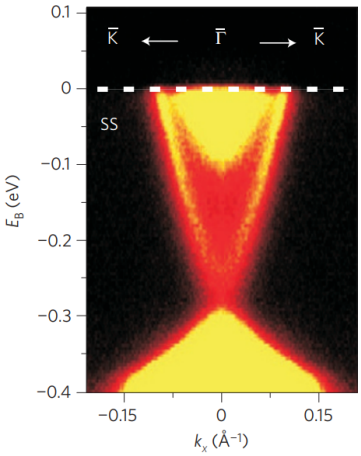

Figure 4: Experimental observation of a surface state forming a Dirac cone at the boundary of a 3D topological insulator. Reproduced from [17]

.

Another success of the bulk-edge correspondence is its generalization in other dimensions. For instance, it was observed in a 3D topological insulator, the existence of surface states which are also topologically protected [17,18] (see figure 4). Actually, this success of the bulk-boundary correspondence was twofold because those $3D$ topological insulators were protected by the existence of a time-reversal spin symmetry. This then leads to an extension of the correspondence

depending on the symmetry of the system and in arbitrary dimensions [19–22]. Depending on the case, the bulk topological invariant changes, and accordingly, the nature of the boundary modes it describes.

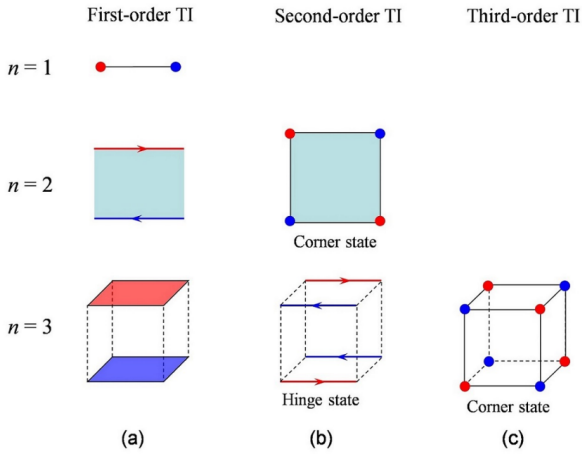

Figure 5: Categorisation of systems into the first or higher order category depending on the localisation of their topologically protected modes (in blue/red). Reproduced from [23].

However, there are many systems with new phenomenologies that do not fit the standard paradigm of bulk-edge correspondence. One important development of the last years was the discovery of higher-order topological insulators, which display a richer hierarchy of topologically protected modes that are not predicted by the usual bulk-boundary correspondence. In $2D$, such gapless modes are localized at corners instead of edges. In $3D$, such materials can host hinge states or corner states rather than surface states (see figure 5) [24–26].

Another important class of systems exhibiting topological properties are semi-metals, and in particular, those hosting Dirac or Weyl cones [27–32]. These are topologically protected structures located at particular wavenumber/valley in the Brillouin zone and surrounded in wavenumber by gapped regions (see figure 6). In this case, the topological nature of such structures is known to be related to the winding or Chern number integrated on a circle or a sphere that encircles the Dirac/Weyl point in the Brillouin zone [33,34]. As everything happens in the bulk, the existence and topological protection of such Dirac cones seem therefore different from that of the bulk-edge correspondence.

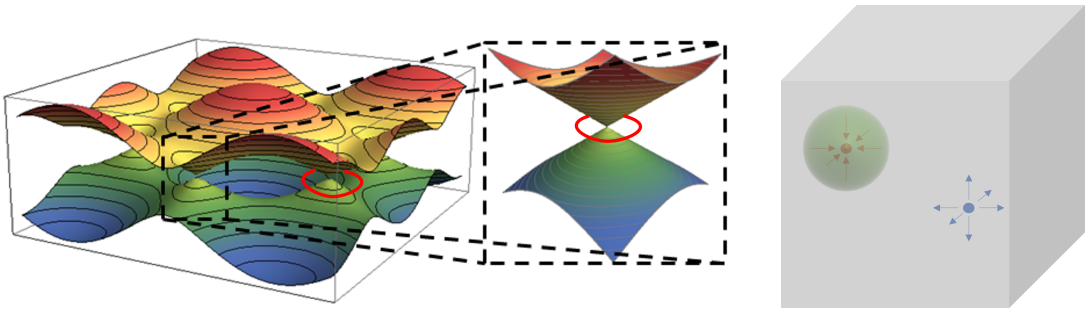

Figure 6: (left) Dispersion relation of graphene hosting topological Dirac point separated in wavenumber. Such Dirac point are protected as long as the Hamiltonian is gapped on a circle encircling them (in red) and on which can be defined a winding number. Reproduced from [35]. (right) Weyl points in the bulk of 3D material, they are protected as long as the Hamiltonian is gapped on the sphere encircling them (in green) and on which can be defined a Chern number.

Another related direction is the study of topological modes in continuous media, mostly motivated by classical wave physics, such as geo- and astrophysical fluids [36–39], active fluids [40], plasmas [37] but also photonics [41, 42]. Of interest was the apparent failure of the bulk-edge correspondence in the absence of a lattice – and thus of a compact reciprocal space –that stimulated several extension works [43–50]. One way to address the problem is to focus on domain-walls made of smooth varying potentials rather than hard wall boundaries. This fruitful approach allows the description of interface modes, at the domain wall, whose topological origin is encoded both in position and wavenumber space rather than only in reciprocal space, leading to what we could call a "phase space - interface/domain wall" correspondence. Similarly to the topological characterization of Weyl nodes in $3D$, such a phase space approach also allows for counting topological modes of $2D$ systems in a specific valley, as encountered in various valley-Hall effects, by assigning them directly an integer-valued topological invariant [45, 51–53], without needing to resort to valley Chern numbers (that are purely defined in k-space) that typically involve half-integer numbers [54–57]. Interestingly, the combined use of real and reciprocal space is also used to characterize the topology of defect modes [58] in insulators and superconductors, which constitutes another important generalization.

In parallel to these efforts to describe topology beyond bulk-edge correspondence, researchers have also tried to extend the bulk-edge correspondence to a wider class of Hamiltonian symmetries, as we already mentioned some examples earlier [16, 18–22, 59–62]. A direction of particular relevance in the past few years concerns non-Hermitian systems. This field of research can somehow be traced back to the finding of topological edge states in periodically driven (Floquet) systems [63–67], quantum walks [68, 69], and scattering networks [70, 71], whose full description is ruled by unitary operators, such as evolution operators or scattering matrices, rather than usual Hermitian Hamiltonians [64, 72]. In that context, the standard bulk-edge correspondence was also found to fail, but suitable generalizations, with new topological invariants that account for the periodic dynamics, were then found out in various symmetry classes [64, 65, 73, 74]. More recently, non-Hermitian topology rather more implicitly designates classical or quantum systems whose dynamics displays topological properties that are dictated by non-unitary evolutions, whether because of different sources of gain or loss [75–97].

Finally, an even more recent direction of research has been the extension of the bulk-edge correspondence to nonlinear systems. Such a new interest can be explained by the fact that nonlinearities are of particularly importance in classical waves [98–101]. Therefore, there is a need to understand how the topology phenomena observed in the linear regime are modified in the presence of nonlinearities. This has sparked much research in a field which remains relatively new [81, 82, 102–114].

0.3 Goals and outline

In this thesis, I will have two goals. The first one is to provide a unifying theory that offers a common understanding of all the possible directions mentioned above. The second one will be to extend the application of topology to relatively new fields. Concerning the goal of providing a unifying theory, I will present a formalism I developed during my thesis called the "mode-shell correspondence"; this will be the focus of the first three chapters. Regarding the goal of extending topology to new fields, I will present extensions of wave topology to non-Hermitian physics in the fourth chapter and to non-linear physics in the last chapter. In practice, achieving the first objective will positively impact the second one. Establishing the general mode-shell formalism will enable us to discuss new topological phenomena. It will also provide us with useful tools for analyzing non-Hermitian and non-linear systems later on.

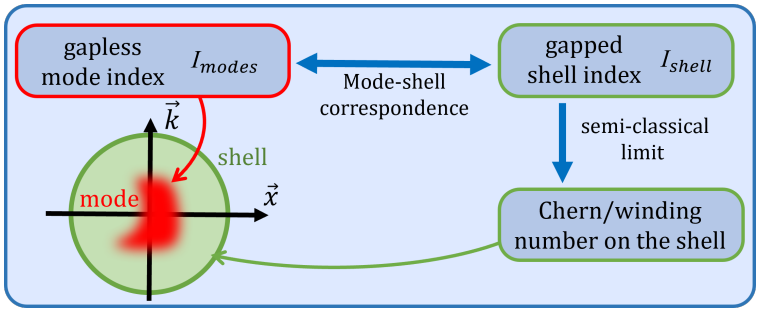

Figure 7: Summary diagram of the mode-shell correspondence. A mode index, characterising a gapless property of the operator is related to an index defined on the shell which is the surface surrounding the gapless region in phase space. In the semi-classical limit, the shell index reduces to either a winding or a Chern number on the shell.

Let us now discuss in more detail the content of the chapters, starting with the mode-shell correspondence. As mentioned earlier, our aim is to build a theory that unifies many cases presented in the previous section. Such a theory must therefore apply to any dimension, account for discrete and continuous spaces, be independent of translation invariance, describe both boundary and interface states, as well as higher-order hinge or corner states. It should also capture topological modes that are not purely localized in space, but instead reside in a delimited region of reciprocal/wavenumber space, such as a valley. We refer to this theory as the "mode-shell" correspondence. Similarly to index theories, the mode-shell correspondence states the equality between two integer-valued indices: $\mathcal{I}_{\text{modes}} = \mathcal{I}_{\text{shell}}$. The first index gives the number of "modes" (e.g., edge states) in a certain energy region, while the second one is an invariant defined on a "shell" surrounding those "modes" in phase space $(x, k) \in \mathbb{R}^{2n}$, where the Hamiltonian (or more generically, the wave operator) is assumed to be gapped. This general and basic equality is the first cornerstone of the theory. While the two indices can in principle always be computed numerically, it is unrealistic to expect them to be computable analytically in general. However, one may hope to have a simpler formulation in systems with some structure. This brings us to the second step of the theory, which consists of a semiclassical approximation [115] of the shell invariant $\mathcal{I}_{\text{shell}}$. When such an approximation is possible, $\mathcal{I}_{\text{shell}}$ can be expressed as an integral over the shell. In that limit, one recovers well-known expressions of so-called bulk topological invariants, such as winding numbers and Chern numbers, but integrated in general on the shell instead of the bulk Brillouin zone which becomes just a particular case (see figure 7).

In this introduction, I choose to remain relatively general in the presentation of the theory of the bulk-edge correspondence. The reason is that we will recover the bulk-edge correspondence as a particular case of the mode-shell correspondence, so it will be discussed later in the thesis. Additionally, I decided not to present the concepts of Berry phase and Berry curvature [116], which are a fairly common way to define bulk invariants [4,34,117,118]. One reason is that such a formalism is only usable in gapped regions to define the shell/bulk index but is ill-suited to study $\mathcal{I}_{\text{modes}}$ which is associated to gapless phenomena. Moreover, even for gapped invariants, I found it rather cumbersome to use in higher-dimensional cases (typically referred to as the "non-Abelian" cases). Therefore, in this thesis, I prefer to use an operator formalism which may seem more abstract at first, but allows for easier computation in most cases covered by the mode-shell correspondence.

The first three chapters of the thesis will be devoted to the study of the mode-shell correspondence which will be split depending on the mode invariant $\mathcal{I}_{\text{modes}}$ used (see figure 8).

In the first chapter, our focus lies on Hermitian wave operators with chiral symmetry. Specifically, we focus on the scenario where the mode index describes the count of "zero-dimensional

mode index I_{mode}	number of zero modes	spectral flow	number of Dirac cones	number of Weyl cones
D_M	0	1	2	3
Chapter	1	2	3	3
D_S partity	odd	even	odd	even
shell index I_{shell}	winding number	Chern number	winding number	Chern number

Figure 8: Summary of the different mode indices $\mathcal{I}_{\text{modes}}$ covered in the different chapters. The integer D_M is the dimension of the topological modes captured by $\mathcal{I}_{\text{modes}}$. D_S is the dimension of the shell on which is defined $\mathcal{I}_{\text{shell}}$ which encloses these modes in phase space.

zero-energy modes," referred simply as zero-modes hereafter. These modes are typically associated with the edge states of $1D$ systems in the AIII symmetry class of the tenfold way classification of topological insulators and superconductors [19]. The term "zero-dimensional" implies that these modes are localized in "every" direction. While these zero-modes are captured by a single mode index $\mathcal{I}_{\text{modes}}$ we will show that the semiclassical expression of $\mathcal{I}_{\text{shell}}$ changes depending on the configuration at hand (lattice model, continuous domain wall, higher-order topological insulator, etc.) but can systematically be determined by the mode-shell correspondence.

In the second chapter, we delve into scenarios where the mode index is a 1D-spectral flow index, which counts the number of unidirectional modes crossing the Fermi energy. This index is particularly significant as it describes the topology of the low-energy modes of systems like the Quantum Hall effect or Chern Insulators. Its associated shell invariant is then, in this case, the Chern number in the bulk. However, beyond the usual 2D bulk-edge correspondence, we will also see that the spectral flow index is useful for describing unidirectional modes localized in valleys separated in wavenumber or higher-order situations.

Moving on to the third chapter, we discuss cases where the mode index is higher dimensional. Specifically, we study cases where such an index is either the number of 2D-Dirac points or the number of 3D-Weyl points. We derive the mode-shell correspondence and explain models where these topological phenomena occur, ranging from localized band crossing in the bulk Brillouin zone to edge modes of 3D and 4D insulators.

In the last two chapters of the thesis, we partially move away from the mode-shell correspondence and study the topological aspects of wave operators beyond the Hermitian and linear hypothesis.

In the fourth chapter we explore the realm of non-Hermitian physics. We explain the differences and specificities of this class of wave operators. We also explain key ideas, and concepts useful for analyzing these systems (line/point gap, eigenvalue sensitivity, singular value decomposition). We then show how one can extend the mode-shell correspondence to these systems to analyze non-Hermitian phenomena beyond the bulk-edge correspondence.

Finally, in the fifth and last chapter, we discuss the extension of wave topology to nonlinear systems. This task is nontrivial, as the linearity assumption is pervasive in topology, from the notion of eigenvalue and gap to the notion of topological eigenmodes. We show that finding stationary modes in nonlinear systems can be broken down into solving a series of linear systems through adiabatic deformation. We demonstrate that topological modes can be preserved when adding nonlinearities with particular symmetry, focusing our discussion on the case of chiral systems with zero modes at the edges. We also present an experimental realization and observation of these modes.

List of papers

[1] L. Jezequel and P. Delplace, "Nonlinear edge modes from topological one-dimensional lattices," *Physical Review B*, vol. 105, no. 3, p. 035410, 2022.

[2] L. Jezequel, C. Tauber, and P. Delplace, "Estimating bulk and edge topological indices in finite open chiral chains," *Journal of Mathematical Physics*, vol. 63, Dec. 2022.

[3] L. Jezequel and P. Delplace, "Non-Hermitian spectral flows and Berry-Chern monopoles," *Phys. Rev. Lett.*, vol. 130, p. 066601, Feb 2023.

[4] A. Leclerc, L. Jezequel, N. Perez, A. Bhandare, G. Laibe, and P. Delplace, "Exceptional ring of the buoyancy instability in stars," *Phys. Rev. Res.*, vol. 6, p. L012055, Mar 2024.

[5] L. Jezequel and P. Delplace, "Mode-shell correspondence, a unifying phase space theory in topological physics - Part I: Chiral number of zero-modes," *SciPost Phys.*, vol. 17, p. 060, 2024.

[6] X. Guo, L. Jezequel, M. Padlewski, H. Lissek, P. Delplace, and R. Fleury, "Practical realization of chiral nonlinearity for strong topological protection," *arXiv preprint arXiv:2403.10590*, 2024.

[7] L. Jezequel and P. Delplace, "Mode-shell correspondence, a unifying theory in topological physics – part II: Spectral flow and higher-dimensional spectral invariants," in preparation.

Part I

Mode-shell correspondence

Chapter 1

Mode-shell correspondence for chiral zero modes

In this chapter I would like to present the mode-shell correspondence in one of the simplest set-up which is the case the topological property is the chiral number of *zero-dimensional zero-energy modes*. The *zero-dimensional* denomination means that those modes are localized in "every" direction (with a finite short extension) like at edges of 1D insulators of at corner of higher order insulators. Here, our aim is extract the key ideas of mode shell correspondence as well as the many topological aspects of this single and apparently simple case and derive a systematic expression for the shell invariant.

The outline of the chapter is as follows. In section 1.1, we present a non technical overview of the mode-shell correspondence. In particular, we introduce the mode invariant $\mathcal{I}_{\text{mode}}$ for chiral symmetric systems, and show how it is related to the shell invariant $\mathcal{I}_{\text{shell}}$. We introduce the notion of the symbol Hamiltonian $H(x,k)$ that is a phase space representation of the operator Hamiltonian $\hat{H}(x,\partial_x)$ through a Wigner-Weyl transform. We discuss the semi-classical approximation that simplifies the shell invariant into a general winding number for arbitrary dimensional systems. Section 1.2 is dedicated specifically to $1D$ systems. The mode-shell correspondence is then derived and illustrated on models for $1D$ lattices, continuous bounded and continuous unbounded geometries. From there, we show that the mode-shell correspondence includes the bulk-edge and bulk-interface correspondences, where zero-energy modes are localized in position x-space at a boundary or an interface, but it also describes a dual situation where the topological modes are localized in wavenumber k-space, and even an hybrid situation with a confinement in $x-k$ phase space. Section 1.3 is devoted to higher dimensional chiral symmetric systems hosting such zero-modes or other apparently different modes whose topological origin can eventually be reduced to that of the chiral zero-modes described in section 1.2. Those cases include (but are not restricted to) weak and higher order topological insulators.

1.1 Overview of the mode-shell correspondence for chiral symmetric systems

The aim of this section is to introduce, in a non technical way, the mode-shell correspondence by focusing on the zero-dimensional zero-energy modes of chiral symmetric systems.

1.1.1 Chiral symmetry and chiral index

In this section, we introduce an index, denoted by $\mathcal{I}_{\text{modes}}$, that counts the number of chiral zero-energy modes. This index can be used when the Hamiltonian $\hat{H}$ has a chiral symmetry, that is, when there exists a unitary operator $\hat{C}$ satisfying the anti-commutation relation $\hat{H}\hat{C}+\hat{C}\hat{H}=0$. This symmetry typically appears when the system is bi-partied in two groups of degrees of freedom A and B, such that the Hamiltonian only couples A and B. These two groups can, for example, be two groups of atoms that interact in a lattice through a nearest neighbor interaction (see Figure 1.1).

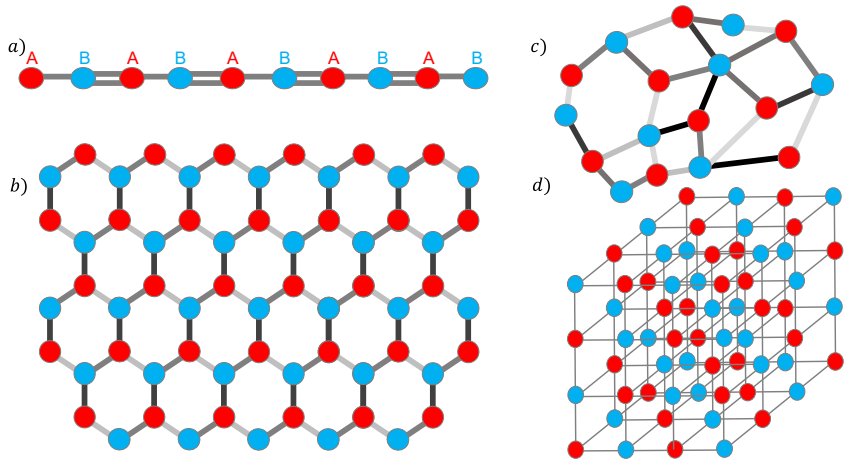

Figure 1.1: Examples of chiral lattices in a) $1D$, b) and c) $2D$ and d) $3D$. The example c) illustrates a disordered (amorphous) lattice which is still chiral symmetric. The red/blue dots represent the sites of opposite chirality and the grey links represent the different couplings between those sites. All these lattices can host topological modes for well-chosen Hamiltonians.

Chiral symmetry is given by a diagonal operator in the $A-B$ block basis, with coefficients $+1$ on A and -1 on B, that is

$$\hat{C}=\begin{pmatrix}\mathbb{1}_A & 0\\ 0 & -\mathbb{1}_B\end{pmatrix} \tag{1.1}$$

where $\mathbb{1}$ denotes the identity operator. We shall call such a basis the *chiral basis* in the following. The *chirality* of a mode $|\psi\rangle$ then refers to the eigenvalues of the chiral operator; it is $+1$ for the modes $|\psi\rangle$ satisfying $\hat{C}|\psi\rangle=|\psi\rangle$ and -1 for those satisfying $\hat{C}|\psi\rangle=-|\psi\rangle$. The chirality is a signature of the polarisation of the modes on the A or B degrees of freedom. In the chiral basis, the Hamiltonian is off-diagonal

$$\hat{H}=\begin{pmatrix}0 & \hat{h}^\dagger\\ \hat{h} & 0\end{pmatrix} \tag{1.2}$$

and the operators $\hat{h}$ and $\hat{h}^\dagger$ encode the couplings between A and B degrees of freedom. It follows from (1.1) and (1.2) that the identity $\hat{C}\hat{H}+\hat{H}\hat{C}=0$ is automatically satisfied. A direct consequence of chiral symmetry is that every eigenstate $|\psi\rangle$ of $\hat{H}$ with a non-zero eigen-energy E comes with a chiral symmetric partner $\hat{C}|\psi\rangle$ of opposite energy $-E$.

A special attention will be paid on zero-energy modes of chiral symmetric systems (usually simply dubbed *zero-modes*). The key point is that those zero-modes are topologically protected when they are exponentially localized in *regions* outside of which the Hamiltonian is gapped. Those regions can for instance correspond to edges, interfaces or defects in real space, and the

zero-modes then correspond to various kinds of boundary states. But we will see that those regions may also more generally designate a part of phase space (position and wavenumber space). Here we are concerned with a *chiral index* that counts algebraically the number of localized zero-energy modes in those regions, with a sign given by their chirality. In other words, the chiral index counts the total chirality of the zero-modes and can thus be formally introduced as

$$\mathcal{I}_{\text{modes}} = \#\,\text{zero-modes of chirality } +1 - \#\,\text{zero-modes of chirality } -1\ . \tag{1.3}$$

An alternative (although equivalent) definition of the chiral index can be found by using the off-diagonal structure (1.2) of $\hat{H}$ in the chiral basis, so that the zero-modes $|\psi\rangle = (|\psi\rangle_A\,, |\psi\rangle_B)^t$ must satisfy

$$\hat{H}\,|\psi\rangle = 0 = \begin{pmatrix} \hat{h}^\dagger\,|\psi\rangle_B \\ \hat{h}\,|\psi\rangle_A \end{pmatrix}. \tag{1.4}$$

It follows that the zero-modes $|\psi\rangle$ of positive chirality are in bijection with the $|\psi\rangle_A$ in the kernel of $\hat{h}$. The zero modes of negative chirality are as well in bijection with the $|\psi\rangle_B$ in the kernel of $\hat{h}^\dagger$. So one can rewrite the index in the commonly used form

$$\mathcal{I}_{\text{modes}} = \dim\ker(\hat{h}) - \dim\ker(\hat{h}^\dagger) \equiv \text{Ind}(\hat{h}). \tag{1.5}$$

where $\text{Ind}(\hat{h})$ is known as the analytical index of the operator $\hat{h}$.

It is worth stressing here that chiral symmetry is not restricted to lattices, and can also be encountered when dealing with classical waves in continuous media. Actually, it turns out that chiral symmetry of the wave operator for fluid models follows from time-reversal symmetry of the original set of primitive differential equations. This is because primitive equations – basically momentum conservation and mass conservation – are first order differential equations in time. Indeed, they yield a relation between fields that are odd with respect to time inversion $t \to -t$, such as velocity fields $v(t) \to -v(-t)$, and fields that are even with respect to time reversal, such as pressure fields $p(t) \to p(-t)$. When time-reversal symmetry is satisfied, the left and right members of those equations must have the same parity under time reversal. But because of the first order differentiation of those fields with respect to time, that also changes sign under time-reversal $\partial_t \to -\partial_t$, the time derivative of the odd fields is only given by even fields, and *vice versa*. This automatically creates a bipartition between the physical fields depending on their parity in time, which eventually translates into a chiral symmetry of the wave operator in phase space. Such a structure appears in geo- and astrophysical fluid dynamics in the absence of Coriolis force [38, 51] and in plasmas models [37, 39] provided the magnetic field is off [1] .

In the rest of the thesis, we develop a theory that applies for both discrete and continuous media, quantum or classical, and we keep the notation $\hat{H}$ when referring to classical wave operators, that are assumed to be Hermitian, and even abusively call them "Hamiltonians" for the sake of standardizing the notations.

[1] Let us stress that in classical waves systems, time-reversal symmetry is just an orthogonal symmetric matrix which is 1 on even degrees of freedom and -1 on the odds ones. This is different from quantum mechanics where the Schrödinger equation carries a complex structure and where time-reversal symmetry is encoded as a complex conjugation or in general as an anti-unitary operator. This may cause confusion when one wants to apply to classical waves the ten-fold classification [19, 20] which was constructed with the quantum version of the time-reversal symmetry in mind.

1.1.2 Role and necessity of a smooth energy filter $f(E)$

Actually, the definitions (1.3) and (1.5) of the chiral index only work in idealized infinite systems but are difficult to manipulate or to approximate in finite size systems. Indeed, in finite size systems, the zero-modes of the different regions are always coupled with each other through exponentially small but non-zero overlapping. This coupling, in general, shifts the energy of the modes such that, in perfect rigour, one never reaches perfect zero-energy modes. To overcome this limitation, we introduce a formulation of the chiral index that is continuous in the coefficients of $\hat{H}$, making it easier to manipulate in practical computations and simulations.

To do so, we first assume the system to be gapped far away from the zero-mode, and we denote by $\Delta > 0$ the half-amplitude of the gap $[-\Delta, \Delta]$. Then we define the operator $\hat{H}_F = f(\hat{H})$ where we choose f to be an odd function taking the value -1 for negative gapped energies $E < -\Delta$ and $+1$ for positive gapped energies $E > \Delta$ with a smooth transition in the gapless region in between (see Figure 1.2). This means that $\hat{H}_F$ is the operator with the same eigenmodes as $\hat{H}$ but with rescaled energies $E \to f(E)$. This operation flattens the gapped bands and hence $\hat{H}_F$ can be seen as a flatten Hamiltonian. Then the chiral index can be formally defined as

$$\mathcal{I}_{\text{modes}} = \mathrm{Tr}\Big(\hat{C}(1 - \hat{H}_F^2)\Big) \ . \tag{1.6}$$

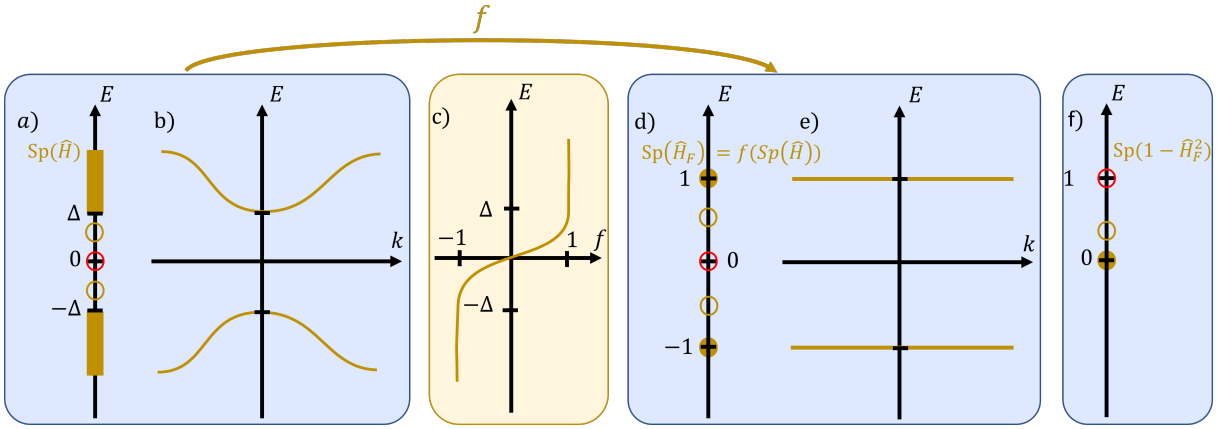

Figure 1.2: a) Projected energy spectrum denoted $\mathrm{Sp}(\hat{H})$ of a typical topological Hamiltonian $\hat{H}$. United stripes denote the gapped bulk bands, circles denote the isolated eigenvalue of modes localised at the edge and red circles denote the topological zero modes. b) Dispersion relation in the bulk where edge modes cannot be seen. c) Sketch of a possible smooth flattening function. d-e) Spectrum of the operator $\hat{H}_F = f(\hat{H})$ where the bulk bands are flattened. f) Spectrum of $1 - \hat{H}_F^2$, where only a finite number of non-zero excitations remains: the bulk excitations vanish and the original zero-modes are dominant.

To see why (1.6) is indeed a meaningful definition of the chiral index, we express it in a common diagonal basis $\{|\psi_\lambda\rangle\}$ of $\hat{C}$ and $\hat{H}^2$ (which is always possible since $[\hat{H}^2, \hat{C}] = 0$ as $\{\hat{H}, \hat{C}\} = 0$) and we get

$$\mathcal{I}_{\text{modes}} = \sum_\lambda C_\lambda (1 - f(E_\lambda)^2) \, \langle \psi_\lambda | \psi_\lambda \rangle = \sum_\lambda C_\lambda (1 - f(E_\lambda)^2) \tag{1.7}$$

with C_λ and E_λ^2 the eigenvalues $\hat{C}$ and $\hat{H}^2$. The term $1 - f(E_\lambda)^2$ is identically zero for all the modes that do not lie in the gap $[-\Delta, \Delta]$. We are thus left with the zero modes we would like to keep (full circles in figure 1.2), and *a priori* other gapless but non-zero modes (hollow circles in figure 1.2). As a matter of fact, the latest come by pairs of opposite chirality, due to chiral symmetry as if $|\psi\rangle$ is an eigenmode of both $\hat{H}^2$ and $\hat{C}$ with eigenvalues E_λ^2 and C_λ then $H|\psi\rangle$ is

also an eigenmode with eigenvalues E_λ^2 and $-C_\lambda$ except when $H|\psi\rangle = 0$. They therefore cancel out two by two in the sum thanks to the introduction of the chiral operator $\hat{C}$ in the definition of $\mathcal{I}_{\text{modes}}$. The only contributions that remain are those of the zero-energy modes $\hat{H}|\psi_\lambda\rangle = 0$ that do not allow a valid way to construct a symmetric partner of opposite chirality. So we end up with $\mathcal{I}_{\text{modes}} = \sum_{\lambda, E_\lambda=0} C_\lambda$ which is exactly the chirality of the zero-modes.

The two equivalent expressions (1.3) and (1.6) of the chiral index $\mathcal{I}_{\text{modes}}$ show that the number of zero-modes of the Hamiltonian $\hat{H}$ is a topological quantity: (1.3) shows that $\mathcal{I}_{\text{modes}}$ is an integer number while (1.6) shows that it depends continuously of the Hamiltonian. $\mathcal{I}_{\text{modes}}$ is therefore an integer that is stable under smooth variations of the coefficients of $\hat{H}$, hence its topological nature.

However, as they are written, the different expressions of $\mathcal{I}_{\text{modes}}$ count the *total* number of zero-modes of $\hat{H}$. This is an issue when dealing with finite size systems, or with numerical simulations, that involve more than one gapless region (e.g. two edges, multiple corners ...). In those cases, one is more interested in the chirality of the modes localised in specific sub-regions of phase space (just counting the zero-modes near an edge/corner/...) than the total chirality of the zero-modes of the entire system, which is also often trivial. One therefore needs a cut-off in phase space to obtain this *local* topological information, a process we now aim at describing.

1.1.3 Role and necessity of a phase space filter $\hat{\theta}_\Gamma$

In order to capture the chiral zero-modes in specific regions of phase space, one needs to add, to the definition of $\mathcal{I}_{\text{modes}}$, a function $\hat{\theta}_\Gamma$ that selects the a zero-mode in phase space. (sketched in red in figure 1.3). Such a *cut-off operator* is close to identity over a gapless target region that encloses the zero-mode, over a typical distance Γ (in green in figure 1.3), and then drops to zero away from it, where the Hamiltonian is gapped. We shall later refer to the domain where $\hat{\theta}_\Gamma$ drops as the *shell*. In this way, the selected zero-modes are localised within the shell, while the other zero-modes remain outside (in blue in figure 1.3). A *local* version of the the chiral index thus reads

$$\mathcal{I}_{\text{modes}} = \text{Tr}\Big(\hat{C}(1 - \hat{H}_F^2)\hat{\theta}_\Gamma\Big) \tag{1.8}$$

and which, by construction, counts the chirality of the zero-modes in a selected region of phase space. More formally, this phase space representation of zero-modes is typically made possible thanks to a Wigner transform, that we introduce in section 1.1.5. The red and blue gapless regions in figure 1.3 are thus sketches of the amplitude of the Wigner function of the zero-modes.

Importantly, the quantisation of the index does not strongly depend on the shape of the shell, nor on how the cut-off operator is explicitly defined, as long as it is close to identity in the target gapless region (where the Wigner representation of the zero-mode is located) within the shell and close to zero in the other gapless regions, outside the shell. As we will see below, the target region, defined in phase space, is in correspondence with the localisation of the zero-modes, and many situations can be covered by the same local chiral index (1.8), which makes it quite general and powerful.

For instance, if we are interested in finding a zero-mode localized in real space, at an edge of a $1D$ chain, positioned around $x \sim 0$, the cut-off operator should target a region in phase space which is therefore only constrained in the x direction and not in wavenumber k. Its profile can be a simple Gaussian $\hat{\theta}_\Gamma = e^{-x^2/\Gamma^2}$ or a function with a sharper transition like $\hat{\theta}_\Gamma = (1 + e^{x^2-\Gamma^2})^{-1}$. In those expressions, the cut-off parameter Γ determines how big is the selected region. This is the example illustrated in figure 1.3 a) and discussed in details in section 1.2.1.

Our formalism allows to tackle the dual situation of the previous case on the same footing, where the zero-modes are now localized in wavenumber, for instance in the slow varying modes

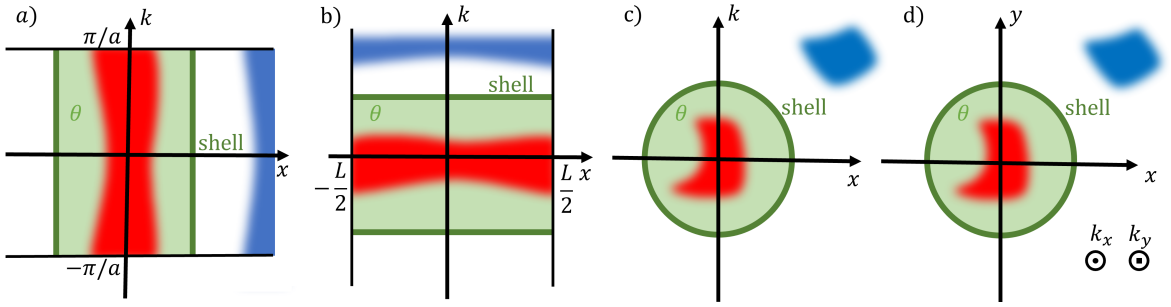

Figure 1.3: Sketches of the Wigner representation of zero-modes (in red/blue depending of their positive/negative chirality) embedded in different phase spaces with examples where the zero-modes are localised a) in position but not in wavenumber b) in wavenumber but not in position c) in position and in wavenumber d) in position but in a $2D$ space. The cut-off function θ selects a region that encloses one zero-mode by taking the value $\theta \sim 1$ (green), while dismissing the other gapless regions ($\theta \sim 0$ in white). The transition region where the cut-off goes from one to zero is called the shell (dark green line).

region of a continuous Hamiltonian. Possible cut-off operators then read $\hat{\theta}_\Gamma = e^{\Delta/\Gamma^2} \approx e^{-k^2/\Gamma^2}$ or $\hat{\theta}_\Gamma = (1+e^{-\Delta-\Gamma^2})^{-1} \approx (1+e^{k^2-\Gamma^2})^{-1}$ where Δ is the Laplacian operator, and the associated target region in phase space is represented in figure 1.3 b). This formalism is then similar to the so-called heat kernel approach used in the context of the Atiyah-Singer index theorem. A model displaying such zero-modes is addressed in section 1.2.2.

More generally, the zero-modes can also be localised in a mixed way in position/wavenumber and cut-off operators can then be chosen as $\hat{\theta}_\Gamma = e^{(-x^2+\partial_x^2)/\Gamma^2} \approx e^{-(x^2+k^2)/\Gamma^2}$ or $\hat{\theta}_\Gamma = (1+e^{x^2-\partial_x^2-\Gamma^2})^{-1} \approx (1+e^{x^2+k^2-\Gamma^2})^{-1}$ in that case[2]. The shell enclosing the target region in phase space is then typically a circle (figure 1.3 c) and a corresponding example is shown in section 1.2.3.

Finally, this approach can be generalized to higher dimensions, to address zero-modes in higher-order topological insulators with chiral symmetry. A simple example is that of corner states of a $2D$ system. In that case, cut-off operators can be chosen as $\hat{\theta}_\Gamma = e^{-(x^2+y^2)/\Gamma^2}$ or $\hat{\theta}_\Gamma = (1+e^{x^2+y^2-\Gamma^2})^{-1}$, and the target region in phase space is shown in figure 1.3 d). This higher dimensional case, is discussed among others in section 1.3.

In finite systems, the necessary introduction of a cut-off operator alters the quantisation of the chiral index, which is no longer exactly an integer. However, in large systems, when the gapless regions we want to select are far away from each other in phase space and Γ is large, the correction to an integer value decays exponentially fast with the sizes of the system as shown in my paper [119] and it is reasonable to still talk about quantised index with a satisfying approximation. Moreover in the limit case of infinite systems, the cut-off parameter Γ can be put to infinity, so that $\hat{\theta}_\Gamma$ is replaced by the identity and we recover the previous exact index (1.6).

In all those cases, the notion of "large system" should be understood as large compared to the typical coupling distances of the Hamiltonian $\hat{H}$ in phase space. So, if the cut-off operator acts in position space, we need $\hat{H}$ to be short-range in position space, and the system's size must be large compared to the typical coupling distance in position. The unbounded limit $L \to \infty$ in figure 1.4 satisfies this condition. If the cut-off operator acts in wavenumber space, we need $\hat{H}$ to be short-range in wavenumber space and the lattice wavenumber $k_0 = 2\pi/a$ to be large compared to typical coupling distance in wavenumber. The continuous limit $a \to 0$ in figure 1.4

[2]We choose to work with adimensioned models, hence the adimensioned expression in x and k.

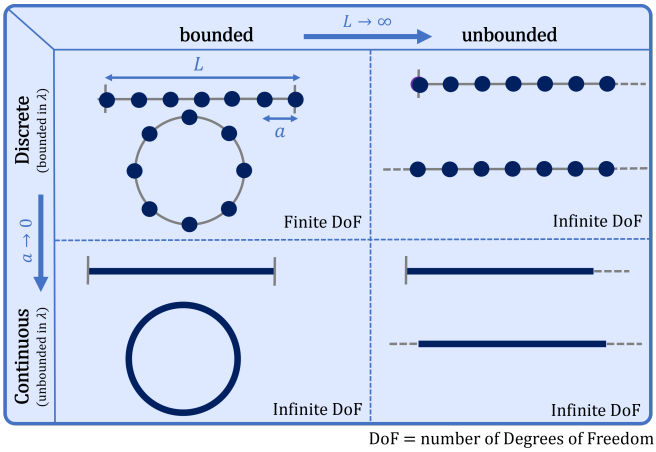

Figure 1.4: Table summarising the different categories of systems according to two infinite limits: a large length limit, where the length L of the system is considered as infinitely large, and a small length limit where the characteristic distance a between two sites becomes infinitely small and where therefore the set of possible wavenumbers becomes unbounded.

satisfies this condition.

1.1.4 Mode-shell correspondence

The chiral index we have introduced requires the use of the cut-off operator that embeds a gapless target region in phase space where zero-modes live. The boundary of this embedding, namely the shell, plays a crucial role in the theory that we now want to emphasize. This is due to the fact that, up to a rearrangement of its terms the index $\mathcal{I}_{\text{modes}}$ can be shown to be equal to an invariant $\mathcal{I}_{\text{shell}}$, that essentially depends on the properties of $\hat{H}$ *on* the shell, the region where the cut-off drops from the identity to zero. This index reads

$$\mathcal{I}_{\text{shell}} = \mathrm{Tr}\Big(\hat{C}\hat{\theta}_\Gamma\Big) + \frac{1}{2}\,\mathrm{Tr}\Big(\hat{C}\hat{H}_F[\hat{\theta}_\Gamma, \hat{H}_F]\Big)\ . \tag{1.9}$$

The first term $\mathrm{Tr}\Big(\hat{C}\hat{\theta}_\Gamma\Big)$ does not depend on $\hat{H}$. It is the polarisation in the number of degrees of freedoms of positive/negative chirality, weighted by $\theta_\Gamma(x)$. For example, in a lattice, this term is just the polarisation in the number of sites of positive/negative chirality (again weighted by $\theta_\Gamma(x)$). In this thesis we will mostly deal with situations where the density of states of positive/negative chirality is *balanced* and where this term therefore vanishes. If such density of states does not compensate, then this term is necessary to recover the mode-shell correspondence [120–122].

The second term, $\frac{1}{2}\,\mathrm{Tr}\Big(\hat{C}\hat{H}_F[\hat{\theta}_\Gamma, \hat{H}_F]\Big)$, does depend on $\hat{H}$. However, the trace contains the commutator $[\hat{H}_F, \hat{\theta}_\Gamma]$ which vanishes both *inside* the shell, where $\hat{\theta}_\Gamma \approx \mathbb{1}$ (any operators commutes with the identity), and *away* from the shell since there $\hat{\theta}_\Gamma \approx 0$. Therefore, the non-negligible contributions of the trace only come from the shell which is the region where $\hat{\theta}_\Gamma$ goes from the identity to zero. This property explains the appellation of the index $\mathcal{I}_{\text{shell}}$.

The fact that $\mathcal{I}_{\text{modes}}$ can be re-expressed into $\mathcal{I}_{\text{shell}}$ is proved in a few lines of algebra. In fact it suffices to use the anti-commutation relation with the chirality operator $\hat{C}\hat{H}_F = \hat{C}f(\hat{H}) = f(-\hat{H})\hat{C} = -\hat{H}_F\hat{C}$ (remember that f is an odd function) as well as the cyclicity of the trace to

rearrange the terms in the following order[3], and we get

$$\begin{aligned}\mathcal{I}_{\text{modes}} &= \mathrm{Tr}\Big(\hat{C}\hat{\theta}_\Gamma(1-\hat{H}_F^2)\Big)\\ &= \mathrm{Tr}\Big(\hat{C}\hat{\theta}_\Gamma\Big) - \mathrm{Tr}\Big(\hat{C}\hat{\theta}_\Gamma\hat{H}_F^2\Big)\\ &= \mathrm{Tr}\Big(\hat{C}\hat{\theta}_\Gamma\Big) - \frac{1}{2}\left(\mathrm{Tr}\Big(\hat{H}_F^2\hat{C}\hat{\theta}_\Gamma\Big) + \mathrm{Tr}\Big(\hat{H}_F\hat{C}\hat{\theta}_\Gamma\hat{H}_F\Big)\right)\\ &= \mathrm{Tr}\Big(\hat{C}\hat{\theta}_\Gamma\Big) + \frac{1}{2}\,\mathrm{Tr}\Big(\hat{C}\hat{H}_F[\hat{\theta}_\Gamma,\hat{H}_F]\Big)\end{aligned} \tag{1.10}$$

which shows the equality

$$\mathcal{I}_{\text{modes}} = \mathcal{I}_{\text{shell}} \tag{1.11}$$

that we call the *mode-shell correspondence*, as it relates the number of chiral zero-modes to a property on the shell surrounding those modes in phase space. Because of this equality, we can use the notation $\mathcal{I}$ to denote both indices.

In general, the index $\mathcal{I}$ can be computed numerically and is prone to describe the topology of inhomogeneous or disordered systems since its definition does not rely on any periodicity assumption. However the shell formulation of the invariant is particularly suitable to semi-classical approximations [115] in a lot of systems which simplifies its computation and provides another topological meaning to the index.

1.1.5 winding numbers as semi-classical limits of the chiral invariant in phase space

The index formulation we developed is made at the operator level whereas semi-classical approximations are usually performed in phase space (x,k) ($\hbar = 1$ in the quantum situations). The connection between, on one hand, operators such as the cut-off operator $\hat{\theta}_\Gamma$ or the Hamiltonian $\hat{H}$, and, on the other hand, functions in phase space, is made possible by Wigner-Weyl calculus. In particular, we can use the Wigner transform of the Hamiltonian operator, defined as (see Appendix B)

$$H(x,k) = \int_{\mathbb{R}} dx' \left\langle x + \frac{x'}{2}\right| \hat{H} \left| x - \frac{x'}{2}\right\rangle e^{-ikx'} \tag{1.12}$$

with $k \in \mathbb{R}$ when the Hamiltonian $\hat{H} = H(x,\partial_x)$ is a differential operator that describes a continuous model, and as

$$H(n,k) = \sum_{n'} \langle n'|\, \hat{H}\, |n\rangle\, e^{-ik(n'-n)} \tag{1.13}$$

with periodic parameter $k \in [0,2\pi]$ to address the discrete case, where the lattice sites (or unit cells) are labelled by an integer n. Those expressions generalize straightforwardly to higher dimensions. In both cases, we refer to $H = H(x,k)$ as the *symbol* of $\hat{H}$. It is a reduced operator acting only on the internal degrees of freedom of the systems, but parametrized in phase space. Similarly, zero-modes can be represented in phase space by a Wigner transform of their density matrix, leading schematically to the red and blue spots in figure 1.3. The mapping of the Hamiltonian $\hat{H}$ into a symbol Hamiltonian $H(x,k)$ allows us to express the chiral index as a generalized winding number, given by an integral over the $2D-1$-dimensional shell in phase space

$$\mathcal{I} \underset{\text{S-C lim}}{=} \frac{-2(D)!}{(2D)!(2i\pi)^D} \int_{\text{shell}} \mathrm{Tr}^{\text{int}}(U^\dagger dU)^{2D-1} \equiv \mathcal{W}_{2D-1} \tag{1.14}$$

[3] This derivation can be performed even in infinite systems as the cut-off operator makes the trace finite.

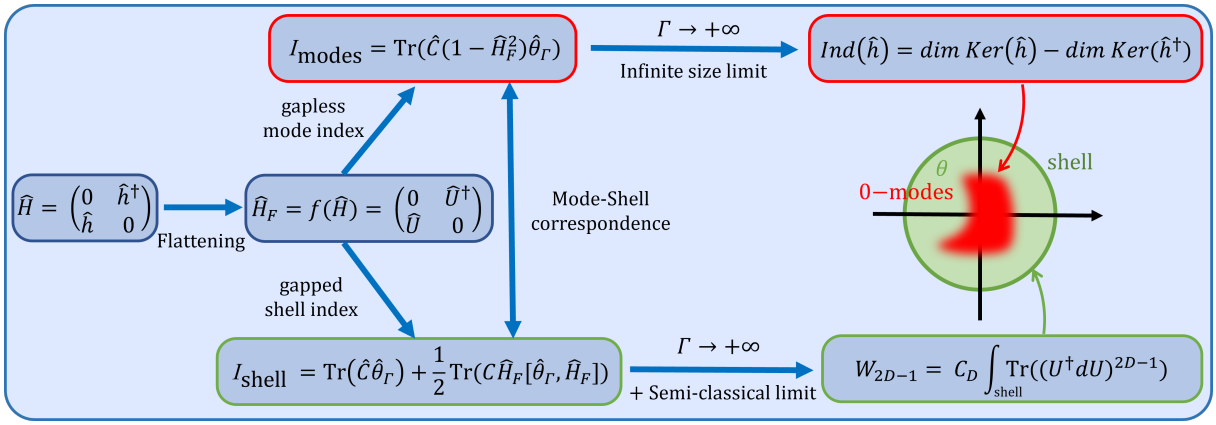

Figure 1.5: Summary diagram of the mode-shell correspondence. We use a smoothly flatten version $\hat{H}_F$ of the Hamiltonian $\hat{H}$ to define two indices: I_{modes} counting the chiral number of zero-modes localised in a target gapless region in phase space, a gapless property of $\hat{H}$, and I_{shell} measuring gapped properties on the boundary enclosing the gapless region (namely the shell) and which reduces, in a semi-classical limit, to a (higher) winding number. Both indices are equal due to the mode-shell equality (1.11). The prefactor C_D of W_{2D-1} is given in (1.14).

where D is the dimension of the system, the trace Tr^{int} only acts on the internal degrees of freedom and $U(x,k)$ is a unitary operator that constitutes the off-diagonal component of the symbol of the flatten Hamiltonian $H_F = \left(\begin{smallmatrix} 0 & U^\dagger \\ U & 0 \end{smallmatrix}\right)$ that acts on the internal degrees of freedom of the system. Since, on the shell, the Hamiltonian has no gapless mode, H_F has energies $E_F = \pm 1$ and can thus be written as $H_F(x,k) = H(x,k)/\sqrt{H(x,k)^2}$. The notation dU denotes the 1-differential form in phase space $dU = \sum_i (\partial_{x_i} U)dx_i + (\partial_{k_i} U)dk_i$. $(U^\dagger dU)^{2D-1}$ is then a $2D-1$-form which is an anti-symetrised sum of all possible orders of derivatives $\partial_{z_j} U$ in the product $(U^\dagger dU)^{2D-1}$ where z_j is a phase space coordinate (either position or wavenumber). For a given set of phase space coordinates $(z_1, \dots, z_{2D-1})$, the related component of the form reads

$$\sum_{j_1,\cdots,j_{2D-1}=1}^{2D-1} \epsilon_{j_1,\cdots,j_{2D-1}} \prod_{m=1}^{2D-1} \left(U^\dagger \partial_{z_{j_m}} U\right) \tag{1.15}$$

where $\epsilon_{j_1,\cdots,j_{2D-1}}$ is the antisymetrised Levi-Civita tensor with convention $+1$ for the basis $\prod_i dk_i \wedge dx_i$. For example, when $D = 2$, the phase space has 4 dimensions. The form $\text{Tr}\left(U^\dagger dU\right)^3$ is then a 3-form with 4 components in phase space, which reduces to one component when projecting on the shell. As an instance, the component in $dx \wedge dk_x \wedge dk_y$ reads

$$\text{Tr}\Big(U^\dagger \partial_x U [U^\dagger \partial_{k_x} U, U^\dagger \partial_{k_y} U] + [U^\dagger \partial_{k_x} U, U^\dagger \partial_{k_y} U] U^\dagger \partial_x U\Big), \tag{1.16}$$

and similarly for the three others components. We will provide an explicit demonstration of the formula in $1D$ cases later in this chapter and refer to the appendix of my paper [123] for a proof of the general case.

The formula (1.14) can be seen as a generalization of the bulk-edge correspondence. When dealing with bounded one-dimensional ($1D$) lattices with open boundary conditions, $\mathcal{I}$ can be seen as an *edge index* that counts the chirality of the zero-modes at one boundary, while $\mathcal{W}_1$ is the usual *bulk* winding number expressed as an integral over the $1D$ Brillouin zone in k-space. However, the formula (1.14) describes a much richer class of chiral systems that goes well beyond $1D$ lattices. Indeed, the system of interest can be of higher dimension, discrete or continuous,

bounded or unbounded, and the zero-modes characterized by (1.14) can be localized in position (such as edge states), but also in wavenumber space.

The surface of integration, i.e. the shell, is a surface of dimension $2D-1$ that encloses the chiral zero-mode in phase space of dimension $2D$. The shell is therefore always a surface of odd dimension. This contrasts the celebrated classification of topological insulators where the chiral symmetric class (AIII) is known to allow topologically non-trivial phases in odd dimensions only [19]. The fact that our formula (1.14) predicts the existence of chiral zero-modes also in even dimension D is because the shell lives in phase space, and is therefore not restricted to the k-space Brillouin zone.

The formula (1.14) also includes other previously existing results in topological physics that differ from the standard bulk-edge correspondence. It includes for example the formula derived by Atyiah and Singer in the 60s [124] for continuous operators when the position manifold is a torus [4] and where the shell is therefore the unit sphere in wavenumber space tensored with the manifold in position space $(x,k) \in \mathbb{T}^d \times \mathbb{S}^{d-1}$. Our formula also includes the formula proposed by Teo and Kane to classify topological point defects zero-modes [58]. In that case, the shell consists of the sphere enclosing the zero-modes in position space tensored with the Brillouin zone $(x,k) \in \mathbb{S}^{d-1} \times \mathbb{T}^d$. Finally it also includes the Callias index formula [44,125] (also derived by Hornander [126] generalising a result by Fedosov [127]) which deals with defects localised in position space, as in the Teo and Kane's work, but for continuous operators, and where the shell is then the phase space sphere $(x,k) \in S^{2d-1}$ (localised in position and wavenumber). Our general formula (1.14) thus unifies all these results. The generality of the formula makes it more flexible and covers for examples the cases with both continuous and discrete dimensions, which would not fit into any of the previously cited theories.

Note that an equivalent expression of the winding number in (1.14), can be obtained by homotopy in terms of $h(x,k)$, the symbol of $\hat{h}$, as

$$\mathcal{W}_{2D-1} = \frac{-2(D)!}{(2D)!(2i\pi)^D} \int_{\text{shell}} \text{Tr}^{\text{int}} (h^{-1}dh)^{2D-1} \ . \tag{1.17}$$

This expression could be of practical interest since it bypasses the computation of H_F.

Finally, we should note that the formula (1.14) is obtained in a certain *semi-classical limit*, hence the subscript "S-C lim" (we shall just write *lim* in the rest of the thesis). This limit is reached when the variations of the symbol in position x or in wavenumber k become small compared to the gap of the symbol. This hypothesis can be stated as follow (see appendix (B) for justification):

Semi-classical hypothesis: *For a given symbol $H(x,k)$, its characteristic variation distances in position d_x and wavenumber d_k spaces can be estimated through the formula*

$$1/d_{x/k} \sim \|\partial_{x/k} H(x,k)\|/\Delta(x,k) \tag{1.18}$$

where $\Delta(x,k)$ is the gap of the symbol $H(x,k)$. The semi-classical limit is reached asymptotically near the shell when $\epsilon \equiv 1/(d_x d_k) \ll 1$.

For example, in $1D$ lattices, the symbol of the Hamiltonian becomes completely independent of position in the bulk, so that $1/d_x \to 0$. In most of the examples treated here, we have $\epsilon = 1/(d_x d_k) = O(1/\Gamma)$. In other words, (at least) one of the characteristic distances of variation becomes small for points (x,k) in phase space which are close to the shell. Hence,

[4] This restriction comes from simplifying hypotheses in the semi-classical expansion. Manifold with curvature lead to more complex expressions which would go beyond the scope of the thesis.

the semi-classical approximation becomes exact in the asymptotic limit $\Gamma \to +\infty$. This semi-classical approximation makes the winding number $\mathcal{W}_{2D-1}$ in general simpler to calculate than the original chiral index $\mathcal{I}$, making the formula (1.14) of practical interest. All those results are recapped in figure 1.5.

1.2 Mode-shell correspondences in $1D$ spaces

1.2.1 The bulk-edge correspondence for $1D$ unbounded chiral lattices

General results

In this section, we discuss the particular case of Hamiltonians on $1D$ lattices with edges and show how the usual winding number is obtained as a semi-classical approximation of the shell index and therefore counts the number of chiral zero energy edge states: a result known as the *bulk-edge correspondence*, which is well established for $1D$ lattices, both physically and mathematically [120,121,128–133]. This derivation serves as a pedagogical example to introduce a few key tools and concepts in more details. We shall also treat in parallel the case of *interface* zero-modes, in contrast with *edge* modes. We therefore assume that the gapless target region is either an edge, or an interface, located at $x \sim 0$, so that the cut-off operator can be chosen as $\hat{\theta}_\Gamma = e^{-x^2/\Gamma^2}$. The chirality of zero-modes localised in that region is given by the shell index (1.9) with that specific cut-off operator. Let us now show how, under some assumptions, a semi-classical approximation of this index is made possible and yields a more familiar and simpler expression.

In the following, $n \in \mathcal{L}$ is the unit cell index of the lattice, it runs over $\mathcal{L} = \mathbb{N}$ if we deal with a lattice with an edge and over $\mathcal{L} = \mathbb{Z}$ in the case of an interface. We also introduce α to label the (finite) internal degrees of freedom (e.g. orbital, spin...). We assume the chiral operator $\hat{C}$ to be diagonal in the (n, α) basis and independent of the unit cell, and denote by C_α the chirality of the internal degrees of freedom. We then use the discrete Weyl transform (1.13) where $\langle n'| \hat{H} |n\rangle$ is the matrix containing the couplings between the internal degrees of freedom of the unit cells n and n'. The symbol Hamiltonian $H(n,k)$ we obtain thus acts only on the internal degrees of freedoms, with parameters $(n,k) \in \mathcal{L} \times S^1$ living on the discrete phase space. In some sense, this discrete Wigner transform can be seen as a generalisation of the Bloch transform to non-periodic couplings on a grid.

We then make the following hypothesis: we assume that the Hamiltonian $\hat{H}$ is asymptotically periodic far from the boundary/interface. More precisely, in the case of an edge ($\mathcal{L} = \mathbb{N}$), we assume that the symbol Hamiltonian $H(n,k)$ converges asymptotically to a *bulk*, (i.e. position independent) Hamiltonian $H^+(k)$ when $n \to +\infty$. Similarly, in the case of an interface ($\mathcal{L} = \mathbb{Z}$), we ask that the symbol Hamiltonian converges toward two bulk Hamiltonians far to the left/right of the interface, that is $H(n,k) \to H^\pm(k)$ when $n \to \pm\infty$.[5]

Let us now estimate the term $\mathrm{Tr}\Big(\hat{C}\hat{H}_F[\hat{\theta}_\Gamma, \hat{H}_F]\Big)$ of the chiral index, with $\hat{\theta}_\Gamma = e^{-x^2/\Gamma^2}$ in the limit $\Gamma \to +\infty$. For that purpose, we first rewrite the trace as an integral in phase space by using the Moyal $\star$ product between symbols as

$$\mathrm{Tr}\Big(\hat{A}\hat{B}\Big) = \frac{1}{2\pi} \sum_n \int_0^{2\pi} dk\, \mathrm{Tr}^{\mathrm{int}}((A \star B)(n,k)) \tag{1.19}$$

[5] In general, we only need the weaker assumption $\frac{1}{d_x d_k} \to 0$, as defined in (1.18), to obtain a valid semi-classical limit which is useful in some cases.

where $\mathrm{Tr}^{\mathrm{int}}$ is the trace on the internal degrees of freedom only (see appendix B). We obtain

$$\frac{1}{2}\mathrm{Tr}\Big(\hat{C}\hat{H}_F[\hat{\theta}_\Gamma,\hat{H}_F]\Big)=\frac{1}{4\pi}\sum_{n\in\mathcal{L}}\int_0^{2\pi}dk\ \mathrm{Tr}^{\mathrm{int}}((C\star H_F\star[\theta_\Gamma,H_F]_\star)(n,k)) \tag{1.20}$$

where $[A,B]_\star=A\star B-B\star A$ is the Moyal commutator. Next we take the limit $\Gamma\to+\infty$. As discussed in the previous section, in that limit, $\theta_\Gamma\approx\mathbb{1}$ near the interface/boundary, $\mathcal{I}$ is the topological index describing the chiral number of the zero-modes localised at the interface/boundary. Moreover as $\Gamma\to+\infty$, $\theta_\Gamma(n)$ varies slower and slower with n, so that we probe a region which is further and further in the bulk where $H(n,k)$ has asymptotically no dependence in position, by hypothesis. The product of the symbols $H(n,k)$ with $\theta_\Gamma(n)$ is therefore prone to a semi-classical approximation, obtained in the limit $\Gamma\to+\infty$.

The leading term of such a semi-classical expansion is obtained by simply replacing all the Moyal products by standard product $A\star B\sim AB$, and the Moyal commutator by a Poisson bracket $[A,B]_\star\sim i\{A,B\}$ (see Appendix B), so that

$$\frac{1}{2}\mathrm{Tr}\Big(\hat{C}\hat{H}_F[\hat{\theta}_\Gamma,\hat{H}_F]\Big)=\frac{-1}{4i\pi}\sum_{n\in\mathcal{L}'}\int_0^{2\pi}dk\,\mathrm{Tr}^{\mathrm{int}}(\,CH_F(n,k)\delta_n\theta_\Gamma(n)\partial_kH_F(n,k))+O(1/\Gamma) \tag{1.21}$$

where $\delta_n\theta_\Gamma(n,k)=\theta_\Gamma(n+1,k)-\theta_\Gamma(n,k)$ is the discrete derivative. Note that we do not have the term $\partial_k\theta_\Gamma(n)\delta_nH_F(n,k)$ in the Poisson bracket because $\theta_\Gamma(n)$ has no dependence k. As we will see, this first term of the semi-classical expansion converges already to a finite constant when $\Gamma\to+\infty$. So, the next term of the semi-classical expansion, which must be of smaller order in Γ, vanishes when $\Gamma\to+\infty$ and there is no need to consider them. We use the notation $\underset{\lim}{=}$ to mean that an equality is true up to the vanishing of higher order terms in the limit $\Gamma\to+\infty$. Then, since the variation of $\theta_\Gamma(n)$ mainly comes from the high $|n|\gg1$ region, we can approximate $H_F(n,k)$ by its bulk limit.

Let us focus first on the interface case ($\mathcal{L}=\mathbb{Z}$). We substitute $H_F(n,k)$ by $H_F^+(k)$ for $n>0$ and by $H_F^-(k)$ for $n<0$ leading to

$$\begin{aligned}\frac{1}{2}\mathrm{Tr}(\hat{C}\hat{H}_F[\hat{\theta}_\Gamma,\hat{H}_F])&\underset{\lim}{=}\\ &\frac{-1}{4i\pi}\int_0^{2\pi}dk\,\mathrm{Tr}^{\mathrm{int}}\,(C\left(H_F^+(k)\sum_{n>0}\delta_n\theta_\Gamma(n)\partial_kH_F^+(k)+H_F^-(k)\sum_{n<0}\delta_n\theta_\Gamma(n)\partial_kH_F^-(k)\right))\,.\end{aligned} \tag{1.22}$$

The sum over n is performed by using $\sum_{n>0}\delta_n\theta_\Gamma(n)=\theta_\Gamma(+\infty)-\theta_\Gamma(0)=-1$ and $\sum_{n<0}\delta_n\theta_\Gamma(n)=\theta_\Gamma(0)-\theta_\Gamma(-\infty)=1$, and we obtain

$$\frac{1}{2}\mathrm{Tr}\Big(\hat{C}\hat{H}_F[\hat{\theta}_\Gamma,\hat{H}_F]\Big)\underset{\lim}{=}\frac{1}{4i\pi}\int_0^{2\pi}dk\,\mathrm{Tr}^{\mathrm{int}}(\,C\left(H_F^+(k)\partial_kH_F^+(k)-H_F^-(k)\partial_kH_F^-(k)\right))\,. \tag{1.23}$$

Since $H_F^2=\mathbb{1}$ in the bulk, we can introduce the unitaries $U^\pm$ such that

$$H_F^\pm=\begin{pmatrix}0&(U^\pm)^\dagger\\U^\pm&0\end{pmatrix} \tag{1.24}$$

and rewrite (1.23) as

$$\frac{1}{2}\mathrm{Tr}\Big(\hat{C}\hat{H}_F[\hat{\theta}_\Gamma,\hat{H}_F]\Big)\underset{\lim}{=}\frac{1}{2i\pi}\int_0^{2\pi}dk\,\mathrm{Tr}^{\mathrm{int}}\,\Big((U^+)^\dagger(k)\partial_kU^+(k)-(U^-)^\dagger(k)\partial_kU^-(k)\Big) \tag{1.25}$$

where we recognize the winding number $W \equiv \frac{1}{2i\pi}\int_0^{2\pi} dk\, \mathrm{Tr}\, U^\dagger \partial_k U \in \mathbb{Z}$ of the unitary map $k \in S^1 \to U(k) \in S^1$, which leads to

$$\frac{1}{2}\,\mathrm{Tr}\Big(\hat{C}\hat{H}_F[\hat{\theta}_\Gamma, \hat{H}_F]\Big) \underset{\lim}{=} W_\uparrow^+ - W_\uparrow^- \tag{1.26}$$

with $W_\uparrow^+$ and $W_\uparrow^-$ the winding numbers of U^+ and U^- defined in the bulks far to the positive and negative sides of the interface respectively, and integrated over the $1D$ Brillouin zone. The vertical arrow $\uparrow$ specifies the direction of integration in k, from 0 to 2π.

If the lattice has "balanced unit cells", that is when there is an equal number of degrees of freedom of positive and negative chirality C_α per unit cell n ($\sum_\alpha C_\alpha = 0$), this imply that the terms $\mathrm{Tr}\Big(\hat{C}\hat{\theta}_\Gamma\Big) = \sum_n \sum_\alpha C_\alpha \theta_\Gamma(n) = 0$. Therefore, in that case, one recovers the expected bulk-interface correspondence for $1D$ chiral chains in the limit $\Gamma \to +\infty$

$$\mathcal{I} \underset{\lim}{=} W_\uparrow^+ - W_\uparrow^- \ . \tag{1.27}$$

which is a particular case of our general formula (1.14) that we derive through relatively simple consideration.

Otherwise, if the unit-cell structure is broken at the boundary, this equality must be corrected by the term $\mathrm{Tr}\,\hat{C}\hat{\theta}_\Gamma$ to account for the chirality of the lattice's sites [120–122]. The term $\mathrm{Tr}\,\hat{C}\hat{\theta}_\Gamma$ is also non-zero when the bulk unit cell is unbalanced in chirality $\sum_\alpha C_\alpha \neq 0$. However, this case is excluded from our theory because such imbalanced systems have flat zero bands in the bulk that violate the gap hypothesis.

The case of an edge, rather than an interface, is obtained similarly. The only difference being that the sum in n runs now over $\mathcal{L} = \mathbb{N}$ (for a left edge) instead of $\mathbb{Z}$. As a consequence, the second term in the right hand side of the equation (1.22) is missing, and we end up with the bulk-edge correspondence

$$\mathcal{I} \underset{\lim}{=} W_\uparrow^+ \tag{1.28}$$

that relates the chirality of zero-energy edge modes, at a given edge, to a winding number in the bulk of the lattice.

We now illustrate this approach on the seminal example of the dimerized chain: the so-called Su–Schrieffer–Heeger model.

Example: The Su–Schrieffer–Heeger (SSH) chain

A seminal example of a $1D$ chiral symmetric lattice model exhibiting zero-energy edge modes, is that of a $1D$ dimerised chain, often referred to as the Su-Schrieffer-Heeger (SSH) model [134] (see figure 1.6) even though there is an overlap with other types of dimerised model, like the Shockley chain [135, 136]. In any case, the unit cell owns two internal degrees of freedom denoted A and B (being the even/odd sites n in the SSH case), and the model consists of nearest neighbour staggered couplings of amplitude t and t' between A and B. Let us revisit this celebrated SSH/Shockley model in the light of the mode-shell correspondence. In fact, this model is simple enough to be analytically solvable, and we are thus able to derive the bulk-edge correspondence explicitly.

The corresponding Hamiltonian $\hat{H} = \hat{H}_{\mathrm{SSH}}$ reads

$$\hat{H} = \sum_n t\,|B,n\rangle\langle A,n| + t'\,|B,n-1\rangle\langle A,n| + h.c. \tag{1.29}$$

except at the edges where the hopping term t' leads to an empty site outside the lattice. In that case, it is put to zero (open boundary condition). Since this Hamiltonian only couples A

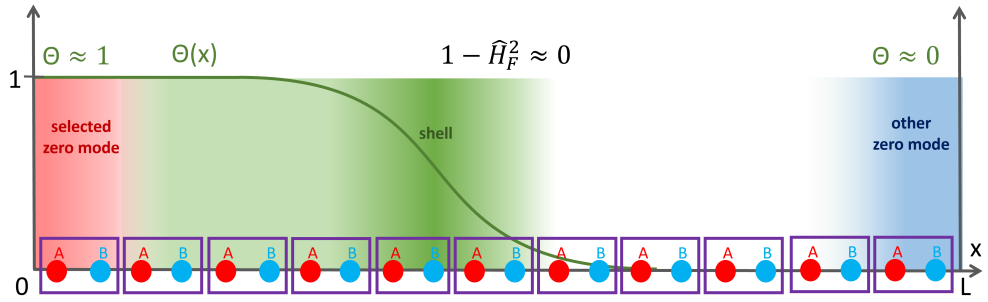

Figure 1.6: Representation of a SSH chain of $N = 10$ unit cells delimited in purple. The left red edge is the gapless region where we want to compute the chiral number of zero-modes. The right blue edge is the other gapless region of opposite chirality that is dismissed through the cut-off function $\theta(x)$ in green. The dark green zone is the shell where is evaluated the bulk-index $\frac{1}{2}\,\mathrm{Tr}\Big(\hat{C}\hat{H}_F[\hat{\theta}_\Gamma, \hat{H}_F]\Big)$ since the coefficients of the trace quickly vanish away from it.

sites with B sites, it is chiral symmetric and the chiral operator reads $\hat{C} = \sum_n |A,n\rangle\langle A,n| - |B,n\rangle\langle B,n|$. We can therefore define a chiral index $\mathcal{I}$. Then, far in the bulk, the Hamiltonian is invariant by translation and the Wigner-Weyl transform reduces to a discrete Fourier transform where

$$H(n,k) = \begin{pmatrix} 0 & t + t'e^{-ik} \\ t + t'e^{ik} & 0 \end{pmatrix} = H(k) \tag{1.30}$$

and whose energy spectrum E is gapped for $t \neq t'$. Next, we want to compute the "flatten" version of the symbol, H_F. To do so, we use the fact that, at first order of the semi-classical expansion, the symbol of $\hat{H}_F = f(\hat{H})$ is simply given by applying directly the function f to the symbol $H(n,k)$, that is $H_F = f(H(k))$. Moreover, we have chosen f such that, for gapped states of energy E, we have $f(E) = E/\sqrt{E^2}$ so, in the bulk, $H_F(x,k) = H(x,k)/\sqrt{H(x,k)^2}$. Therefore, since $H^2(n,k) = |t + t'e^{ik}|^2\,\mathbb{1}$, we deduce that

$$H_F(k) = \frac{1}{|t + t'e^{ik}|}\begin{pmatrix} 0 & t + t'e^{ik} \\ t + t'e^{-ik} & 0 \end{pmatrix}. \tag{1.31}$$

This allows us to identify $U = (t + t'e^{ik})/|t + t'e^{-ik}|$ which is just a unit complex number here. A direct computation of the winding number $W_\uparrow = \frac{1}{2i\pi}\int_{k\in S^1} dk\,\mathrm{Tr}^{\mathrm{int}}(U^\dagger(k)\partial_k U(k))$ yields $W_\uparrow = +1$ for $|t'| > |t|$ and $W_\uparrow = 0$ for $|t'| < |t|$.

We now turn to the computation of zero-modes localized at a single edge. We thus assume the lattice to be semi-infinite, with no boundary to the right and a left boundary at $n = 0$. The zero-modes of this model can be analytically found by searching them of the form $|\psi\rangle = \sum_{n\geq 0} \psi_{A,n}|A,n\rangle + \psi_{B,n}|B,n\rangle$ such that $\hat{H}|\psi\rangle = 0$. Combined with the boundary condition $\langle B,-1|\psi\rangle = 0$, we obtain the constraints

$$\begin{aligned} \langle B,n|\hat{H}|\psi\rangle &= t\psi_{A,n} + t'\psi_{A,n+1} = 0 && n \geq 0 \\ \langle A,n|\hat{H}|\psi\rangle &= t\psi_{B,n} + t'\psi_{B,n-1} = 0 && n > 0 \\ \langle A,0|\hat{H}|\psi\rangle &= t\psi_{B,0} = 0 && n = 0\,. \end{aligned} \tag{1.32}$$

If we remove the pathological case $t' = 0$, this system implies $\forall n, \psi_{B,n} = 0$ and $\psi_{A,n} = (\frac{-t}{t'})^n\psi_{A,0}$. To correspond to an edge mode, this solution must be normalized, which is only possible when $|t'| > |t|$. We deduce that one zero-energy edge mode of positive chirality (i-e: localised on the A sites only) exists for $|t'| > |t|$, leading to $\mathcal{I} = 1$, while no edge mode exists when $|t'| < |t|$, leading to $\mathcal{I} = 0$. As a result, in both cases we can check that $\mathcal{I} = W_\uparrow$ which is an illustration of the bulk-edge correspondence in a simple but non-trivial example.

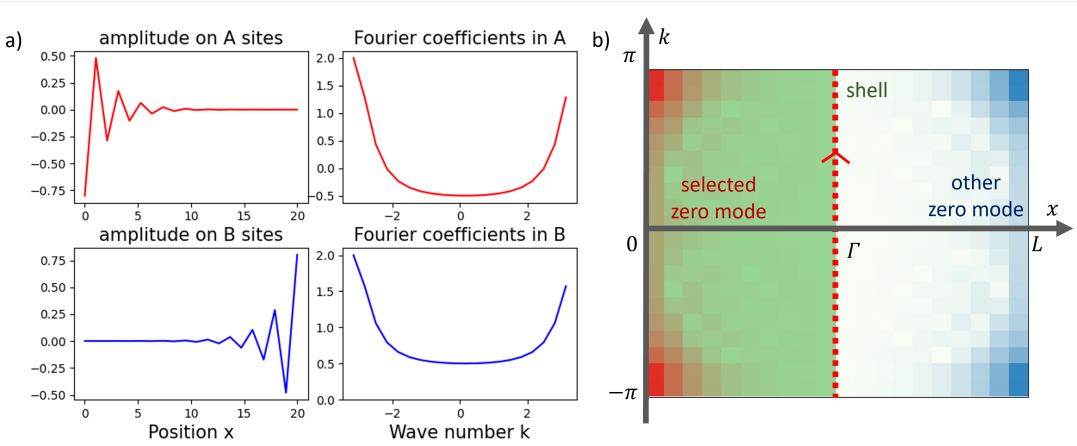

Figure 1.7: (left) Plot of the topological zero-modes of an SSH chain in real and Fourier space with $t' = 1$ and $t = 0.6$ for $N = 10$ dimers. (right) The absolute value of the Wigner-Weyl transform is plotted for the same edge mode in phase space. The region selected by the cut-off is shown in green, and its boundary (the shell), of length Γ in real space, is highlighted by a dotted line along which the winding number is integrated.

Validity of the semi-classical limit

Since the SSH model is invariant by translation far in the bulk, we have $1/d_x \to 0$ on the shell when $\Gamma \to +\infty$. Besides, as $1/d_k$ remains bounded because $\hat{H}$ is short-range in position, it implies $1/(d_x d_k) \to 0$ and therefore the semi-classical limit becomes exact in the limit $\Gamma \to +\infty$.

1.2.2 A dual bulk-boundary correspondence in wavenumber space for bounded continuous systems

General results

In the previous section, we focused on $1D$ discrete lattices and discussed an example where the zero-modes are related to a winding number on a shell defined along the k axis at large x, away from the zero-mode. In the large distance limit the lattice can be seen as infinite, and the different zero-modes, localized at opposite boundaries decouple, can be treated separately. Continuous systems are an other kind of systems with an infinite number of degrees of freedom. This infinity does not come from the the size of the system, but instead from the distance between two sites/degrees of freedom that becomes infinitesimal (see figure 1.4). At the Hilbert-space level, this limit can also be seen as the fast varying functions limit or, in other words, as the large wavenumber $k \to +\infty$ limit. In this section, we discuss how we can exploit such limits to create topologically protected zero-modes which are separated, not in position, but in wavenumber, and how the mode-shell correspondence captures this situation.

We are concerned with $1D$ continuous systems, where the physical quantities are encoded in vector-valued wave-function $|\psi(x)\rangle = (\psi_\alpha(x))_\alpha$ where x is a continuous coordinate and α labels the internal degrees of freedom. These degrees of freedom can, for example, be the spin or pseudo-spin components of quantum (quasi-)particle, like in the Dirac equation, or be a combination of classical fields, like the velocity $v(x)$ and the pressure $p(x)$ in the acoustic wave equation. As in the previous section, we assume that the time evolution of the wave function is encoded by a Hamiltonian $\hat{H}$. Because we now deal with continuous system, $\hat{H}$ is in general be differential operator which depends on position x and of some of its derivatives as $\hat{H} = \sum_n h_n(x)\partial_x^n$, where $h_n(x)$ are operators acting on the internal degrees of freedom.

Similarly to the discrete case, we use a Wigner transform (1.12) which associates, to an operator $\hat{H}$, a symbol $H(x,k)$ parameterised in phase space and acting on the internal degrees of freedom (see Appendix B) where now $k \in \mathbb{R}$ belongs to the whole real line which is not a bounded set (contrary to the lattice case where k is reduced to the Brillouin zone $[0, 2\pi]$). Therefore, the major difference with the lattice case is that there is not only the limit $x \to \pm\infty$ (i-e: far away from an interface/edge) to be considered, but also the $k \to \pm\infty$ limit of fast varying solutions. Since the limit in real space is similar to that discussed previously, we would like to focus only on the momentum limit.

For that purpose, we consider systems where the position space is bounded. Also, we choose to consider the position space as a manifold with no edges. For example, the position space could be a circle (see figure 1.4), a torus, a sphere, etc..., and the differential operators in the Hamiltonian $\hat{H}$ act on continuous functions defined on those manifolds. Then, if the Hamiltonian is gapped in the large wavenumber limit (i.e. when acting on fast varying functions) then one can define the chiral index $\mathcal{I}$ (1.8) with $\hat{\theta}_\Gamma = \exp\{\Delta/\Gamma^2\}$, which is referred to as the heat kernel associated to the Laplacian Δ on the manifold. As we already saw, this index is equal to the chirality of zero-modes through the analytical index (1.5). This framework is actually that discussed in the celebrated Atiyah-Singer index theorem, as it is described in the mathematical community [137–139]. Here, we focus on the $1D$ case where the underlying manifold is the circle, and derive the semi-classical winding number associated to chiral zero-modes. Note that since our position space is a circle, and not just a real line, it implies some subtleties in the definition of the symbol, the formula (1.12) being only valid in the real line case. But, as long as $\hat{H}$ is short range compared to the topology of the manifold, we can always use the definition (1.12) in a local chart around x to extend it to the circle case[6].

In order to derive the semi-classical index, we proceed similarly to the discrete case: We first express the term $\mathrm{Tr}\big(\hat{C}\hat{H}_F[\hat{\theta}_\Gamma, \hat{H}_F]\big)$ of the shell index, in phase space through the trace identity $\mathrm{Tr}\,\hat{A} = \frac{1}{2\pi}\int_{\mathbb{S}} dx \int_{\mathbb{R}} dk\, \mathrm{Tr}^{\mathrm{int}}\, A(x,k)$ with an integration in position on the circle. This operation maps the commutator of operators into the Moyal commutator of their symbols. We then take the limit $\Gamma \to \infty$ and keep the lower order term in $1/\Gamma$, which amounts to approximate the Moyal commutator by a Poisson bracket. This Poisson bracket contains only the term $\partial_k\theta_\Gamma\partial_x H_F$ because here the cut-off function $\theta_\Gamma = e^{-k^2/\Gamma^2}$ depends only on wavenumber and not on position. This leads to the expression

$$\mathcal{I} = \lim \frac{1}{4i\pi}\int_0^{2\pi} dx \int_{-\infty}^{+\infty} dk\, \mathrm{Tr}^{\mathrm{int}}\, C H_F(x,k)\partial_k\theta_\Gamma(k)\partial_x H_F(x,k)\ . \tag{1.33}$$

Next, we perform the integration over k. This is not as simple as the integration over x in the discrete case where we assumed a bulk (i.e. x independent) limit of the symbol Hamiltonian, since here $H_F(x,k)$ may not be totally independent of k. We can however use the fact that the right hand side of (1.33) does not depend of the special shape of $\theta_\Gamma(k)$. Therefore, we can smoothly deform the cut-off function $\theta_\Gamma = \exp(-k^2/\Gamma^2)$ into the sharper one $\tilde{\theta}_\Gamma = \mathbb{1}_{|k|\leq\Gamma}$ such that the derivative $\partial_k\theta_\Gamma$ can be replaced by a δ-Dirac distribution, which transforms the surface

[6] In particular one can use the geodesic chart to describe the neighborhood of x as a subset of $\mathbb{R}$ (see [140] for a more formalised definition). There is however some problem for curved manifold, the semi-classical expansion is modified in those cases. Also our proof of the semi-classical invariants in the higher-dimension case relies on the existence of operators verifying $[a_i, b_j] = \delta_{i,j}\,\mathbb{1}$ which can only be found when the phase space is $\mathbb{R}^d \times \mathbb{R}^d$ or $\mathbb{R}^d \times \mathbb{T}^d$. Therefore our formula (1.56) only works in the case where the position manifold is a n-torus (which has no intrinsic curvature). As the general expression of the symbol index in the Atiyah-Singer theorem involves the curvature of the manifold, it is not surprising that our formula is limited to the n-torus cases which are manifolds of zero curvature. We believe there is a way to derive the general Atiyah-Singer theorem using the fact that any manifold can in fact be embedded in $\mathbb{R}^m$ where our semi-classical formula could be applied. But the derivation of the formula would go beyond the scope of this thesis.

integral in phase space into two line integrals over x at $k = \pm\Gamma$ as

$$\mathcal{I} \underset{\lim}{=} \frac{1}{4i\pi}\int_0^{2\pi} dx\, \mathrm{Tr}^{\mathrm{int}}(C(-H_F(x,\Gamma)\partial_x H_F(x,\Gamma) + H_F(x,-\Gamma)\partial_x H_F(x,-\Gamma))) \tag{1.34}$$

$$\underset{\lim}{=} \frac{1}{2\pi i}\int_0^{2\pi} dx\, \mathrm{Tr}^{\mathrm{int}}\left(-U^\dagger(x,\Gamma)\partial_x U(x,\Gamma) + U^\dagger(x,-\Gamma)\partial_x U(x,-\Gamma)\right) . \tag{1.35}$$

Finally, we obtain that the chiral index is again related to a difference of winding numbers, but where the integration runs now over position space for large positive/negative wavenumbers, as depicted by horizontal dashed lines in figure 1.8. We thus indicate this "horizontal" line integration in phase space by horizontal arrows, so that we get

$$\mathcal{I} \underset{\lim}{=} -W^+_{\rightarrow} + W^-_{\rightarrow} \tag{1.36}$$

where $\pm$ refers to $k = \pm\Gamma$. This is a second application of the mode-shell correspondence in $1D$ where the relation to a difference of winding number $W^{\pm}_{\rightarrow}$ is a particular case of (1.14). It can be seen as dual to the lattice case previously discussed, and in particular, (1.36) can be compared to (1.27). In both cases, the shells correspond to lines in a single subspace, either x or k, and they both enclose chiral-zero modes in phase space. In the present case, those modes are "located" in the region of small wavenumber region, while the shell, in the semi-classical limit, is considered in the region of high wavenumber. The mode-shell correspondence thus better translates here to a correspondence between different region separated in wavenumber, rather than to a *bulk-edge* or *bulk-interface* correspondence in position. We now illustrate this correspondence with an example.

Example: $1D$ Dirac equation on the circle with varying potential and velocity

To illustrate the previous result, we propose the following model of a Dirac Hamiltonian on a circle

$$\hat{H}(x,\partial_x) = \begin{pmatrix} 0 & V(x) + c(x)\partial_x \\ V(x) - \partial_x c(x) & 0 \end{pmatrix} \tag{1.37}$$

where the potential $V(x)$ and the local velocity $c(x)$ are bounded and L-periodic functions that can change sign. The symbol of this operator is obtained by replacing the product of the non-commuting operators $c(x)\partial_x$ by the Moyal product of their symbol $c(x) \star ik = c(x)ik - c'(x)/2$ with $c'(x) \equiv \partial_x c(x)$, that is

$$H(x,k) = \begin{pmatrix} 0 & V(x) + ikc(x) - c'(x)/2 \\ V(x) - ikc(x) - c'(x)/2 & 0 \end{pmatrix} . \tag{1.38}$$

To check if the the semi-classical expression of the shell invariant can be used in the limit $\Gamma = k \to \infty$, we evaluate $1/(d_x d_k) = \|\partial_x H(x,k)\|\|\partial_k H(x,k)\|/\Delta(x,k)^2$ that varies as $\frac{1}{k}|\frac{c'(x)}{c(x)}|$ in that limit. The semi-classical criteria $1/(d_x d_k) \ll 1$ is thus reached, unless $c(x)$ vanishes, a situation we consider here. In that case, the term $1/d_k$ accidentally vanishes and we should check the next order term of the semi-classical expansion, $\|\partial_x\partial_k H/\Delta\|_{c=0} = c'(x)/(V(x) - c'(x)/2)|_{c=0}$. This term is not necessary negligible in general, and in particular when the amplitude of the potential $V(x)$ is comparable with that of the gradient of the velocity $c'(x)$ (the gap may even close). One way to make this term small, is to consider a very large periodic system $L \to \infty$ such that the gradient of velocity can be re-expressed as $c'(x') = c'(x)/L$ after the rescaling $x = Lx'$, and becomes negligible compared to $V(x')$. The small parameter $\epsilon \equiv 1/L$ thus controls the semi-classical limit, when $V(x)$ and $c'(x)$ are comparable in amplitude. By setting $\Gamma = k \sim 1/\epsilon \to \infty$,

one gets the semi-classical symbol

$$H(x,k) \simeq \begin{pmatrix} 0 & V(x)+ikc(x) \\ V(x)-ikc(x) & 0 \end{pmatrix} \tag{1.39}$$

(where we have substituted the notation $x' \to x$) which is indeed uniformly gapped in phase space and satisfies $1/(d_x d_k) \ll 1$ when $k \to \infty$. From now, we can set $V(x) = \cos(x)$ and $c(x) = \sin(x)$ in the operator (1.37), and get a semi-classical description in the large system limit $L \gg 1$ with (1.39), where the shell invariant can be expressed as the winding number $W_{\to}$. Note that the term $c'(x)$ may be kept in the symbol of other models, in particular if $c(x)$ is not allowed to vanish, as encountered for instance in [38, 141], and where the topological number must be extracted from a slightly more involved symbol Hamiltonian than cannot be obtained from the operator by simply substituting $x \to x$ and $\partial_x \to ik$.

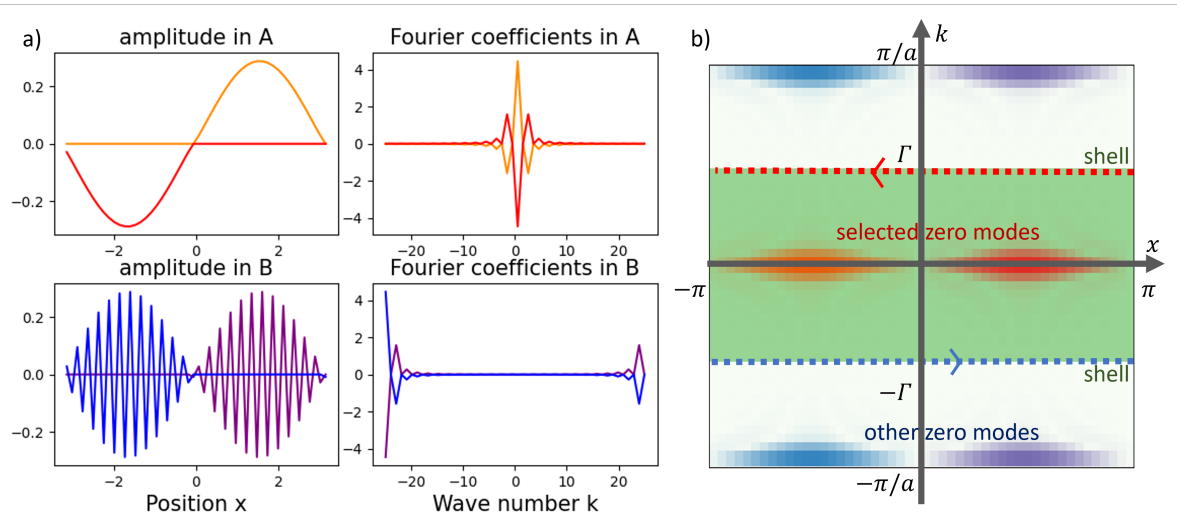

Figure 1.8: a) Zeros-modes of a discretised version of (1.37) where continuous derivatives are replaced by their discrete counterparts, with $\epsilon = 1/L = 0,05$ and $N = 50$ sites (containing each two degrees of freedoms A/B) and therefore an inter-site distance of $a = 2\pi/N$. The zero-modes are shown in real space (left) and in wavenumber space (right). Those modes are stationary with an exponentially small error $\|\hat{H}\,|\psi\rangle\,\| \sim 10^{-9}$. b) Absolute value of the Wigner-Weyl transform of the different zero-modes in phase space. The integration contours of the winding numbers correspond to the shell enclosing the low wavenumber zero-modes and are denoted by two dotted lines.

To compute the winding numbers $W_{\to}$ for the model above, we introduce the shell $\{(x,k), x \in [0,2\pi], k = \pm\Gamma\}$ which consists in two circles in position at fixed $k = \pm\Gamma$ in a cylindrical phase space. The off diagonal component of the Hamiltonian is just $h(x,k) = \cos(x) - i\epsilon k \sin(x)$ so one can compute the winding numbers and we find $W_{\to}^{+} = -1$ for positive k and $W_{\to}^{-} = 1$ for negative k (for $\epsilon > 0$). Therefore, according to the mode-shell correspondence the total chirality of zero-modes of $\hat{H}$ should be $\mathcal{I} = -(-1) + 1 = 2$. One thus expects the operator $\hat{H}$ to have at least two zeros-modes of positive chirality in the relatively slowly varying region. This is indeed the result obtained for numerical simulations of the model (see Figure 1.8), where we indeed find 2 zero-modes of positive chirality (i.e. fully polarized on the A degrees of freedom) and located in the low-wavenumber $k \sim 0$ region. Due to the discretisation procedure when solving the model numerically, we moreover find two other zero-modes localised at high wavenumber. Those additional zero-modes have together a chirality of -2 (i.e. fully polarized on the B degrees of freedom) that balance the total chirality of zero-modes in this discretised version of the model.

Remarks on the protection of zero-modes separated in wavenumber space

It is clear that for the finite size topological insulators, such as the SSH chain, boundary modes localised at opposite edges can hybridise. The coupling between those modes can however be negligible whenever the lattice is sufficiently long, that is, more precisely, when the characteristic distance d_x of the coupling elements $\hat{H}_{x,x'}$ in position space remains much smaller than the size L of the lattice.

Similarly to the example discussed above, the discretisation of a continuous model typically induces multiple gapless modes which are separated from each other in wavenumber. Using the duality between wavenumber and position space we can translate the previous criteria of weak hybridization into wavenumber space, by demanding that the couplings in wavenumber space $\hat{H}_{k,k'}$ are short-range and decays with a characteristic distance d_k in wavenumber which is much smaller than the lattice wavenumber $k_0 = 2\pi/a$ of the lattice (where a is the lattice spacing). Using the Wigner-Weyl transform, this is equivalent to demand that the symbol Hamiltonian $H(x,k)$ varies slowly in position space (see appendix A and B): its typical variations must evolve over a much larger distance than the inter-site spacing.

One should note that this condition for the non-hybridization of the zero-modes in wavenumber space is quite different from the position case, and may be difficult to reach in practice, depending on the physical context of interest. For example, in condensed matter systems, the introduction of an impurity or a vacancy in the lattice induces variations of the electronic potential over a characteristic distance equivalent to the size of the lattice and immediately hybridises edge states separated in wavenumber, and thus gap them [142]. Therefore, condensed matter applications would require a strict limitation of such impurities. In other physical systems, like in fluid mechanics or in acoustics, the smooth variation of the system's parameters in space is probably more naturally realised due to local homogenisation.

1.2.3 A mixed $x-k$ correspondence in phase space for unbounded continuous $1D$ systems

In the previous sections, we explained how the topological nature of chiral zero-modes is revealed by isolating them through large gapped regions which surround them either in position (case of unbounded $1D$ lattices) or in wavenumber (case of bounded continuous $1D$ systems). In the present section, we want to address the mixed case where the modes are surrounded by a gap region both in position and momentum directions.

For that purpose, let us consider unbounded $1D$ continuous systems. We make use of the continuous Wigner transform (1.12) to map the Hamiltonian $\hat{H}$ to the symbol $H(x,k)$ acting on internal degrees of freedom, and parameterised in phase space $(x,k) \in \mathbb{R}\times\mathbb{R}$ (see Appendix B). We therefore have to deal with both limits $x \to \pm\infty$ (i.e. far away from an interface hosting zero-modes) and $k \to \pm\infty$ (i.e. fast varying solutions). We thus consider a mixed cut-off operator such as $\hat{\theta}_\Gamma = e^{-(x^2-\partial_x^2)/\Gamma^2}$ of symbol $\theta_\Gamma(x,k) \approx e^{-(x^2+k^2)/\Gamma^2}$ at first order of the semi-classical expansion. Now, the gap hypothesis means that we assume the symbol $H(x,k)$ to be gapped both when $|x| \to \infty$ and when $|k| \to +\infty$ (even for x near the interface). For example, $H(x,k) = \left(\begin{smallmatrix} 0 & x+ik \\ x-ik & 0 \end{smallmatrix}\right)$ satisfies such requirement since its spectrum $\pm\sqrt{x^2+k^2}$ converges uniformly toward infinity for both $x \to \pm\infty$ and $k \to \pm\infty$.

We can then derive the semi-classical expression of the chiral invariant by rewriting the term $\mathrm{Tr}\Big(\hat{C}\hat{H}_F[\hat{\theta}_\Gamma, \hat{H}_F]\Big)$ similarly to the two previous sections (the term $\mathrm{Tr}\,\hat{C}\hat{\theta}_\Gamma$ vanish to preserve the gap assumption if we have a balanced number of degrees of freedom), that is by turning the trace into an integral over phase space and then expanding to lowest order in $1/\Gamma$ by assuming

that $H_F(x,k)$ varies slowly for large $|(x,k)|$, which leads to

$$\mathcal{I} \underset{\text{lim}}{=} \frac{-1}{4i\pi}\int_{\mathbb{R}} dx \int_{\mathbb{R}} dk\, \mathrm{Tr}^{\text{int}}(CH_F(\partial_x\theta_\Gamma\partial_k H_F - \partial_k\theta_\Gamma\partial_x H_F)) \ . \tag{1.40}$$

Note that all the terms of the Poisson bracket appear, in contrast with the winding numbers previously derived in sections 1.2.1 and 1.2.2. If we denote by $dA = \partial_x A\, dx + \partial_k A\, dk$ the differential one-form of the symbol A, the expression (1.40) can be written in a more compact fashion as

$$\mathcal{I} \underset{\text{lim}}{=} \frac{-1}{4i\pi}\int_{\mathbb{R}^2} \mathrm{Tr}^{\text{int}}(CH_F d\theta_\Gamma \wedge dH_F) \tag{1.41}$$

where $\wedge$ is the usual anti-symmetric wedge product. Moreover since $H_F(x,k)$ is assumed to vary slowly, the integration of $d\theta_\Gamma$ can be done independently. The integration on the two-form is then reduced to the integration of a one-form on the circle of radius Γ, which is tangent to the gradient of θ. This leads to the final result

$$\mathcal{I} \underset{\text{lim}}{=} \frac{1}{4i\pi}\int_{S^1(\Gamma)} \mathrm{Tr}^{\text{int}}(CH_F dH_F) \tag{1.42}$$

$$\underset{\text{lim}}{=} \frac{1}{2i\pi}\int_{S^1(\Gamma)} \mathrm{Tr}^{\text{int}}(U^\dagger dU) \equiv W_{\circlearrowleft} \tag{1.43}$$

which is again a winding number, but where the integration runs now over the circle $x^2+k^2=\Gamma^2$ in phase space instead of the Brillouin zone $k \in [0, 2\pi]$ (for discrete unbounded systems) or the position space $x \in [0, 2\pi]$ (for continuous circular systems). This is therefore a different semi-classical manifestation of the mode-shell correspondence, where the circle encloses the zero-mode in phase space.

Example: The Jackiw-Rebbi model

The simplest example of a continuous $1D$ Hamiltonian operator $\hat{H}$ involving both x and ∂_x which is topological is given by the celebrated Jackiw-Rebbi model

$$\hat{H} = \begin{pmatrix} 0 & x-\partial_x \\ x+\partial_x & 0 \end{pmatrix} . \tag{1.44}$$

This Hamiltonian can be thought of as a one dimensional Dirac Hamiltonian $\hat{H} = -i\partial_x\sigma_y$ with a linearly varying potential $V(x)\sigma_x$ that can be seen as a mass term.[7] Such a Hamiltonian can for instance be obtained in stratified and/or compressible fluids where the pressure and velocity are additionally coupled through an acoustic-buoyant frequency $S(x) = V(x)$ [38,51] which changes sign in space. This coupling can have many origins, for example in fluids, where the sound velocity varies in space and reaches a minimum. We will also see later that this Hamiltonian can be obtained as a continuous version of an SSH model with slowly varying couplings.

The Hamiltonian (1.44) is easily diagonalizable by introducing the bosonic creation-annihilation operators $a = (x+\partial_x)/\sqrt{2}$ and $a^\dagger = (x-\partial_x)/\sqrt{2}$

$$\hat{H} = \sqrt{2}\begin{pmatrix} 0 & a^\dagger \\ a & 0 \end{pmatrix} . \tag{1.45}$$

One can then easily check that $\hat{H}$ has a unique zero-mode $(e^{-x^2/2}/\sqrt{2\pi}, 0)^t$ (see figure 1.9) with positive chirality in the convention $\hat{C} = \left(\begin{smallmatrix} 1 & 0 \\ 0 & -1 \end{smallmatrix}\right)$.

[7] Usually the potential is written as $V(x)\sigma_z$ but this is equivalent to our model up to a change of basis which exchanges $\sigma_z \leftrightarrow \sigma_x$.

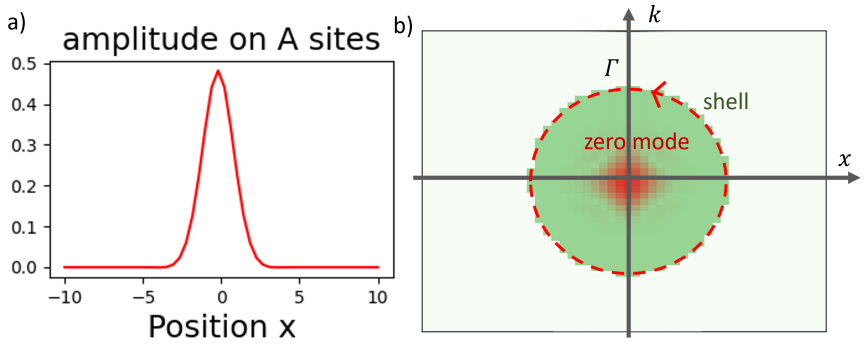

Figure 1.9: a) Amplitude of the zero mode of the Jackiw-Rebbi model in position b) Wigner-Weyl representation of the zero mode in phase space

The symbol of this Hamiltonian has the simple form

$$H = \begin{pmatrix} 0 & x - ik \\ x + ik & 0 \end{pmatrix} \tag{1.46}$$

and its energy spectrum reads $\pm\sqrt{k^2 + x^2}$ which indeed satisfies the gap condition when $|x|$ or $|k|$ is large. Moreover, the symbol of the flatten Hamiltonian can be computed easily as $H_F(x,k) = f(H(x,k)) = H(x,k)/\sqrt{H(x,k)^2}$. By using $H(x,k)^2 = (x^2 + k^2)\,\mathbb{1}$, we obtain

$$H_F(x,k) = \frac{1}{\sqrt{x^2+k^2}} \begin{pmatrix} 0 & x - ik \\ x + ik & 0 \end{pmatrix} = \begin{pmatrix} 0 & e^{-i\phi} \\ e^{i\phi} & 0 \end{pmatrix} \tag{1.47}$$

which yields the expression for $U = e^{i\phi}$. One can then compute $U^\dagger dU = id\theta$ so that the winding number $W_{\circlearrowleft} = \frac{1}{2i\pi}\int_{S^1} \mathrm{Tr}^{\mathrm{int}}(U^\dagger dU)$ gives $W_{\circlearrowleft} = 1$ in agreement with the number of chiral zero-modes.

Validity of the semi-classical limit

In this example, we have $\partial_{x/k} H = \sigma_{x/y}$ and therefore $\|\partial_{x/k} H\| = 1$, which does not decrease when (x,k) is large. However, because the gap of $H(x,k)$ varies as $\sqrt{x^2+k^2}$, our definition of $1/d_{x/k} = \|\partial_{x/k} H(x,k)\|/\Delta(x,k)$ yields $1/d_{x/k} = O(1/\sqrt{x^2+k^2})$ and hence $1/(d_x d_k) \to 0$. So, this is an example where, even though the variations of the symbol do not vanish at infinity, we still have an exact semi-classical limit because those variations become small compared to the gap.

1.2.4 Discrete approximations of continuous/unbounded topological models

In the previous section, we introduced the topological Hamiltonian (1.44) which acts on a continuous system that is unbounded both in position and wavenumber spaces. However, in practice, there are physical or numerical limitations which impose bounds on the validity of the model at high position/wavenumber. It is therefore instructive to study finite versions of such models with cut-offs in wavenumber and position. Such finite models are therefore defined on a lattice of lattice spacing a and size L.

For example, the Hamiltonian (1.44) can be seen as a continuous limit of a discrete SSH Hamiltonian with varying coefficients. If one takes the symbol of the discrete SSH model (1.31) and replaces the constant coefficients t and t' by $t' = 1/a$ and $t = -1/a + \sin(2\pi x/L)L/(2\pi)$,

one obtains a discrete Hamiltonian on a finite lattice of lattice spacing a and length $L >> a$ with periodic boundary conditions, whose symbol reads

$$H_I(x,k) = \begin{pmatrix} 0 & \sin\left(\frac{2\pi x}{L}\right)\frac{L}{2\pi} + \frac{e^{-ika}-1}{a} \\ \sin\left(\frac{2\pi x}{L}\right)\frac{L}{2\pi} + \frac{e^{ika}-1}{a} & 0 \end{pmatrix} \tag{1.48}$$

and which, by construction, approximates the Jackiw-Rebbi model in the limit $a \to 0$ and $L \to +\infty$.

We now want to determine the points (x,k) of phase space where band crossings occur at zero-energy (see figure 1.10). Indeed, if such singular points exist and are surrounded by sufficiently large gapped regions in phase space, their non-zero winding number would be associated with topologically protected chiral zero-modes at the operator level (see figure 1.11). Those points are solution of the equation

$$\sin(2\pi x/L)L/(2\pi) + (e^{ika}-1)/a = 0 \iff \begin{cases} \sin(ak)/a = 0 \\ (\cos(ka)-1)/a + \sin(2\pi x/L)L/(2\pi) = 0 \end{cases}. \tag{1.49}$$

This system has the expected solution $(x,k) = (0,0)$ of winding number $W_{\circlearrowleft} = +1$ consistently

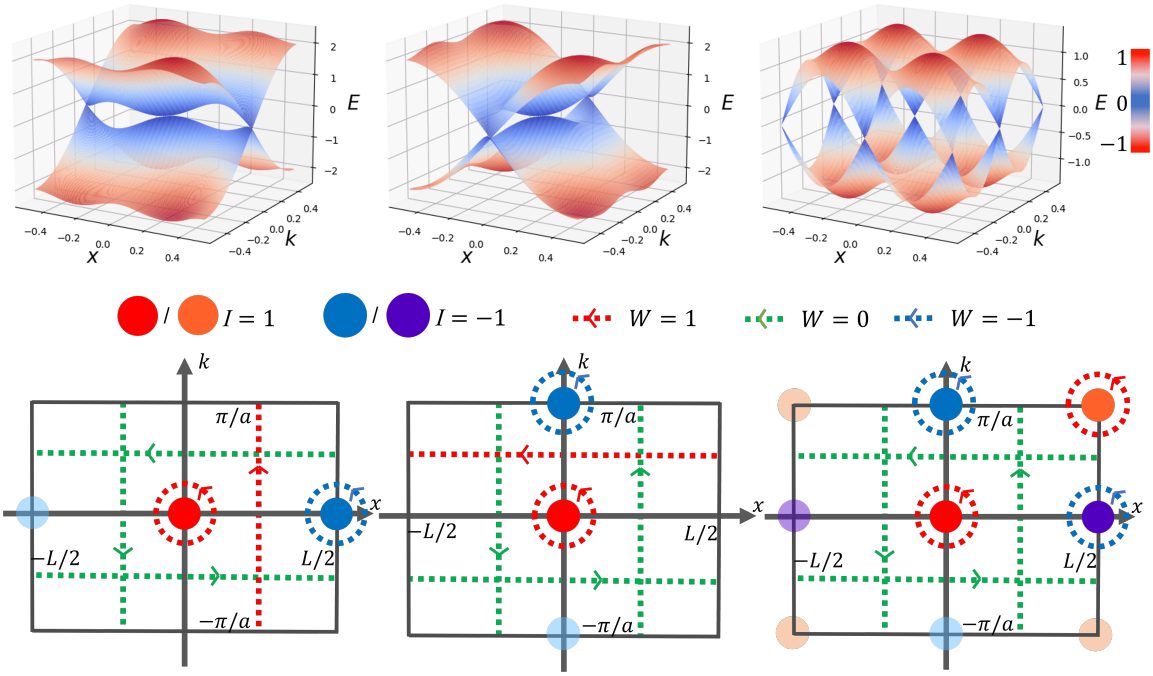

Figure 1.10: (top) Energies of the symbol Hamiltonians for (left) the model H_I in the regime $4\pi/(aL) > 1$, (center) the model H_{II} in the regime $La/\pi > 1$ and (right) the model H_{III}. (bottom) Position of the gap closing points of in phase space. Those positions are denoted by a red/blue dot depending on the chirality of the zero-mode associated to them at the operator level (light color is used for the equivalent periodic images). The different values of the winding number W is enhanced by a red/blue/green color.

with the fact that this model is built in order to approximate the continuous Jackiw-Rebbi model whose symbol (1.46) also has this singular point. However, due to the discretisation process, we also get another singular point $(x,k) = (L/2,0) = (-L/2,0)$ (due to the L periodicity in x), and whose winding number is found to be $W_{\circlearrowleft} = -1$ (see figure 1.10). The two winding

numbers therefore sum up to zero as it is expected for finite lattices with equal number of sites of positive/negative chirality. This is due to the fact the total chiral number of zero modes of a finite Hilbert space is given by $\mathcal{I}_{\text{modes}}$ where the cut-off is the identity $\theta_\Gamma = \mathbb{1}$. Therefore its corresponding shell index (1.9) must vanish ($[\mathbb{1}, \hat{H}_F] = 0$). The existence of such a second singular point due to the discretisation process is therefore topologically constrained.

Note that those two singular points are the only existing ones when $4\pi/(aL) > 1$. In the case $4\pi/(aL) < 1$, two other points also appear at $(x,k) = (\arcsin(4\pi/(aL))/(2\pi)L, \pi/a)$ and $(x,k) = (L/2 - \arcsin(4\pi/(aL))/(2\pi)L, \pi/a)$ which are also characterized by a non-zero winding numbers that sum up to zero. For the sake of brevity and simplicity, we shall however only focus our discussion on the case $4\pi/(aL) > 1$ that yields only two singular points.

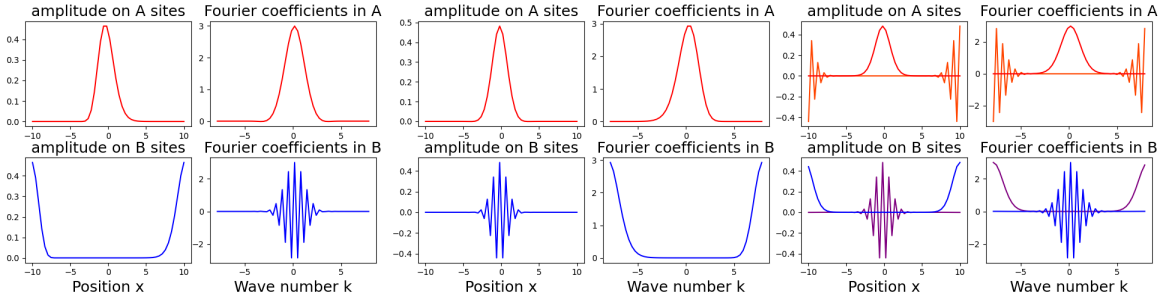

Figure 1.11: Plots of the different zero-modes of the operator associated to the symbol (left) H_I, (center) H_{II}, and (right) H_{III} with $L = 20$ and $a = 0.4$. We plot in red/orange the modes of positive chirality and in blue/purple the modes of negative chirality in real space and Fourier space. All those modes are zero-modes in a very good approximation $\|H\,|\psi\rangle\,\| < 10^{-9}$.

In that case, the two chiral zero-modes associated, at the operator level, to these two degeneracy points of opposite winding numbers, resemble the two edge states of the standard SSH model with open boundary conditions, in that they are well separated in position space, around $x = 0$ and $x = L/2$, the only difference being that the new system displays smoother interfaces. Therefore, one can also apply the usual bulk-edge correspondence, by relating the existence of a topological zero-mode with the difference of Brillouin zone winding numbers $W_\uparrow$ far to the left/right side of the mode in position space (vertical dashed lines in figure 1.10). The two results agree i.e. the value of the winding number $W_{\circlearrowleft}$, when the shell circles around a zero-energy degeneracy point, corresponds to the difference of the Brillouin zone winding numbers $W_\uparrow$ from each side of the interface (see figure 1.10).

One should nevertheless notice that this equivalence is only well established here because there is no other singular mode in the vertical line ($x = 0, k \in [0, 2\pi/a]$) and so that the circle surrounding a degeneracy point can be smoothly deformed into two vertical lines along the Brillouin zone without crossing another band crossing. This is not always the case, and a good illustration is the following dual model of (1.48) where position and wavenumber play inverted roles

$$H_{II}(x,k) = \begin{pmatrix} 0 & -i\frac{\sin(ak)}{a} + i(e^{-i2\pi x/L} - 1)\frac{L}{2\pi} \\ i\frac{\sin(ak)}{a} - i(e^{i2\pi x/L} - 1)\frac{L}{2\pi} & 0 \end{pmatrix} . \tag{1.50}$$

The Jackiw-Rebbi model is again recovered in the limit $a \to 0$, $L \to +\infty$, but this second discretized model also exhibits two singular points (in the regime $La/\pi > 1$) $(x,k) = (0,0)$ and $(x,k) = (0,\pi/a)$ which are now separated in wavenumber space rather than in position space. The associated chiral zero-modes, at the operator level, are thus only separated in wavenumber space, unlike the previous discrete model[8]. As such, the difference of Brillouin zone winding

[8] As discussed at the end of the section 1.2.2, this make the zero modes typically less protected in condensed

numbers $W_\uparrow$ vanishes and is thus unable to detect the existence of chiral zero-modes. This is an example where the bulk-edge correspondence of a discretized version of a continuous model is not appropriate to identify chiral zero-modes, while the mixed $x-k$ correspondence, applied locally in phase space, still is. The difference of position winding numbers $W_\rightarrow$ along horizontal lines of positive/negative wavenumber – as in the bounded continuous case of section 1.2.2 – however coincides with the value of $W_\circlearrowleft$, since no low-wavenumber singular points is here to prevent the deformation of the circle contour into the horizontal one.

Finally, since the topological index only accounts for modes localised both in position and wavenumber spaces, pairs of spurious zero-modes of opposite chirality separated in either or both position/wavenumber directions could appear when one studies finite approximations of a continuous model. A last example where zero-modes appear on both directions is provided by the model

$$H_{III}(x,k) = \begin{pmatrix} 0 & -i\frac{\sin(ak)}{a} + \sin(2\pi x/L)\frac{L}{2\pi} \\ i\frac{\sin(ak)}{a} - \sin(2\pi x/L)\frac{L}{2\pi} & 0 \end{pmatrix} \tag{1.51}$$

which again converges to the Jackiw-Rebbi model in the limit $L \to +\infty$ and $a \to 0$, but displays now 4 singular points in phase space: 2 of winding number $W_\circlearrowleft = +1$ at $(x,k) = 0$ and $(x,k) = (L/2, \pi/a)$, and 2 of winding number $W_\circlearrowleft = -1$ at $(x,k) = (L/2, 0)$ and $(x,k) = (0, \pi/a)$. Therefore, the only winding numbers that can detect the presence of chiral zero-modes are the $W_\circlearrowleft$'s of the mixed $x-k$ mode-shell correspondence, that are evaluated on $(x-k)$-circle in phase space, since the position and Brillouin zone winding numbers $W_\rightarrow$ and $W_\uparrow$ both vanish.

Those three examples illustrate why the mode-shell correspondence is a natural and general formalism to describe in a unified fashion the existence of all the topologically protected chiral zero-modes. The bulk-edge correspondence and the low-high-wavenumber correspondence are just particular cases which, alone, are not always able to predict the existence of topologically protected chiral zero-modes.

1.3 Higher dimensional chiral mode-shell correspondences

1.3.1 Expression of the general chiral index

In the previous sections, we focused on the mode-shell correspondence in systems of dimension $D = 1$ since this is where the semi-classical invariant takes the simplest forms. However the mode-shell correspondence generalizes when chiral zero-modes are embedded in a space of higher dimension $D > 1$. While this correspondence can still easily be shown to satisfy $\mathcal{I}_{\text{modes}} = \mathcal{I}_{\text{shell}}$, the main difficulty is to obtain a semi-classical expression of the invariant $\mathcal{I}_{\text{shell}}$.

In practice, a naive semi-classical expansion of the shell index for $D \geqslant 1$ (i.e. with cut-off parameter $\Gamma \to +\infty$), would lead to an expansion of the form

$$\mathcal{I}_{\text{shell}} = \sum_{k=1}^{D_\mathcal{I}} c_k \Gamma^{D_\mathcal{I}-k} + O(1/\Gamma) \tag{1.52}$$

where $D_\mathcal{I}$ is the number of infinite dimensions (in position and in wavenumber) of the problem. In the $1D$ case, one can show that $c_0 = \sum_\alpha C_\alpha$ is the sum of the chirality of the internal degrees of freedom of the lattice (which in practice, always vanish in model with a bulk gap) and $c_1 = W^+ - W^-$. In general, because the index must converge toward an integer in the $\Gamma \to +\infty$ limit, some cancellations must occur so that $c_k = 0$ for $k < D_\mathcal{I}$ and only the term $c_{D_\mathcal{I}}$ remains, which turns out to be a (higher dimensional)-winding number. However it is not easy

matter applications as they can now be mixed in presence of lattice impurities which induce long range wavenumber couplings in phase space.

to prove that $c_k = 0$ for all $k < D_{\mathcal{I}}$ in an explicit way. More importantly, because we would need to carry the naive semi-classical expansion of $\mathcal{I}_{\text{shell}}$ to a higher order term, in order to capture the converging component $c_{D_{\mathcal{I}}}$, the number of terms in the expression of $c_{D_{\mathcal{I}}}$ should rise, which is difficult to manage and simplify.

In the appendix of the paper [123], we developed a systematic method to make the cancellations apparent at the level of the operators. We are therefore able to obtain an operator expression of the shell index whose semi-classical limit gives directly the coefficient $c_{D_{\mathcal{I}}}$ as the leading term. This allows us to obtain a meaningful semi-classical expression of the shell index, as a generalized winding number $\mathcal{W}_{2D-1}$ in $2D-1$ dimensions as

$$\mathcal{I}_{\text{shell}} \underset{\text{lim}}{=} \frac{-2(D!)}{(2D)!(2i\pi)^D} \int_{\text{shell}} \text{Tr}^{\text{int}}(U^\dagger dU)^{2D-1} \equiv \mathcal{W}_{2D-1} \tag{1.53}$$

which is the expression anticipated in the introductory general outlines (1.14). This is one of the key results of this thesis. We now provide some elements of the proof of this formula to give some intuition of the result while keeping the more computational intensive part in the appendix of the paper [123].

Consider a D-dimensional system whose Hilbert space basis is labelled by $\mathbb{Z}^n \times \mathbb{R}^m \times [\![1, K]\!]$ with $n + m = D$, where n is the number of discrete dimensions, m is the number of continuous dimensions and K is the number of internal degrees of freedom. Sub-systems of $\mathbb{Z}^n \times \mathbb{R}^m \times [\![1, K]\!]$ such as e.g. the discrete and continuous half-planes ($\mathbb{N} \times \mathbb{Z}$ and $\mathbb{R}^+ \times \mathbb{R}$ respectively) as well as finite lattices, could also be included as we often have a natural way to extend the sub-system Hamiltonian to a larger system by introducing trivial coefficients with no inter-site coupling elsewhere.

After assuming this structure, we assign to each continuous dimension i a position operator x_i and a wavenumber operator ∂_{x_i} which satisfy $[\partial_{x_i}, x_i] = \mathbb{1}$. Similarly, to each discrete dimension i is assigned a position operator n_i and a translation operator T_i which satisfy $T_i^\dagger n_i T_i - n_i = \mathbb{1}$. To treat the continuous and discrete cases in a unified way, we can define the operator $\hat{a}_i$ as $\hat{a}_{2j} = x_j$ and $\hat{a}_{2j+1} = i\partial_{x_j}$ in the continuous case, and as $\hat{a}_{2j} = T_j^\dagger n_j$ and $\hat{a}_{2j+1} = -iT_j$ in the discrete case, so that we have the single commutation relation $[\hat{a}_{2j+1}, \hat{a}_{2j}] = i\,\mathbb{1}$.

Since this commutation relation is proportional to the identity, it allows us to use an "integration by part trick". Indeed, similarly to functions, where $\int dx a(x) = -\int dx x \partial_x a(x)$, we also have the following relation for operators

$$\text{Tr}\,\hat{A} = \text{Tr}\Big([\partial_x, x]\hat{A}\Big) = -\,\text{Tr}\Big(x[\partial_x, \hat{A}]\Big)\,. \tag{1.54}$$

In the appendix of the paper [123] we use such an integration by part to make appear some cancellations at the operator level, and thus obtain another expression of the shell index which reads

$$\begin{aligned}\mathcal{I} = (-i)^D \frac{D!}{(2D)!} \Bigg(&\text{Tr}\left(\sum_{j_1 \dots j_{2D}=1}^{2D} \varepsilon_{j_1,\dots,j_{2D}} \hat{C}\hat{H}_F \prod_{l=1}^{2D-1} [\hat{a}_{j_l}, \hat{H}_F][\hat{a}_{2D}, \hat{\theta}_\Gamma] \right) \\ &+ \frac{1}{2}\,\text{Tr}\left(\sum_{j_1 \dots j_{2D}=1}^{2D} \varepsilon_{j_1,\dots,j_{2D}} \hat{C}\hat{H}_F \prod_{l=1}^{2D} [\hat{a}_{j_l}, \hat{H}_F][\hat{\theta}_\Gamma, \hat{H}_F] \right) \Bigg) + O(\Gamma^{-\infty})\end{aligned} \tag{1.55}$$

where $\epsilon_{j_1,\cdots,j_{2D}}$ is the antisymetrised Levi-Civita tensor with orientation convention such that $(k_1, x_1, \dots, k_D, x_D)$ is a direct base. $O(\Gamma^{-\infty})$ means that the equality is valid up to terms which decay faster than any polynomial in Γ.

The equality (1.55) can be obtained by assuming only that $\hat{H}$ is gapped deep inside the shell. But if moreover the symbol $H(x, k)$ admits a semi-classical limit when $\Gamma \to +\infty$, we can show

that (1.55) reduces to the simplified expression

$$\mathcal{I}_{\text{shell}} \underset{\text{lim}}{=} \frac{D!}{(2D)!(-2i\pi)^D} \int_{\text{shell}} \text{Tr}^{\text{int}}(CH_F(dH_F)^{2D-1}) \tag{1.56}$$

where dH_F is now the differential 1-form of H_F in phase space which replaces the commutators $[\hat{a}_{j_l}, \hat{H}_F] \approx i\partial_{j_l}\hat{H}_F$ in the semi-classical limit, dH_F^{2D-1} is the $2D-1$-wedge product of dH_F, and the shell is the $2D-1$ dimensional surface enclosing the zero-mode in phase space. The final result (1.53) is then obtained by substituting H_F by

$$H_F = \begin{pmatrix} 0 & U^\dagger \\ U & 0 \end{pmatrix} \tag{1.57}$$

in (1.56). Note that, by homotopy, this formula can also be transformed into

$$\mathcal{W}_{2D-1} = \frac{-2(D!)}{(2D)!(2i\pi)^D} \int_{\text{shell}} \text{Tr}^{\text{int}}(h^{-1}dh)^{2D-1} \tag{1.58}$$

where $h(x,k)$ is the lower off-diagonal block of the symbol $H(x,k)$ (see (1.2)). The homotopy invariance is obtained from the smooth deformation of h into U through the homotopic map $h_t = h(1-t+t\sqrt{h^\dagger h})^{-1}$, with t varying from 0 to 1.

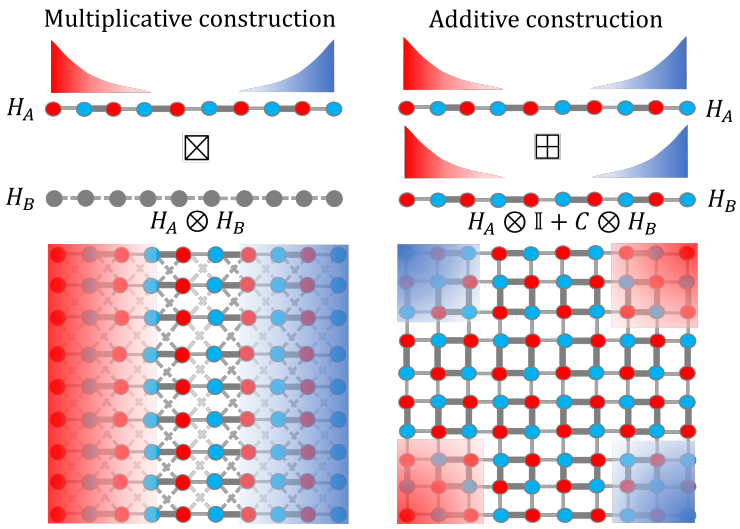

Figure 1.12: Sketched of $2D$ lattices built out of (a) the multiplicative tensor product construction and (b) the additive tensor product construction, from lower dimensional Hamiltonians H_A and H_B. The density of the zero-modes is represented in red/blue depending on their positive/negative chirality; while grey sites denote non chirality. The thickness of the bounds represent the amplitude of the coupling.

In the next two sections, we present different examples of chiral topological systems in higher ($D > 1$) dimensions and analyse how the mode-shell correspondence stated above can be applied to those examples. In order to simplify the analysis, we focus on examples in $D = 2$ dimensions. We present two general methods that provide those simple-to-analyse higher-dimensional examples, combining lower-dimensional examples through tensor product structures. The first method, that we refer to as the *multiplicative* tensor product construction and denote with the symbol $\boxtimes$, yields examples of weak insulators, that exhibit a macroscopic number of boundary

states, while the second method, that we refer to as the *additive* tensor product construction and denote with the symbol $\boxplus$, provides examples of higher-order insulators that exhibit e.g. corner states (see figure 1.12). The systems serving as building blocks for these construction can be discrete or continuous, and of any dimension. Also, those constructions can be combined or used multiple times to create examples in even higher dimension (see figure 1.13 for $D = 3$).

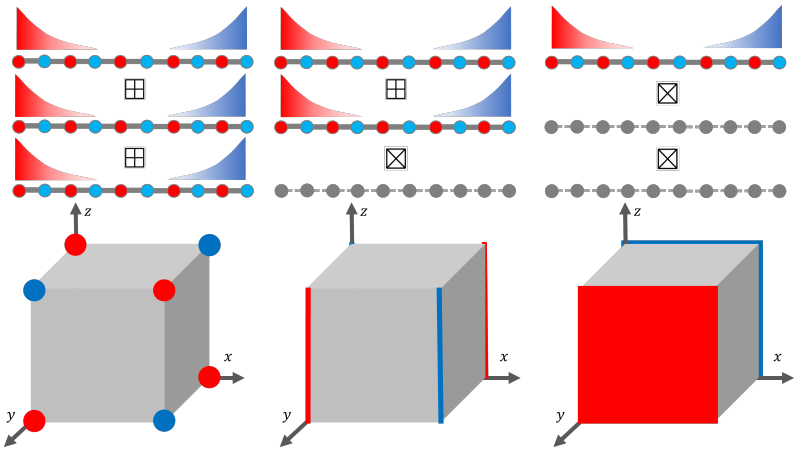

Figure 1.13: Sketches of possible of $3D$ topological systems obtained by applying (left) twice the additive tensor product construction yielding zero-modes corner states, (center) both the additive and the multiplicative tensor product construction, providing an extensive number of zero-modes states localised on hinges, and (right) twice the multiplicative tensor product construction leading to an extensive number of zero-modes states localised on surfaces.

1.3.2 Chiral Weak-insulators and flat-band topology

One way to engineer topological states in higher dimension is to stack $1D$ topological systems, such like SSH chains. We would then have a number of gapless modes growing extensively with the transverse size (say y) of the sample as it would be equal to the number of copies N_y. The zero-modes would then gradually form a flat zero-energy band in this transverse direction, a phenomenon observed experimentally [120, 121, 128, 143].

Such stacked systems result is what is often called "weak topological insulators" in the literature [4, 143–151]. Stacked versions of $2D$ quantum spin Hall [60, 61, 152] or quantum Hall [153] phases are other $3D$ examples beyond the chiral. The adjective "weak" was originally used since the edge states were first expected not to be topologically protected against disorder or inter-layer couplings [4, 144], but it was later realized that they turned out to be robust to such kinds of perturbations [145–148] making the terminology nowadays a little bit outdated. Also, a weak topological insulator is usually characterized by a topological index associated to a reduced Brillouin zone (and thus dubbed *weak invariant*) in contrast with *strong* topological insulators whose (strong) invariants encompass the entire Brillouin zone. We recall that $1D$ strong chiral topological insulators are the only strong insulators that are captured by the chiral index defined in this chapter. The mode-shell correspondence with higher-dimensional strong invariants will be exposed in the next chapters.

In this section, we analyse chiral weak insulators through the mode-shell correspondence. To do so, we consider $2D$ systems, such as those depicted in figure 1.14 and 1.15, where the left and right edges host a macroscopic number of edge modes in the y direction. To select the leftmost extended edge states, we then choose a cut-off operator which is uniform in the y direction and localised near the left edge. Next, if the system is such that its bulk is gapped,

and if its upper and lower edges are also gapped, then the invariant $\mathcal{I} = \mathrm{Tr}\Big(\hat{C}(1-\hat{H}_F^2)\hat{\theta}_\Gamma\Big)$ can be shown to be quantised as in the $1D$ case. The only difference with the $1D$ case is that the index $\mathcal{I}$ is (macroscopically) much larger and depends of the transverse length N_y of the lattice. The proof of the quantisation of the number of edge modes only requires chiral symmetry and is insensitive to the presence of disorder or inter-layer couplings, which shows the robustness of those modes.

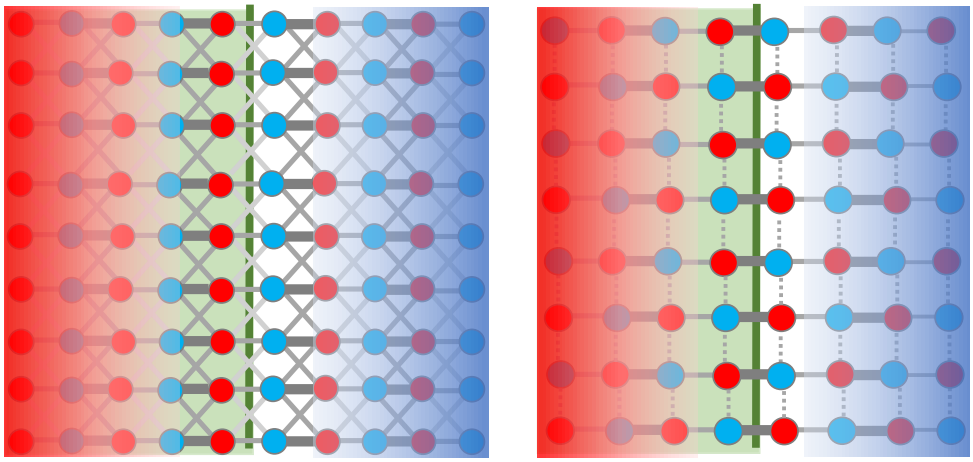

Figure 1.14: Two examples of lattices with a macroscopic number of chiral zero-modes on the left vertical edge. (Left) Stacking of topological chiral SSH chains in the vertical direction with inter-layer couplings that preserve chiral symmetry. (Right) Stacking of staggered trivial and topological SSH chains that preserve chiral symmetry. This example has the advantage of involving only nearest neighbour interactions without breaking chiral symmetry. To compute the macroscopic topological index associated to these lattices, one needs to chose a cut-off which is uniform in the vertical coordinate and decreases only in the horizontal coordinate.

Let us now compute the shell invariant in phase space using the Wigner-Weyl transform. One gets

$$\mathcal{I} = \frac{1}{2}\sum_{(x,y)\in\mathcal{L}} \int_0^{2\pi}\frac{dk_x}{2\pi}\int_0^{2\pi}\frac{dk_y}{2\pi}\,\mathrm{Tr}^{\mathrm{int}}(C\star H_F\star[\theta_\Gamma,H_F]_\star)\ . \tag{1.59}$$

The next step is to perform a semi-classical expansion in terms of $1/\Gamma$ and keep the dominant term. To be valid, this approximation requires the Hamiltonian to vary slowly in position (x,y) (see section 1.1.5); this is valid in the major part of the shell which is in the bulk as we have translation invariance in both directions. However, it is invalid near the upper and lower edges since there the Hamiltonian varies sharply in the y direction. If we were ignoring the perturbations due to the edges, we would be allowed to perform a semi-classical expansion in both directions and we would get a bulk index $\mathcal{I}^b \sim \mathcal{I}$

$$\begin{aligned}\mathcal{I}^b &\underset{\lim}{=} \frac{1}{2}\int_0^{2\pi}\frac{dk_y}{2\pi}\int_0^{2\pi}\frac{dk_x}{2\pi}\,\mathrm{Tr}^{\mathrm{int}}(CH_F^b i\partial_{k_x}H_F^b\sum_{(x,y)\in\mathcal{L}}\delta_x\theta_\Gamma(x,y))\\ &\underset{\lim}{=} N_y\int_0^{2\pi}\frac{dk_y}{2\pi}\int_0^{2\pi}\frac{dk_x}{4i\pi}\,\mathrm{Tr}^{\mathrm{int}}(CH_F^b\partial_{k_x}H_F^b)\end{aligned} \tag{1.60}$$

where N_y is the number of stacked chains and H_F^b is the symbol of $\hat{H}_F$ in the bulk. In the right hand-side of the expression, the term

$$\frac{1}{4i\pi}\int_{k_x\in[0,2\pi],k_y=k_{y0}} dk_x\,\mathrm{Tr}^{\mathrm{int}}(CH_F^b\partial_{k_x}H_F^b)\equiv\mathcal{I}_{\mathrm{weak}}(k_{y_0}) \tag{1.61}$$

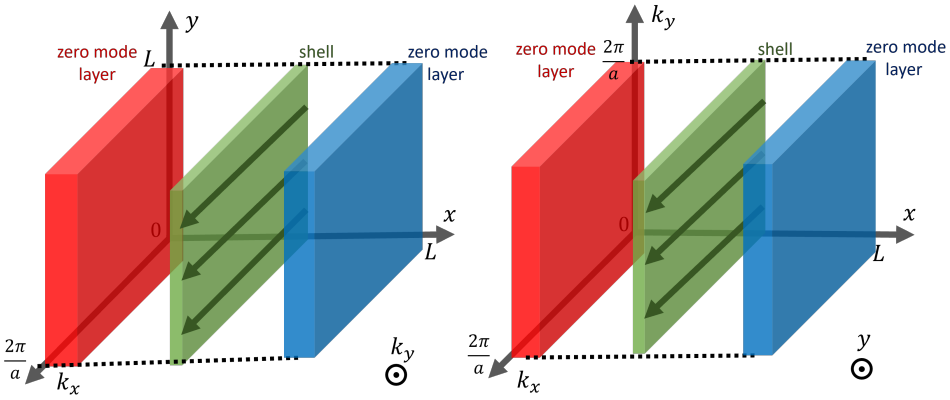

Figure 1.15: Phase space representation of the macroscopic number of zero-modes (in red and blue) and the shell (in green) for weak insulators such as depicted in figure 1.14. In the bulk where semi-classical limit occurs, the shell invariant can be reduced to a weak invariant which is a winding number in the k_x direction (green arrows) and a multiplicative constant depending on the y and k_y directions.

is known to be a topological invariant which remains constant when deforming the symbol H_F^b without closing the gap. As a result, it does not depend on the choice of k_{y_0}, so the average $\int_0^{2\pi} dk_x$ can be replaced by the integration over any line of constant k_y in Fourier space. Such an invariant is sometimes called weak invariant because the integration only runs over a one-dimensional path while the system is two-dimensional. The bulk invariant then reads

$$\mathcal{I}^b = N_y \, \mathcal{I}_{\text{weak}} \, . \tag{1.62}$$

By ignoring the effect of the edges, $\mathcal{I}^b$ is in principle an approximation of $\mathcal{I}$. To recover $\mathcal{I}$, one thus needs to add a correction term Δ_{edge} coming from the fact that the actual Hamiltonian near the edges at $y = 0$ and $y = L_y$ differs from the bulk Hamiltonian, that is

$$\mathcal{I} = \mathcal{I}^b + \Delta_{\text{edge}} \, . \tag{1.63}$$

This correction can be computed numerically by evaluating $\mathcal{I}$ before the semi-classical expansion. Since $\mathcal{I}$, N_y and $\mathcal{I}_{\text{weak}}$ are all integers, Δ_{edge} must also be an integer and its specific value may *a priori* depend on the boundary conditions. However, since the correction term only originates from the sites located close to a boundary, this term is bounded and thus cannot scale with N_y. As a result, even the strangest boundary condition cannot change the fact that there is a macroscopic number of zero-modes localised on the left edge of the $2D$ lattice. In fact even if one has a boundary condition that closes the gap on the upper/lower boundary, the computation above mostly remains the same and we still have the relation (1.63). Furthermore, since the chiral index also reads $\mathcal{I} = \operatorname{Tr} \hat{C}(1-\hat{H}_F^2)\hat{\theta}_\Gamma$, and since $(1-\hat{H}_F^2)$ is only non-zero for modes of very small energy, it follows that there should be a macroscopic number of very small energy modes on the left edge. However, $\mathcal{I}$ and Δ_{edge} may in that case no longer be integers and deviate from quantisation. But the massive polarisation of the zero-modes remains. Those are still protected as long as $\mathcal{I}_{\text{weak}} \neq 0$ which is guaranteed since $\mathcal{I}_{\text{weak}}$ is a bulk topological invariant which cannot change as long as there is a bulk gap.

It should be noted that weak invariants are also used to prove the existence of edge Fermi arcs in semi-metals like graphene and Weyl semimetals [128, 153, 154]. If we decide to not add this example in order to not further lengthen the size of the article, it can be understood in a similar manner as the previous presentation, the only difference being that we have to introduce, in the

definition of the index, a cut-off in wavenumber space of the direction tangent to the edge in order to select the part of the Fourier space where Fermi arcs exists (between the edge projection of two bulk Dirac/Weyl cones where the bulk gap closes).

Multiplicative tensor product construction ⊠

In this section, we present a simple but general mathematical procedure to generate such staking of chiral topological systems. At the Hamiltonian level, it simply consists in defining a Hamiltonian $\hat{H}$ as the tensor product of two lower dimensional gapped Hamiltonians $\hat{H}_A$ and $\hat{H}_B$ [155] as

$$\hat{H} = \hat{H}_A \otimes \hat{H}_B \tag{1.64}$$

where $\hat{H}_A$ is chiral symmetric, while $\hat{H}_B$ encodes the coupling between the stacked copies. Such a procedure was recently referred to as "multiplicative topology" in the literature [156–158]. If $\hat{H}_A$ and $\hat{H}_B$ are Hamiltonians on lattices or continuous spaces of dimension D_A and D_B, then $\hat{H}$ is a Hamiltonian which acts on a $D = D_A + D_B$ dimensional space. Moreover, if we denote by $\hat{C}_A$, the chiral symmetry operator of $\hat{H}_A$, then $\hat{H}$ has the chiral symmetry $\hat{C} = \hat{C}_A \otimes \mathbb{1}$.

Importantly, the spectral properties of $\hat{H}$ are entirely determined by those of the sub-systems $\hat{H}_A$ and $\hat{H}_B$. Indeed, if $\left|\psi_n^A\right\rangle$ is an eigenbasis of $\hat{H}_A$ with energies E_n^A and $\left|\psi_m^B\right\rangle$ is an eigenbasis of $\hat{H}_B$ with energies E_m^B, then $\left|\psi_n^A\right\rangle \otimes \left|\psi_m^B\right\rangle$ is an eigenbasis of $\hat{H}$ with energies $E_n^A E_m^B$. In particular the zero-modes of $\hat{H}$ are those which are of the form (or a linear combination of) $\left|\psi_n^A\right\rangle \otimes \left|\psi_m^B\right\rangle$ where either $\left|\psi_n^A\right\rangle$ or $\left|\psi_m^B\right\rangle$ a zero-mode. This means that if $\hat{H}_B$ acts on a finite space with N sites, then for each zero-mode $\left|\psi_{n_0}^A\right\rangle$ of $\hat{H}_A$, one can associate N zero-modes of $\hat{H}$ since no matter what is $\left|\psi_m^B\right\rangle$, $\left|\psi_{n_0}^A\right\rangle \otimes \left|\psi_m^B\right\rangle$ remains a zero-mode.

In particular, if $\hat{H}_A$ is just the identity operator on a finite lattice of N_y sites, i.e. $\hat{H}_B = \sum_{j=1}^{N_y} |j\rangle\langle j|$, then $\hat{H} = \hat{H}_A \otimes \hat{H}_B$ is just the Hamiltonian of N_y stacked copies of topological chiral systems described by $\hat{H}_A$ with no coupling between the different copies. If $\mathcal{I}_A$ is the non-trivial chiral topological index of $\hat{H}_1$ with respect to a cut-off operator $\hat{\theta}_\Gamma$, and if $\hat{H}_B$ is gapped, then, as we detail below, one can check that $\hat{H}$ has also a well defined topological index $\mathcal{I}$ associated to the cut-off operator $\hat{\theta}_\Gamma \otimes \mathbb{1}$ which is given by

$$\mathcal{I} = \mathcal{I}_A \times N_y \,. \tag{1.65}$$

We thus naturally end up with a number of chiral zero-modes that grows extensively with the stacking direction of the system. The zero-modes would then gradually form a zero energy flat-band in this direction, a phenomenon observed experimentally [120, 121, 128, 143].



Figure 1.16: Tensor product structure which generates the model illustrated in figure 1.14 a) The left model, given by H_A is a topological SSH models. The right model, given by H_B, is a 1D chain with some on-site and nearest neighbour couplings.

Example 1: One can use this multiplicative construction to generate some of the lattices in the figure 1.12 and 1.14. For example, the model described in the left parts of these figures can be generated from the tensor product of a topological SSH model, i.e. $\hat{H}_1 = \hat{H}_{\text{SSH}}$ given by (1.29), with a simple non-chiral model of the form $\hat{H}_2 = \sum_n |n\rangle\langle n| + t''(|n\rangle\langle n+1| + |n+1\rangle\langle n|)/2$ which,

in the bulk, has the symbol $H_2(n,k) = 1 + t'' \cos(k_y)$ and is hence gapped when $|t''| < 1$. In the multiplicative construction, the t'' coefficient then creates vertical couplings between different SSH layers which preserve chiral symmetry and the existence of topological zero-modes. The symbol of the tensored Hamiltonian $\hat{H} = \hat{H}_1 \otimes \hat{H}_2$ reads

$$H(n_x, n_y, k_x, k_y) = \begin{pmatrix} 0 & t + t' e^{ik_x} \\ t + t' e^{-ik_x} & 0 \end{pmatrix} (1 + t'' \cos(k_y)) \tag{1.66}$$

which is just the symbol of the SSH model multiplied by a scalar constant depending of k_y. Therefore, when computing the weak index $\mathcal{I}_{\text{weak}}(k_{y_0})$ as described by the formula (1.65), we obtain that, for $|t''| < 1$, $\mathcal{I}_{\text{weak}}(k_{y_0}) = \mathcal{W}_1$ with $\mathcal{W}_1$ the winding number of the $1D$ SSH model. The $1D$ mode-shell correspondence gives us $\mathcal{I}_1 = \mathcal{W}_1$ and the multiplicative structure implies $\mathcal{I} = \mathcal{I}_1 \times N_y$. One can therefore verify that at the leading order in N_y we have

$$\mathcal{I} \underset{N_y}{\sim} \mathcal{I}_{\text{weak}}(k_{y_0}) N_y \tag{1.67}$$

which is indeed the result predicted by the mode-shell correspondence. In this system, this relation is in fact an equality, due to the multiplicative structure which forbids edge corrections of the formula to occur.

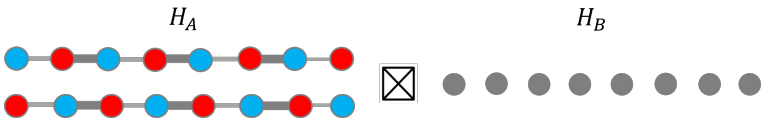

Figure 1.17: Tensor product structure which generates the model illustrated in figure 1.14 b) up to the addition, *a posteriori*, of inter-layer couplings. The left model, given by H_A is the superposition of a topological and trivial SSH models. The right model, given by H_B, is a trivial chain with constant onsite coupling $\hat{H}_B = \sum_n |n\rangle \langle n| = \mathbb{1}$.

Example 2: One problem one may have with the above example is that nearest neighbour couplings are forbidden because they would break chiral symmetry. There are models which do not have this drawback. For example, one could first stack a topological chain with a trivial SSH chain as depicted in figure 1.17 and then use the tensor product construction to create a $2D$ stack of this two-layer quasi-$1D$ model. If one adds nearest neighbour interactions between the layers, one would then obtain the model depicted in the right part of the figure 1.14. This inter-layer coupling breaks the multiplicative structure but the existence of chiral zero-modes only relies on the chiral symmetry and on a gap on the shell, two assumptions which are not broken by those couplings. So, as long as these inter-layer couplings are not too strong to close the gap, the macroscopic number of chiral zero-modes on the left edge remains topologically protected.

1.3.3 Higher-order chiral insulators

In this section, we discuss how the modes-shell correspondence can be applied to describe higher-order chiral insulators which exhibit zero-modes localised in more than 1 dimensions. To generate higher-dimensional chiral topological examples which are simple to study, we follow a procedure that we call the *additive tensor product construction* and we refer to it by the symbol $\boxplus$. We use this method to generate two examples in $D = 2$: one lattice model and one continuous model on which we verify, illustrate and discuss the predictions of the mode-shell correspondence theory.

Additive tensor product construction ⊞

The additive tensor product construction is another procedure [159, 160] by which one can generate a higher-dimensional topological chiral Hamiltonian $\hat{H}$ from two lower dimensional Hamiltonians $\hat{H}_1$ and $\hat{H}_2$. It requires that both $\hat{H}_A$ and $\hat{H}_B$ are chiral symmetric with chiral operators $\hat{C}_A$ and $\hat{C}_B$ respectively. A chiral higher dimensional Hamiltonian can then defined as

$$\hat{H} = \hat{H}_A \otimes \mathbb{1} + \hat{C}_A \otimes \hat{H}_B \tag{1.68}$$

or equivalently by substituting A by B. If this additive construction seems a little bit more involved than the multiplicative one, the spectral properties of $\hat{H}$ are still determined by those of $\hat{H}_1$ and $\hat{H}_2$ since

$$\hat{H}^2 = \hat{H}_A^2 \otimes \mathbb{1} + \mathbb{1} \otimes \hat{H}_B^2 + \{\hat{H}_1, \hat{C}_1\} \otimes \hat{H}_2 = \hat{H}_A^2 \otimes \mathbb{1} + \mathbb{1} \otimes \hat{H}_B^2 \ . \tag{1.69}$$

Therefore, if $\left|\psi_n^A\right\rangle$ is an eigenbasis of $\hat{H}_A$ with energies E_n^A and $\left|\psi_m^B\right\rangle$ is an eigenbasis of $\hat{H}_B$ with energies E_m^B, then $\left|\psi_n^A\right\rangle \otimes \left|\psi_m^B\right\rangle$ is the eigenbasis of $\hat{H}^2$ with energies $(E_n^A)^2 + (E_m^B)^2$, so that the eigenvalues of $\hat{H}$ are $\pm\sqrt{(E_n^A)^2 + (E_m^B)^2}$. It follows that the zero-modes of $\hat{H}$ are of the form $\left|\psi_{n_0}^A\right\rangle \otimes \left|\psi_{m_0}^B\right\rangle$ where $\left|\psi_{n_0}^A\right\rangle$ *and* $\left|\psi_{m_0}^B\right\rangle$ are zero-modes respectively of $\hat{H}_A$ and $\hat{H}_B$. This is quite different from the additive construction, since we need here the two Hamiltonians $\hat{H}_A$ and $\hat{H}_B$ to have of zero-modes, and not only one of them. As a result, this procedure generates higher order chiral insulators with few zero-modes, in contrast with weak chiral insulators (see figure 1.12). Indeed, if $\hat{H}_A$ and $\hat{H}_B$ have each a well defined chiral topolgical index $\mathcal{I}_A$ and $\mathcal{I}_B$ (with respect to the cut-off operators $\hat{\theta}_{\Gamma,A}$ and $\hat{\theta}_{\Gamma,B}$), then one can check that $\hat{H}$ has also a well defined chiral index $\mathcal{I}$, associated to the cut-off operator $\hat{\theta}_{\Gamma,A} \otimes \hat{\theta}_{\Gamma,B}$. We then use the fact that the chiral polarisation of the zero-modes $\left|\psi_{n_0}^A\right\rangle \otimes \left|\psi_{m_0}^B\right\rangle$ is the product of the chiral polarisation of each individual mode, which leads to

$$\mathcal{I} = \mathcal{I}_A \times \mathcal{I}_B \ . \tag{1.70}$$

Of course, since the higher-dimensional Hamiltonian $\hat{H}$ is itself chiral symmetric, it can serves as a new block to apply the procedure again. By induction, we get the more general formula

$$\hat{H} = \hat{H}_1 \otimes \mathbb{1}^{\otimes(N-1)} + \hat{C}_1 \otimes \hat{H}_2 \otimes \mathbb{1}^{\otimes(N-2)} + \cdots + \hat{C}_1 \otimes \cdots \otimes \hat{C}_{N-1} \otimes \hat{H}_N \tag{1.71}$$

of a chiral Hamiltonian resulting from the additive tensor product construction with N chiral symmetric Hamiltonians $\hat{H}_j$ of chiral symmetry operator $\hat{C}_j$ and chiral topological index $\mathcal{I}_j$ $(j = 1 \dots N)$. The chiral symmetry operator of $\hat{H}$ is then given by the tensor product $\hat{C}_1 \otimes \cdots \otimes \hat{C}_N$, and the zero-modes of $\hat{H}$ have a chiral index $\mathcal{I} = \mathcal{I}_1 \times \cdots \times \mathcal{I}_N$.

The next two paragraphs are dedicated to two simple illustrations of the additive tensor product construction in $D = 2$ and to the analysis of the resulting models through the higher-dimensional mode-shell correspondence.

Example 1: $2D$ Jackiw-Rossi model with smooth potentials

We discuss an example of the higher-dimensional mode-shell correspondence for a chiral zero-mode trapped at a domain wall where the Hamiltonian is smoothly varying. Such a situation has been studied in the literature in the context of defects modes [58, 161]. It allows for a

full semi-classical limit of the shell index leading to the Teo and Kane formula in the case of discrete lattice [58] and the Callias index formula in the continuous case [125]. As both discrete and continuous cases are relatively similar, we made the choice to focus our attention to the continuous case in this section.

For that purpose, we revisit the Jackiw-Rossi model [162] which follows from the same construction as the BBH model above: The two-dimensional Jackiw-Rossi Hamiltonian $\hat{H}$ is obtained by combining, in perpendicular directions x and y, two one-dimensional Jackiw-Rebbi Hamiltonians $\hat{H}_{\mathrm{JR}}$ introduced in (1.44), by following the additive tensor product construction, that is

$$\hat{H} = \hat{H}_{\mathrm{JR}}(x, \partial_x) \otimes \mathbb{1} + \sigma_z \otimes \hat{H}_{\mathrm{JR}}(y, \partial_y) \tag{1.72}$$

where σ_z is the chiral-symmetric operator of the two underlying Jackiw-Rebbi models, and which, in a more explicit form, reads

$$\hat{H} = \begin{pmatrix} 0 & y - \partial_y & x - \partial_x & 0 \\ y + \partial_y & 0 & 0 & x - \partial_x \\ x + \partial_x & 0 & 0 & -(y - \partial_y) \\ 0 & x + \partial_x & -(y + \partial_y) & 0 \end{pmatrix} . \tag{1.73}$$

Similarly to the previous example with open conditions, this Hamiltonian has a chiral symmetry with a chiral operator $\hat{C} = \sigma_z \otimes \sigma_z$. Writing $\hat{H}^2 = \hat{H}^2_{\mathrm{JR}}(x, \partial_x) \otimes \mathbb{1} + \mathbb{1} \otimes \hat{H}^2_{\mathrm{JR}}(y, \partial_y)$ implies that the chiral zero-modes of $\hat{H}$ must also be chiral zero-modes of $\hat{H}_{\mathrm{JR}}(x, \partial_x)$ and $\hat{H}_{\mathrm{JR}}(y, \partial_y)$ on each part of the tensor product. Those modes must thus be of the form $\psi_x \otimes \psi_y = (e^{-(x^2+y^2)/2}, 0, 0, 0)^t$ where $\psi(x) = (e^{-x^2/2}, 0)^t$ is the zero-mode of the Jackiw-Rebbi model. Therefore, $\hat{H}$ has one topological zero-mode of chirality $+1$ and thus $\mathcal{I} = 1$ for the cut-off $\hat{\theta}_\Gamma = e^{-(x^2+y^2-\partial_x^2-\partial_y^2)/\Gamma^2}$ which acts here both in position and wavenumber. The corresponding shell is a $3D$ sphere enclosing the chiral zero-mode in $4D$ phase space, as sketched in figure 1.18.

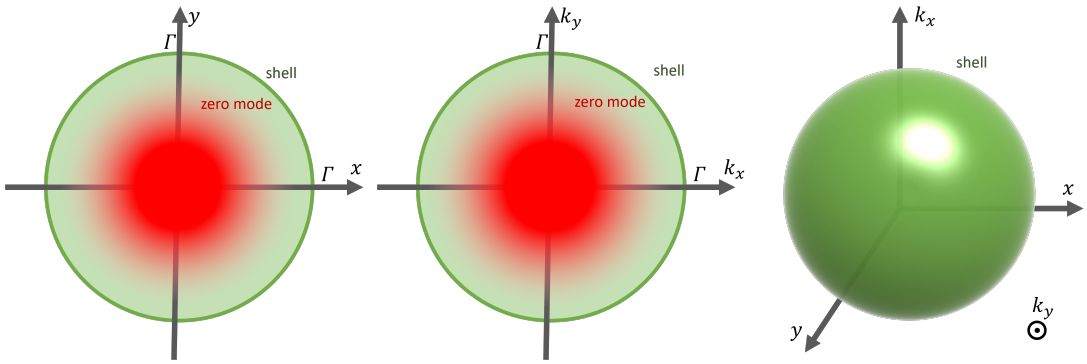

Figure 1.18: Amplitude of the zero-mode $\psi_x \otimes \psi_y = (e^{-(x^2+y^2)/2}, 0, 0, 0)^t$ of the Hamiltonian (1.72) in real space (left) and in Fourier space (center). The cut-off operator $\hat{\theta}_\Gamma = e^{-(x^2+y^2-\partial_x^2-\partial_y^2)/\Gamma^2}$ selects the zero-mode both in position and in wavenumber directions. It is represented in green and has the form of a $4D$-ball in phase space, with the shell being a $3D$ sphere (right).

The symbol H of the Jackiw-Rossi Hamiltonian reads

$$H = \begin{pmatrix} 0 & x - ik_x \\ x + ik_x & 0 \end{pmatrix} \otimes \mathbb{1} + \sigma_z \otimes \begin{pmatrix} 0 & y - ik_y \\ y + ik_y & 0 \end{pmatrix} \tag{1.74}$$

from which we deduce

$$\begin{aligned} H_F &= \frac{H}{\sqrt{x^2+y^2+k_x^2+k_y^2}} \\ &= \cos(\theta)\begin{pmatrix} 0 & e^{-i\phi_1} \\ e^{i\phi_1} & 0 \end{pmatrix} \otimes \mathbb{1} + \sigma_z \otimes \sin(\theta)\begin{pmatrix} 0 & e^{-i\phi_2} \\ e^{i\phi_2} & 0 \end{pmatrix} \end{aligned} \tag{1.75}$$

where $(\theta, \phi_1, \phi_2) \in [0, \pi/2] \times [0, 2\pi]^2$ are the Hopf-coordinates of S^3. One can then compute analytically $\int_{S^3} \mathrm{Tr}^{\mathrm{int}}(CH_F dH_F^3) = -12(2\pi)^2$ which is exactly the normalisation needed to have $\mathcal{I} = 1$.

Example 2: The Benalcazar-Bernevig-Hughes (BBH) model with open boundary conditions

Higher-order topological insulators (HOTI) constitute a class of systems where topological zero-modes are embedded in a higher dimensional phase space. Those zero-modes could then be trapped at the corners of a material where the trapping potential varies sharply at the edges [24, 25, 160, 163–166]. The archetypal lattice model describing such a situation is the Benalcazar, Bernevig, Hughes (BBH) model [24], depicted in figure 1.19, which essentially consists in "crossing" arrays of SSH models along the x and y directions such that chiral symmetry is preserved. The resulting Hamiltonian follows the additive construction and reads

$$\hat{H} = \hat{H}_{\mathrm{SSH},x} \otimes \mathbb{1} + \sigma_z \otimes \hat{H}_{\mathrm{SSH},y} \tag{1.76}$$

where σ_z is the chiral-symmetric operator of the two underlying SSH models, and which, in a more explicit form, becomes

$$\hat{H} = \begin{pmatrix} 0 & t + t'T_y^\dagger & t + t'T_x^\dagger & 0 \\ t + t'T_y & 0 & 0 & t + t'T_x^\dagger \\ t + t'T_x & 0 & 0 & -(t + t'T_y^\dagger) \\ 0 & t + t'T_x & -(t + t'T_y) & 0 \end{pmatrix} \tag{1.77}$$

where $T_x = \sum_{n_x,n_y} |n_x + 1, n_y\rangle \langle n_x, n_y|$ and $T_y = \sum_{n_x,n_y} |n_x, n_y + 1\rangle \langle n_x, n_y|$ are the translation operators of one lattice unit along x and y respectively. We also impose open boundary conditions as in figure 1.19.

The Hamiltonian $\hat{H}$ inherits chiral symmetry from the two underlying chiral symmetric lower dimensional systems, and its chiral operator reads $\hat{C} = \sigma_z \otimes \sigma_z$. The chiral zero-modes of $\hat{H}$ can then be easily found: using the additive chiral construction, we know that the zero-modes of $\hat{H}$ must also be zero-modes of $\hat{H}_{\mathrm{SSH},x}$ and $\hat{H}_{\mathrm{SSH},y}$ on each part of the tensor product. They must therefore be of the form $\psi_x \otimes \psi_y$ where $\psi_{x/y}$ is the zero-mode in the x/y direction of the SSH model. It follows that for $|t'| > |t|$, where the SSH models are topological, the BBH model $\hat{H}$ has one topological zero-mode of chirality $+1$ in its bottom-left corner, and therefore, it has $\mathcal{I} = 1$ for the cut-off $\hat{\theta}_\Gamma = e^{-(x^2+y^2)/\Gamma^2}$, which acts in both position directions.

The use of the shell invariant is, however, not as straightforward as in the previous cases. The reason is that the shell, that encircles the corner of interest (see figure 1.19), runs not only over the bulk but also over the sharp edges where the Hamiltonian does not vary smoothly. Therefore, taking the limit $\Gamma \to \infty$ in the shell invariant does not guarantee the semi-classical limit in every directions. As a consequence, we cannot derive an expression of the shell index which is as simple as (1.53).

We can still simplify partially the expression by using the translation invariance of $\hat{H}_F$ in the direction parallel to each edge. In fact, one can show (see appendix C) that the index can be written as the sum of two contributions $\mathcal{I}_{\mathrm{shell}} = \mathcal{I}_{\mathrm{edge},x} + \mathcal{I}_{\mathrm{edge},y}$ where each contribution is

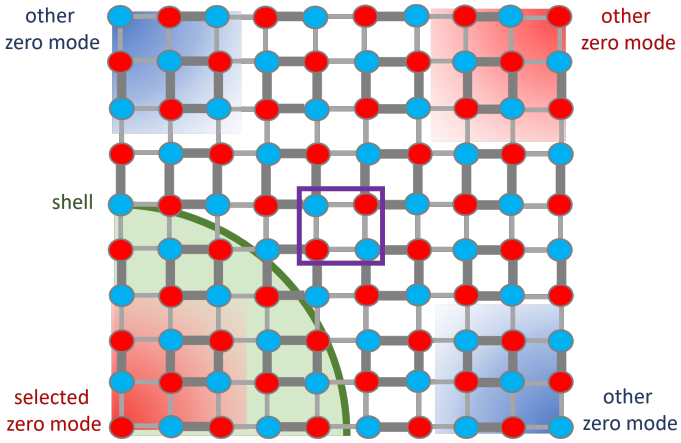

Figure 1.19: Lattice BBH model with chiral zero-modes of positive/negative chirality depicted in red/blue. The shell is shown in green, an example of unit cell is shown in purple. The thickness of the links represents the strength of the coupling. The system has open boundary conditions with edges given by the horizontal and vertical lines $x = 0$, $x = L$, $y = 0$, $y = L$.

localised at one of the two edges and where we can use the Fourier transform in the direction parallel to that edge. In particular, $\mathcal{I}_{\text{edge},x}$ can be written as

$$\mathcal{I}_{\text{edge},x} = \frac{-1}{24\pi} \int_0^{2\pi} dk_x \tilde{\text{Tr}} \left(\tilde{C} \tilde{H}_F [\tilde{d}, \tilde{H}_F]^3 \right) \tag{1.78}$$

where the notation $\sim$ means that the Wigner-Weyl transform is performed in the tangent direction only. The operator $\tilde{d}$ is for example $\tilde{d} = \partial_x dk_x + T_y^\dagger n_y dy - iT_y dk_y$. The expression of $\mathcal{I}_{\text{edge},x}$ is obtained by switching the x and y coordinates.

Since the semi-classical treatment is invalid in the perpendicular direction to the edge, $\mathcal{I}_{\text{edge},x}$ (or equivalently $\mathcal{I}_{\text{edge},y}$) remains cumbersome to manipulate by hand.[9] So we prefer here to evaluate $\mathcal{I}_{\text{edge},x/y}$ numerically. This also gives us the opportunity to show explicit examples of numerical codes that compute numerical approximations of the indices. Those can be found in Appendix C. One of these codes computes the index $\mathcal{I}_{\text{modes}}$ directly from the initial formula (1.8) while the other one compute $\mathcal{I}_{\text{shell}}$ using the formulation with partial semi-classical limit (1.78). For lattices of length $L = 10$ sites, both codes give $\mathcal{I} = 1$ up to a deviation of less than 1%, which validates numerically the mode-shell correspondence for the BBH model.

We can mention that the recourse to additional symmetries is commonly used in the literature of higher-order topological insulators. Those symmetries can be interpreted as a way to reduce the complexity of the computation of the shell index by re-expressing it as a pure bulk quantity. For instance in [24], it is claimed that due to the C_4 rotational symmetry which is present in the BBH model, the quadruple moment is a topological invariant in the bulk related to the number of corner modes.

In conclusion, we explained how the BBH model is an example of chiral higher-order insulator with topologically protected zero modes that fit in the mode-shell correspondence paradigm.

[9] In principle, a way to compute it analytically would be to list the bulk eigenmodes of the form $\psi(n_y, k_x) = \psi(k_x) z^{n_y}$ with z a complex number and n_y the index of the unit-cell in the y-direction. Then, solving the eigenmodes of energy E in the semi-infinite geometry (with one edge) can be done by searching them as a sum of eigenmodes of the bulk problem with the same energy E and with z such that $|z| \leq 1$ (not exponentially increasing) and then imposing the boundary conditions. Doing so allows for diagonalising $H(k_x)$, from which one can deduce $\tilde{H}_F(k_x)$ and then finally compute $\mathcal{I}_{\text{edge},x}$. But these computations would be long and not particularly enlightening

This is a case where a full semi-classical limit cannot be obtained and where analytical expressions of the shell invariant are therefore difficult. However we used this last example to show how the mode and shell invariants can, in general, be computed numerically. This is a strength of the formalism as, even if semi-classical limit is useful to obtain closed analytical expressions for the different pedagogical examples we discuss extensively in this thesis, semi-classical is not mandatory and we wanted to show an example where we go beyond it using numeric.

1.4 Conclusion

In this chapter, we have discuss the mode-shell correspondence in the case where the mode-index is the chiral number of zero mode. We have shown that this correspondence unifies several results in wave topology, from the bulk-edge correspondence, higher-order topological phases, to the Callias index formula and the Atiyah-Singer index theory. We provided a wide variety of examples, for discrete and continuous systems, in one and higher dimensions, to illustrate the mode-shell correspondence in concrete models. In particular, we showed how the mode-shell correspondence describes not only zero-energy edge states, but also zero-modes that can be more generally localized in a region of phase space. We also discussed two systematic methods, dubbed "additive" and "multiplicative" tensor products constructions, to simply elaborate topological examples in higher $D > 1$ dimensions.

Chapter 2

Mode-shell correspondence for spectral-flow systems

In the previous chapter we showed that many topological phenomena in topological physics are captured by a low energy index which counts the chiral number of zero modes located in a particular region of phase space and developed the mode-shell correspondence formalism for this case. In this chapter we would like to discuss the phenomenology and cases involving another particularly important invariant, the 1D spectral flow, and show how a similar mode-shell correspondence can be applied to it.

2.1 Spectral flow and mode-shell correspondence

2.1.1 Spectral flow index

Within this section, we start by introducing the mode index of this chapter which is the spectral flow invariant [43, 45, 46]. It is defined as a property of the spectrum of a Hamiltonian operator $\hat{H}(\lambda)$ which depends on a parameter λ. Physically, such a parameter can either have an external origin, as in a pump or designate a coordinate in phase space. In this case, the most common example is the wave number coordinate $\lambda = k$. Such a situation is encountered in continuous wave systems, for which $k \in \mathbb{R}$, but also in lattice models where k is a Bloch quasi-momentum $k \in \mathbb{S}^1$ and is instead bounded [1].

The spectral flow is then defined as the number of eigenenergies $E(\lambda)$ of $\hat{H}(\lambda)$ that algebraically cross a reference energy E_0 when varying λ, that is

$$\mathcal{I}_{\text{s-f}}(E = E_0) = (\#\text{crossings from } E < E_0 \text{ to } E > E_0) - (\#\text{crossings from } E > E_0 \text{ to } E < E_0). \tag{2.1}$$

A simple illustration is sketched in Figure 2.1. By construction, $\mathcal{I}_{\text{s-f}}$ is obviously an integer. However it is not obvious that it is a continuous function of the Hamiltonian $\hat{H}(\lambda)$ that is robust to deformations. So, similarly to the chiral number of zero-modes discussed in the preivous chapter, we want to formulate an equivalent but smooth formulation of the spectral index.

[1] In fact, translation invariance is not strictly required to invoke $\lambda = k_i$, as such a continuous parameter can in principle follow more generally from a valid Wigner-Weyl transform when a semi-classical limit makes sense in the direction conjugate x_i.

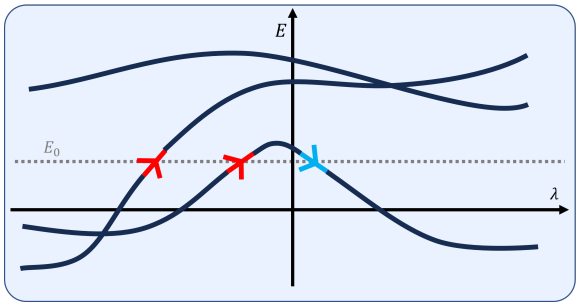

Figure 2.1: Example of evolution of the energies of the modes of an Hamiltonian depending on λ. The positive crossing of the energy level E_0 from below to above are denoted in red and the negative crossing from above to below are denoted in blue. The overall spectral-flow index of such system is therefore $\mathcal{I}_{\text{s-f}} = 2 - 1 = 1$

2.1.2 Smooth formulation of the index

To define a smooth version of the spectral index, we introduce, in the same fashion as in the previous chapter, a smoothly flatten version of the Hamiltonian, $\hat{H}_F(\lambda) = f(\hat{H}(\lambda))$ that has the same eigenmodes as $\hat{H}$ but with a smooth flattening of the energies to ± 1 above some threshold $|E - E_0| < \Delta$, and smoothly interpolating in between (see figure 2.2). Typically, we choose the gap threshold Δ such that there is only a finite number of modes of $\hat{H}(\lambda)$ which are gapless. Next, we introduce the unitary $\hat{U}(\lambda) \equiv -e^{i\pi \hat{H}_F(\lambda)}$ to re-express the spectral flow as the winding number of $\hat{U}(\lambda)$ when λ spans either $\mathbb{R}$ or $\mathbb{S}^1$. Indeed, if a mode n participates positively to the spectral flow, it means that its energy $E_n(\lambda)$ bridges continuously the gap that separates states of energy $E < E_0 - \Delta$ to the states of energy $E > E_0 + \Delta$, when varying λ. Its rescaled energy $f(E_n(\lambda))$ then varies continuously from -1 to $+1$, so that the unitary eigenvalue $u_n \equiv -e^{i\pi f(E_n(\lambda))}$ winds counterclockwise once around the unit circle, yielding a winding number of $+1$ (see figure 2.2). Similarly, a mode that contributes negatively to the spectral flow has an energy that bridges the gap in the opposite way when sweeping λ, so that it contributes to a winding of -1. In contrast, gapped modes with an energy above the gap $E > E_0 + \Delta$ have a rescaled energy that maps to $+1$ on the unit circle, and therefore do not yield any winding contribution. In the same way, gapped modes with an energy below the gap $E < E_0 - \Delta$ have a rescaled energy that also maps to $+1$ on the unit circle, and do not contribute neither. The net spectral flow thus corresponds to the sum of the winding numbers $\frac{1}{2i\pi}\int_\Lambda u_n^\dagger \partial_\lambda u_n$ of all the rescaled energies of all the nodes n, that reads

$$\mathcal{I}_{\text{s-f}} = \frac{1}{2i\pi}\int_\Lambda d\lambda \,\text{Tr}\Big(\hat{U}^\dagger(\lambda)\partial_\lambda \hat{U}(\lambda)\Big) \equiv \mathcal{W}_1(\hat{U}) \tag{2.2}$$

Since $\hat{U} = -e^{i\pi f(\hat{H})}$ is a smooth function of $\hat{H}$, the index $\mathcal{I}_{\text{s-f}}$ is a continuous function of the Hamiltonian. It is therefore a topological integer stable to smooth deformations of $\hat{H}$.

However similarly to what happens for the chiral number of zero modes, in finite systems, the total winding number is often zero. Therefore one would like to select a particular crossing in a sub-region of phase space with gapless spectra (confined in position at an edge or an hinge, or confined in wavenumber). This can be done in a very similar way by adding a cut-off $\hat{\theta}_\Gamma$

$$\mathcal{I}_{\text{s-f}} = \mathcal{W}_1(\hat{U}) = \frac{1}{2i\pi}\int d\lambda \,\text{Tr}\Big(\hat{U}^\dagger(\lambda)\partial_\lambda \hat{U}(\lambda)\hat{\theta}_\Gamma\Big) \tag{2.3}$$

where $\hat{\theta}_\Gamma$ is close to the identity in the sub-region we want to select, and vanishes in the other gapless regions. When such gapless regions are separated enough in phase space by a region

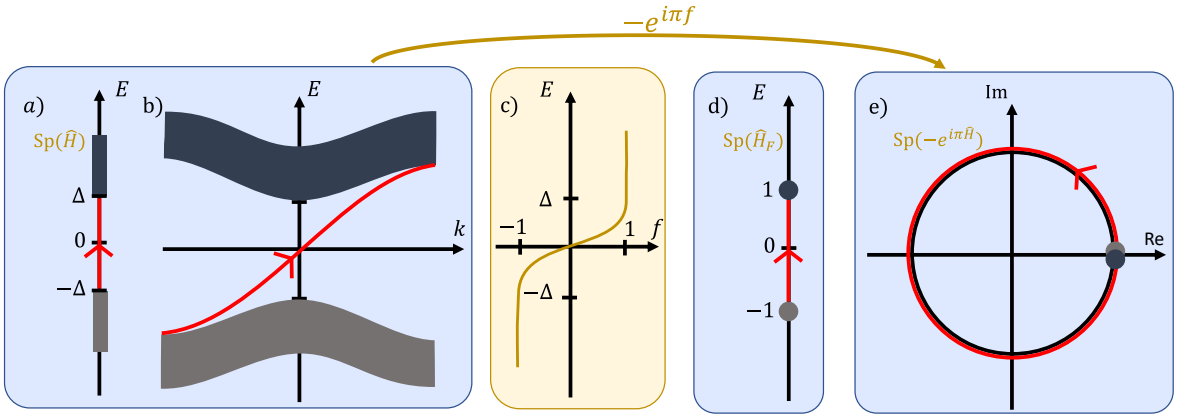

Figure 2.2: a) Projected energy spectrum denoted Sp($\hat{H}$) of a typical topological Hamiltonian $\hat{H}$. United stripes denote the gapped bulk bands, the red line denotes a gapless mode confined at the edge with positive spectral flow. b) Sketch of a possible smooth flattening function. c) Spectrum of the operator $\hat{H}_F = f(\hat{H})$ where the bulk bands are flattened. d) Spectrum of $-e^{i\pi\hat{H}_F}$, where all gapped modes are mapped to 1 and the gapless mode of positive spectral flow is now mapped to a mode of positive winding number.

where $\hat{H}$ is gapped; and when $\hat{H}$ has a short-range behavior in the direction of separation, the addition of a cut-off does not alter the quantisation of the winding number which remains an integer up to exponentially small deviations. Similar to what we discuss in the previous chapter, the cut-off can take many form by selecting modes confined in one (topological insulator) or several directions (higher-order insulator) in position or in wavenumber. Moreover the cut-off can also be in the parameter λ which is useful in the case where it is unbounded ($\lambda \in \mathbb{R}$). Modes with different localisation in phase space with their natural choice of cut-off are illustrated in figure 2.3.

It is interesting to note that the formulation of the spectral flow (capturing gapless topology), can be formulated as a winding number. Such a kind of topological invariant can also be obtained in the context of bulk invariants (capturing gap topology) of 1D systems with a chiral symmetry. This is a remnant of the fact that invariant capturing low-energy topology are often related to invariants describing gapped topology but in a different symmetry class.

In fact if we define the operator $\hat{H}'$ such that

$$\hat{H}' = \begin{pmatrix} 0 & -e^{-i\pi\hat{H}_F} \\ -e^{i\pi\hat{H}_F} & 0 \end{pmatrix} = -\sigma_x e^{-i\pi\sigma_z \otimes \hat{H}_F} \tag{2.4}$$

We can observe that it has a chiral symmetry $\{\sigma_z, \hat{H}'\}$ and is gapped as $\hat{H}'^2 = \mathbb{1}$. Moreover its topology is linked to that of $\hat{H}$ as we have

$$\mathcal{I}_{\text{s-f}} = \frac{1}{4i\pi} \int d\lambda \, \text{Tr}'(\sigma_z \hat{H}'(\lambda) \partial_\lambda \hat{H}'(\lambda) \hat{\theta}_\Gamma) \tag{2.5}$$

where Tr′ denote the trace on the new Hilbert space which is now twice as big. Such expression is similar to the expression of the bulk-index in 1D chiral systems encountered in the previous chapter.

The mode-shell correspondence of the spectral flow: Similar to the chiral number of zero modes that we studied in the previous chapter, the spectral flow index also verifies a mode-shell correspondence. This means that it can be express, up to a rearranging of the terms, as an

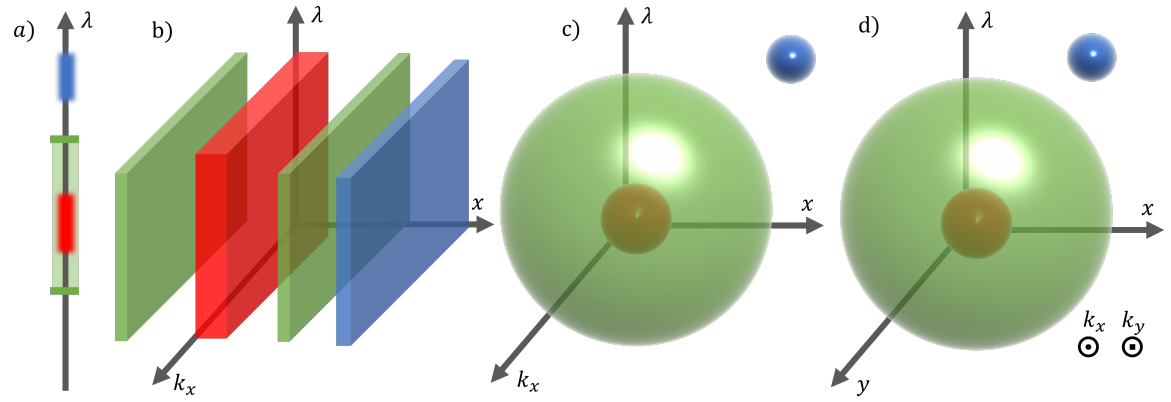

Figure 2.3: Figures illustrating different possible cut-off in different situations a) a cut-off which is in the parameter λ b) a cut-off which is only in position x as in the 2D quantum hall effect c) a cut-off which is in both x, k_x, λ as in the 2D valley quantum hall effect d) in x, y as in a higher-order insulator. The location of the gapless modes of positive/negative spectral is denoted in red/blue, the shell induced by the cut-off in green.

index which is defined in the shell region which surround the gapless mode in phase space and where $\hat{H}$ is gapped.

To make this appearent we introduce the path of unitaries $\hat{U}_t = -e^{it\hat{H}_F}$ and correspondingly chiral operators $\hat{H}'_t = \begin{pmatrix} 0 & \hat{U}_t^\dagger \\ \hat{U}_t & 0 \end{pmatrix}$ which interpolates between a trivial state $U_0 = \mathbb{1}$ of zero winding number and our target unitary $\hat{U}_1 = \hat{U}$. If we differentiate the spectral flow-index (2.3) with respect to t and integrate by part in ∂_λ, we obtain

$$\begin{aligned}
\mathcal{I}_{\text{s-f}} &= \frac{1}{4i\pi}\int_0^\pi dt \int d\lambda \,\mathrm{Tr}'(\hat{\sigma}_z \partial_t \left(\hat{H}'_t \partial_\lambda \hat{H}'_t\right)\hat{\theta}_\Gamma) \\
&= \frac{1}{4i\pi}\int_0^\pi dt \int d\lambda \,\mathrm{Tr}'(\hat{\sigma}_z \left(\partial_t \hat{H}'_t \partial_\lambda \hat{H}'_t + \hat{H}'_t \partial_{t,\lambda} \hat{H}'_t\right)\hat{\theta}_\Gamma) \\
&= \frac{1}{4i\pi}\int_0^\pi dt \int d\lambda \,\mathrm{Tr}'(\hat{\sigma}_z \left(\partial_t \hat{H}'_t \partial_\lambda \hat{H}'_t - \partial_\lambda \hat{H}'_t \partial_t \hat{H}'_t\right)\hat{\theta}_\Gamma) - \mathrm{Tr}'(\hat{\sigma}_z \hat{H}'_t \partial_t \hat{H}'_t \partial_\lambda \hat{\theta}_\Gamma)
\end{aligned} \tag{2.6}$$

By then using the identity $(\hat{H}'_t)^2 = \mathbb{1}$ and its differentiated version $\{\hat{H}'_t, \partial_{t/\lambda}\hat{H}'_t\} = 0$ we can obtain

$$\mathcal{I}_{\text{s-f}} = \frac{-1}{4i\pi}\int_0^\pi dt \int d\lambda \frac{1}{2}\,\mathrm{Tr}'(\hat{\sigma}_z \hat{H}'_t \partial_t \hat{H}'_t \left(\partial_\lambda \hat{H}'_t [\hat{\theta}_\Gamma, \hat{H}'_t] - [\hat{\theta}_\Gamma, \hat{H}'_t]\partial_\lambda \hat{H}'_t\right)) + \mathrm{Tr}'(\hat{\sigma}_z \hat{H}'_t \partial_t \hat{H}'_t \partial_\lambda \hat{\theta}_\Gamma) \tag{2.7}$$

which is an expression which is contained on the shell as all its terms contains either a commutator of the cut-off $[\hat{\theta}_\Gamma, \hat{H}_F]$ or a derivative $\partial_\lambda \hat{\theta}_\Gamma$. Therefore we can now use that, in this region $\hat{H}_F^2 = \mathbb{1}$ and therefore $-e^{it\hat{H}_F} = -\cos(t) - i\sin(t)\hat{H}_F$ and so $\hat{H}' = -\sigma_x \cos(t) - \sigma_y \sin(t)\hat{H}_F$ which leads to the following expression for the shell invariant

$$\begin{aligned}
\mathcal{I}_{\text{s-f}} &= \frac{-1}{4i\pi}\int_0^\pi dt \int d\lambda i \sin(t)^2 \,\mathrm{Tr}\Big(\hat{H}_F \left(\partial_\lambda \hat{H}_F [\hat{\theta}_\Gamma, \hat{H}_F] - [\hat{\theta}_\Gamma, \hat{H}_F]\partial_\lambda \hat{H}_F\right)\Big) + 2i\,\mathrm{Tr}\Big(\hat{H}_F \partial_\lambda \hat{\theta}_\Gamma\Big) \\
&= -\int d\lambda \frac{1}{2}\,\mathrm{Tr}\Big(\hat{H}_F \partial_\lambda \hat{\theta}_\Gamma\Big) + \frac{1}{4}\,\mathrm{Tr}\Big(\hat{H}_F \partial_\lambda \hat{H}_F [\hat{\theta}_\Gamma, \hat{H}_F]\Big) \equiv \mathcal{I}_{\text{shell}}
\end{aligned} \tag{2.8}$$

Similarly to the phenomenology we observed in the previous chapter, the shell invariant is more prone to semi-classical limits. When its occurs, the shell index can be reduced to a

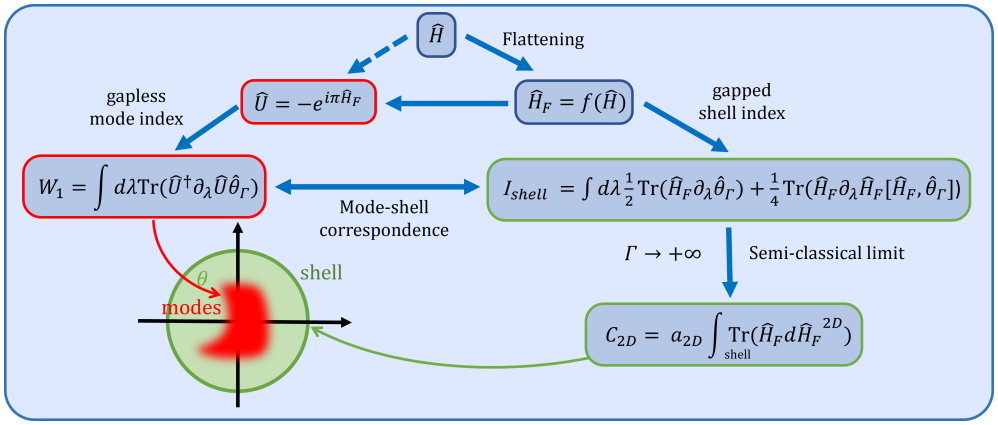

Figure 2.4: Summary diagram of the mode-shell correspondence when the mode invariant is the spectral flow. We use a smoothly flatten version $\hat{H}_F$ of the Hamiltonian $\hat{H}$ and the derived unitary $\hat{U} = -e^{i\pi\hat{H}_F}$ to define two indices: the $\mathcal{W}_1$ of $\hat{U}$ counting the spectral flow of $\hat{H}$, a gapless property, and I_{shell} measuring gapped properties on the boundary enclosing the gapless region (namely the shell) and which reduces, in a semi-classical limit, to a (higher) Chern number. The prefactor a_D of $\mathcal{C}_{2D}$ is given in (2.9).

(higher)-Chern number

$$\mathcal{I}_{\text{s-f}} = \frac{1}{2^{2D+1} D! (-2i\pi)^D} \int_{\text{shell}} \mathrm{Tr}\Big(H_F (dH_F)^{2D}\Big) = \mathcal{C}_{2D} \tag{2.9}$$

where $2D = \mathrm{D_S}$ is the dimension of the shell which is in general even (otherwise, $\mathcal{C}_{\mathrm{D_S}} = 0$). When $\mathrm{D_S} = 2$, $\mathcal{C}_2$ is the usual first Chern number, when $\mathrm{D_S} \geq 4$, it is a higher-Chern number and when $\mathrm{D_S} = 0$, the shell is zero-dimensional and therefore a collection of point on which $\mathrm{Tr}(H_F)$ is just the number of positive energies minus the number of negative energies of H on those points.

Instead of working with the flatten Hamiltonian H_F, one can also work with the Fermi projector P on the negative bands of H. Since the Hamiltonian is gapped, we have the relation $H_F = 1 - 2P$ and therefore we can have

$$\mathcal{I}_{\text{s-f}} = \frac{-1}{D! (-2i\pi)^D} \int_{\text{shell}} \mathrm{Tr}\Big(P (dP)^{\mathrm{D_S}}\Big) = \mathcal{C}_{\mathrm{D_S}} \tag{2.10}$$

which is a formula equivalent to the Berry curvature formalism [34, 74] using $P = \sum_i |\psi_i\rangle \langle\psi_i|$ where $|\psi_i\rangle$ are the bands selected by the projector.

2.1.3 Spectral flow and quantised conductance

In the previous section, we developed an expression of the spectral flow where it is relatively easy to show that it is a topological index which verifies a mode-shell correspondence. However, an other important part associated to the existence of a spectral flow $\lambda = k$ in quantum materials is the existence of a quantised conductance which is associated to dissipation-less currents. Such a result is known as the Landaueur formula [167, 168]. We would like to revisit this result in this section, with the particular tools of our formalism.

For that we proceed in two parts. In the first part, we explain how one can compute the conductance in systems where the gapless excitations are sufficiently separated in phase space so that scattering is highly suppressed. In the second one we show how to manipulate our original formulation of the spectral flow to make appear explicitly the conductance expression.

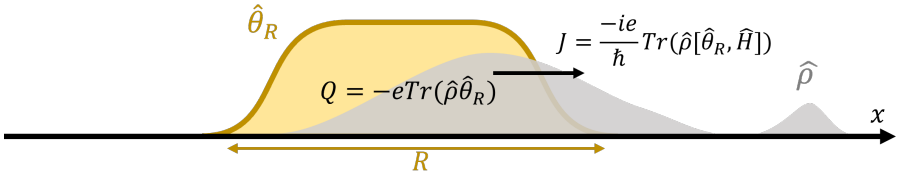

Figure 2.5: Computation of the charge in the region $\mathcal{R}$ and the current going trough it's boundary. The probability density ρ of the electron wave is denoted in grey, the function $\theta_{\mathcal{R}}$ selecting the $\mathcal{R}$ region is denoted in yellow.

To compute the conductance, one can first start by finding expression for the electric current. If $\theta_{\mathcal{R}}$ is a function which is 1 inside a region $\mathcal{R}$, 0 outside and has intermediate values near its boundary (see figure 2.5) then for a density matrix ρ, the charge contained inside $\mathcal{R}$ is given by

$$Q = -e \operatorname{Tr}\Big(\hat{\rho}\hat{\theta}_{\mathcal{R}}\Big) \tag{2.11}$$

The time evolution of the density matrix is given by $\partial_t \rho = \frac{i}{\hbar}[\rho, H]$ so we have

$$j = \frac{\partial Q}{\partial t} = \frac{-ie}{\hbar} \operatorname{Tr}\Big([\hat{\rho}, \hat{H}]\hat{\theta}_{\mathcal{R}}\Big) = \frac{-ie}{\hbar} \operatorname{Tr}\Big(\hat{\rho}[\hat{H}, \hat{\theta}_{\mathcal{R}}]\Big) \tag{2.12}$$

Because the commutator $[\hat{H}, \hat{\theta}_{\mathcal{R}}]$ appears in this expression, j is a quantity which is confined at the boundary of $\mathcal{R}$ and measures the flux of charges which cross it.

If we are interested in the current propagating in the, let's say, x direction around $x = 0$, one then take the function $\theta_{\mathcal{R}}$ which is 1 on the sites where $x < 0$ and 0 on the other. Then the quantity (2.12) is a measure of such a current. If we assume that our system is invariant by translation in the y direction with $\left\langle n'_y \right| \hat{\theta} \left| n_y \right\rangle = \rho_{n'_y - n_y}$ and $\left\langle n'_y \right| \hat{H} \left| n_y \right\rangle = \hat{H}_{n'_y - n_y}$ and perform a Wigner-Weyl transform in the y direction, the expression (2.12) becomes

$$\begin{aligned} j &= \frac{-e}{2\pi\hbar} \int dk_y \int dy \operatorname{Tr}\Big(\hat{\rho}(k_y)\partial_{k_y}\hat{H}(k_y)\partial_y \theta_{\mathcal{R}}(y)\Big) \\ &= \frac{e}{2\pi\hbar} \int dk_y \operatorname{Tr}\Big(\hat{\rho}(k_y)\partial_{k_y}\hat{H}(k_y)\Big) \end{aligned} \tag{2.13}$$

as every other orders in the semi-classical expansion of the Moyal product have vanishing integral in y [2].

Using this formalism one could, for example, compute the current of a system at thermal equilibrium where $\hat{\rho}_{\beta,\mu} = (1 + \exp\Big(\beta(\hat{H} - \mu)\Big))^{-1}$ where μ is the chemical potential and $\beta = 1/(k_b T)$. However, as long as the original model is discrete ($k_y \in [-\pi/a, \pi/a]$ bounded to a Brillouin zone) and that $\rho(k_y)$ has a finite number of degrees of freedom, it is possible to show that such equilibrium current must vanish.

However if an Hamiltonian has gapless modes which are sufficiently far away in phase space so that scattering is suppressed between those modes, it is possible to define out-of equilibrium states which are stationnary (up to exponentially slow correction) with a non-vanishing current. Typically in this case one can define a thermal state where the chemical potential between the gapless modes differs. Because the scattering between the modes is supposed to be suppressed, no thermalisation between the different modes occurs and it is an almost steady state.

[2] After the Wigner-Weyl transform, we should, in theory not use the same notation for the trace as the Hilbert space has changed and not put a hat on the symbol operator. However this Wigner-Weyl transform is partial and distinct from full semi-classical limit we will do later in the chapter. So to avoid multiplying the notations and be consistent with the rest of the chapter, we keep it as it is.

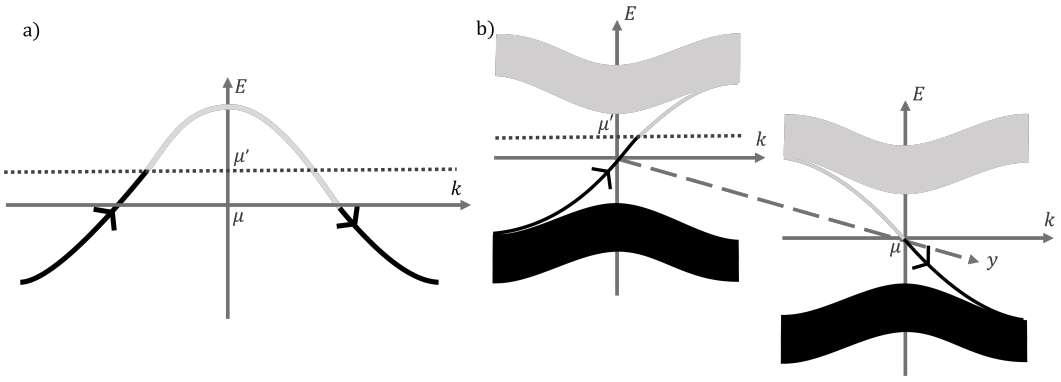

Figure 2.6: Off-equilibrium distribution of $\hat{\rho}_{\beta,\mu} + (\hat{\rho}_{\beta,\mu'} - \hat{\rho}_{\beta,\mu})\theta$ in the case where a) the modes are separated in wavenumber as in the bulk of 1D chain of section 2.2.1 b) separated in position as at the different edges of 2D Chern insulator of section 2.3.1. Despite being off equilibrium, the relaxation time is slow as the separation in phase space inhibit the scattering.

Such a state can be describe as follows

$$\hat{\rho} = \hat{\rho}_{\beta,\mu} + (\hat{\rho}_{\beta,\mu'} - \hat{\rho}_{\beta,\mu})\hat{\theta} \tag{2.14}$$

where μ and μ' are two different chemical potentials lying inside the gap. θ is a cut-off operator (not to be confused with $\hat{\theta}_{\mathcal{R}}$ introduced earlier to compute the current) which is the identity $\mathbb{1}$ near the gapless modes which are at chemical potential μ' and vanishes near the one which are at chemical potential μ (see figure 2.6). Since we assume that the gapless modes are separated in phase space by a gapped region, we have that $[\hat{\rho}, \hat{H}] = (\hat{\rho}(\mu') - \hat{\rho}(\mu))[\hat{\theta}, \hat{H}] \approx 0$ as $(\hat{\rho}(\mu') - \hat{\rho}(\mu))$ is only non-zero on the gapless modes and $[\hat{\theta}, \hat{H}]$ is located in the intermediate region where $\hat{\theta}$ goes from the identity to zero which is in the gapped region. Hence the $\hat{\rho}$ state has an almost stationnary evolution.

Now if we compute the current associated to this state we obtain

$$j = \frac{e}{2\pi\hbar} \operatorname{Tr}((\hat{\rho}(\mu') - \hat{\rho}(\mu))\theta\partial_k H) \tag{2.15}$$

Our goal is to show now that this current can be written up as

$$j = -\frac{e(\mu' - \mu)}{2\pi\hbar}\mathcal{I}_{\text{s-f}}. \tag{2.16}$$

For that purpose we start by recognising that one way to construct the flatten Hamiltonian used in the spectral-flow definition 2.3 is through thermal density. Indeed, as long as β is small compared to the gap and the chemical potential μ lies inside the gap, gapped modes are either completely filled or completely empty depending on if they are above or below the gap, so $\hat{H}_F = \mathbb{1} - 2\hat{\rho}_{\beta,\mu}$ is, in this case, a valid flatten Hamiltonian.

Then, we use the fact that $\hat{U} = \int dt\tilde{g}(t)e^{it\hat{H}}$[3] where $\tilde{g}(t)$ is the Fourier transform of $g(E) = -\exp(i\pi(1 - 2\rho_{\beta,\mu}(E)))$ with $\rho_{\beta,\mu}(E)$ the electron filling function. Then we can rewrite the expression 2.3 of the spectral flow index as

$$\begin{aligned}
\mathcal{I}_{\text{s-f}} &= \frac{1}{2i\pi}\int dk \operatorname{Tr}\left(\hat{U}^\dagger\partial_k\hat{U}\hat{\theta}\right) \\
&= \frac{1}{2i\pi}\int dk \operatorname{Tr}\left(\hat{U}^\dagger\int dt\tilde{g}(t)\partial_k e^{it\hat{H}}\hat{\theta}\right) \\
&= \frac{1}{2i\pi}\int dk \operatorname{Tr}\left(\hat{U}^\dagger\int dti\tilde{g}(t)\int_0^t dt' e^{i(t-t')\hat{H}}(\partial_k\hat{H})e^{it'\hat{H}}\hat{\theta}\right)
\end{aligned} \tag{2.17}$$

[3] can be simply checked in a diagonalisation basis of $\hat{H}$

Because the index is only non zero on gapless modes, it confines us in the gapless region and so commutators with θ must vanish. Therefore we obtain

$$\begin{aligned}\mathcal{I}_{\text{s-f}} &= \frac{1}{2i\pi}\int dk\,\mathrm{Tr}\Big(\hat{U}^\dagger\int dt it\tilde{g}(t)e^{it\hat{H}}(\partial_k\hat{H})\hat{\theta}\Big)\\ &= \frac{1}{2i\pi}\int dk\,\mathrm{Tr}\Big(\hat{U}^\dagger\int dt it\tilde{g}(t)e^{it\hat{H}}(\partial_k\hat{H})\hat{\theta}\Big).\end{aligned} \tag{2.18}$$

If we then use that $it\tilde{g}(t)$ is the Fourier transform of $g'(E) = -i2\pi\rho'_{\beta,\mu}(E)g(E)$ so

$$\int dt it\tilde{g}(t)e^{it\hat{H}} = -i2\pi\hat{U}\partial_\mu\hat{\rho}_{\beta,\mu}, \tag{2.19}$$

and therefore

$$\mathcal{I}_{\text{s-f}} = -\int dk\,\mathrm{Tr}\Big(\partial_\mu\hat{\rho}_{\beta,\mu}(\partial_k\hat{H})\hat{\theta}\Big) \tag{2.20}$$

Then, because the spectral flow doesn't change as long as μ stays inside the gap, we can integrate over μ using $\hat{\rho}(\mu') - \hat{\rho}(\mu) = \int_\mu^{\mu'} d\mu''\partial_{\mu''}\hat{\rho}_{\beta,\mu''}$, and obtain the wanted result

$$j = -\frac{e(\mu'-\mu)}{2\pi\hbar}\mathcal{I}_{\text{s-f}} \tag{2.21}$$

If we took now $\mu' - \mu = -eV$ where V is the difference of electric potentials between the two modes and use that $2\pi\hbar = h$, we obtain

$$j = \frac{e^2V}{h}\mathcal{I}_{\text{s-f}} \tag{2.22}$$

which proves the quantisation of the conductance.

2.2 Mode-shell correspondence in $1D$ and $2D$ systems

2.2.1 1D quantum channel

Let us start with the most simple example which exhibits a spectral flow. Let us consider the bulk of a 1D metal. Typically, there is a spectral flow at each point of the Fermi surface.

We can consider the simple 1D Hamiltonian with a hopping terms t between neighbouring sites and no on-site potential.

$$\hat{H} = \sum_n t/2(|n\rangle\langle n+1| + |n+1\rangle\langle n| \tag{2.23}$$

This Hamiltonian is invariant by translation, so the Wigner-Weyl transform coincides with the Bloch transform here

$$\hat{H}(k) = 2t\cos(k) \tag{2.24}$$

If we assume that the Fermi energy is zero $E_F = 0$ we see that the spectrum of the Bloch Hamiltonian crosses twice the Fermi energy, at $k = -\pi/2$ and at $k = \pi/2$ (see figure 2.7). This Hamiltonian is therefore gapless and the associated material metallic.

If we focus our attention on those individual crossings, we see that the one at $k = -\pi/2$ is a crossing of positive spectral flow $\mathcal{I}_{\text{s-f}} = 1$ (with flow parameter $\lambda = k_x$) while the one at $k = \pi/2$ is associated to a negative spectral flow $\mathcal{I}_{\text{s-f}} = -1$. In that case the cut-off $\hat{\theta}_\Gamma$ should be in wavenumber to separate one crossing from the other (see figure 2.7).

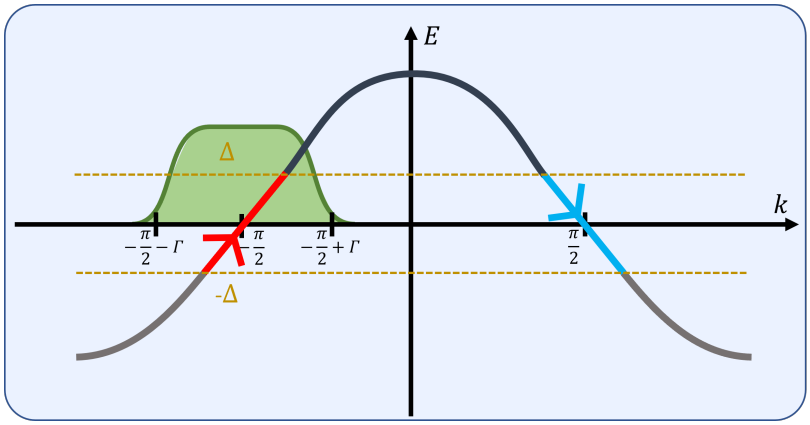

Figure 2.7: Schematic band dispersion of the 1D chain (2.23). It crosses in $k = -\pi/2$ and $k = \pi/2$ the zero energy line with respectively a positive and negative spectral flow. If one want to isolate the spectral flow in $k = \pi/2$, one can choose a cut-off like the one denoted in green.

At first order in the semi-classical limit, the shell invariant gives

$$\mathcal{I}_{\text{shell}} = -\int d\lambda \frac{1}{2}\,\mathrm{Tr}\Big(\hat{H}_F \partial_\lambda \hat{\theta}_\Gamma\Big) + \frac{1}{4}\,\mathrm{Tr}\Big(\hat{H}_F \partial_\lambda \hat{H}_F [\hat{\theta}_\Gamma, \hat{H}_F]\Big) \xrightarrow{S-C} -\int d\lambda \frac{1}{2}\,\mathrm{Tr}(H_F \partial_\lambda \theta_\Gamma) \quad (2.25)$$

If we define $\hat{P}(k) = (\mathbb{1} - \hat{H}_F(k))/2$, the Fermi projector on eigenvector of energy below the Fermi energy $E_F = 0$ and take a sufficiently sharp cut-off profile, $\hat{\theta}_\Gamma \to \mathbb{1}_{[k_0-\Gamma,k_0+\Gamma]}$ (where k_0 is the position of the crossing and Γ is the radius of the shell) such expression reduces to $\mathcal{I}_{\text{shell}} = \mathrm{Tr}(P(k_0 - \Gamma)) - \mathrm{Tr}(P(k_0 + \Gamma))$. The shell invariant is therefore the number of negative band eigenvalues on the left minus the number of negative eigenvalues on the right. It can be check easily that we indeed have that $\mathcal{I}_{\text{shell}} = 1$ around $k_0 = -\pi/2$ and $\mathcal{I}_{\text{shell}} = -1$ around $k_0 = \pi/2$, therefore mode-shell correspondence is verified.

Those indices remain quantised and topologically protected as long as there is a gap which separate them in phase space, but also as long as the Hamiltonian is short range in wavenumber. This is here insured by the fact that the Hamiltonian is invariant by translation and hence diagonal in wavenumber. In general, we do not need perfect invariance by translation and could allow the coefficients of the Hamiltonian to be slowly varying in position space (compared to the inter site distance). For example, phonons of large wavelength (compared to the lattice wavelenght) induce only small deformations of the Hamiltonian, so the scattering they generate between the two valleys would sill be exponentially small.

1D ballistic conductors are examples of materials where the mean free-path associated to the scattering is small compared to the lenght of the material. In those materials, quantisation of the conductance, as predicted by Landaueur [169], was indeed observed [168].

The main problem in condensed-matter applications is that defects in the lattice structure (vacancies, impurities, ...) induce perturbations which do not evolve slowly compared to the inter-site distance. This can therefore induce a scattering between the two valleys and could therefore destroy the topological protection.

We study, in the next section, the case of Chern insulators where spectral flow modes are separated in position which provides enhanced topological protection compared to the separation in wavenumber discussed here.

2.3 2D cases

2.3.1 2D lattice Chern insulator

In this section we illustrate how the mode-shell correspondence coincides with the bulk-edge correspondence in the case of Chern insulator on 2D discrete lattices. We consider a Hamiltonian $\hat{H}$ on this 2D lattice. We call x and y the spatial dimension of the lattice. For simplicity, we assume that the lattice is invariant by translation in the y direction so that k_y can serve as a spectral flow parameter. We then consider that the lattice has an edge/interface near $x = 0$ where the Hamiltonian $\hat{H}$ may have gapless edge/interface and is gapped far away from it. In particular we study the case where the Hamiltonian converges toward the bulk Hamiltonians $\hat{H}_\pm$ far on the left/right of the interface.

Since we work on a lattice, the wavenumber are bounded and so one can choose a cut-off which is only in position like for example $\hat{\theta}_\Gamma = \exp\{-x^2/\Gamma^2\}$ or $\hat{\theta}_\Gamma = (1+\exp\{x^2-\Gamma^2\})^{-1}$. Because of that, the term $\mathrm{Tr}\Big(\hat{H}_F\partial_\lambda\hat{\theta}_\Gamma\Big)$ in the expression of the shell invariant vanishes (2.8). If we do a semi-classical approximation of the other terms by replacing the commutators by Poisson brackets we obtain

$$\mathcal{I}_{\mathrm{shell}} = \frac{-1}{8i\pi}\int_0^{2\pi} dk_y \int_0^{2\pi} dk_x \sum_{n_x} \mathrm{Tr}\Big(H_F\partial_{k_x}H_F\partial_{k_y}H_F\delta_{n_x}\theta_\Gamma\Big) \tag{2.26}$$

which when we sum over n_x the discrete lattice coordinate associated to x using that $\sum_{n_x>0}\delta_{n_x}\theta_\Gamma = -1$ and $\sum_{n_x<0}\delta_{n_x}\theta_\Gamma = 1$ gives that shell index reduces to the difference of Chern number integrated on the 2D-Brillouin zone in the bulk far on the right (denoted $+$) and on the left (denoted $-$) of the interface/edge

$$\begin{aligned}\mathcal{I}_{\mathrm{shell}} &= \frac{-1}{8i\pi}\int_{[0,2\pi]^2} dk_x dk_y\, \mathrm{Tr}\Big(H_{F,+}\partial_{k_x}H_{F,+}\partial_{k_y}H_{F,+}\Big) - \mathrm{Tr}\Big(H_{F,-}\partial_{k_x}H_{F,-}\partial_{k_y}H_{F,-}\Big)\\ &= \frac{1}{i\pi}\int_{[0,2\pi]^2} dk_y dk_x\, \mathrm{Tr}\Big(P_+\partial_{k_x}P_+\partial_{k_y}P_+\Big) - \mathrm{Tr}\Big(P_-\partial_{k_x}P_-\partial_{k_y}P_-\Big)\\ &\equiv \mathcal{C}_+ - \mathcal{C}_-\end{aligned} \tag{2.27}$$

where P is the Fermi projector on the negative bands satisfying $H_F = 1 - 2P$.

Through theses explicit computations, we therefore recover the expected bulk-edge correspondence as a semi-classical limit of the shell index.

An example of Chern insulator: The Qi-Wu-Zhang model An example of model which exhibits a spectral flow is the well known Qi-Wu-Zang (QWZ) model [170]

$$\hat{H} = \begin{pmatrix} \sin(k_y) & \sum_n |n+1\rangle\langle n| + (M+\cos(k_y))\mathbb{1} \\ \sum_n |n\rangle\langle n+1| + (M+\cos(k_y))\mathbb{1} & -\sin(k_y)\end{pmatrix} \tag{2.28}$$

where k_y is the wavenumber associated to the y direction and n is a lattice number associated to the x direction.

Spectral flow occurs in this model when the lattice has an edge with an open boundary condition. The way to see this is to first realise that this model can be decomposed as a sum of a SSH model with a term breaking the chiral symmetry

$$\hat{H}(k_y) = \sigma_z \sin(k_y) + \hat{H}_{\mathrm{SSH}}(k_y) \tag{2.29}$$

where $\hat{H}_{\mathrm{SSH}}(k_y)$ is the SSH model as presented earlier in section 1.2.1 with coefficient $t' = 1$ and $t = M+\cos(k_y)$, while σ_z is the chiral operator associated to this SSH model $\{\sigma_z, \hat{H}_{\mathrm{SSH}}(k_y)\} = 0$. We therefore have

$$\hat{H}^2(k_y) = \sin(k_y)^2 + \hat{H}_{\mathrm{SSH}}(k_y)^2 \tag{2.30}$$

so we can only have modes $|\psi(k_y)\rangle$ crossing the zero-energy if $k_y = 0$ or if $k_y = \pi$. Moreover those modes must be zero modes of the SSH model $\hat{H}_{\text{SSH}}(k_y)\,|\psi\rangle = 0$. With our knowledge of the SSH model, we know that this can only happen when $|t'| = 1 > |M + \cos(k_y)| = |t|$ and is confined on the edges. On the left edge, we moreover know that the mode is of positive chirality $|\psi(k_y)\rangle = \begin{pmatrix} |\psi(k_y)\rangle_+ \\ 0 \end{pmatrix}$. It follows that, at first order in k_y around the crossing point, we have that

$$\hat{H}(k_y)\,|\psi(k_y)\rangle = (\begin{pmatrix} \sin(k_y) & 0 \\ 0 & -\sin(k_y) \end{pmatrix} + \hat{H}_{\text{SSH}}(k_y)) \begin{pmatrix} |\psi(k_y)\rangle_+ \\ 0 \end{pmatrix} \approx \pm k_y\,|\psi(k_y)\rangle \tag{2.31}$$

where $\pm 1 = 1$ when the crossing point is at $k_y = 0$ and -1 when it is at $k_y = \pi$. Therefore the crossing point is associated respectively to a positive/negative spectral flow. Moreover the overall spectral flow depends on if $\hat{H}_{\text{SSH}}(k_y)$ is topological or not at $k_y = 0$ and at $k_y = \pi$. If it is topological in either position, there is no spectral flow. If it is topological $k_y = 0$ but not at $k_y = \pi$, there is a positive spectral flow. If it is topological at $k_y = \pi$ but not at $k_y = 0$, there is a negative spectral flow. And if it is topological in both, the two local spectral flow cancel each other and the overall spectral flow vanishes. Doing such analysis using that $\hat{H}_{\text{SSH}}(k_y)$ is topological if and only if $|t'| > |t|$, we obtain the following phase diagram 2.8 depending on the M parameter.

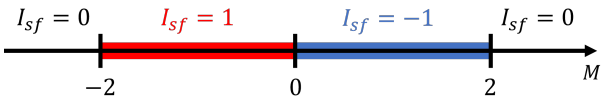

Figure 2.8: Different values of the total spectral flow index depending on the M parameter. When $|M| > 2$, $\hat{H}_{\text{SSH}}(k_y)$ is trivial both for $k_y = 0$ and $k_y = \pi$ so there is no spectral flow. When $-2 < M < 0$, $\hat{H}_{\text{SSH}}(k_y)$ is topological at $k_y = 0$ and trivial at $k_y = \pi$ leading to a positive spectral flow. When $0 < M < 2$, $\hat{H}_{\text{SSH}}(k_y)$ becomes trivial at $k_y = 0$ while becoming topological at $k_y = \pi$ leading to a negative spectral flow.

The shell/bulk invariant is then derived from the symbol/Bloch transform of this Hamiltonian in the bulk which is

$$H = \begin{pmatrix} \sin(k_y) & \sum_n e^{-ik_x} + M + \cos(k_y) \\ e^{ik_x} + M + \cos(k_y) & -\sin(k_y) \end{pmatrix} \tag{2.32}$$

using the expression (2.26).

Such Chern number is, to our knowledge, difficult to compute directly in an analytical way. One could use degrees formula [45] or numerical methods to compute it. In all cases, one can recover the same diagram as in figure 2.8. It is still interesting to note that the mode index is easier to compute than the bulk one in this model.

2.3.2 2D continuous case

In this section we present the case of continuous systems where a spectral flow can also occurs. In continuous systems, wavenumber is unbounded as $k \in \mathbb{R}$ (contrary to discrete systems where $k \in [0, 2\pi]$). As λ is typically interpreted as a wavenumber, we also assume that it is unbounded $\lambda \in \mathbb{R}$ Therefore one needs to consider a cut-off which selects not only in position x but also in wavenumber k and λ, for example taking $\hat{\theta}_\Gamma = (1 + \exp(x^2 - \partial_x^2 + \lambda^2 - \Gamma^2))^{-1}$. This therefore changes the shape of the shell in phase-space which is no longer a Brillouin zone in the bulk as in the discrete case but instead a sphere (x, k, λ) of radius Γ (as in figure 2.3.c). The semi-classical

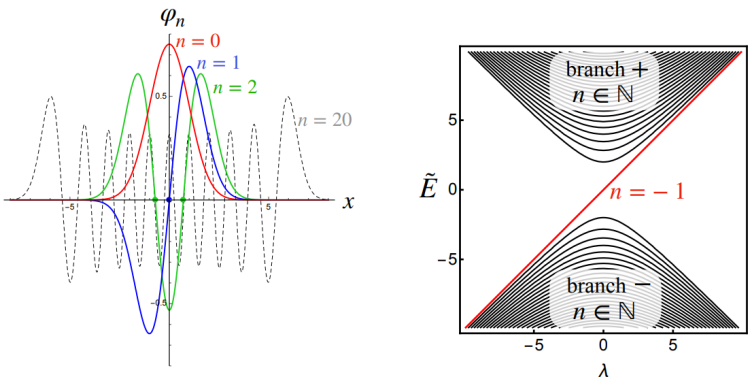

Figure 2.9: Spectrum of the modified Jackiw-Rebbi model. (left) spatial amplitude of the modes (right) associated energies. Modes are labeled by an integer n, the mode for $n = -1$ is the spectral flow mode denoted in red.

limit of the shell index (2.8) gives [4]

$$\mathcal{I}_{\text{shell}} \to \frac{-1}{i16\pi} \int_{x^2+k_x+\lambda^2=\Gamma^2} \text{Tr}(H_F dH_F dH_F) \tag{2.33}$$

with differential $dH_F = \partial_x H_F dx + \partial_{k_x} H_F dk_x + \partial_\lambda H_F d\lambda$.

An example: generalised Jackiw-Rebbi model/2D fermion with varying mass One of the advantage of studying spectral flows in a continuous regime is that there is a particularly simple example which is topological that is easy to analyse completely. To generate such an example, one takes the Jackiw-Rebbi Hamiltonian discussed in 1.2.3 $\hat{H}_{\text{jr}} = \begin{pmatrix} 0 & x+\partial_x \\ x-\partial_x & 0 \end{pmatrix}$ and add a term proportional to $-\partial_x \sigma_z$ giving the Hamiltonian

$$\hat{H} = \begin{pmatrix} k_y & x+\partial_x \\ x-\partial_x & -k_y \end{pmatrix}. \tag{2.34}$$

We call this model, a generalised Jackiw-Rebbi model. One can also see this Hamiltonian as a 2D Dirac operator with a varying mass $m(x) = x$ in σ_x [10, 45].

Since, as in the previous example, $k_y\sigma_z$ anticommutes with $\hat{H}_{\text{jr}}$, we can show that if there is a mode $|\psi(k_y)\rangle$ that crosses the zero-energy, then this crossing must be at $k_y = 0$ and moreover $|\psi(k_y = 0)\rangle$ must be a zero mode of $\hat{H}_{\text{jr}}$.

As the Jackiw-Rebbi model has exactly one zero-mode $(e^{-x^2/2}/\sqrt{2\pi}, 0)^t$ of positive chirality, there is exactly one crossing. Moreover, since k_y is an increasing function, such a crossing is associated to a positive spectral flow (see figure 2.9. The model is therefore topological.

The generalised Jacky-Rebby model can be understood as a continuous version of the QWZ model. Therefore we only have one crossing at $k_y = 0$ (the other possible crossing at $k_y = \pi/a$ is sent to infinity when the inter-site distance $a \to 0$). The other difference is that the mass coefficient $m(x)$ is not discontinuous as with open-boundary conditions but instead is smooth.

Since such a model is more simple, it is easy to compute the shell index analytically.

We need to first compute the symbol which is

$$H = \begin{pmatrix} k_y & x+ik_x \\ x-ik_x & -k_y \end{pmatrix}. \tag{2.35}$$

[4] Such semi-classical limit is more difficult to obtain than its discrete counter-part of the previous section. This is due to the fact that in the expression of the shell index (2.8), the terms in $\text{Tr}\big(\hat{H}_F \partial_\lambda \hat{\theta}_\Gamma\big)$ no longer vanishes and whose semi-classical limit is not obviously of the following form and need additional treatment.

$H_F^2 = k_x^2 + k_y^2 + x^2$ can then show that the flatten Hamiltonian $\hat{H}_F$ writes

$$H_F = \frac{1}{\sqrt{k_x^2 + k_y^2 + x^2}} \begin{pmatrix} k_y & x + ik_x \\ x - ik_x & -k_y \end{pmatrix}. \tag{2.36}$$

if we introduce spherical coordinate $(k_y = \Gamma\cos(\theta), x = \Gamma\sin(\theta)\cos(\phi), k_x = \Gamma\sin(\theta), \cos(\phi)$ on the shell then gives

$$H_F = \begin{pmatrix} \cos(\theta) & \sin(\theta)e^{i\phi} \\ \sin(\theta)e^{-i\phi} & -\cos(\theta) \end{pmatrix}. \tag{2.37}$$

One can then compute $\mathrm{Tr}(H_F dH_F dH_F) = -4i\sin(\theta)$ which, once integrated on the shell, gives that $\mathcal{I}_{\text{shell}} = \frac{-1}{16i\pi}\int_0^\pi d\theta \int_0^{2\pi} d\phi 4\sin(\theta) = 1$ and therefore both sides of the mode-shell correspondence can be verified analytically.

2.4 Higher dimensional construction

2.4.1 Weak/stacked topology

Similarly to what we did for the chiral number of zero modes, it is possible to create systems with a very high spectral flow number by just stacking layers of $1D$ channel or of $2D$ Chern insulators in a perpendicular direction. This can be useful as the resistance quantum associated to a single channel is quite large $R = h/e^2 \approx 26k\Omega$. When there are multiple channels, this resistance becomes $R = h/(e^2 N)$ where N is the number of stacked channels. In condensed matter application, the distance between layers can be as low as $10^{-9\sim10}m$ so N can be quite large and the theoretical resistance of the sample can become quite small for macroscopical transverse lenght which can be of interest for practical applications.

A simple model with such a phenomenology is made of N uncoupled stacked layers of some QWZ Chern insulator which reads

$$\hat{H} = \begin{pmatrix} \sin(k_y) & \sum_n |n+1\rangle\langle n| + (M + \cos(k_y))\mathbb{1} \\ \sum_n |n\rangle\langle n+1| + (M + \cos(k_y))\mathbb{1} & -\sin(k_y) \end{pmatrix} \otimes \sum_{m=1}^{N} |m\rangle\langle m| \tag{2.38}$$

where m is the index of the layer and N is the number of layers. In this case the model has a spectral flow index of $\mathcal{I}_{\text{s-f}} = N$.

One can consider the stacking of uncoupled 1D quantum channel, which can be done in two transverse directions

$$\hat{H} = \sum_n t/2(|n\rangle\langle n+1| + |n+1\rangle\langle n| \otimes \sum_{m,m'=1}^{N} |m,m'\rangle\langle m,m'| \tag{2.39}$$

where m and m' are the index of the layers in the two transverse directions.This model has therefore a spectral flow index of $\mathcal{I}_{\text{s-f}} = N^2$.

The fact that we consider uncoupled layers is just for the sake of having, quick to solve, models. One can add inter-layer couplings without breaking the topological protection. The only constraint is that the coupling between the layers must be weak enough[5] to not close the gap in the region separating the modes of opposite group velocity. In the case of the stack of Chern insulators, the additional inter-layer couplings must not close the bulk gap. In the case

[5] meaning that the coupling between the atoms must be quite anisotropic, strong inside the layer, weak between them.

of the stack of 1D chains, the Fermi surface must keep the property of being split in two distinct connected component, one of positive group velocity, and one of negative group velocity[6].

The main challenge to the use of those dissipation-less currents in electronic transport are the conditions needed to obtain these unidirectional zero modes with topologically suppressed scattering (by the separation in phase space). In the case of the quantum hall effect or the Chern insulator, this require quite low temperature or/and high magnetic field [5, 171, 172]. In the case of the 1D chain, the topological protection provided by the separation in wavenumber is weaker. It may suppress the scattering by perturbation (like phonon) of low wavenumber but are still sensible to the scattering of abrupt perturbation (like defects or short range interaction) which would generate dissipation. Therefore the material would need to be particularly pure to obtain good transport properties.

2.4.2 Higher-order topology

In the same way as in the previous chapter, there are also higher-order insulator where the spectral flow modes are confined in more than one dimension. To generate such higher-dimensional insulator simple to study we also use the same *additive tensor product construction*, introduced in section 1.3.3, up to a difference of symmetry.

Additive tensor product construction $\boxplus$

Indeed if $\hat{H}_A$ and $\hat{H}_B$ are two Hamiltonian with H_A an Hamiltonian with chiral symmetry $\hat{C}_A$, it is still possible to combine them through the construction

$$\hat{H} = \hat{H}_A \otimes \mathbb{1} + \hat{C}_A \otimes \hat{H}_B \tag{2.40}$$

although $H$is, in this case, no longer a chiral Hamiltonian.

We still have the relation

$$\hat{H}^2 = \hat{H}_A^2 \otimes \mathbb{1} + \mathbb{1} \otimes \hat{H}_B^2 + \{\hat{H}_1, \hat{C}_1\} \otimes \hat{H}_2 = \hat{H}_A^2 \otimes \mathbb{1} + \mathbb{1} \otimes \hat{H}_B^2 \ . \tag{2.41}$$

so the spectrum of $\hat{H}$ is still of the form $\pm\sqrt{(E_n^A)^2 + (E_m^B)^2}$ with $E_n^{A/B}$ eigenenergies of $\hat{H}_{A/B}$. In particular we also have that the zeros modes of $\hat{H}'$ is a product $\left|\psi_n^A\right\rangle \otimes \left|\psi_m^B\right\rangle$ of zero modes of $\hat{H}_{A/B}$ which is confined in both the gapless region of $\hat{H}_A$ and the one of $\hat{H}_B$.

One important use of this construction is to take a chiral higher-order insulator and generate a higher-order insulator with spectral flow. In this case we want to take an Hamiltonian $\hat{H}$ with chiral symmetry $\hat{C}$ that has topological zero mode and transform it into an Hamiltonian with topological spectral flow. We use the additive construction using $\hat{H}_A = \hat{H}$ and $\hat{H}_B = \lambda$ which generate the Hamiltonian $\hat{H}'$.

$$\hat{H}' = \lambda \boxplus \hat{H} \equiv \lambda \hat{C} + \hat{H} \tag{2.42}$$

In the section 2.3.2, we already encounter a model of this type and we already argued that each zero mode of positive chirality of $\hat{H}$ is associated to a mode of positive spectral flow of $\hat{H}'$ and vice-versa for zero modes of negative chirality which are associated to a negative spectral flow.

In those constructions, the spectral flow dimension is unbounded. If we want a bounded spectral flow parameter $\lambda \in \mathcal{S}^1$ as for wavenumber in discrete model, we need to tweak such an expression. One way is to do replace k by $\sin(k)$ as

$$\hat{H}' = \sin(\lambda)\hat{C} + \hat{H}. \tag{2.43}$$

[6] This is quite non-standard. In most material, the Fermi surface is a sphere (as in the Fermi gas problem) or a deformed sphere and therefore has a single connected component with no splitting.

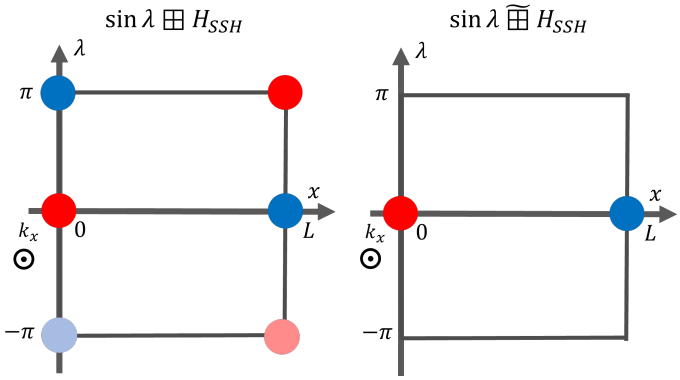

Figure 2.10: Localisation of the zero modes in phase space depending on the construction used. Modes zero-modes with positive/negative spectral flow are denoted in red/blue. (left) regular additive construction of an SSH model using 2.43 (right) modified additive construction of an SSH model using 2.44 .

This construction creates another zero mode of opposite spectral flow at $k = \pi$ and which is therefore separated only in wavenumber (see left of figure 2.10). If one wants to have a model where the zero-modes are only separated in position, it is possible to use another construction which if $C = \sigma_z$ define H' as

$$\hat{H}' = \sin(\lambda)\sigma_z + \sigma_x + (\hat{H} - \sigma_x)(1 + \cos(\lambda))/2 \tag{2.44}$$

which has the same spectral flow mode at $\lambda = 0$ as $H'(\lambda) \underset{\lambda\sim 0}{\approx} \lambda\sigma_z + \hat{H}$. Moreover it is gapped for $\lambda \neq 0$ as $\sin(\lambda) \neq 0$ and has no spectral flow modes at $k = \pi$ as $H'(\pi) = \sigma_x$ is now gapped (see right of figure 2.10). This is a similar situation to the QWZ model we encounter in section 2.3.1.We use the notation $\hat{H}' = \sin(k)\tilde{\boxplus}\hat{H}$ to refers to this useful construction.

When we instead take for $\hat{H}$ an chiral higher-order insulator, we obtain an higher-order insulator with spectral flow.

Example 1: 3D continuous higher-order insulator For that example we take the continuous 2D Jacky-Rossy model (1.72) $\hat{H}_{2D-JR}$ of the previous chapter and add a $\lambda\sigma_z \otimes \sigma_z$ ($\sigma_z \otimes \sigma_z$ is the chiral operator of the Jacky-Rossy model) to transform it into a model with spectral flow. This gives the model

$$\hat{H} = \begin{pmatrix} \lambda & y - \partial_y & x - \partial_x & 0 \\ y + \partial_y & -\lambda & 0 & x - \partial_x \\ x + \partial_x & 0 & -\lambda & -(y - \partial_y) \\ 0 & x + \partial_x & -(y + \partial_y) & \lambda \end{pmatrix} = \lambda \boxplus \hat{H}_{2D-JR} \ . \tag{2.45}$$

The Jacky-Rossy model can itself be decomposed into two blocks of Jacky-Rebby model $\hat{H}_{2D-JR} = \hat{H}_{\mathrm{JR}} \boxplus \hat{H}_{\mathrm{JR}}$. Therefore, the overall can be decomposed as the sum of 3 simple building blocks.

$$\hat{H} = \lambda\sigma_z \otimes \sigma_z + \hat{H}_{\mathrm{jr}}(x, \partial_x) \otimes \mathbb{1} + \sigma_z \otimes \hat{H}_{\mathrm{jr}}(y, \partial_y) \equiv \lambda \boxplus \hat{H}_{\mathrm{JR}} \boxplus \hat{H}_{\mathrm{JR}} \tag{2.46}$$

The symbol of this model is simple to calculate

$$\hat{H} = \begin{pmatrix} \lambda & y - ik_y & x - ik_x & 0 \\ y + ik_y & -\lambda & 0 & x - ik_x \\ x + ik_x & 0 & -\lambda & -(y - ik_y) \\ 0 & x + ik_x & -(y + ik_y) & \lambda \end{pmatrix} \ . \tag{2.47}$$

The shell is here the $4D$ sphere $\lambda^2 + x^2 + y^2 + k_x^2 + k_y^2 = \Gamma^2$ (see figure 2.3.d) so it makes sense to introduce spherical coordinates. If we compute the symbol of the flatten Hamiltonian in such coordinates, we obtain

$$\hat{H}_F = \cos(\theta_2)\left(\cos(\theta_1)\begin{pmatrix} 0 & e^{-i\phi_1} \\ e^{i\phi_1} & 0 \end{pmatrix} \otimes \mathbb{1} + \sigma_z \otimes \sin(\theta_1)\begin{pmatrix} 0 & e^{-i\phi_2} \\ e^{i\phi_2} & 0 \end{pmatrix}\right) + \sin(\theta_2)\sigma_z \otimes \sigma_z \tag{2.48}$$

whose higher-Chern number can be computed from the uniform higher-Berry curvature $\mathrm{Tr}^{\mathrm{int}}(H_F dH_F^4)$ on the sphere which gives $\mathcal{I}_{\mathrm{shell}} = -1/(256\pi^2)\int_{\mathcal{S}^4} \mathrm{Tr}^{\mathrm{int}}(H_f dH_F^4) = 1$ which therefore satisfies the mode-shell correspondence.

Example 2: 3D higher-order insulator on a lattice One can do a similar procedure using the BBH model (1.76) and create an example of a $3D$ higher-order insulator but which is defined on a lattice with topological zero modes confined at edges separated in position

$$\hat{H} = \sin(\lambda)\tilde{\boxplus}\hat{H}_{\mathrm{BBH}}. \tag{2.49}$$

As the BBH model is itself a sum of SSH model $\hat{H}_{\mathrm{BBH}} = \hat{H}_{\mathrm{SSH},x} \boxplus \hat{H}_{\mathrm{SSH},y}$, the general model can be decomposed into three basic blocs

$$\begin{aligned} \hat{H} =& \sin(\lambda)\sigma_z \otimes \sigma_z + \sigma_z \otimes \sigma_x(1-\cos(\lambda))/2 \\ &+ (1+\cos(\lambda))/2\left(\begin{pmatrix} 0 & t + t'T_x^\dagger \\ t + t'T_x & 0 \end{pmatrix} \otimes \mathbb{1} + \sigma_z \otimes \begin{pmatrix} 0 & t + t'T_y^\dagger \\ t + t'T_y & 0 \end{pmatrix}\right) \\ \equiv& \sin(\lambda)\tilde{\boxplus}\hat{H}_{\mathrm{SSH},x} \boxplus \hat{H}_{\mathrm{SSH},y} \end{aligned} \tag{2.50}$$

or can also be decomposed as a sum of a QWZ model with an SSH model

$$\hat{H} = (\sin(\lambda)\tilde{\boxplus}\hat{H}_{\mathrm{SSH},x}) \boxplus \hat{H}_{\mathrm{SSH},y} = \hat{H}_{\mathrm{QWZ}} \boxplus \hat{H}_{\mathrm{SSH}}. \tag{2.51}$$

Similarly to the BBH or the QWZ model which are its building blocks. The shell invariant is difficult to obtain explicitly, without using the mode-shell correspondence or using numerical methods. We therefore do not compute it here. However the import message is that tensor constructions are powerful tools to create, easy to analyse, models.

2.5 Conclusion

In this chapter, we have discussed the mode-shell correspondence when the mode index is the spectral flow. We showed how it includes the bulk-edge correspondence as a particular example. We also demonstrated that the mode-shell correspondence is a more general formalism beyond the case of unidirectional modes localized in position in 2D lattices. We discussed how the mode-shell can adapt to many situations beyond this case. We presented models that are continuous rather than discrete. We introduced models where modes are localized in wavenumber instead of position. Finally, we explored higher dimensional cases such as layer models with a macroscopic spectral flow as well as higher order models where modes are localized in more than one direction. All these generalizations are similar to those presented in the previous chapter. This, therefore, shows that, up to the changes in the mode index, all the mode-shell phenomenology remains qualitatively the same.

Chapter 3

Mode-shell correspondence: $2D$-Dirac cones and $3D$-Weyl cones

3.1 Construction of modes invariants and their mode-shell correspondence

In the previous chapter, we constructed the 1D spectral flow, which is a topological mode invariant applicable to Hamiltonians that depend on a single parameter λ. In this section, we will demonstrate how it is possible to define topological invariants for Hamiltonians that depend on more than one variable $(\lambda_1, \ldots, \lambda_{\mathrm{D_M}})$. Similarly to the spectral flow case, those parameters can either have an external origin, as in a pump or designate a coordinate in phase space. In particular, we will focus on the $\mathrm{D_M} = 2$ and $\mathrm{D_M} = 3$ cases where the parameters are wavenumbers $\lambda_i = k_i$ coming from a Fourier/Bloch transform of the operator. We will see that, in these cases, the $\mathrm{D_M} = 2$ and $\mathrm{D_M} = 3$ mode indices capture the number of $2D$-Dirac cones and $3D$-Weyl cones in the gapless spectrum of the Hamiltonian. In this case $\mathrm{D_M}$ therefore represent the number of dimensions on which the gapless mode can propagate. In the first chapter where we studied chiral zero modes we therefore had $\mathrm{D_M} = 0$ while in the second chapter where we studied the spectral flow invariant we had $\mathrm{D_M} = 1$.

To study both $2D$-Dirac cones and $3D$-Weyl cones, we distinguish two types of situations for the Hamiltonian. In the case of $2D$-Dirac cones, and generally when $\mathrm{D_M}$ is even, we consider Hamiltonians $\hat{H}$ with a chiral symmetry $\hat{C}$ such that $\{\hat{H}, \hat{C}\} = 0$. (Note: Dirac cones can also be protected by time-reversal symmetry, but we don't take that approach here.) In the case of 3D-Weyl cones, and generally when $\mathrm{D_M}$ is odd, we consider Hamiltonians $\hat{H}$ with no particular symmetry.

In both cases, we aim to describe topological phenomena occurring in the region of phase space where $\hat{H}$ is gapless. In the previous chapter, we reformulated the spectral flow, a low-energy invariant, as an invariant (a winding number) defined on a gapped Hamiltonian $\hat{H}'$ derived from $\hat{H}$. We follow a similar strategy here and define, depending on the chiral/non-chiral case, the Hamiltonian

$$\begin{aligned} &\text{non-chiral symmetric } (\hat{H} \text{ in class A}): \hat{H}' = \begin{pmatrix} 0 & -e^{-i\pi\hat{H}_F} \\ -e^{i\pi\hat{H}_F} & 0 \end{pmatrix} = -\sigma_x e^{-i\pi\sigma_z \otimes \hat{H}_F} \\ &\text{chiral symmetric } (\hat{H} \text{ in class AIII}): H' = \sin\Big(\pi\hat{H}_F\Big) - C\cos\Big(\pi\hat{H}_F\Big) = -\hat{C}e^{-\pi\hat{C}\hat{H}_F}. \end{aligned} \tag{3.1}$$

The Hamiltonians $\hat{H}'$ are trivial outside the gapless region. Because $\hat{H}_F^2 = 1$ we have that $-e^{-i\pi\hat{H}_F} = 1$ and therefore $\hat{H}' = \left(\begin{smallmatrix} 0 & \mathbb{1} \\ \mathbb{1} & 0 \end{smallmatrix}\right)$ in the non-chiral case and similarly $\hat{H}' = \hat{C}$ in the chiral

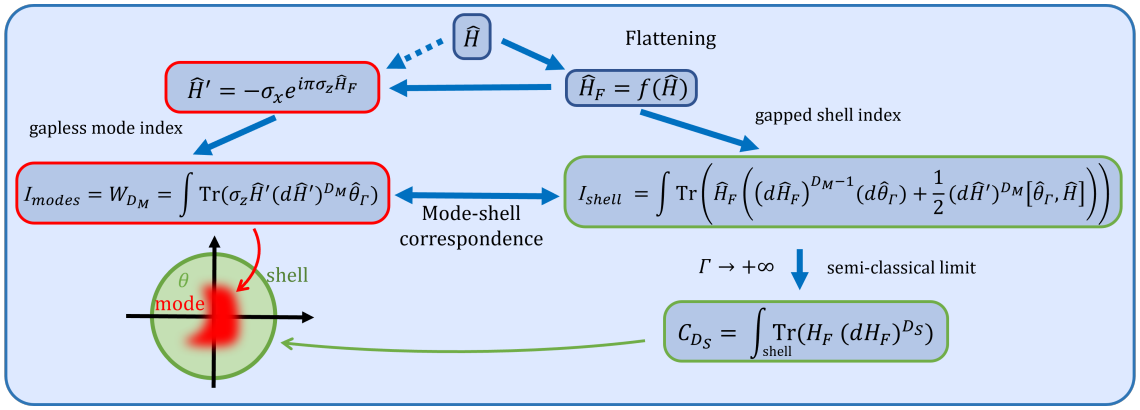

Figure 3.1: Summary diagram of the mode-shell correspondence in odd mode dimensions $\mathrm{D_M}$. In this case the mode-index is a higher winding number. The correspondence relate it to an index defined on the shell I_{shell} which reduces to a Chern number in the semi-classical limit. Similar diagram exist in even dimension.

case, which are both topologically trivial Hamiltonians with no inter-site couplings. Therefore, the topologically non-trivial behavior of $\hat{H}'$ is concentrated in the gapless region. It should be noted that with such a definition, if $\hat{H}$ is chiral symmetric, the corresponding $\hat{H}'$ has no particular symmetry. In the opposite case where $\hat{H}$ has no symmetry, the corresponding $\hat{H}'$ is chiral symmetric. In both cases, $\hat{H}'$ is built in such a way that $\hat{H}'^2 = \mathbb{1}$, so it is a gapped operator on which we can apply the known theory of topological invariants, and in particular express the mode index $\mathcal{I}_{\mathrm{mode}}$ as a (higher) Chern or a (higher) winding number

$$\begin{aligned}
\hat{H} \text{ in class A: } \mathcal{I}_{\mathrm{mode}} &= \mathcal{W}_{\mathrm{D_M}}(\hat{H}') = a_{\mathrm{D_M}} \int \mathrm{Tr}\Big(\hat{\sigma}_z \hat{H}'(d\hat{H}')^{\mathrm{D_M}}\hat{\theta}_\Gamma\Big) \\
\hat{H} \text{ in class AIII: } \mathcal{I}_{\mathrm{mode}} &= \mathcal{C}_{\mathrm{D_M}}(\hat{H}') = b_{\mathrm{D_M}} \int \mathrm{Tr}\Big(\hat{H}'(d\hat{H}')^{\mathrm{D_M}}\hat{\theta}_\Gamma\Big) \\
a_{\mathrm{D_M}} &= \frac{((\mathrm{D_M}+1)/2)!}{(\mathrm{D_M}+1)!(-2i\pi)^{(\mathrm{D_M}+1)/2}}, \qquad b_{\mathrm{D_M}} = \frac{1}{2^{\mathrm{D_M}+1}(\mathrm{D_M}/2)!(-2i\pi)^{\mathrm{D_M}/2}}
\end{aligned} \tag{3.2}$$

The notation $d\hat{H}' = \sum_i \partial_{\lambda_i}\hat{H}' d\lambda^i$ is a form notation, and the notation $(d\hat{H})^{\mathrm{D_M}}$ should be understood as an antisymmetrized sum of all possible products of derivatives. For example, in $\mathrm{D_M} = 2$, we have that $(d\hat{H})^2 = \partial_{\lambda_1}\hat{H}\partial_{\lambda_2}\hat{H} - \partial_{\lambda_2}\hat{H}\partial_{\lambda_1}\hat{H}$. The operator $\hat{\theta}_\Gamma$ is a cutoff operator that selects a particular low-energy region of phase space similar to the spectral flow case. Finally the integral runs over the parameters λ_i where typically $\lambda_i \in \mathbb{S}^1$ or $\lambda_i \in \mathbb{R}$.

With this convention, $\mathcal{W}_1$ and $\mathcal{C}_2$ are respectively the first winding number and the first Chern number while $\mathcal{W}_{2D+1}$ and $\mathcal{C}_{2D}$ for $D > 1$ are their higher-dimensional counterparts.

Those mode invariants also satisfy a mode-shell correspondence has they can be re-expressed as the following invariants which are defined in the shell region (of dimension $\mathrm{D_S}$) where $\hat{H}$ is gapped:

$$\begin{aligned}
\hat{H} \text{ in class A: } \mathcal{W}_{\mathrm{D_M}}(\hat{H}') &= b_{\mathrm{D_M}-1} \int \Big(\mathrm{Tr}\Big(\hat{H}_F(d\hat{H}_F)^{\mathrm{D_M}-1}d\hat{\theta}_\Gamma\Big) + \mathrm{Tr}\Big(\hat{H}_F(d\hat{H}_F)^{\mathrm{D_M}}[\hat{\theta}_\Gamma, \hat{H}_F]\Big)\Big) \\
\hat{H} \text{ in class AIII: } \mathcal{C}_{\mathrm{D_M}}(\hat{H}') &= -a_{\mathrm{D_M}-1} \int \Big(\mathrm{Tr}\Big(\hat{C}\hat{H}_F(d\hat{H}_F)^{\mathrm{D_M}-1}d\hat{\theta}_\Gamma\Big) + \mathrm{Tr}\Big(\hat{C}\hat{H}_F(d\hat{H}_F)^{\mathrm{D_M}}[\hat{\theta}_\Gamma, \hat{H}_F]\Big)\Big)
\end{aligned} \tag{3.3}$$

where the right hand side is therefore a shell index $\mathcal{I}_{\mathrm{shell}}$. The proof of this result can be found in appendix D. When those invariants have a semi-classical limit, the shell index reduces to a

Chern or a winding number which is defined on the shell

$$\begin{aligned}\hat{H} \text{ in class A: } \mathcal{W}_{\mathrm{D_M}}(\hat{H}') &= b_{\mathrm{D_S}} \int_{\text{shell}} \mathrm{Tr}\Big(\hat{H}_F (d\hat{H}_F)^{\mathrm{D_S}}\Big) = \mathcal{C}_{\mathrm{D_S}}(H_F) = \mathcal{I}_{\text{shell}} \\ \hat{H} \text{ in class AIII: } \mathcal{C}_{\mathrm{D_M}}(\hat{H}') &= a_{\mathrm{D_S}} \int_{\text{shell}} \mathrm{Tr}\Big(\hat{C}\hat{H}_F (d\hat{H}_F)^{\mathrm{D_S}}\Big) = \mathcal{W}_{\mathrm{D_S}}(H_F) = \mathcal{I}_{\text{shell}}\end{aligned} \tag{3.4}$$

where $\mathrm{D_S}$ is the dimension of the shell in phase space.

So in the case where $\hat{H}$ is chiral, we have an equality between a (higher) Chern number $\mathcal{C}_{\mathrm{D_M}}(\hat{H}')$, integrated on $(\lambda_1, \ldots, \lambda_{\mathrm{D_M}}$, which associated to gapless properties of $\hat{H}$ and a (higher) winding number $\mathcal{W}_{\mathrm{D_S}}(H_F)$ integrated on the shell where $\hat{H}$ is gapped. In the non-chiral case, we have a (higher) winding number $\mathcal{W}_{\mathrm{D_M}}(\hat{H}')$, integrated on $(\lambda_1, \ldots, \lambda_{\mathrm{D_M}}$, which is associated to gapless properties of $\hat{H}$, which is equal to a (higher) Chern number on the shell $\mathcal{C}_{\mathrm{D_S}}(H_F)$ where $\hat{H}$ is gapped (see figure 3.1). This is the mode-shell correspondence in the semi-classical case.

We now explore how the mode-shell correspondence and its phenomenology are verified in particular examples in the $\mathrm{D_M} = 2$ and $\mathrm{D_M} = 3$ cases.

3.2 Examples of models with Dirac and Weyl cones

3.2.1 General remarks and constructions

In these sections, we study systems hosting Dirac and Weyl cones through the prism of the mode-shell correspondence. We start with the basic example of a single Dirac/Weyl cone and verify that it is considered topological by $\mathcal{I}_{\text{shell}}$ and therefore by $\mathcal{I}_{\text{modes}}$ for respectively $\mathrm{D_M} = 2$ and $\mathrm{D_M} = 3$. This justifies that the mode indices "count" the number of Dirac/Weyl cones. We then move to more involved systems and see that Dirac/Weyl cones can either be separated in wavenumber as in the bulk of a semi-metal or be separated in position, at the edges of a topological insulator (see figure 3.2.

Additive construction $\boxplus$ Similarly to the previous sections, we use tensor product constructions to obtain simple-to-analyze examples. We reuse the additive constructions introduced in the previous chapters but also introduce a new one.

In the previous chapters, we introduced an additive tensor product construction which takes as input two chiral Hamiltonians $\hat{H}_A$ and $\hat{H}_B$ and generates a new one $\hat{H}' = \hat{H}_A \otimes \mathbb{1} + \hat{C}_A \otimes \hat{H}_B$, which is higher-dimensional. We also explained how if $\hat{H}_B$ is not chiral, such a construction is still valid, except that $\hat{H}'$ is then no longer chiral.

Here we introduce an analogous construction, which covers the last case where neither $\hat{H}_A$ nor $\hat{H}_B$ is chiral. In this case, we can generate a chiral $\hat{H}'$ using the construction:

$$\hat{H}' = \hat{H}_A \boxplus \hat{H}_B \equiv \hat{H}_A \otimes \mathbb{1} \otimes \sigma_x + \mathbb{1} \otimes \hat{H}_B \otimes \sigma_y. \tag{3.5}$$

where σ_x and σ_y are the usual Pauli matrices. Therefore, the tensored Hilbert space is twice larger and $\mathbb{1} \otimes \mathbb{1} \otimes \sigma_z$ is a chiral symmetry of $\hat{H}'$.

In particular, if we take $\hat{H}_B = k$, it allows us to generate from an Hamiltonian $\hat{H}_A = \hat{H}$ with a spectral flow, a model $\hat{H}'$ with a $2D$-Dirac cone defined as:

$$H' = H \otimes \sigma_x + k\mathbb{1} \otimes \sigma_y. \tag{3.6}$$

Similarly to what we did in section 2.4.2 of the previous chapter, we need to modify the construction in the discrete case as:

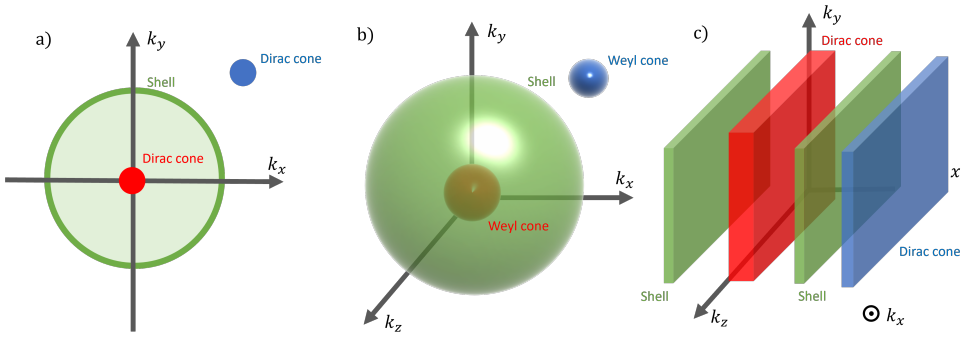

Figure 3.2: Form of the shell denoted in green around a) a Dirac cone confined in wavenumber where the shell forms a circle b) a Weyl cone confined in wavenumber where the shell forms a sphere c) a Dirac cone localised at the edge of a 3D insulators where the shell is two 3D Brillouin zone located in the two bulks surrounding the edge.

$$\hat{H}' = \hat{H} \tilde{\boxplus} \sin(k) \equiv (\mathbb{1} + (\hat{H} - \mathbb{1})(1 + \cos(k))/2) \otimes \sigma_x + \sin(k)\mathbb{1} \otimes \sigma_y \tag{3.7}$$

which avoids unnecessary doubling of the number of Dirac/Weyl cones at $k = \pi/2$. With this modification, the system is now gapped at $k = \pi$ as $\hat{H}'(k = \pi) = \mathbb{1} \otimes \sigma_x$.

3.2.2 Single Dirac/Weyl cones

With this method, it is relatively easy to construct characteristic examples of Dirac/Weyl cones.

2D-Dirac Cones: For the Dirac case, it is simple to check that

$$k_x \boxplus k_y = \begin{pmatrix} 0 & k_x - ik_y \\ k_x + ik_y & 0 \end{pmatrix} \equiv \hat{H}_{\text{Dirac}} \tag{3.8}$$

whose spectrum is $E = \pm\sqrt{k_x^2 + k_y^2}$, and therefore the Dirac cone is centered at $(k_x, k_y) = (0, 0)$ (see Figure 3.3.a). In this case, the shell is the circle $k_x^2 + k_y^2 = \Gamma^2$ (see Figure 3.2.a). We can use the wavenumbers as parameters $\lambda_1 = k_x$ and $\lambda_2 = k_y$, because there is no additional dimension besides those, the model is already in a symbol formulation.

With those dimensions, we can define the mode index

$$\mathcal{C}_2(\hat{H}') = \frac{-1}{8i\pi} \int \text{Tr}\Big(\hat{H}'(d\hat{H}')^2\hat{\theta}_\Gamma\Big). \tag{3.9}$$

with cut-off $\hat{\theta}_\Gamma = (1 + \exp\Big(k_x^2 + k_y^2 - \Gamma^2\Big)^{-1}$. The equation 3.4 then proves that this mode index is equal to a shell index that is the winding number on the circle (see figure 3.2.a).

One can check that the Dirac Hamiltonian is similar to the symbol of the Jackiw-Rebbi Hamiltonian of section 1.2.3, except that the phase space is now (k_x, k_y) instead of (x, k)[1]. The winding number is therefore identical, and we have that

$$\mathcal{W}_1(\hat{H}_{\text{Dirac}}) = 1 \tag{3.10}$$

[1] A difference is however that x and k are only commuting variables in the semi-classical picture while k_x and k_y are good quantum numbers which do not necessitate a semi-classical approximation. If the shell invariants are the same, the gapless properties of the operator and the mode indices $\mathcal{I}_{\text{mode}}$ are different. The Jackiw-Rebby model has a single zero mode while the Dirac model has a Dirac cone.

which means that his model is considered as topological by our shell index and therefore our mode index. If one flip the sign of one direction ($k_x \to -k_x$), one could check that the shell index of the new Dirac Hamiltonian as the opposite sign. In the literature, the first Dirac Hamiltonian is called of "positive chirality" while the second one is called of "negative chirality" [33]. Such a difference of chirality is captured by the sign of $\mathcal{I}_{\text{mode}}$.

Therefore, with a slight abuse of notation, we can say that the $2D$ mode index "counts" the number of $2D$ Dirac cones with a sign depending on their chirality.

3D Weyl Cones: For the Weyl cones, we can extend the dynamics using the additive chiral construction:

$$\hat{H}_{\text{Dirac}} \boxplus k_z = k_x \boxplus k_y \boxplus k_z = \begin{pmatrix} k_z & k_x - ik_x \\ k_x + ik_y & -k_z \end{pmatrix} \equiv \hat{H}_{\text{Weyl}} \tag{3.11}$$

whose spectrum is $E = \pm\sqrt{k_x^2 + k_y^2 + k_z^2}$, and therefore the Weyl cone is centered at $(k_x, k_y, k_z) = (0, 0, 0)$. In this case, the shell is the sphere $k_x^2 + k_y^2 + k_z^2 = \Gamma^2$. We can use the wavenumbers as parameters $\lambda_1 = k_x$, $\lambda_2 = k_y$ and $\lambda_4 = k_z$, because there is no additional dimension besides those, the model is already in a symbol formulation.

With those dimensions, we can define the mode index

$$\mathcal{W}_3(\hat{H}') = \frac{-1}{48\pi^2} \int \text{Tr}\Big(\sigma_z \hat{H}' (d\hat{H}')^3 \hat{\theta}_\Gamma\Big). \tag{3.12}$$

with cut-off $\hat{\theta}_\Gamma = (1 + \exp\Big(k_x^2 + k_y^2 + k_z^2 - \Gamma^2\Big)^{-1}$. The equation 3.4 then proves that this mode index is equal to a shell index that is the Chern number on the sphere (see Figure 3.2.b). This is similar to the Chern number we had to compute in the modified Jackiw-Rebbi model of Section 2.3.2, except that the phase space is now (k_x, k_y, k_z) instead of (k_y, x, k_x). The Chern number is therefore identical, and we have that

$$\mathcal{C}_2(\hat{H}_{\text{Weyl}}) = 1 \tag{3.13}$$

which means that this model is considered as topological by our shell index and therefore our mode index. If one flip the sign of one direction ($k_x \to -k_x$), one could check that the shell index of the new Weyl Hamiltonian as the opposite sign. In the literature, the first Weyl Hamiltonian is called of "positive chirality" while the second one is called of "negative chirality" [33]. Such a difference of chirality is captured by the sign of $\mathcal{I}_{\text{mode}}$.

Therefore, with a slight abuse of notation, we can say that the $3D$ mode index "counts" the number of $3D$ Weyl cones with a sign depending on their chirality.

3.2.3 Bulk Dirac/Weyl cones separated in wavenumber

An important situation where Dirac/Weyl cones appear is in the bulk of semimetals. In this case, they appear in pairs of opposite chirality. This is known as the Nielsen-Ninomiya theorem [173, 174]. This theorem can be easily understood with the mode-shell correspondence. In systems where the set of parameter λ_i is bounded (as in the case of a Brillouin zone), the total number of Dirac/Weyl cones is given by the mode index (3.2) with $\theta = \mathbb{1}$. However, the corresponding shell index is zero as both $d\theta$ and $[\theta, H]$ vanish in this case. Therefore, the total numbers of Dirac/Weyl cones of positive and negative chirality must cancel each other out.

To generate such models with pairs of Dirac/Weyl cones, we can again use the additive construction as

$$\hat{H}^{\text{lattice}}_{\text{4-Dirac}} = \sin(k_x) \boxplus \sin(k_y) = \begin{pmatrix} 0 & \sin(k_x) - i\sin(k_y) \\ \sin(k_x) + i\sin(k_y) & 0 \end{pmatrix} \tag{3.14}$$

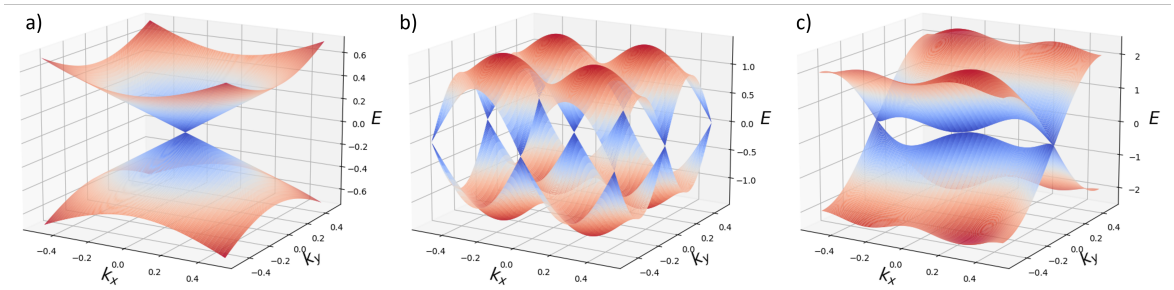

Figure 3.3: Spectrum of different model hosting Dirac cones. a) single Dirac cone model (3.8) b) the model (3.14) with 4 Dirac cones c) the model (3.16) with 2 Dirac cones/

or

$$\hat{H}^{\text{lattice}}_{\text{8-Weyl}} = \sin(k_x) \boxplus \sin(k_y) \boxplus \sin(k_z) = \begin{pmatrix} \sin(k_z) & \sin(k_x) - i\sin(k_y) \\ \sin(k_x) + i\sin(k_y) & -\sin(k_z) \end{pmatrix} \tag{3.15}$$

These have the disadvantage of having, respectively, 4 Dirac cones (see Figure 3.3.b) and 8 Weyl cones, instead of the minimal number of 2. To get a lattice model with only one pair of Dirac/Weyl cones, we can use the modified additive structure

$$\hat{H}^{\text{lattice}}_{\text{2-Dirac}} = \sin(k_x) \tilde{\boxplus} \sin(k_y) = (\mathbb{1} + (\sin(k_x) - \mathbb{1})(1 + \cos(k_y))/2)\, \sigma_x + \sin(k_y)\sigma_y \tag{3.16}$$

or

$$\begin{aligned} \hat{H}^{\text{lattice}}_{\text{2-Weyl}} &= \sin(k_x) \tilde{\boxplus} \sin(k_y) \tilde{\boxplus} \sin(k_z) = \sigma_z(1 - \cos(k_z))/2 + \sin(k_z)\sigma_z \\ &+ (\mathbb{1} + (\sin(k_x) - \mathbb{1})(1 + \cos(k_y))/2)\sigma_x + \sin(k_y)\sigma_y)\, /2 \end{aligned} \tag{3.17}$$

whose spectrum now only has 2 Dirac/Weyl cones (see Figure 3.3.c). A well-known model hosting only 2 Dirac cones is the tight-binding system [175] modeling Graphene close to the Fermi surface.

In all these examples, as the Dirac/Weyl cones are only separated in wavenumber, we have the same phenomenology as the examples of Section 1.2.2, 1.2.4, and 2.2.1. The cones are protected against perturbations of the Hamiltonian which are slowly varying in position but not to those which vary quickly (as impurities in the crystal structure).

To enhance the protection, one may therefore want to separate the Dirac/Weyl cones in position.

3.3 Dirac/Weyl cones confined in position

In this section, we study models hosting Dirac cones which are localised in position. For that we consider some continuous model which tends to be simple to analyse than their discrete counterpart wediscuss in the next section. To obtain a model confined in position, we can again, we can use the additive construction to combine a Dirac/Weyl Hamiltonian with a Jackiw-Rebby model which confines the mode in the new direction.

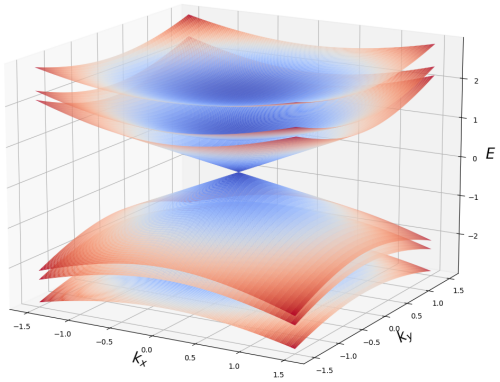

Figure 3.4: Spectrum of the Hamiltonian $\hat{H}_{\text{Dirac-JR}}$. The model has one Dirac cones while the other bands are gapped.

3D model with a Dirac cone confined at an interface For the Dirac case, such a construction gives the model

$$\begin{aligned}\hat{H}_{\text{Dirac-JR}} &= \hat{H}_{\text{Dirac}} \boxplus \hat{H}_{\text{JR,z}} = k_x \boxplus k_y \boxplus \hat{H}_{\text{JR,z}} \\ &= \begin{pmatrix} 0 & k_x - ik_y & z - \partial_z & 0 \\ k_x + ik_y & 0 & 0 & z - \partial_z \\ z + \partial_z & 0 & 0 & -k_x + ik_y \\ 0 & z + \partial_z & -k_x - ik_y & 0 \end{pmatrix}\end{aligned} \tag{3.18}$$

Since this model is an additive construction, we know that its eigenvalue are of the form $\sqrt{k_x^2 + k_y^2 + \lambda_n^2}$ where λ_n are the eigenvalue of the Jackiw-Rebby model (see figure 3.4). Because such a model has a zero modes $\psi_0 = (\exp(-z^2/2), 0)^T$ with $\lambda_0 = 0$, the model $\hat{H}_{\text{Dirac-JR}}$ has a Dirac cone centered in $(k_x, k_y) = (0, 0)$ and near $z \sim 0$. In particular the reduced Hamiltonian for modes of the form $\psi(k_x, k_y) \otimes \psi_0$ is just the Dirac Hamiltonian $\hat{H}_{\text{Dirac}}$ of positive chirality. So the mode index of such a model is $\mathcal{I}_{\text{modes}} = 1$.

The shell index is meanwhile the higher winding number on the 3-sphere $k_x^2 + k_y^2 + z^2 + k_z^2 = \Gamma^2$ of the symbol

$$H_{\text{Dirac-JR}} = \begin{pmatrix} 0 & k_x - ik_y & z - ik_z & 0 \\ k_x + ik_y & 0 & 0 & z - ik_z \\ z + ik_z & 0 & 0 & -k_x + ik_y \\ 0 & z + ik_z & -k_x - ik_y & 0 \end{pmatrix} \tag{3.19}$$

Such a symbol is similar to the Jackiw-Rossi model we studied in section 2.3.2 of first chapter. Therefore we know that the shell index is $\mathcal{I}_{\text{shell}} = \mathcal{W}_3(H_F) = 1$. So the mode-shell correspondence is verified.

4D model with a Weyl cone confined at an interface For the Dirac case, such a construction gives the model

$$\begin{aligned}\hat{H}_{\text{Weyl-JR}} &= \hat{H}_{\text{Weyl}} \boxplus \hat{H}_{\text{JR,u}} = k_x \boxplus k_y \boxplus k_z \boxplus \hat{H}_{\text{JR,u}} \\ &= \begin{pmatrix} k_z & k_x - ik_y & u - \partial_u & 0 \\ k_x + ik_y & -k_z & 0 & u - \partial_u \\ u + \partial_u & 0 & -k_z & -k_x + ik_y \\ 0 & u + \partial_u & -k_x - ik_y & k_z \end{pmatrix}\end{aligned} \tag{3.20}$$

Since this model is an additive construction, we know that its eigenvalue are of the form $\sqrt{k_x^2+k_y^2+k_z^2+\lambda_n^2}$ where λ_n are the eigenvalue of the Jackiw-Rebby model (see figure 3.4). Because such a model has a zero modes $\psi_0 = (\exp(-u^2/2), 0)^T$ with $\lambda_0 = 0$, the model $\hat{H}_{\text{Weyl-JR}}$ has a Weyl cone centered in $(k_x, k_y, k_z) = (0, 0)$ and near $u \sim 0$. In particular the reduced Hamiltonian for modes of the form $\psi(k_x, k_y, k_z) \otimes \psi_0$ is just the Weyl Hamiltonian $\hat{H}_{\text{Weyl}}$ of positive chirality. So the mode index of such a model is $\mathcal{I}_{\text{modes}} = 1$.

The shell index is meanwhile the higher winding number on the 4-sphere $k_x^2 + k_y^2 + k_z^2 + u^2 + k_u^2 = \Gamma^2$ of the symbol

$$H_{\text{Weyl-JR}} = \begin{pmatrix} k_z & k_x - ik_y & u - ik_u & 0 \\ k_u + ik_u & -k_z & 0 & u - ik_u \\ u + ik_u & 0 & -k_z & -k_u + ik_u \\ 0 & u + ik_u & -k_x - ik_y & k_z \end{pmatrix} \tag{3.21}$$

Such a symbol is similar to the higher-order model with spectral flow we studied in section 2.4.2 of the second chapter. Therefore we know that the shell index is $\mathcal{I}_{\text{shell}} = \mathcal{C}_4(H_F) = 1$. So the mode-shell correspondence is verified.

3.4 Dirac/Weyl cones at edges of topological insulators

To construct discrete models with Dirac/Weyl cones confined at the boundaries, and therefore separated in position, we need to use the modified additive construction to avoid other gap closing elsewhere in wavenumber. This make the Hamiltonians more complicated but the philosophy remains the same.

To construct a 3D topological insulator with a single $2D$-Dirac cone confined at each boundary we use the modified additive construction on a QWZ model (see section 2.3.1):

$$\begin{aligned} \hat{H}_{3D\text{-TI}} &= \hat{H}_{\text{QWZ}} \tilde{\boxplus} \sin(k_z) \\ &= (\mathbb{1} + (\hat{H}_{\text{QWZ}} - \mathbb{1})(1 + \cos(k_z))/2) \otimes \sigma_x + \sin(k_z)\mathbb{1} \otimes \sigma_y \end{aligned} \tag{3.22}$$

For the case of a 4D topological insulator with a single $3D$-Weyl cone confined at each boundary we use the modified additive construction on the previous model:

$$\begin{aligned} \hat{H}_{4D\text{-TI}} &= \hat{H}_{3D\text{-TI}} \tilde{\boxplus} \sin(k_u) \\ &= (\sigma_x + (\hat{H}_{3D\text{-TI}} - \sigma_x)(1 + \cos(k_u))/2) + \sin(k_u)\sigma_z \end{aligned} \tag{3.23}$$

In those cases, the shell invariant would be respectively a higher-winding number integrated on the bulk $3D$-Brillouin zone (see figure 3.2.c) and a higher Chern number integrated on the bulk $4D$-Brillouin zone.

For the $3D$ topological insulator case:

$$\mathcal{W}_3(H_F) = \frac{-1}{12(2\pi)^2} \int_{k_x,k_y,k_z \in [0,2\pi]} dk_x dk_y dk_z \, \text{Tr}\left(\hat{C}\hat{H}_F (d\hat{H}_F)^3\right) \tag{3.24}$$

And for the $4D$ topological insulator case:

$$\mathcal{C}_4(H_F) = \frac{-1}{256\pi^2} \int_{k_x,k_y,k_z,k_t \in [0,2\pi]} dk_x dk_y dk_z dk_u \, \text{Tr}\left(\hat{H}_F (d\hat{H}_F)^4\right) \tag{3.25}$$

In the case of $3D$ topological insulators, isolated Dirac cones have been experimentally observed at the boundary of 3D topological insulators [17, 18]. Observing $3D$-Weyl cones confined at the

edge of $4D$ material is however more difficult due to the fact that we live only in a 3-dimensional world. However, the idea can still be explored as one can replace a physical dimension by either a pumping parameter [176, 177] or using internal degrees of freedom such as spin or polarisation as a synthetic dimension [178]. Even if it is not a space dimension, synthetic dimensions can plays the same role and as long as the coupling in those dimensions remains short range, the edge modes remain uncoupled, in a way which may be stronger than if they where separated in wavenumber.

3.5 Conclusion

In this chapter, we discussed the topological aspects of $2D$-Dirac and $3D$-Weyl cones. We provided topological mode invariants that characterize the topology of these structures and showed that such invariants verify a mode-shell correspondence. We then discussed different cases where Dirac/Weyl cones are either confined in wavenumber or in position and discussed the differences in phenomenology. To construct examples that are simple to analyze, we once again used some additive tensor product constructions, demonstrating their effectiveness.

Part II

Topological ascpects beyond Hermitian linear systems

Chapter 4

Non-Hermitian topology

4.1 Why non-hermiticity in physics

In all previous chapters of the thesis, we have always assumed that the Hamiltonians we encounter were Hermitians. This is quite natural because the topology of operators was first studied in a quantum mechanical context, and in closed systems of quantum mechanics, the dynamic ise always described by a Schrödinger equation

$$i\hbar\partial |\psi\rangle = \hat{H} |\psi\rangle \tag{4.1}$$

with a Hamiltonian on the right side which is Hermitian. However, there are two fields of research in which this hypothesis is no longer true. The first is the study of the dynamics of open quantum systems [78, 179, 180], the second is the study of the dynamics of classical wave systems [38, 51, 82, 181].

Open quantum systems are part of quantum mechanics when trying to describe the evolution of a system $\mathcal{H}_S$ coupled to a bath $\mathcal{H}_B$ which can be large and cannot be completely simulated. In a large class of systems with appropriate assumptions, people have been able to derive an efficient evolution equation that involves only the $\mathcal{H}_S$ degrees of freedom of the system while taking into account the coupling to such an environment.

Such Linbladian evolution equation can be written as following [180]

$$\partial\hat{\rho} = \mathcal{L}[\rho] = -\frac{i}{\hbar}[\hat{H}, \hat{\rho}] + \sum_j \gamma_j \left(L_j \rho L_j^\dagger + -\frac{1}{2}\{L_j L_j^\dagger, \hat{\rho}\} \right) \tag{4.2}$$

where $\hat{\rho}$ is the reduced density matrix on the system $\mathcal{H}_S$, $\hat{H}$ is the Hermitian evolution of the system without the bath and L_i are jump operators coming from the interaction with the bath.

If one defines the effective (non-Hermitian) Hamiltonian

$$\hat{H}_{\text{eff}} = \hat{H} - \frac{i}{2}\sum_j L_j^\dagger L_j \tag{4.3}$$

The master equation can be rewritten as

$$\partial\hat{\rho} = \mathcal{L}[\rho] = -\frac{i}{\hbar}\left(\hat{H}_{\text{eff}}\hat{\rho} - \hat{\rho}\hat{H}_{\text{eff}}^\dagger\right) + \sum_j \gamma_j L_j \rho L_j^\dagger \tag{4.4}$$

where the effective Hamiltonian can be interpreted as the evolution of the individual trajectory $i\hbar\partial_t |\psi_j\rangle = \hat{H}_{\text{eff}} |\psi_j\rangle$ of the states $|\psi_j\rangle$ contained the density matrix $\rho = \sum_j |\psi_j\rangle \langle\psi_j|$ and the term

$\sum_j \gamma_j L_j \rho L_j^\dagger$ as quantum jumps between these trajectories. If we are in a regime where these quantum jumps are negligible, the dynamics is then governed by the non-Hermitian Hamiltonian. The study of the properties of such Hamiltonians is then crucial to understand the dynamics of such open systems.

Another important case of non-Hermitian operators appears in the study of classical waves [38,51,82,181]. In this case the wave is not a density probability as in the Schrodinger equation but classical fields like pressure, velocities, etc. If $|\psi\rangle = (a(x), b(x), \cdot)$ is the vector containing all the fields relevant for the dynamic, then the evolution equation can often be written as a system of first order equation

$$\partial_t |\psi\rangle = A |\psi\rangle \tag{4.5}$$

where $H = iA$ is an operator that plays a role equivalent to the Hamiltonian in the Schrodinger equation. The multiplication by i is a bit artificial because classical waves are real and do not need it, but it prevents the notion of Hermitian and anti-Hermitian ($H^\dagger = -H$) from being reversed, which is useful for consistency with the remainder of the thesis.

An important difference with the quantum case is that in the classical wave realm, there is no reason for $H = iA$ to be Hermitian and this is often not the case. This of course happens when we add damping or forcing into the system but we will see that it can also happen in closed systems and cause instabilities.

4.2 Hermiticity, non-Hermiticity and associated properties

An Hamiltonian is said to be be Hermitian when it is an operator which verify

$$\hat{H} = \hat{H}^\dagger \tag{4.6}$$

Such a condition has quite important consequences on the properties of $\hat{H}$. Indeed, an important element associated with the existence of Hermiticity condition is the spectral theorem which states that $\hat{H}$ can be decomposed as a sum of orthogonal eigenstates $|\psi_i\rangle$ of real eigenvalues λ_i.

$$\hat{H} = \sum_i \lambda_i |\psi_i\rangle \langle\psi_i| \tag{4.7}$$

another way to formulate this is to say that their is a unitary matrix U verifying

$$\hat{H} = U \begin{pmatrix} \lambda_1 & & & \\ & \lambda_2 & & \\ & & \ddots & \\ & & & \lambda_n \end{pmatrix} U^\dagger. \tag{4.8}$$

When the Hermiticity condition is no longer verified, this result breaks and two phenomena can appear. The first is that eigenvalues are no longer limited to be real and can become complex. The other one is that diagonalization is no longer always possible and that the common understanding of the spectrum can be challenged and have its limits.

4.3 Line gap and point gap

One consequence of having a complex spectrum is that we have two ways to generalise the notion of gap we have in Hermitian systems to the non-Hermitian case. In the Hermitian case, eigenvalues are located on a line so a gap can be defined as a point of the spectrum where there is no eigenvalue near by. When eigenvalues become complex, one can still define the gap as a

point of the complex plane where there is no eigenvalue near by: this is the notion of "point gap". But one can also generalise this notion of gap by saying that instead a gap is a line in the complex plane where there is no eigenvalues near by: this is the notion of "line gap" (see figure 4.1) [75–77].

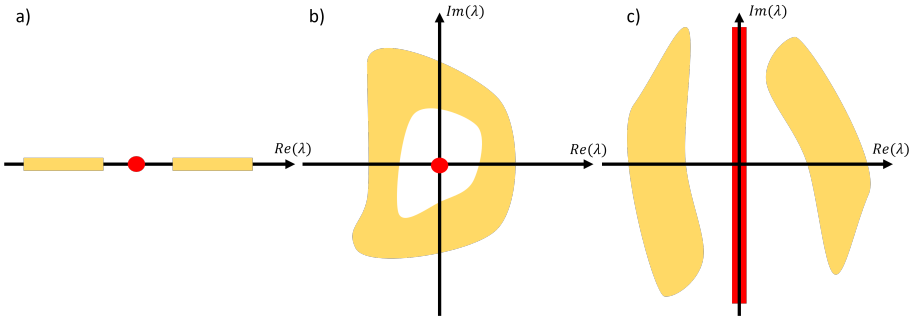

Figure 4.1: Different notions of gap in the real and complex cases. The eigenvalue λ are in yellow while the point or line that identify point or line gaps are shown in red a) point gap in the real case b) point gap in the complex plane c) line gap in the complex case

The two situations have a different topology and are thus not equivalent. We will see that the line gap case remains relatively close to the Hermitian case while the point gap case is more different.

4.4 Sensitivity of the non-Hermitian spectrum

For finite matrices, the diagonalization decomposition is replaced by a Jordan block decomposition which states that until a change of basis (not necessarily orthogonal), the matrix can be block diagonalised into Jordan blocks of the following form

$$J = \begin{pmatrix} \lambda & 1 & & & \\ & \lambda & 1 & & \\ & & \ddots & \ddots & \\ & & & \lambda & 1 \\ & & & & \lambda \end{pmatrix} \tag{4.9}$$

The number of 1 in such a block determines its rank. If a matrix can only be decomposed into zero-order Jordan blocks, then it is diagonalizable. If there is a block with a rank greater than 1, it is called in the physics literature an "exceptional point".

There are many reasons why physicists are interested in the existence of exceptional points in non-Hermitian systems. The most important of such point is that the operator's spectrum becomes particularly sensitive in the vicinity of an exceptional point.

The simplest example showing that is the following one

$$J_r = \begin{pmatrix} \lambda & 1 & & & \\ & \lambda & 1 & & \\ & & \ddots & \ddots & \\ & & & \lambda & 1 \\ r & & & & \lambda \end{pmatrix} \tag{4.10}$$

where have perturbed the exceptional point by adding a command term r. If we look for the eigenvalues E_j of J_r we find that they satisfy $E_j = \lambda + \sqrt[n]{r}e^{i2\pi j/n}$ which is a deviation of order

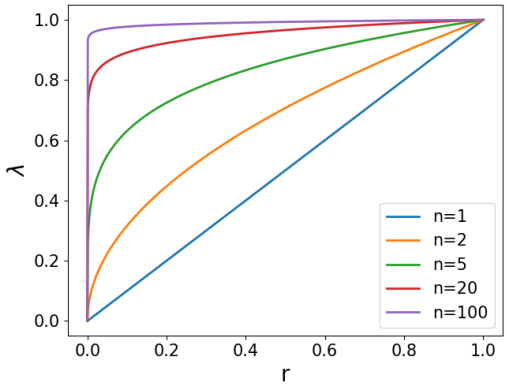

Figure 4.2: Evolution of the norm of the eigenvalues of the matrix J_r as a function of r and for different values of exceptional point degeneracy n. When n is large, there is a huge sensitivity of the value of r close to $r = 0$ with an almost discontinuous profile.

$\sqrt[n]{r}$ where n is the order of the exceptional point. Compared to the Hermitian case where such a deviation must be of the order r the sensitivity is extremely increased. For an exceptional point of very large order $n \to \infty$, this implies that even for an arbitrarily small order, the deviation could be of the order of 1 [80].

Such situations with extreme sensitivity to the eigenvalues of certain non-Hermitian systems call into question the very notion of spectrum in non-Hermitian systems. Indeed the matrix J is only the off-diagonal block $H_{\text{SSH}} = \begin{pmatrix} 0 & J_r \\ J_r^\dagger & 0 \end{pmatrix}$ of an SSH network of size $L = n$ for $t = 0$ and $t' = 1$ which is topological as long as $|\lambda|$ <1. So as long as $|E| < 1$, we have than

$$|\psi\rangle = \sum_n \lambda^n |n\rangle \tag{4.11}$$

is an almost eigenvector of J with eigenvalue λ. The error to be a true eigenvector is of the order λ^L which becomes exponentially small for a large L (see figure 4.3). The only "true" eigenvalue of J is $\lambda = 0$, which does not accurately represent the fact that there is a much wider range of "almost" eigenvalues around it. This is different from the Hermitian case where these almost eigenvalues are always adjacent to the real eigenvalues. Such kind of phenomena is called "skin effect" in the literature and have been widely studied [85, 86, 95, 182].

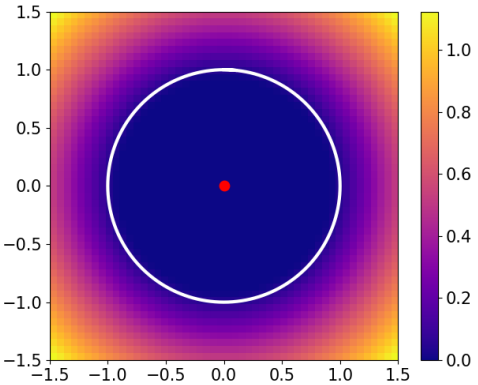

Figure 4.3: Plot of the lowest singular value of $H - \lambda$ for different complex value of λ for an exceptional point of size $L = 50$. The red point is the only eigenvalue of H for $\lambda = 0$. The white line delimits the region $\lambda < 1$ where $H - \lambda$ has an exponentially small singular value denoting the existence of an almost eigenvector.

4.5 Singular value decomposition

One way to better capture the existence of a near-eigenvector is to use singular decomposition. Such a decomposition is the main other way to generalize the eigenvalue decomposition to the non-Hermitian case. It states that any non-Hermitian operator can be decomposed as [80, 183]

$$H = VDU^\dagger \tag{4.12}$$

where U and V are unitary matrices and D is the diagonal matrix with positive coefficients. The coefficients of such a diagonal matrix are called singular values of H. We can think of U and V as the diagonalization basis of $H^\dagger H = UD^2U^\dagger$ and $HH^\dagger = VD^2V^\dagger$ respectively. Meanwhile, singular values can be interpreted as the square root of the eigenvalue of these operators.

If H has a vanishing singular value, then H has also a zero eigenvalue with an eigenvector $U|n\rangle$ such that $HU|n\rangle = 0$. In general, the eigenvalues λ of H are associated with the fact that $H - \lambda$ has zero singular value. Therefore, finding the zero-singular value of different operators $H_\lambda = H - \lambda$ is a good way to obtain information about the spectrum of H.

4.6 Hermitian mapping and topological invariants

This approach has two advantages and one disadvantage. The disadvantage is that for different eigenvalues λ_1 and λ_2 of H, it is necessary to do two decompositions into singular values, one for $H - \lambda_1$ and one for $H - \lambda_2$, which increases the number of computation. There are however advantages, the first one is that the singular value decomposition is more stable than non-Hermitian eigenvalues and detects the existence of almost eigenvectors. Indeed if H has an almost eigenvalue $\lambda_n \ll 1$ then $\|HU|n\rangle\| = \lambda_n \|V^\dagger U|n\| \ll 1\rangle$ so $U|n\rangle$ is an almost eigenvector. Vice versa if u is an almost eigenvector $\|Hu\| \ll 1$ then this means that $\|H^\dagger Hu\| \ll 1$ and therefore the Hermitian operator must have an eigenvalue $\lambda \ll 1$ almost zero and therefore H must have an almost zero eigenvalue $\sqrt{\lambda} \ll 1$.

The other advantage of the singular spectrum is that it can be mapped to an Hermitian problem. Indeed for each non-zero singular-value λ_n, the couple of vectors $u_n = U|n\rangle$ and $v_n = V|n\rangle$ verify

$$\begin{aligned} Hu_n &= \lambda_n v_n \\ H^\dagger v_n &= \lambda_n u_n \end{aligned} \tag{4.13}$$

which is equivalent to say that

$$\begin{pmatrix} 0 & H^\dagger \\ H & 0 \end{pmatrix} \begin{pmatrix} u \\ v \end{pmatrix} = \lambda_n \begin{pmatrix} u \\ v \end{pmatrix} \text{ and } \begin{pmatrix} 0 & H^\dagger \\ H & 0 \end{pmatrix} \begin{pmatrix} u \\ -v \end{pmatrix} = -\lambda_n \begin{pmatrix} u \\ -v \end{pmatrix}. \tag{4.14}$$

So in fact non-zero singular values of H are associated to the eigenvalues of the Hermitian (chiral) Hamiltonian [77, 183]

$$H' = \begin{pmatrix} 0 & H^\dagger \\ H & 0 \end{pmatrix}. \tag{4.15}$$

Such correspondence can be extended to zero-eigenvalue/zero-singular value through the fact that $Hu = 0$ implies that $H' \begin{pmatrix} u & 0 \end{pmatrix}^t = 0$ and $H^\dagger v = 0$ implies that $H' \begin{pmatrix} 0 & v \end{pmatrix}^t = 0$.

There is therefore a correspondence between the existence of (almost) zero modes located on the degrees of freedom of positive chirality of H' and the existence of (almost) zero modes of H. Conversely, if H' is gapped, then J cannot have (almost) zero modes. With this, we can map the point-gapped/gapless topology of the non-Hermitian operator H to the point-gapped/gapless topology of the chiral Hermitian operator H' that we know very well.

For example the number of zero modes of positive/negative chirality of H' is a topological property equal to the index of H

$$\mathcal{I}_{\text{modes}}(H') = \dim\ker(H) - \dim\ker(H^\dagger) = \text{Ind}(H) \tag{4.16}$$

In fact for $H = J$, H' is the SSH model and therefore the existence of almost zero modes in the entire region $|\lambda| < 1$ can be understood as a topological property in a bulk-edge correspondence setting.

We could in general use this mapping with the mode-shell correspondence to describe the properties of non-Hermitian point gap properties in other configurations where the modes are rather localized at the corner or separated in wavenumber. One could also use a higher topological chiral invariant such as the number of Dirac points to describe different non-Hermitian topologies. This go beyond the scope of this thesis but open interesting perspectives.

For now we only describe the case of a point gap, however such a correspondence can also be made in the case of a line gap. The idea is relatively simple. A line is a collection of points. So H has a gap line if and only if $H - \lambda$ is gapped for each eigenvalue λ belonging to the line. Thus, the topological line gap property of H can in fact correspond to the topological property of the family of Hermitian Hamiltonians

$$H'(t) = \begin{pmatrix} 0 & H^\dagger - \bar{\lambda}(t) \\ H - \lambda(t) & 0 \end{pmatrix} \tag{4.17}$$

where $t \in \mathbb{R}$ is an additional parameter such that $\lambda(t)$ span the line of the line gap.

Such a mapping to a Hermitian system can be used to create topological invariants for a non-Hermitian Hamiltonian with line gap. For example, for the case of 2D Hamiltonians, we can construct the global invariant

$$\mathcal{I} = \int_{-\infty}^{\infty} dt \int_0^{2\pi} dk_x \int_0^{2\pi} dk_y \,\text{Tr}\Big(CH'_F\partial_t H'_F[\partial_{k_x}H'_F, \partial_{k_y}H'_F]\Big) \tag{4.18}$$

where $H'_F(t, k_x, k_y)$ is the flattened Hamiltonian of $H'(t, k_x, k_y)$, t is the line spacing parameter and k_x, k_y are wavenumbers.

Such topological invariant can be constructed for all different cases of mode-shell correspondence, we just need to use t as an additional parameter. For example, in a continuous medium, the non-Hermitian invariant can be defined as

$$\mathcal{I} = \int_{-\infty}^{\infty} dt \int_{(x,k_x,k_y)\in\mathcal{S}^2} \text{Tr}(CH'_F\partial_t H'_F dH'_F, dH'_F) \tag{4.19}$$

where $dH'_F = \partial_x H'_F dx + \partial_{k_x} H'_F dk_x + \partial_{k_y} H'_F dk_y$

In the case where H is Hermitian and the line gap is the imaginary line $it \in i\mathbb{R}$, it is not difficult to show that such invariants coincide with the usual Chern numbers of H with Fermi projector P

$$\mathcal{C} = \int_0^{2\pi} dk_x \int_0^{2\pi} dk_y \,\text{Tr}\Big(P[\partial_{k_x}P, \partial_{k_y}P]\Big) \tag{4.20}$$

and

$$\mathcal{C} = \int_{(x,k_x,k_y)\in\mathcal{S}^2} \text{Tr}(PdP \wedge dP) \tag{4.21}$$

which confirms that such a line gap invariant is an extension of the Chern number to the non-Hermitian case.

Another possible way to extend the definition of Chern number to the non-Hermitian case is through the use of non-Hermitian projectors. In fact if a non-Hermitian Hamiltonian H has a

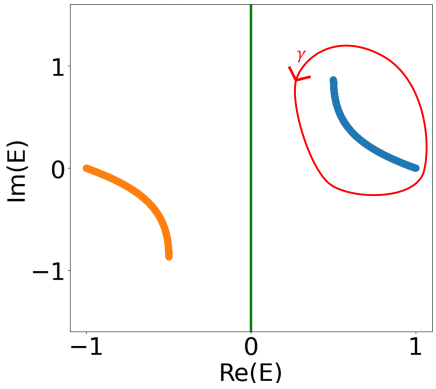

Figure 4.4: Example of a spectrum of a non-Hermitian Hamiltonian with a line-gap. The energy bands of such Hamiltonian are shown in orange/blue. The line separating those two bands is denoted in green. An example of possible path γ for the residue formula selecting the right band is denoted in red.

line gap separating the complex plane in two regions (see figure 4.4), one can define the projector on a given set of bands using the formula

$$P = \int_\gamma \frac{1}{H - z} dz \tag{4.22}$$

where γ is a path encircling these bands of the complex. Such a path exists due to the line-gap assumption. The above formula uses the well-known residue formula in complex analysis which states that $\frac{1}{2\pi i}\int_\gamma \frac{1}{E-z}dz$ is 1 for energies E inside the contour and 0 for the energies that are outside.

If one uses such a non-Hermitian projector in the formulas (4.20) and (4.21), one still obtains formulas which are quantised and can be shown to coincide with the invariants (4.18) and (4.19) respectively, so the formalisms are equivalent.

One may argue that the formula using the non-Hermitian projector are more intuitive. The mapping to the Hermitian operator $H'(z)$ is however more general as it can be applied in both point gap and line gap cases and for all dimensions. It can also be used to define gapless invariant (while non-Hermitian projectors are purely defined in the gapped region). No matter what, one needs to remember that the spectrum in non-Hermitian systems is more traitorous and finding the exact eigenvalues are not enough to define a gap. One needs also to search for approximate eigenvalue/singular values, especially in proximity of exceptional point of high ranks.

Example of line gap topology Let us present a simple example of non-Hermitian system which exhibit a generalised spectral flow topology. For that we will take the simple Hermitian model of 2.3.2 and add non-Hermiticity on the diagonal to create the non-Hermitian model

$$\hat{H}[\lambda] = \begin{pmatrix} \lambda & \mathrm{e}^{i\theta}(x - \partial_x) \\ \mathrm{e}^{i\theta}(x + \partial_x) & -\lambda \end{pmatrix} \tag{4.23}$$

such system remains analytically solvable and one can find that its eigenvalues are of the form (see Figure 4.5).

$$E^{\pm}_{\theta,n} = \pm\sqrt{\lambda^2 + e^{2i\theta}\sqrt{2}(n+1)} \qquad n \in \mathbb{N} \tag{4.24}$$

$$E_{-1} = \lambda\ . \tag{4.25}$$

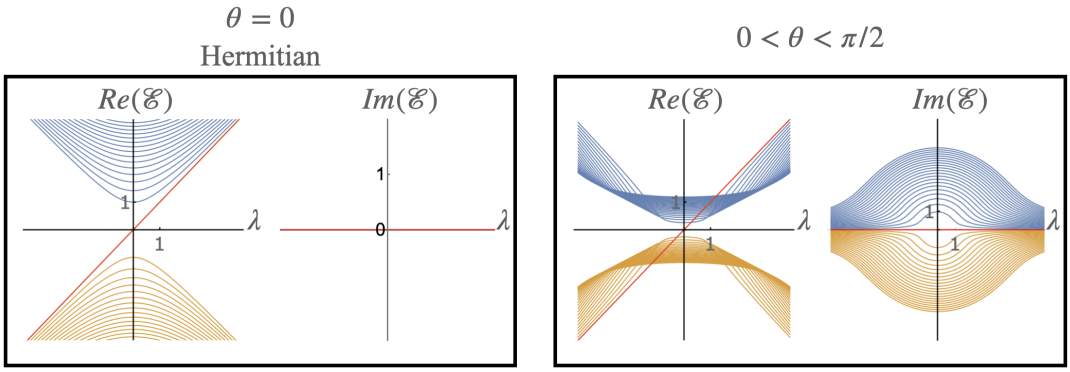

Figure 4.5: Eigenvalues of the different bands of the model (4.23). The band of positive/negative real part are denoted in blue/yellow. The spectral flow mode crossing the line-gap is denoted in red.

When $\theta = 0$, we recover the previously known, Hermitian system. When $-\pi/2 < \theta < \pi/2$, the system becomes non-Hermitian. There is however still a bi-partition of the system between band of positive/negative real part creating a line-gap[1]. There is just the mode E_{-1} which cross the line-gap with a positive spectral flow. We recover the fact that the spectral-flow topology is preserved under the non-Hermitian line gap assumption.

The symbol of such model is then

$$H_\theta[\lambda; x, p] = \begin{pmatrix} \lambda & e^{i\theta}(x - ip) \\ e^{i\theta}(x + ip) & -\lambda \end{pmatrix} . \tag{4.26}$$

If one compute, analytically or numerically, the generalised Chern number of such model, one still find that $\mathcal{C} = 1$, preserving the correspondence. This can be understood simply by the fact that such model are smooth deformation of an Hermitian model which already have a non-trivial Chern number which must be preserved by homotopy.

4.7 Conclusion

In this chapter, we have explored the specificities and challenges of non-Hermitian physics and topology. We have explained how such wave systems can originate in physics. We discussed how different the spectrum of such system is different from their Hermitian counterpart. From their complex nature which bring the notion of line and point gap, to the potential extreme sensitivity of the spectrum. We presented how this last point can be circumvented using instead the singular spectrum. We also shown how such consideration maps, quite naturally, such problem to Hermitian problem of a different symmetry class. This mapping allowed us to apply the full power of the mode-shell correspondence to the non-Hermitian case. This fact is of quite importance, as it allows to study topological properties of non-Hermitian systems beyond the bulk-edge phenomenology.

[1] When $\theta = \pi/2$, the line-gap closes and the topology may changed. In fact, due to particular symmetry of this model, the spectral flow is preserved. A more detailed analysis is provided in the paper [184].

Chapter 5

Non-linear topology

5.1 Non-linearity and deformation of zero-modes

In the general theory of the topology of wave operators, the assumption of linearity of the operator is used almost everywhere. We need it to define its spectrum which is an essential concepts of the theory. We need to know the eigenvalues of an operator to determine if it is gapped or not. The eigenstates are also used to defined the gapless and gapped topological properties. Furthermore, in the definition of invariants, we also use concepts like the trace or the determinant which are intrinsically concepts of linear algebra. All these tools are lost, a priori, when working with nonlinear operators and extending topological concepts to the nonlinear case may seem an impossible task.

The question of whether some generalization is possible is particularly interesting because there are many nonlinear wave equations in physics. In fact, linear equations are special cases that are only valid in a specific regime. For example, many platforms hosting topological phenomena, such as polaritons, photonic networks, fluids, and networks of springs and electrical circuits, naturally exhibit high-amplitude nonlinear behaviors. We can then ask ourselves whether the topological properties which exist in the linear regime are preserved when the non-linearities become non-negligible. We will study in particular the stability of edge modes with the addition of nonlinearities.

We focus on nonlinear Schrödinger equations on 1D lattices, whose nonlinear Hamiltonian H_ψ splits into a linear topological part H_{topo} and a nonlinear one $H_{\psi,\text{NL}}$ as

$$i\partial_t |\psi\rangle = H_\psi |\psi\rangle = (H_{\text{topo}} + H_{\psi,\text{NL}}) |\psi\rangle \ . \tag{5.1}$$

The burning question to ask is then: What are the conditions for the edge states of the linear topological model H_{topo} to survive the presence of nonlinearities $H_{\psi,\text{NL}}$? To answer this question, we can use a method based on exact perturbation theory that generates the edge modes and their energy of nonlinear systems of the form (5.1). The idea is to start with the edge mode of the linearised system at small amplitude and then increase smoothly the amplitude of the mode. As the relative strength of the nonlinearities increases, we are then able to deform the initial linear edge mode in a way that it remains a stationary edge solution of the nonlinear dynamics. The method can eventually reach nonlinear edge modes with a quite high amplitude as long as their energy remains in the spectral gap of the linearized dynamics. If this condition stops being fulfilled, the nonlinear edge state is then quickly delocalised into the bulk [102] and become unstable [103]. Then, we extend the notion of chiral symmetry to nonlinear systems, and show that chiral symmetric nonlinearities prevent such a delocalisation, thus protecting the nonlinear edge state. We then characterize those robust nonlinear edge modes with a local topological

index. The theory is illustrated with two nonlinear generalisations of the SSH model – one being chiral and one which is not – and confirmed numerically.

A concrete situation where the nonlinear Schrödinger equation modifies a 1D topological lattice model, is that of an SSH chain with couplings t_1 and t_2 between nearest neighbors and a on-site Kerr-like nonlinearity [82,104] similar to those appearing in the Gross-Pitaevskii equation for Bose-Einstein condensates [105]:

$$\begin{cases} i\partial_t a_j = t_1 b_j + t_2 b_{j-1} + |a_j|^2 a_j \\ i\partial_t b_j = t_1 a_j + t_2 a_{j+1} + |b_j|^2 b_j \ . \end{cases} \tag{5.2}$$

A state $|\psi\rangle$ of the system can be decomposed in the basis of the two sublattices as

$$|\psi\rangle = \begin{pmatrix} |\psi_A\rangle \\ |\psi_B\rangle \end{pmatrix} = \begin{pmatrix} \sum_j a_j \, |j, A\rangle \\ \sum_j b_j \, |j, B\rangle \end{pmatrix} \tag{5.3}$$

where j labels the unit cell. Such systems can be describes using the non-linear Hamitlonian

$$H_\psi = \sum_j \begin{pmatrix} |a_j|^2 & t_1 \\ t_1 & |b_j|^2 \end{pmatrix} |j\rangle \langle j| + \begin{pmatrix} 0 & t_2 \\ t_2 & 0 \end{pmatrix} |j\rangle \langle j-1| \ . \tag{5.4}$$

The linear SSH model is recovered when $|\psi\rangle$ is small in amplitude. In that case, this model is known to have a gap in energy around $E = 0$ when $|t_1| < |t_2|$, except for stationary topological edge modes which are localised at each end of the chain [128,185]. We then would like to know how these edge modes survive the introduction of the nonlinearities, such as in (5.4). We show below that edge states exist in nonlinear Schrödinger models when three conditions are met:

- (i) The linearised model has an edge state which is in the gap of the bulk bands.
- (ii) The linearisation H_{eff} of H_ψ around any state $|\psi\rangle$ is Hermitian.
- (iii) The nonlinear Hamiltonian H_ψ verifies the $U(1)$-symmetry $H_{e^{i\phi}\psi} = H_\psi$ for all $|\psi\rangle$.

Assumption (i) is quite natural, as we search nonlinear edge states as resulting from the deformation of linear ones. Assumption (ii) is made to guarantee that the energy E of the state remains real. And assumption (iii) is needed to insure that finding non-linear states of real energy $i\partial_t |\psi\rangle = E |\psi\rangle = H_\psi |\psi\rangle$ also generates solutions of (5.1) of the form $|\psi(t)\rangle = |\psi\rangle e^{-iEt}$. Note that our model (5.2) satisfies these three conditions. Note that those general hypothesis do not depend on the order of the nonlinear terms. Our method is thus not specific to Kerr-like terms and applies to arbitrary nonlinearities as long as the three hypothesis above are satisfied.

We now provide an explicit method to construct the nonlinear edge modes assuming that the three conditions above are met. For that let us study the space of edge states $|\psi\rangle$ of energy E of H_ψ that we define as being spanned by the doublet $(E, |\psi\rangle)$. The key idea to explore this space is to parameterize it with a continuous parameter s and to derive the evolution equation for the states close in s. If $(E_s, |\psi_s\rangle)$ is a doublet such that for all s, $|\psi_s\rangle$ is a solution of:

$$E_s \, |\psi_s\rangle = H_\psi \, |\psi_s\rangle \tag{5.5}$$

then, by differentiating this equation along s, one finds that the condition for this path to exist is to satisfy the following evolution equation:

$$(H_{\text{eff},s} - E_s) \, |\partial_s \psi_s\rangle = (\partial_s E_s) \, |\psi_s\rangle \tag{5.6}$$

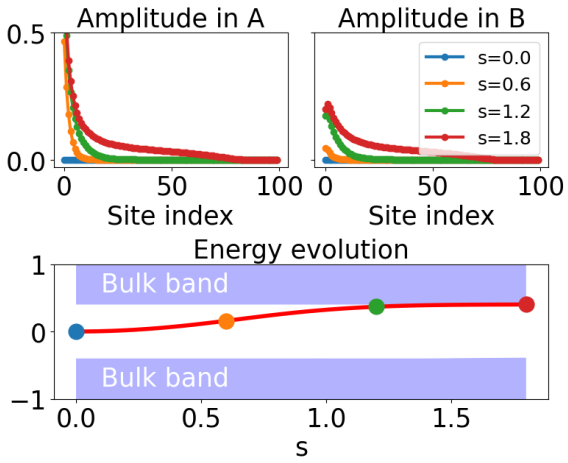

Figure 5.1: Numerical resolution of (5.6) for the left edge modes of model (5.2). We work with 100 pairs of sites and the constants $t_1 = 0.6$ and $t_2 = 1$. The amplitude of ψ_s is given on the sites of type A (up left) and B (up right) for different s. (center) The evolution of the energy E_s of ψ_s is drawn in red and the bulk bands of $H_{\text{eff},s}$ in light blue.

where $H_{\text{eff},s}$ is a linear operator that describes the linearised dynamic of H_ψ for a small perturbation $|\delta\psi\rangle$ around $|\psi_s\rangle$.

$$H_{\psi_s+\delta\psi}(|\psi_s + \delta\psi\rangle) = H_{\psi_s}|\psi_s\rangle + H_{\text{eff},s}|\delta\psi\rangle + O(\delta\psi^2) \tag{5.7}$$

We can always solves the system (5.6) and find values of $|\partial_s\psi_s\rangle$ and $\partial_s E_s$ which satisfies it. Moreover (ii) implies that there is solution with $\partial_s E_s$ real. One can therefore reconstruct from (5.6) a continuous family of stationary solutions $(E_s, |\psi_s\rangle)$ of (5.5), given an initial condition at $s = 0$, that we choose to be $(E_{s=0}, |\psi_{s=0}\rangle) = (0, \epsilon|\psi\rangle)$ with ϵ arbitrarily small and $|\psi\rangle$ a topological zero modes of the linearised problem at zero amplitude.

Solving this differential system, one can therefore generate nonlinear edge states $|\psi_s\rangle$ with a growing amplitude as s increases. If the linear model hosts multiple zero-energy edge modes as the SSH model (one on each edge), all of them could be used for the dynamic, leading to different non-linear edge modes.

So far, we have obtained the existence of solutions $(\partial_s E_s, |\partial_s\psi_s\rangle)$ for (5.5) but we have not shown yet that they remain localised near the edge. The question is the following: If the linear model at $s = 0$ has an edge mode, is $|\psi_s\rangle$ also localised near the edge for $s > 0$? In systems where coupling constants between sites decay quickly with their distance as in our illustrative nonlinear SSH model (5.2), the answer is given by the Combes-Thomas theorem [186,187]. This theorem states that solutions $|\partial_s\psi_s\rangle$ of (5.6) are localised around $|\psi_s\rangle$ as long as E_s lies in the bulk gap of $H_{\text{eff},s}$. If this condition stops being satisfied, $|\psi_s\rangle$ can quickly be delocalised as $|\partial_s\psi_s\rangle$ starts to strongly resonate with the nearby bulk modes.

In most cases, the system (5.6) must be solved numerically, using standard algorithmic methods [188]. In particular we can solve this system for the Kerr-like nonlinear SSH model (5.2) as an illustration. As this is a model which verifies the general hypothesis (i-iii) we can therefore generate left edge states with a growing amplitude as s increases (see Fig 5.1). For small amplitude, their shape remains close to the exponential shape of the edge states of the linearized model. But as the relative strength of the nonlinearities increase, the nonlinear edge states become more and more deformed. In particular, we observe that the nonlinear edge states becomes less localised as their energy E_s approaches the bulk bands of $H_{\text{eff},s}$. Around $s \sim 1.5$ the energy touch those bands and the edge state becomes strongly delocalised. Therefore, the edge state is not topologically protected in the strong amplitude regime.

5.2 Generalised non-linear chiral symmetry

In practical situations, one would like to prevent this band touching to occur by constraining the energy at zero, in the middle of the gap of $H_{\text{eff},s}$. In 1D insulators, this protection role is made by the presence of a chiral symmetry. To follow that spirit, we introduce a generalisation of the chiral symmetry to nonlinear systems. This allows us to identify nonlinearities that forbid the energy-shift and therefore host edge states that are robust and topologically protected. Besides, unlike the general case discussed so far, the result does not require H_ψ to satisfy a $U(1)$-symmetry, nor $H_{\text{eff},s}$ to be Hermitian.

We say that a nonlinear operator H_ψ satisfies a chiral symmetry if there is a bi-partition A and B of the degrees of freedom – e.g. two sublattices – such that H_ψ is off-diagonal in the chiral basis

$$H_\psi = \begin{pmatrix} 0 & H_\psi^{AB} \\ H_\psi^{BA} & 0 \end{pmatrix} \tag{5.8}$$

which is a natural generalisation of the chiral symmetry to the nonlinear case.

We can observe that the Kerr nonlinearity in the model (5.2) do not have such off-diagonal structure and is therefore not chiral symmetric. Instead, we can introduce the Kerr *inter-site* nonlinearity, of the form

$$H_{\text{inter-Kerr},\psi} = \sum_j \begin{pmatrix} 0 & b_j^2 \\ a_j^2 & 0 \end{pmatrix} \mathrm{j} \tag{5.9}$$

that have such chiral symmetry.

Importantly, when H_ψ is chiral symmetric, an initial linear edge state $|\psi_{s=0}\rangle$ living on a given sublattice can evolve through (5.6) as a stationary solution $|\psi_{s>0}\rangle$ that remains on the same sublattice. Indeed if $|\psi_s\rangle$ is a solution of (5.6) satisfying $|\psi_0\rangle = 0$ and $|\psi_s\rangle_B = 0$, $\forall s$, then by writing (5.6) by blocks while assuming $E_s = 0$, one obtains

$$\begin{pmatrix} H_{\text{eff,s}}^{AA} & H_{\text{eff,s}}^{AB} \\ H_{\text{eff,s}}^{BA} & H_{\text{eff,s}}^{BB} \end{pmatrix} \begin{pmatrix} |\partial_s \psi_s\rangle_A \\ 0 \end{pmatrix} = 0 \ . \tag{5.10}$$

$$|\psi\rangle = \begin{pmatrix} |\psi_A\rangle \\ 0 \end{pmatrix} \tag{5.11}$$

But one can check that, if $|\psi_s\rangle$ is only localised on the A sublattice, then the chiral symmetry (5.8) imply that $H_{\text{eff},s}^{AA} = 0$. So (5.10) reduces to

$$H_{\text{eff,s}}^{BA} |\partial_s \psi_s\rangle_A = 0 \ . \tag{5.12}$$

In order to know whether $H_{\text{eff,s}}^{BA}$ has localised zero-modes for each s, we use the bulk-edge correspondence. As explained in the previous chapter, the number of zero mode of $H_{\text{eff,s}}^{BA}$ is capture by the topology of the chiral Hermitian operator $H'_{\text{eff,s}}$

$$H'_{\text{eff,s}} = \begin{pmatrix} 0 & H_{\text{eff,s}}^{BA} \\ H_{\text{eff,s}}^{BA\,\dagger} & 0 \end{pmatrix} \qquad C = \begin{pmatrix} \mathbb{1}_A & 0 \\ 0 & -\mathbb{1}_B \end{pmatrix} \tag{5.13}$$

If we introduce the cut-off/step-function $\theta_j(j')$ which is 1 for $j' \geq j$ and 0 otherwise as well as the (smoothly) flatten Hamiltonian $H'_{F,s}$ of $H'_{\text{eff,s}}$, we can define the *topological order parameter*

$$\mathcal{I}(j) = \frac{-1}{8} \operatorname{Tr}\left(C \left[\hat{\theta}_j, H'_{F,s} \right] H'_{F,s} \right) \tag{5.14}$$

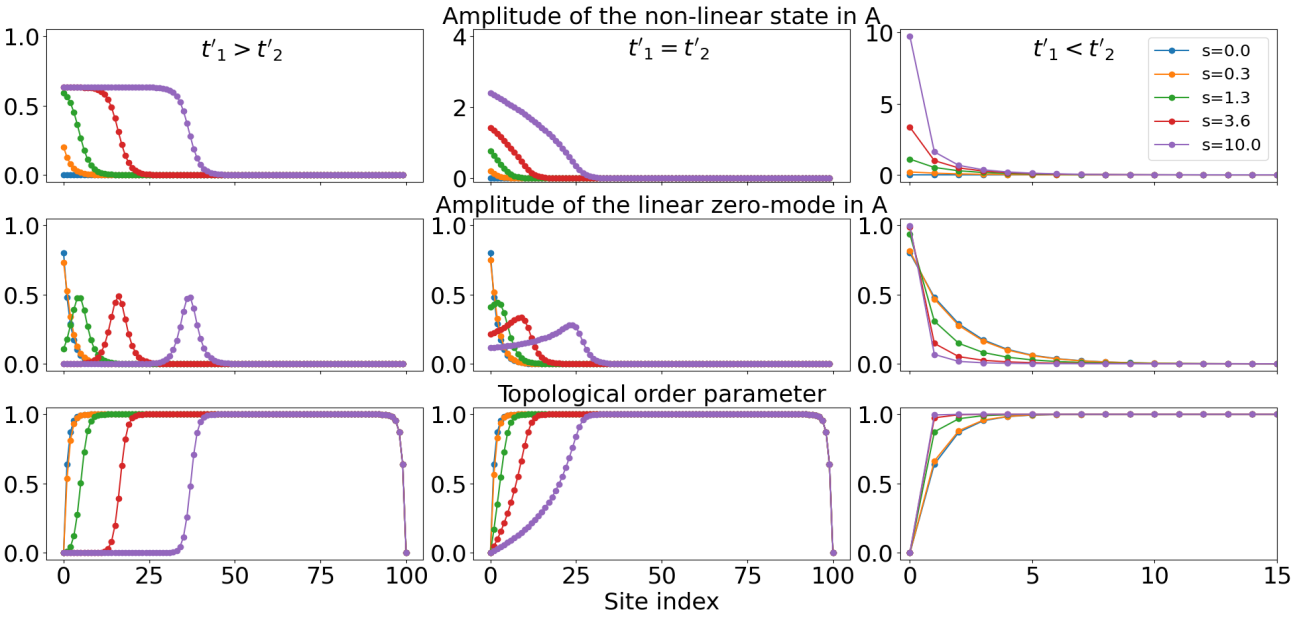

Figure 5.2: Numerical resolution of (5.12) for the left edge modes of the model (5.15). We work with 100 pairs of sites and $t_1 = 0.6$ $t_2 = 1$ everywhere. For the nonlinear couplings we take (left) $t'_1 = 1$ $t'_2 = 0$ (center) $t'_1 = 1$ $t'_2 = 1$ (right) $t'_1 = 0$ $t'_2 = 1$. We draw (up) the amplitude of ψ_s on the A-sites (center) the zero-energy state of $H^{AB}_{\text{eff,s}}$ (down) the topological order parameter $I(x)$ where we took $\epsilon = \frac{1}{100}$

which is the bulk index of the bulk-edge correspondence, depending of the position j of the transition of the cut-off. Therefore we know it is an integer (related to the winding number in the periodic case [189]) in regions where $H'_{\text{eff,s}}$ has no zero-modes and can only change when crossing regions with zeros modes of $H^{BA}_{\text{eff,s}}$ or of$H^{BA,\dagger}_{\text{eff,s}}$. In particular, we know there is a correspondence connecting the index variation $\Delta\mathcal{I} = \mathcal{I}(j_2) - \mathcal{I}(j_1)$ to the number of zero modes of $H^{BA}_{\text{eff,s}}$ localised in the interval $j_1 \leq j \leq j_2$ minus those of $H^{BA,\dagger}_{\text{eff,s}}$. In particular, when $\Delta\mathcal{I} > 0$, this correspondence implies that $H^{BA}_{\text{eff,s}}$ has at least $\Delta\mathcal{I}$ zero modes localised between j_2 and j_1.

If we take $j_1 = 0$ we can prove that $\mathcal{I}(j_1) = 0$ as $\hat{\theta}_{j=0} = \mathbb{1}$. Moreover, as long as the edge state do not invade the whole bulk, we have that $H_{\text{eff,s}} \approx H_{\text{eff},0}$ far from the edges. So if we take j_2 far enough from the edges, then $\mathcal{I}(j_2)$ is just the index one would obtain in the bulk of the linearised model at small amplitude. Thus if we denote $\mathcal{I}$ this topological number, we see that $H^{BA}_{\text{eff,s}}$ is constrained to have at least $\mathcal{I}$ zero-modes localised on the left part of the chain. If $|\psi_s\rangle$ is a nonlinear edge mode it thus implies that we have at least $\mathcal{I}$ possible choices for $|\partial_s\psi_s\rangle$ which are localised and verify (5.12).

We now apply our nonlinear chiral theory to a concrete model that we solve numerically. As mentioned above, inter-sites Kerr nonlinearities $H_{\text{inter-Kerr},1}|\psi\rangle = t'_1 \sum_j b_j^3 |j,A\rangle + a_j^3 |j,B\rangle$ are chiral symmetric. For the same reason, the nonlinearities $H_{\text{inter-Kerr},2}|\psi\rangle = t'_2 \sum_j b_j^3 |j+1,A\rangle + a_j^3 |j-1,B\rangle$ are also chiral. However, $H_{\text{inter-Kerr},1}$ reinforces the *intra*-cell coupling $|j,A\rangle\langle j,B|$ while $H_{\text{inter-Kerr},2}$ reinforces the *inter*-cell coupling $|j+1,A\rangle\langle j,B|$. Those nonlinearities appear for example in photonic [190], electrical systems [191] and even in phononic devices under some approximations [109]. We thus consider a finite SSH chain with such chiral nonlinearities

$$\begin{cases} i\partial_t a_j = (t_1 + t'_1|b_j|^2)b_j + (t_2 + t'_2|b_{j-1}|^2)b_{j-1} \\ i\partial_t b_j = (t_1 + t'_1|a_j|^2)a_j + (t_2 + t'_2|a_{j+1}|^2)a_{j+1} \ . \end{cases} \tag{5.15}$$

At small amplitude, the linearisation of (5.15) yields the usual SSH model, and we find

$\mathcal{I}(j) = 1$ for $|t_1| < |t_2|$ and j far from the edges. Thus, we predict the existence of a family of chiral nonlinear edge modes $|\psi_s\rangle$ localised on the left A-sites of the lattice (a similar argument would also predicts the existence of non-linear edge modes localised on the right B-sites). This is confirmed by our numerical integration of (5.12) for the model (5.15) with various choices of parameters (t_1, t_2, t_1', t_2') (the first row of figure 5.2). Interestingly, depending on the competition between inter-cell and intra-cell nonlinear couplings, we find very different behaviours: When $|t_1'| > |t_2'|$, the amplitude of the edge mode saturates, and the mode becomes a domain wall which invades progressively the bulk. Such a phenomenon was noticed in simulations [109] and an experimental setup [192], both in mechanical lattices. We unveil here the key hidden role of the generalized chiral symmetry to achieve such a nonlinear topological mode. However, this is not the only possible behavior constrained by chiral symmetry. Indeed, when $|t_1'| < |t_2'|$, we find in contrast that the edge mode remains localized at the boundary, with an increasing amplitude concentrated almost on a single site. For the critical value $|t_1'| = |t_2'|$, the edge mode invades the bulk as in the first case, but with a shape that never saturates. Note that these different behaviors as s varies can in principle be probed experimentally by forcing or pumping the system.

The origin of these different scenarios can be understood by recalling that the nonlinear modes $|\psi_s\rangle$ are obtained by adding iteratively the zero-modes $|\partial_s\psi_s\rangle$ of $H_{\text{eff,s}} = \mathrm{d}H^{BA}_{\psi_s}$ whose locations are themselves accounted by the variation of $I(x)$ (figure 5.2). Since $\mathrm{d}H^{BA}_{\psi}$ reads

$$\langle j, B|\, \mathrm{d}H^{BA}_{\psi}\, |\delta\psi\rangle_A = t_{1,\text{eff}}\delta a_j + t_{2,\text{eff}}\delta a_{j+1} \tag{5.16}$$

with $t_{1,\text{eff}} = t_1 + 3t_1'|a_j|^2$ and $t_{2,\text{eff}} = t_2 + 3t_2'|a_{j+1}|^2$, then, when the a_j's are small enough, $|t_{1,\text{eff}}| < |t_{2,\text{eff}}|$ so that $\mathrm{d}H^{BA}_{\psi}$ is in the topological phase with $\mathcal{I}(j) = 1$ in the bulk. But when increasing the amplitude of the a_j's, one may switch to the trivial phase $\mathcal{I}(j) = 0$ where $|t_{1,\text{eff}}| > |t_{2,\text{eff}}|$. If one assumes for simplification that $|a_j| \sim |a_{j+1}| \sim a$, it is clear that the system remains topological even in the high amplitude regime provided that $|t_1'| < |t_2'|$. On the contrary, if $|t_1'| > |t_2'|$, the system undergoes a transition toward a trivial regime where $|t_{1,\text{eff}}| > |t_{2,\text{eff}}|$. Lastly, when $|t_1'| = |t_2'|$, one gets $|t_{1,\text{eff}}| \sim |t_{2,\text{eff}}|$ at high amplitude leading to a gapless system with $0 < \mathcal{I}(j) < 1$.

As the amplitude a_j actually depends on the position, the system must be though as being divided into two regions separated by some threshold position j_s: The region $j > j_s$ where $|t_{1,\text{eff}}| < |t_{2,\text{eff}}|$ corresponding to the topological phase ($I(j) = 1$)), and the region $j < j_s$ where $|t_{1,\text{eff}}| > |t_{2,\text{eff}}|$ corresponding to the trivial one ($I(j) = 0$)). At the edge of the topological phase, $I(j)$ must interpolates between 0 and 1 implying therefore the existence of a zero-mode of $\mathrm{d}H^{BA}_{\psi}$ near by. As long as $|t_1'| < |t_2'|$, a transition toward the trivial region cannot occur, and so the zero-energy mode remains localised near the edge. In contrast, if $|t_1'| > |t_2'|$, the effective boundary j_s shifts when increasing the amplitude and dissociates from the physical boundary of the chain. Since $|\partial_s\psi_s\rangle$ is localised around j_s, it shifts toward the bulk while keeping its shape. As a result, $|\psi_s\rangle$ saturates and invades the bulk. The same reasoning applies when $|t_1'| = |t_2'|$, except that j_s becomes an interface between a topological and a *gapless* phase. As a result, $|\partial_s\psi_s\rangle$ decreases slowly far away from j_s into the gapless region, leading to a profile of $|\psi_s\rangle$ which is neither flat ($|t_1'| > |t_2'|$) nor exponential ($|t_1'| < |t_2'|$).

In summary, we studied the fate of topological edge states in 1D nonlinear networks and showed that these eventually disappear at a sufficiently large amplitude, unless the nonlinearities satisfy generalized chiral symmetry. In this case, a local topological index correctly accounts for the existence and spatial extension of nonlinear edge modes, whose real profile depends on the interaction between the nonlinearities and the underlying topology of the family of linearized Hamiltonians. Our theoretical approach is based on the general hypothesis (i), (ii), (iii) then on the chiral condition (5.8) under which the systems (5.6) and (5.12) can still be constructed.

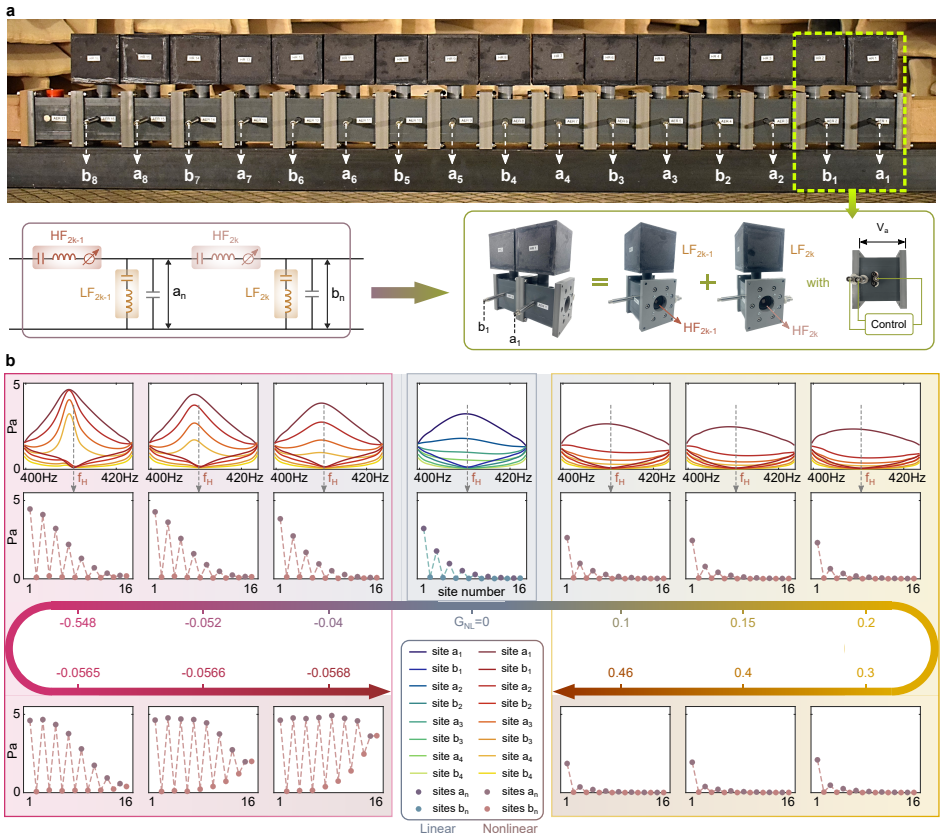

Figure 5.3: **Evolution of the chiral symmetry protected nonlinear topological edge state: experimental validation in an active nonlinear acoustic system.** **a**, The experimental system hosting nonlinear edge modes a. The unit cell consists of two passive linear Helmholtz resonators (acting as LF_n) and two active nonlinear loudspeakers (acting as HF_n). The whole system has a lenght of 8 unit cells, it starts and ends both with the controlled loudspeakers. **b**, Nonlinear topological edge states, measured as nonlinearity is progressively altered using the constant control parameter G_{NL}. The hopping ratios on sublattice A are increased (decreased) along $G_{NL} < 0$ ($G_{NL} > 0$). The edge state frequency f_H is identified from the spectra of a_i and b_i ($i = 1, 2, 3, 4$).

Of the two phenomenologies, it is the one with chiral symmetry which is the newest and the most interesting. We therefore started an experimental collaboration with Romain Fleury and Xinxin Guo from EPFL to observe it in a real physical system.

5.3 Experimental realisation

In this collaboration, one of the challenges was to find a system that accommodates topological edge modes in the linear regime and where one can generate chiral nonlinearities relatively easily. After some discussions, the system that was chosen is an acoustic system composed of a network of resonators coupled to each other. The resonators are passive Helmholtz resonators while the coupling between the resonators is achieved by active speakers (see figure 5.3.a). Such loudspeakers are controlled via a feedback loop which allows non-linear phenomena to be generated with great flexibility. In particular, such control makes it possible to generate nonlinearities exhibiting such chiral symmetry. To explain this, we use the electro-acoustic analogy. In this analogy, air pressure is mapped to electric potential and air speed to electric current. In this

analogy, the Helmholtz resonator and loudspeaker can be modeled as a combination of a capacitance and an inductance. For the Helmholtz resonator they are fixed while for the loudspeaker they can be adjusted via the feedback control. If we adjust the speaker capacitance to be alternately weak and strong, we can simulate behavior similar to the SSH model where inter-cell couplings are alternately weak and strong. Our system therefore have a unit cell composed of two passive linear Helmholtz resonators and two loudspeakers (see figure 5.3.a). In the nth unit cell, we denote a_n as the pressure in the first Helmholtz resonator and b_n as the pressure in the second.

The effect of the (linear) capacitor in the loudspeaker is to couple the charge polarisation q_n at the capacitor, to the potential difference $a_n - b_n$ (or $b_{n-1} - a_n$) through the equation $q_n = C(a - b)$. Thanks to the feedback control on the speaker, we can modify it so that it now verifies $q = (C + G_{NL}(a_n + b_n)^2)(a_n - b_n)$ where G_{NL} is the strength of the nonlinear constant. We can show that if we alternate the sign of G_{NL} between the loudspeaker coupling a_n and b_n Helmholtz resonator and the loudspeaker coupling the resonator a_n and b_{n-1}, the system verifies, in an appropriate regime, a stationary equation of the same family as the chiral model (5.15), i.e.

$$0 = \mathrm{t_{0a}} \mathrm{a}_{n+1} + \mathrm{t_{1a}} \mathrm{a}_n, \qquad 0 = \mathrm{t_{0b}} \mathrm{b}_{n-1} + \mathrm{t_{1b}} \mathrm{b}_n, \tag{5.17}$$

but with coefficients which have a slightly more complex, although with still a chiral nonlinear component

$$\begin{cases} \mathrm{t_{1a}}(\mathrm{a}_{n+1}, \mathrm{b}_n) = \mathrm{C_1}^{(\mathrm{HF})} + \mathrm{G_{NL}} \mathrm{C}^{(\mathrm{HF})} \left(\mathrm{a}_{n+1}^2 + \mathrm{b}_n \mathrm{a}_{n+1} - \mathrm{b}_n^2\right), \\ \mathrm{t_{0a}}(\mathrm{a}_n, \mathrm{b}_n) = \mathrm{C_2}^{(\mathrm{HF})} - \mathrm{G_{NL}} \mathrm{C}^{(\mathrm{HF})} \left(\mathrm{a}_n^2 + \mathrm{b}_n \mathrm{a}_n - \mathrm{b}_n^2\right), \\ \mathrm{t_{1b}}(\mathrm{b}_{n-1}, \mathrm{a}_n) = \mathrm{C_1}^{(\mathrm{HF})} + \mathrm{G_{NL}} \mathrm{C}^{(\mathrm{HF})} \left(\mathrm{b}_{n-1}^2 + \mathrm{a}_n \mathrm{b}_{n-1} - \mathrm{a}_n^2\right), \\ \mathrm{t_{0b}}(\mathrm{b}_n, \mathrm{a}_n) = \mathrm{C_2}^{(\mathrm{HF})} - \mathrm{G_{NL}} \mathrm{C}^{(\mathrm{HF})} \left(\mathrm{b}_n^2 + \mathrm{a}_n \mathrm{b}_n - \mathrm{a}_n^2\right), \end{cases}$$

depending on how alternate the sign of G_{NL}, t_{0a} becomes stronger than t_{1a} at high amplitude, or at the opposite, become even weaker at high amplitude.

The experiment is therefore capable of exploring both the left regime and the right regime of the figure 5.2. When such an experiment was set up and conducted by Xinxin Guo, she was able to observe the fact that the topological edge modes remain stable in the high amplitude regime with unchanged frequency (see figure 5.3.b). Furthermore she was able to observe that the mode is deformed in this non-linear regime with a deformation which reproduces the phenomenology highlighted in the model (5.15) which are the formation of a domain wall in one case and the focusing of the amplitude on a single site in the other.

This therefore shows that such deformation of zero modes in nonlinear regime can be observed in real physical systems and constitutes a stable phenomenon. Furthermore, the fact that physical systems observe a similar phenomenology even if the nonlinear expression of the jump coefficient is more complex than in the theoretical model (5.15), shows that such a phenomenology is rather general and does not does not depend heavily on the detail of a particular model.

5.4 Conclusion

In this chapter, we have examined the extension of topological properties from linear to nonlinear operators. Specifically, we have demonstrated that the effects of nonlinearity on edge modes can be mappped on a series of linear perturbation problems. This allows us to develop an explicit method to construct nonlinear modes.

Furthermore, we introduced a generalized chiral symmetry tailored for nonlinear operators, revealing that nonlinear edge modes can also exhibit topological protection akin to their linear

counterparts. This finding show the robustness of certain nonlinear phenomena against perturbations, offering potential avenues for harnessing nonlinear effects in practical applications.

To corroborate these theoretical findings, we established an experimental collaboration to validate the existence of these topologically protected nonlinear modes in a physical system. The experimental realization, provide empirical evidence for the theoretical predictions, and demonstrate a concrete application of such a theory.

Conclusion

In this thesis, I delved into various aspects of wave operator topology and developed a formalism called the "mode-shell correspondence," which unifies many results in topological physics. This ranges from the bulk-edge correspondence to higher-order topological insulators, from situations where modes are confined in position to those where they are confined in wavenumber space. I have shown that in all those situations there is a general duality between the index describing the topological properties of gapless modes of the operator and an index defined on the surface called "the shell," which encloses those modes in phase space and where the operator is gapped. In the different chapters, we explored the different possible mode indices: number of zero modes, spectral flow, number of Dirac/Weyl cones, discussing their specificities, but also showing that they are unified by the fact that they all verify a mode-shell correspondence. We then discussed how semi-classical analysis is a useful tool to characterize the topology of many systems by reducing the shell index to a (higher) Chern or winding number, which is more often analytically solvable. We also presented some tensor product constructions and showed that they are powerful tools to generate, easy-to-analyze, topological systems of many different phenomenologies.

The thesis also explored extensions of topological physics to nonlinear and non-Hermitian systems, which hold particular importance for studying the topological properties of effective quantum systems or classical waves. In the non-Hermitian case, I explained how the usual notion of spectrum is modified by the loss of Hermitian symmetry. I presented the notion of line and point gap and showed how the non-Hermitian spectrum can become extremely sensitive. I discussed how the singular value spectrum is instead a more stable alternative, which moreover allows us to map non-Hermitian models to Hermitian ones of a different symmetry class. In particular, it then allows us to apply the full power of the mode-shell correspondence to the non-Hermitian case and go beyond the bulk-edge correspondence.

For nonlinear systems, I explored how the topological properties of operators in the linear case can be extended to nonlinear operators. Specifically, I demonstrated how the deformation of edge modes by nonlinearity can be mapped to a series of perturbation problems that are linear. I introduced a generalized chiral symmetry for nonlinear operators, which topologically protects the nonlinear modes. Through an experimental collaboration, an acoustic system hosting such topologically protected non-linear modes was then realised.

Overall, the work presented here represents a comprehensive exploration of the topology of wave operators, providing insights into both fundamental principles and practical applications in various physical systems.

To continue the work carried out in this thesis, there are several research perspectives. On the theoretical side, it would be interesting to investigate whether the topological $\mathbb{Z}_2$ invariants [19, 21] not covered in this thesis, also adhere to a general mode-shell correspondence beyond the bulk-edge case. If so, it would be valuable to determine which mode/shell invariant governs

them. Additionally, while we extended topology to nonlinear operators by considering edge zero modes in $1D$ chiral chains, it would be intriguing to explore if such results can be extended to different classes of symmetry and dimensions of the mode index.

Throughout the thesis, we also discussed how separating the gapless modes in phase space can suppress scattering between them, leading to transport with greatly reduced dissipation. However, practical implementation requires specific conditions (low temperature, high magnetic field, no impurities), which limits the range of application. Therefore, an important research direction in the field is to discover or better control materials to push these limits as far as possible. It would also be interesting to find models with alternative methods to separate the gapless modes, such as using synthetic dimensions or even using separation in the many-body phase space, which may not have the same limitations.

Bibliography

[1] M. Lachièze-Rey and J.-P. Luminet, "Cosmic topology," *Physics Reports*, vol. 254, p. 135–214, Mar. 1995.

[2] X. Tang and J. V. Selinger, "Orientation of topological defects in 2d nematic liquid crystals," *Soft matter*, vol. 13, no. 32, pp. 5481–5490, 2017.

[3] Y. Tokura and N. Kanazawa, "Magnetic skyrmion materials," *Chemical Reviews*, vol. 121, no. 5, pp. 2857–2897, 2020.

[4] M. Z. Hasan and C. L. Kane, "Colloquium: Topological insulators," *Rev. Mod. Phys.*, vol. 82, pp. 3045–3067, Nov 2010.

[5] K. v. Klitzing, G. Dorda, and M. Pepper, "New method for high-accuracy determination of the fine-structure constant based on quantized hall resistance," *Phys. Rev. Lett.*, vol. 45, pp. 494–497, Aug 1980.

[6] D. J. Thouless, M. Kohmoto, M. P. Nightingale, and M. den Nijs, "Quantized hall conductance in a two-dimensional periodic potential," *Phys. Rev. Lett.*, vol. 49, pp. 405–408, Aug 1982.

[7] Y. Hatsugai, "Edge states in the integer quantum hall effect and the riemann surface of the bloch function," *Phys. Rev. B*, vol. 48, pp. 11851–11862, Oct 1993.

[8] Y. Hatsugai, "Chern number and edge states in the integer quantum hall effect," *Phys. Rev. Lett.*, vol. 71, pp. 3697–3700, Nov 1993.

[9] G. M. Graf and M. Porta, "Bulk-edge correspondence for two-dimensional topological insulators," *Communications in Mathematical Physics*, vol. 324, pp. 851–895, oct 2013.

[10] S. Raghu and F. D. M. Haldane, "Analogs of quantum-hall-effect edge states in photonic crystals," *Phys. Rev. A*, vol. 78, p. 033834, Sep 2008.

[11] Z. Wang, Y. D. Chong, J. D. Joannopoulos, and M. Soljačić, "Reflection-free one-way edge modes in a gyromagnetic photonic crystal," *Phys. Rev. Lett.*, vol. 100, p. 013905, Jan 2008.

[12] Z. Wang, Y. Chong, J. D. Joannopoulos, and M. Soljačić, "Observation of unidirectional backscattering-immune topological electromagnetic states," *Nature*, vol. 461, no. 7265, pp. 772–775, 2009.

[13] L. Lu, J. D. Joannopoulos, and M. Soljačić, "Topological photonics," *Nature Photonics*, vol. 8, pp. 821–829, Nov. 2014.

[14] F. Zangeneh-Nejad, A. Alù, and R. Fleury, "Topological wave insulators: a review," *Comptes Rendus. Physique*, vol. 21, no. 4-5, pp. 467–499, 2020.

[15] V. Lahtinen and J. Pachos, "A short introduction to topological quantum computation," *SciPost Physics*, vol. 3, sep 2017.

[16] C. Beenakker, "Search for majorana fermions in superconductors," *Annual Review of Condensed Matter Physics*, vol. 4, pp. 113–136, apr 2013.

[17] Y. Xia, D. Qian, D. Hsieh, L. Wray, A. Pal, H. Lin, A. Bansil, D. Grauer, Y. S. Hor, R. J. Cava, and M. Z. Hasan, "Observation of a large-gap topological-insulator class with a single dirac cone on the surface," *Nature Physics*, vol. 5, p. 398–402, May 2009.

[18] D. Hsieh, D. Qian, L. Wray, Y. Xia, Y. S. Hor, R. J. Cava, and M. Z. Hasan, "A topological Dirac insulator in a quantum spin Hall phase," *Nature*, vol. 452, pp. 970–974, Apr. 2008.

[19] A. Kitaev, "Periodic table for topological insulators and superconductors," *AIP Conference Proceedings*, vol. 1134, no. 1, pp. 22–30, 2009.

[20] S. Ryu, A. P. Schnyder, A. Furusaki, and A. W. W. Ludwig, "Topological insulators and superconductors: tenfold way and dimensional hierarchy," *New Journal of Physics*, vol. 12, p. 065010, jun 2010.

[21] A. P. Schnyder, S. Ryu, A. Furusaki, and A. W. W. Ludwig, "Classification of topological insulators and superconductors in three spatial dimensions," *Phys. Rev. B*, vol. 78, p. 195125, Nov 2008.

[22] H. Katsura and T. Koma, "The noncommutative index theorem and the periodic table for disordered topological insulators and superconductors," *Journal of Mathematical Physics*, vol. 59, p. 031903, mar 2018.

[23] Z.-X. Li, Y. Cao, and P. Yan, "Topological insulators and semimetals in classical magnetic systems," *Physics Reports*, vol. 915, p. 1–64, June 2021.

[24] W. A. Benalcazar, B. A. Bernevig, and T. L. Hughes, "Quantized electric multipole insulators," *Science*, vol. 357, pp. 61–66, jul 2017.

[25] F. Schindler, A. M. Cook, M. G. Vergniory, Z. Wang, S. S. P. Parkin, B. A. Bernevig, and T. Neupert, "Higher-order topological insulators," *Science Advances*, vol. 4, jun 2018.

[26] X.-J. Luo, "The generalization of benalcazar-bernevig-hughes model to arbitrary dimensions," *arXiv preprint arXiv:2304.07714*, 2023.

[27] P. R. Wallace, "The band theory of graphite," *Phys. Rev.*, vol. 71, pp. 622–634, May 1947.

[28] S. Yue, H. Zhou, D. Geng, Z. Sun, M. Arita, K. Shimada, P. Cheng, L. Chen, S. Meng, K. Wu, and B. Feng, "Experimental observation of dirac cones in artificial graphene lattices," *Phys. Rev. B*, vol. 102, p. 201401, Nov 2020.

[29] J. Wang, S. Deng, Z. Liu, and Z. Liu, "The rare two-dimensional materials with dirac cones," *National Science Review*, vol. 2, no. 1, pp. 22–39, 2015.

[30] C.-K. Chan, Y.-T. Oh, J. H. Han, and P. A. Lee, "Type-ii weyl cone transitions in driven semimetals," *Physical Review B*, vol. 94, no. 12, p. 121106, 2016.

[31] C.-K. Chan, N. H. Lindner, G. Refael, and P. A. Lee, "Photocurrents in weyl semimetals," *Physical Review B*, vol. 95, no. 4, p. 041104, 2017.

[32] K. Landsteiner, "Anomalous transport of weyl fermions in weyl semimetals," *Physical Review B*, vol. 89, no. 7, p. 075124, 2014.

[33] J. Cayssol, "Introduction to dirac materials and topological insulators," *Comptes Rendus Physique*, vol. 14, no. 9-10, pp. 760–778, 2013.

[34] J. Cayssol and J.-N. Fuchs, "Topological and geometrical aspects of band theory," *Journal of Physics: Materials*, vol. 4, no. 3, p. 034007, 2021.

[35] "Dirac cone," Feb. 2024. Page Version ID: 1210210179.

[36] P. Delplace, J. B. Marston, and A. Venaille, "Topological origin of equatorial waves," *Science*, vol. 358, pp. 1075–1077, oct 2017.

[37] H. Qin and Y. Fu, "Topological langmuir-cyclotron wave," *Science Advances*, vol. 9, no. 13, p. eadd8041, 2023.

[38] A. Leclerc, G. Laibe, P. Delplace, A. Venaille, and N. Perez, "Topological modes in stellar oscillations," *The Astrophysical Journal*, vol. 940, p. 84, nov 2022.

[39] J. B. Parker, "Topological phase in plasma physics," *Journal of Plasma Physics*, vol. 87, no. 2, p. 835870202, 2021.

[40] S. Shankar, A. Souslov, M. J. Bowick, M. C. Marchetti, and V. Vitelli, "Topological active matter," *Nature Reviews Physics*, vol. 4, pp. 380–398, may 2022.

[41] T. Van Mechelen and Z. Jacob, "Quantum gyroelectric effect: Photon spin-1 quantization in continuum topological bosonic phases," *Phys. Rev. A*, vol. 98, p. 023842, Aug 2018.

[42] M. G. Silveirinha, "Chern invariants for continuous media," *Phys. Rev. B*, vol. 92, p. 125153, Sep 2015.

[43] G. E. Volovik, *The Universe in a Helium Droplet*. OUP Oxford, 2009.

[44] R. Bott and R. Seeley, "Some remarks on the paper of callias," *Communications in Mathematical Physics*, vol. 62, no. 3, pp. 235–245, 1978.

[45] P. Delplace, "Berry-Chern monopoles and spectral flows," *SciPost Phys. Lect. Notes*, p. 39, 2022.

[46] F. Faure, "Manifestation of the topological index formula in quantum waves and geophysical waves," *arXiv preprint arXiv:1901.10592*, 2019.

[47] A. Venaille, Y. Onuki, N. Perez, and A. Leclerc, "From ray tracing to topological waves in continuous media," *arXiv preprint arXiv:2207.01479*, 2022.

[48] G. M. Graf, H. Jud, and C. Tauber, "Topology in shallow-water waves: A violation of bulk-edge correspondence," *Communications in Mathematical Physics*, vol. 383, pp. 731–761, mar 2021.

[49] G. Bal, "Topological invariants for interface modes," *Communications in Partial Differential Equations*, vol. 47, no. 8, pp. 1636–1679, 2022.

[50] G. Bal, "Topological charge conservation for continuous insulators," *Journal of Mathematical Physics*, vol. 64, no. 3, 2023.

[51] M. Perrot, P. Delplace, and A. Venaille, "Topological transition in stratified fluids," *Nature Physics*, vol. 15, no. 8, pp. 781–784, 2019.

[52] N. Perez, P. Delplace, and A. Venaille, "Unidirectional modes induced by nontraditional coriolis force in stratified fluids," *Phys. Rev. Lett.*, vol. 128, p. 184501, May 2022.

[53] J.-B. Touchais, P. Simon, and A. Mesaros, "Robust propagating in-gap modes due to spin-orbit domain walls in graphene," *Phys. Rev. B*, vol. 106, p. 035139, Jul 2022.

[54] F. Zhang, A. H. MacDonald, and M. E. J., "Valley chern numbers and boundary modesin gapped bilayer graphene," *Proceedings of the National Academy of Sciences*, vol. 110, no. 26, pp. 10546–10551, 2013.

[55] T. Ma and G. Shvets, "All-si valley-hall photonic topological insulator," *New Journal of Physics*, vol. 18, p. 025012, feb 2016.

[56] J. Lu, C. Qiu, W. Deng, X. Huang, F. Li, F. Zhang, S. Chen, and Z. Liu, "Valley topological phases in bilayer sonic crystals," *Phys. Rev. Lett.*, vol. 120, p. 116802, Mar 2018.

[57] K. W. Lee and C. E. Lee, "Quantum valley hall effect in wide-gap semiconductor sic monolayer," *Scientific Reports*, vol. 10, no. 5044, 2020.

[58] J. C. Y. Teo and C. L. Kane, "Topological defects and gapless modes in insulators and superconductors," *Phys. Rev. B*, vol. 82, p. 115120, Sep 2010.

[59] L. Fu, C. L. Kane, and E. J. Mele, "Topological insulators in three dimensions," *Phys. Rev. Lett.*, vol. 98, p. 106803, Mar 2007.

[60] C. L. Kane and E. J. Mele, "Quantum spin hall effect in graphene," *Phys. Rev. Lett.*, vol. 95, p. 226801, Nov 2005.

[61] B. A. Bernevig and S.-C. Zhang, "Quantum spin hall effect," *Phys. Rev. Lett.*, vol. 96, p. 106802, Mar 2006.

[62] D. N. Sheng, Z. Y. Weng, L. Sheng, and F. D. M. Haldane, "Quantum spin-hall effect and topologically invariant chern numbers," *Phys. Rev. Lett.*, vol. 97, p. 036808, Jul 2006.

[63] T. Kitagawa, E. Berg, M. Rudner, and E. Demler, "Topological characterization of periodically driven quantum systems," *Phys. Rev. B*, vol. 82, p. 235114, Dec 2010.

[64] M. S. Rudner, N. H. Lindner, E. Berg, and M. Levin, "Anomalous edge states and the bulk-edge correspondence for periodically driven two-dimensional systems," *Phys. Rev. X*, vol. 3, p. 031005, Jul 2013.

[65] M. Fruchart, "Complex classes of periodically driven topological lattice systems," *Physical Review B*, vol. 93, p. 115429, 2015.

[66] J. Cayssol, B. Dóra, F. Simon, and R. Moessner, "Floquet topological insulators," *physica status solidi (RRL)–Rapid Research Letters*, vol. 7, no. 1-2, pp. 101–108, 2013.

[67] R. Fleury, A. B. Khanikaev, and A. Alù, "Floquet topological insulators for sound," *Nature Communications*, vol. 7, jun 2016.

[68] T. Kitagawa, M. S. Rudner, E. Berg, and E. Demler, "Exploring topological phases with quantum walks," *Phys. Rev. A*, vol. 82, p. 033429, Sep 2010.

[69] J. Wu, W.-W. Zhang, and B. C. Sanders, "Topological quantum walks: Theory and experiments," *Frontiers of Physics*, vol. 14, pp. 1–6, 2019.

[70] A. Khanikaev, R. Fleury, S. Mousavi, and A. Alù, "Topologically robust sound propagation in an angular-momentum-biased graphene-like resonator lattice," *Nature Communications*, vol. 6, p. 8260, 10 2015.

[71] P. A. L. Delplace, "Topological chiral modes in random scattering networks," *SciPost Phys.*, vol. 8, p. 081, 2020.

[72] G. Q. Liang and Y. D. Chong, "Optical resonator analog of a two-dimensional topological insulator," *Phys. Rev. Lett.*, vol. 110, p. 203904, May 2013.

[73] J. K. Asbóth, B. Tarasinski, and P. Delplace, "Chiral symmetry and bulk-boundary correspondence in periodically driven one-dimensional systems," *Phys. Rev. B*, vol. 90, p. 125143, Sep 2014.

[74] D. Carpentier, P. Delplace, M. Fruchart, and K. Gawędzki, "Topological index for periodically driven time-reversal invariant 2d systems," *Phys. Rev. Lett.*, vol. 114, p. 106806, Mar 2015.

[75] H. Shen, B. Zhen, and L. Fu, "Topological band theory for non-hermitian hamiltonians," *Phys. Rev. Lett.*, vol. 120, p. 146402, Apr 2018.

[76] A. Ghatak and T. Das, "New topological invariants in non-hermitian systems," *Journal of Physics: Condensed Matter*, vol. 31, p. 263001, Apr 2019.

[77] Z. Gong, Y. Ashida, K. Kawabata, K. Takasan, S. Higashikawa, and M. Ueda, "Topological phases of non-hermitian systems," *Phys. Rev. X*, vol. 8, p. 031079, Sep 2018.

[78] S. Weimann, M. Kremer, Y. Plotnik, Y. Lumer, S. Nolte, K. G. Makris, M. Segev, M. Rechtsman, and A. Szameit, "Topologically protected bound states in photonic parity–time-symmetric crystals," *Nature Materials*, vol. 16, pp. 433–438, Apr. 2017.

[79] S. Liu, S. Ma, C. Yang, L. Zhang, W. Gao, Y. J. Xiang, T. J. Cui, and S. Zhang, "Gain- and loss-induced topological insulating phase in a non-hermitian electrical circuit," *Physical Review Applied*, vol. 13, Jan 2020.

[80] Y. Ashida, Z. Gong, and M. Ueda, "Non-hermitian physics," *Advances in Physics*, vol. 69, p. 249–435, Jul 2020.

[81] M. A. Bandres, S. Wittek, G. Harari, M. Parto, J. Ren, M. Segev, D. N. Christodoulides, and M. Khajavikhan, "Topological insulator laser: Experiments," *Science*, vol. 359, no. 6381, 2018.

[82] D. Smirnova, D. Leykam, Y. Chong, and Y. Kivshar, "Nonlinear topological photonics," *Applied Physics Reviews*, vol. 7, no. 2, p. 021306, 2020.

[83] S. Longhi, "Non-hermitian tight-binding network engineering," *Physical Review A*, vol. 93, feb 2016.

[84] T. E. Lee, "Anomalous edge state in a non-hermitian lattice," *Phys. Rev. Lett.*, vol. 116, p. 133903, Apr 2016.

[85] Y. Xiong, "Why does bulk boundary correspondence fail in some non-hermitian topological models," *arXiv preprint arXiv:1705.06039*, 2017.

[86] S. Yao and Z. Wang, "Edge states and topological invariants of non-hermitian systems," *Phys. Rev. Lett.*, vol. 121, p. 086803, Aug 2018.

[87] S. Yao, F. Song, and Z. Wang, "Non-hermitian chern bands," *Phys. Rev. Lett.*, vol. 121, p. 136802, Sep 2018.

[88] W. Brzezicki and T. Hyart, "Hidden chern number in one-dimensional non-hermitian chiral-symmetric systems," *Phys. Rev. B*, vol. 100, p. 161105, Oct 2019.

[89] T.-S. Deng and W. Yi, "Non-bloch topological invariants in a non-hermitian domain wall system," *Phys. Rev. B*, vol. 100, p. 035102, Jul 2019.

[90] D. S. Borgnia, A. J. Kruchkov, and R.-J. Slager, "Non-hermitian boundary modes and topology," *Phys. Rev. Lett.*, vol. 124, p. 056802, Feb 2020.

[91] G.-F. Guo, X.-X. Bao, and L. Tan, "The analysis of bulk boundary correspondence under the singularity of the generalized brillouin zone in non-hermitian system," *arXiv preprint arXiv:2106.06384*, 2021.

[92] F. K. Kunst, E. Edvardsson, J. C. Budich, and E. J. Bergholtz, "Biorthogonal bulk-boundary correspondence in non-hermitian systems," *Phys. Rev. Lett.*, vol. 121, p. 026808, Jul 2018.

[93] E. Edvardsson, F. K. Kunst, and E. J. Bergholtz, "Non-hermitian extensions of higher-order topological phases and their biorthogonal bulk-boundary correspondence," *Phys. Rev. B*, vol. 99, p. 081302, Feb 2019.

[94] M. Brunelli, C. C. Wanjura, and A. Nunnenkamp, "Restoration of the non-hermitian bulk-boundary correspondence via topological amplification," *arXiv preprint arXiv:2207.12427*, 2022.

[95] F. Song, S. Yao, and Z. Wang, "Non-hermitian topological invariants in real space," *Phys. Rev. Lett.*, vol. 123, p. 246801, Dec 2019.

[96] Z. Z. Alisultanov and E. G. Idrisov, "Towards the theory of types iii and iv non-hermitian weyl fermions," *arXiv preprint arXiv:2110.13714*, 2021.

[97] M. M. Denner, T. Neupert, and F. Schindler, "Infernal and exceptional edge modes: Non-hermitian topology beyond the skin effect," *arXiv preprint arXiv:2304.13743*, 2023.

[98] T. Dauxois and M. Peyrard, *Physics of solitons*. Cambridge University Press, 2006.

[99] R. K. Dodd, J. C. Eilbeck, J. D. Gibbon, and H. C. Morris, *Solitons and nonlinear wave equations*. Academic Press, Inc.[Harcourt Brace Jovanovich, Publishers], London-New York ..., 1982.

[100] V. V. Konotop, J. Yang, and D. A. Zezyulin, "Nonlinear waves in pt-symmetric systems," *Reviews of Modern Physics*, vol. 88, no. 3, p. 035002, 2016.

[101] R. W. Johnson, *Handbook of fluid dynamics*. CRC press, 2016.

[102] J. R. Tempelman, K. H. Matlack, and A. F. Vakakis, "Topological protection in a strongly nonlinear interface lattice," 2021.

[103] R. Chaunsali, H. Xu, J. Yang, P. G. Kevrekidis, and G. Theocharis, "Stability of topological edge states under strong nonlinear effects," *Phys. Rev. B*, vol. 103, p. 024106, Jan 2021.

[104] Y. P. Ma and H. Susanto, "Existence and stability of one-dimensional nonlinear topological edge states," 2020.

[105] A. J. Leggett, "Bose-einstein condensation in the alkali gases: Some fundamental concepts," *Rev. Mod. Phys.*, vol. 73, pp. 307–356, Apr 2001.

[106] K. Sone, Y. Ashida, and T. Sagawa, "Topological synchronization of coupled nonlinear oscillators," *arXiv preprint arXiv:2012.09479*, 2020.

[107] D. Leykam and Y. D. Chong, "Edge solitons in nonlinear-photonic topological insulators," *Phys. Rev. Lett.*, vol. 117, p. 143901, Sep 2016.

[108] T. Tuloup, R. W. Bomantara, C. H. Lee, and J. Gong, "Nonlinearity induced topological physics in momentum space and real space," *Phys. Rev. B*, vol. 102, p. 115411, Sep 2020.

[109] R. Chaunsali and G. Theocharis, "Self-induced topological transition in phononic crystals by nonlinearity management," *Phys. Rev. B*, vol. 100, p. 014302, Jul 2019.

[110] D. Zhou, D. Z. Rocklin, M. Leamy, and Y. Yao, "Topological invariant and anomalous edge states of strongly nonlinear systems," 2021.

[111] G. Engelhardt, M. Benito, G. Platero, and T. Brandes, "Topologically enforced bifurcations in superconducting circuits," *Physical Review Letters*, vol. 118, May 2017.

[112] T. Tuloup, R. W. Bomantara, C. H. Lee, and J. Gong, "Nonlinearity induced topological physics in momentum space and real space," *Phys. Rev. B*, vol. 102, p. 115411, Sep 2020.

[113] A. Bisianov, M. Wimmer, U. Peschel, and O. A. Egorov, "Stability of topologically protected edge states in nonlinear fiber loops," *Phys. Rev. A*, vol. 100, p. 063830, Dec 2019.

[114] M. Ezawa, "Topological toda lattice and nonlinear bulk-edge correspondence," 2021.

[115] M. Zworski, *Semiclassical analysis*, vol. 138. American Mathematical Society, 2022.

[116] M. V. Berry, "Quantal phase factors accompanying adiabatic changes," *Proceedings of the Royal Society of London. A. Mathematical and Physical Sciences*, vol. 392, no. 1802, pp. 45–57, 1984.

[117] B. A. Bernevig, *Topological insulators and topological superconductors*. Princeton university press, 2013.

[118] M. Fruchart and D. Carpentier, "An introduction to topological insulators," *Comptes Rendus. Physique*, vol. 14, no. 9-10, pp. 779–815, 2013.

[119] L. Jezequel, C. Tauber, and P. Delplace, "Estimating bulk and edge topological indices in finite open chiral chains," *Journal of Mathematical Physics*, vol. 63, Dec. 2022.

[120] C. L. Kane and T. C. Lubensky, "Topological boundary modes in isostatic lattices," *Nature Physics*, vol. 10, pp. 39–45, Jan. 2014.

[121] M. Guzmán, D. Bartolo, and D. Carpentier, "Geometry and topology tango in ordered and amorphous chiral matter," *SciPost Phys.*, vol. 12, p. 038, 2022.

[122] M. Guzman, X. Guo, C. Coulais, D. Carpentier, and D. Bartolo, "Model-free characterization of topological edge and corner states in mechanical networks," *arXiv preprint arXiv:2304.04832*, 2023.

[123] L. Jezequel and P. Delplace, "Mode-shell correspondence, a unifying phase space theory in topological physics - Part I: Chiral number of zero-modes," *SciPost Phys.*, vol. 17, p. 060, 2024.

[124] M. F. Atiyah and I. M. Singer, "The index of elliptic operators: I," *Annals of mathematics*, pp. 484–530, 1968.

[125] C. Callias, "Axial anomalies and index theorems on open spaces," *Communications in Mathematical Physics*, vol. 62, no. 3, pp. 213–234, 1978.

[126] L. Hörmander, "The weyl calculus of pseudo-differential operators," *Communications on Pure and Applied Mathematics*, vol. 32, no. 3, pp. 359–443, 1979.

[127] B. Fedosov, "Analytic formulae for the index of elliptic operators," *Tr. Mosk. Mat. Obs*, vol. 30, pp. 159–241, 1974.

[128] P. Delplace, D. Ullmo, and G. Montambaux, "Zak phase and the existence of edge states in graphene," *Phys. Rev. B*, vol. 84, p. 195452, Nov 2011.

[129] S. Ryu and Y. Hatsugai, "Topological origin of zero-energy edge states in particle-hole symmetric systems," *Phys. Rev. Lett.*, vol. 89, p. 077002, Jul 2002.

[130] P. St-Jean, V. Goblot, E. Galopin, A. Lemaître, T. Ozawa, L. L. Gratiet, I. Sagnes, J. Bloch, and A. Amo, "Lasing in topological edge states of a one-dimensional lattice," *Nature Photonics*, vol. 11, pp. 651–656, sep 2017.

[131] C. Poli, M. Bellec, U. Kuhl, F. Mortessagne, and H. Schomerus, "Selective enhancement of topologically induced interface states in a dielectric resonator chain," *Nature Communications*, vol. 6, apr 2015.

[132] N. Malkova, I. Hromada, X. Wang, G. Bryant, and Z. Chen, "Observation of optical shockley-like surface states in photonic superlattices," *Optics letters*, vol. 34, pp. 1633–5, 07 2009.

[133] G. M. Graf and J. Shapiro, "The Bulk-Edge Correspondence for Disordered Chiral Chains," *Communications in Mathematical Physics*, vol. 363, pp. 829–846, Nov. 2018.

[134] W. P. Su, J. R. Schrieffer, and A. J. Heeger, "Solitons in polyacetylene," *Phys. Rev. Lett.*, vol. 42, pp. 1698–1701, Jun 1979.

[135] S. S. Pershoguba and V. M. Yakovenko, "Shockley model description of surface states in topological insulators," *Phys. Rev. B*, vol. 86, p. 075304, Aug 2012.

[136] J.-N. Fuchs and F. Piéchon, "Orbital embedding and topology of one-dimensional two-band insulators," *Phys. Rev. B*, vol. 104, p. 235428, Dec 2021.

[137] M. F. Atiyah and I. M. Singer, "The index of elliptic operators: I," *Annals of Mathematics*, vol. 87, no. 3, pp. 484–530, 1968.

[138] E. Getzler, "A short proof of the local atiyah-singer index theorem," *Topology*, vol. 25, no. 1, pp. 111–117, 1986.

[139] N. Berline, E. Getzler, and M. Vergne, *Heat kernels and Dirac operators*. Springer Science & Business Media, 2003.

[140] E. Getzler, "Pseudodifferential operators on supermanifolds and the Atiyah-Singer index theorem," *Communications in Mathematical Physics*, vol. 92, pp. 163–178, June 1983.

[141] A. Venaille and P. Delplace, "Wave topology brought to the coast," *Phys. Rev. Research*, vol. 3, p. 043002, Oct 2021.

[142] J.-B. Touchais, P. Simon, and A. Mesaros, "Chiral chains with two valleys and disorder of finite correlation length," *arXiv preprint arXiv:2304.04808*, 2023.

[143] H. Yang, L. Song, Y. Cao, and P. Yan, "Experimental Realization of Two-Dimensional Weak Topological Insulators," *Nano Letters*, vol. 22, pp. 3125–3132, Apr. 2022. Publisher: American Chemical Society.

[144] L. Fu, C. L. Kane, and E. J. Mele, "Topological insulators in three dimensions," *Phys. Rev. Lett.*, vol. 98, p. 106803, Mar 2007.

[145] R. S. K. Mong, J. H. Bardarson, and J. E. Moore, "Quantum transport and two-parameter scaling at the surface of a weak topological insulator," *Phys. Rev. Lett.*, vol. 108, p. 076804, Feb 2012.

[146] Z. Ringel, Y. E. Kraus, and A. Stern, "Strong side of weak topological insulators," *Phys. Rev. B*, vol. 86, p. 045102, Jul 2012.

[147] K. Kobayashi, T. Ohtsuki, and K.-I. Imura, "Disordered weak and strong topological insulators," *Phys. Rev. Lett.*, vol. 110, p. 236803, Jun 2013.

[148] I. C. Fulga, D. I. Pikulin, and T. A. Loring, "Aperiodic weak topological superconductors," *Phys. Rev. Lett.*, vol. 116, p. 257002, Jun 2016.

[149] B. Yan, L. Müchler, and C. Felser, "Prediction of weak topological insulators in layered semiconductors," *Phys. Rev. Lett.*, vol. 109, p. 116406, Sep 2012.

[150] R. Noguchi, T. Takahashi, K. Kuroda, M. Ochi, T. Shirasawa, M. Sakano, C. Bareille, M. Nakayama, M. D. Watson, K. Yaji, A. Harasawa, H. Iwasawa, P. Dudin, T. K. Kim, M. Hoesch, V. Kandyba, A. Giampietri, A. Barinov, S. Shin, R. Arita, T. Sasagawa, and T. Kondo, "A weak topological insulator state in quasi-one-dimensional bismuth iodide," *Nature*, vol. 566, pp. 518–522, Feb. 2019.

[151] P. Zhang, R. Noguchi, K. Kuroda, C. Lin, K. Kawaguchi, K. Yaji, A. Harasawa, M. Lippmaa, S. Nie, H. Weng, V. Kandyba, A. Giampietri, A. Barinov, Q. Li, G. D. Gu, S. Shin, and T. Kondo, "Observation and control of the weak topological insulator state in ZrTe5," *Nature Communications*, vol. 12, p. 406, Jan. 2021.

[152] C. L. Kane and E. J. Mele, "Z_2 topological order and the quantum spin hall effect," *Phys. Rev. Lett.*, vol. 95, p. 146802, Sep 2005.

[153] P. Delplace, J. Li, and D. Carpentier, "Topological weyl semi-metal from a lattice model," *Europhysics Letters*, vol. 97, p. 67004, mar 2012.

[154] M. Milićević, T. Ozawa, G. Montambaux, I. Carusotto, E. Galopin, A. Lemaître, L. Le Gratiet, I. Sagnes, J. Bloch, and A. Amo, "Orbital edge states in a photonic honeycomb lattice," *Phys. Rev. Lett.*, vol. 118, p. 107403, Mar 2017.

[155] S.-J. Huang, H. Song, Y.-P. Huang, and M. Hermele, "Building crystalline topological phases from lower-dimensional states," *Phys. Rev. B*, vol. 96, p. 205106, Nov 2017.

[156] A. M. Cook and J. E. Moore, "Multiplicative topological phases," *Communications Physics*, vol. 5, p. 262, Oct. 2022.

[157] A. Pal, J. H. Winter, and A. M. Cook, "Multiplicative topological semimetals," *arXiv preprint arXiv:2301.02404*, 2023.

[158] A. Pal, J. H. Winter, and A. M. Cook, "Multiplicative majorana zero-modes," *arXiv preprint arXiv:2301.02765*, 2023.

[159] R. Okugawa, S. Hayashi, and T. Nakanishi, "Second-order topological phases protected by chiral symmetry," *Phys. Rev. B*, vol. 100, p. 235302, Dec 2019.

[160] Y.-B. Yang, J.-H. Wang, K. Li, and Y. Xu, "Higher-order topological phases in crystalline and non-crystalline systems: a review," *arXiv preprint arXiv:2309.03688*, 2023.

[161] A. Goft, Y. Abulafia, N. Orion, C. L. Schochet, and E. Akkermans, "Defects in graphene : A topological description," *arXiv preprint arXiv:2304.08905*, 2023.

[162] R. Jackiw and P. Rossi, "Zero modes of the vortex-fermion system," *Nuclear Physics B*, vol. 190, no. 4, pp. 681–691, 1981.

[163] Z. Song, Z. Fang, and C. Fang, "$(d-2)$ -dimensional edge states of rotation symmetry protected topological states," *Physical Review Letters*, vol. 119, dec 2017.

[164] W. A. Benalcazar and A. Cerjan, "Chiral-symmetric higher-order topological phases of matter," *Physical Review Letters*, vol. 128, mar 2022.

[165] E. Khalaf, W. A. Benalcazar, T. L. Hughes, and R. Queiroz, "Boundary-obstructed topological phases," *Physical Review Research*, vol. 3, mar 2021.

[166] J. Langbehn, Y. Peng, L. Trifunovic, F. von Oppen, and P. W. Brouwer, "Reflection-symmetric second-order topological insulators and superconductors," *Phys. Rev. Lett.*, vol. 119, p. 246401, Dec 2017.

[167] R. Landauer, "Spatial variation of currents and fields due to localized scatterers in metallic conduction," *IBM Journal of research and development*, vol. 1, no. 3, pp. 223–231, 1957.

[168] S. Datta, *Electronic transport in mesoscopic systems*. Cambridge university press, 1997.

[169] R. Landauer, "Spatial variation of currents and fields due to localized scatterers in metallic conduction," *IBM Journal of Research and Development*, vol. 1, no. 3, pp. 223–231, 1957.

[170] X.-L. Qi, Y.-S. Wu, and S.-C. Zhang, "Topological quantization of the spin hall effect in two-dimensional paramagnetic semiconductors," *Phys. Rev. B*, vol. 74, p. 085308, Aug 2006.

[171] K. S. Novoselov, Z.-f. Jiang, Y.-s. Zhang, S. Morozov, H. L. Stormer, U. Zeitler, J. Maan, G. Boebinger, P. Kim, and A. K. Geim, "Room-temperature quantum hall effect in graphene," *science*, vol. 315, no. 5817, pp. 1379–1379, 2007.

[172] Y. Tokura, K. Yasuda, and A. Tsukazaki, "Magnetic topological insulators," *Nature Reviews Physics*, vol. 1, no. 2, pp. 126–143, 2019.

[173] H. Nielsen and M. Ninomiya, "Absence of neutrinos on a lattice: (i). proof by homotopy theory," *Nuclear Physics B*, vol. 185, no. 1, pp. 20–40, 1981.

[174] H. Nielsen and M. Ninomiya, "Absence of neutrinos on a lattice: (ii). intuitive topological proof," *Nuclear Physics B*, vol. 193, no. 1, pp. 173–194, 1981.

[175] C. Bena and G. Montambaux, "Remarks on the tight-binding model of graphene," *New Journal of Physics*, vol. 11, no. 9, p. 095003, 2009.

[176] M. Lohse, C. Schweizer, H. M. Price, O. Zilberberg, and I. Bloch, "Exploring 4d quantum hall physics with a 2d topological charge pump," *Nature*, vol. 553, no. 7686, pp. 55–58, 2018.

[177] O. Zilberberg, S. Huang, J. Guglielmon, M. Wang, K. P. Chen, Y. E. Kraus, and M. C. Rechtsman, "Photonic topological boundary pumping as a probe of 4d quantum hall physics," *Nature*, vol. 553, no. 7686, pp. 59–62, 2018.

[178] T. Ozawa, H. M. Price, N. Goldman, O. Zilberberg, and I. Carusotto, "Synthetic dimensions in integrated photonics: From optical isolation to four-dimensional quantum hall physics," *Phys. Rev. A*, vol. 93, p. 043827, Apr 2016.

[179] C.-E. Bardyn, M. A. Baranov, C. V. Kraus, E. Rico, A. İmamoğlu, P. Zoller, and S. Diehl, "Topology by dissipation," *New Journal of Physics*, vol. 15, p. 085001, Aug. 2013.

[180] F. Roccati, G. M. Palma, F. Ciccarello, and F. Bagarello, "Non-hermitian physics and master equations," *Open Systems & Information Dynamics*, vol. 29, Mar. 2022.

[181] A. Leclerc, L. Jezequel, N. Perez, A. Bhandare, G. Laibe, and P. Delplace, "Exceptional ring of the buoyancy instability in stars," *Phys. Rev. Res.*, vol. 6, p. L012055, Mar 2024.

[182] R. Lin, T. Tai, L. Li, and C. H. Lee, "Topological non-hermitian skin effect," *Frontiers of Physics*, vol. 18, July 2023.

[183] L. Herviou, J. H. Bardarson, and N. Regnault, "Defining a bulk-edge correspondence for non-hermitian hamiltonians via singular-value decomposition," *Physical Review A*, vol. 99, May 2019.

[184] L. Jezequel and P. Delplace, "Non-hermitian spectral flows and berry-chern monopoles," *Phys. Rev. Lett.*, vol. 130, p. 066601, Feb 2023.

[185] S. Ryu and Y. Hatsugai, "Topological origin of zero-energy edge states in particle-hole symmetric systems," *Phys. Rev. Lett.*, vol. 89, p. 077002, Jul 2002.

[186] J. M. Combes and L. Thomas, "Asymptotic behaviour of eigenfunctions for multiparticle schrödinger operators," *Comm. Math. Phys.*, vol. 34, no. 4, pp. 251–270, 1973.

[187] A. Michael and S. Warzel, *Random operators : disorder effects on quantum spectra and dynamics*. Graduate studies in mathematics, Providence (R.I.): American Mathematical Society, 2015.

[188] J. C. Butcher, *Numerical Methods for Ordinary Differential Equations*. John Wiley & Sons, Ltd, 2016.

[189] H. Katsura and T. Koma, "The noncommutative index theorem and the periodic table for disordered topological insulators and superconductors," *Journal of Mathematical Physics*, vol. 59, no. 3, p. 031903, 2018.

[190] Y. Hadad, A. B. Khanikaev, and A. Alù, "Self-induced topological transitions and edge states supported by nonlinear staggered potentials," *Phys. Rev. B*, vol. 93, p. 155112, Apr 2016.

[191] Y. Hadad, J. C. Soric, A. B. Khanikaev, and A. Alu, "Self-induced topological protection in nonlinear circuit arrays," *Nature Electronics*, vol. 1, no. 3, pp. 178–182, 2018.

[192] B. G.-g. Chen, N. Upadhyaya, and V. Vitelli, "Nonlinear conduction via solitons in a topological mechanical insulator," *Proceedings of the National Academy of Sciences*, vol. 111, no. 36, pp. 13004–13009, 2014.

Appendices

A Smoothness/fast-decay Fourier duality

In this section, we recall some results about the links between the regularity of a function and the fast decay of its Fourier transform/series at infinity. These properties are fundamental for our purpose and are wildly used in the main text to make bridges between the dual behavior in position and wavenumber spaces.

Let f be a function of one variable $x \in \mathbb{R}$, then one can define its Fourier transform $\tilde{f}$ as a function of the variable $k \in \mathbb{R}$ as

$$\tilde{f}(k) = \int dx f(x) e^{-ikx} \ . \tag{18}$$

If, f is a periodic function with $x \in [0, 2\pi]$, one can associate to f a Fourier series $\tilde{f}(k)$ with discrete parameter $k \in \mathbb{Z}$ such that

$$\tilde{f}(k) = \frac{1}{2\pi} \int_0^{2\pi} dx f(x) e^{-ikx} \ . \tag{19}$$

Importantly, for both Fourier transforms and series, the smoother f is, the faster $\tilde{f}$ decays when $|k| \to \infty$. The first result of this kind is the Riemman-Lebesge lemma that states that if f is a continuous integrable function, then its Fourier transform or its Fourier series goes zero at infinity:

$$\tilde{f}(k) \xrightarrow{|k| \to +\infty} 0 \tag{20}$$

Combined with the well-known Fourier transform/series property that $(\tilde{\partial_x f})(k) = ik\tilde{f}(k)$ this lemma implies that if f is a smooth function with N derivatives which are continuous, then its Fourier transform must decays faster than k^{-N}

$$\tilde{f}(k) = \frac{1}{(ik)^N} (\tilde{\partial_x^N f})(k) = O(\frac{1}{k^N}) \ . \tag{21}$$

Moreover, since the Fourier transform is invertible, this property can be inverted and implies that if the Fourier transform of a function decays sufficiently fast at infinity, then the initial function must be smooth (with enough derivatives).

An example of how these considerations can be useful to study the properties of operators is the following: Let f and g be two periodic functions on $[0, 2\pi]$ and consider the simple Hamiltonian $\hat{H}$ such that

$$(\hat{H} f)(x) = g(x) f(x) \ . \tag{22}$$

Then, if one rewrites the operator in wavenumber space, we would have instead

$$(\hat{H}\tilde{f})(k) = \sum_{k'} \tilde{f}(k-k')\tilde{g}(k') \tag{23}$$

so we see that the multiplication by a function in the initial space translates as a hopping problem in the dual space, where a hopping of a distance n has a strength $\hat{g}(k)$. The regularity/fast-decay is then quite useful since it implies that if g is a smooth function (say C^∞) then $\hat{g}(k)$ decays fastly, making the dual problem a short-range one (and vice-versa), which constrains a lot the properties of the dual problem.

These properties are important to relate the short-range behavior of the operator with the smoothness of the Wigner-Weyl transform, which is the goal of the next appendix.

B Wigner-Weyl transform

B.1 The continuous version

In physics, there are a lot of situations where the relevant information of the system is encoded by continuous (vector valued) functions of $x \in \mathbb{R}^d$, and the properties of the systems are described by operators which act on this space of function. In those cases, the Wigner-Weyl transform is a powerful tool which allows ourselves to map these operators into the simpler objects which are the (matrix valued) functions on the phase space $(x,k) \in \mathbb{R}^d \times \mathbb{R}^d$.

This transformation can be described as follows. If $\hat{A}$ is an operator which acts on a function f, then we can associate to this operator $\hat{A}$ the function $A(x,k)$ which is called the "symbol of the operator" such that

$$A(x,k) = \int_{\mathbb{R}^d} dx'^d \, \langle x + x'/2 | \, \hat{A} \, | x - x'/2 \rangle \, e^{-ikx'} \ . \tag{24}$$

where $\langle x' | \, \hat{A} \, | x \rangle$ is in general called the "kernel" of $\hat{A}$. If one is not comfortable with the notations of quantum mechanics, the kernel can also be denoted $\hat{A}_{x,x'}$ and can be determined as the value in x' of the function $\hat{A}\delta_x$ where δ_x is the Dirac function centered in x, $x' \to \delta(x'-x)$. This kernel may not always be a well defined function in x and x' (see for example $\hat{A} = \partial_x$) but is in general well defined as a distribution. In that case, one may compute the symbol by first regularising the operator with a parameter ϵ (for example $\hat{A}_\epsilon = \int_x (|x\rangle \langle x+\epsilon| - |x\rangle \langle x-\epsilon|)/(2\epsilon)$), compute the symbol for the regularised operator and then take the limit $\epsilon \to 0$. Using this, one can show that the symbol of ∂_x is ik.

Since $A(x,k)$ is defined using a Fourier transform, this formula can be inverted and from the symbol one can determine the operator $\hat{A}$ using the formula

$$\langle x' | \, \hat{A} \, | x \rangle = \int_{\mathbb{R}^d} \frac{dk^d}{(2\pi)^d} \, A(\frac{x+x'}{2}, k) e^{ik(x'-x)} \ . \tag{25}$$

These definitions are extended straightforwardly to the case where functions are vectors with internal degrees of freedom α. The symbol $A(x,k)$ is replaced by a matrix valued symbol $A(x,k) = (A_{\alpha,\alpha'}(x,k))_{\alpha,\alpha'}$ and $\langle x' | \, \hat{A} \, | x \rangle$ should now be interpreted as a matrix $(\langle x', \alpha | \, \hat{A} \, | x, \alpha' \rangle)_{\alpha,\alpha'}$.

A first property associated to this Wigner-Weyl transform is its behavior relative to the trace. Indeed one can show that

$$\operatorname{Tr} \hat{A} = \int_{\mathbb{R}^d} dx^d \operatorname{Tr}^{\text{int}} \langle x | \, \hat{A} \, | x \rangle = \int_{\mathbb{R}^d} dx^d \int_{\mathbb{R}^d} \frac{dk^d}{(2\pi)^d} \operatorname{Tr}^{\text{int}} A(x,k) \tag{26}$$

where $\operatorname{Tr}^{\text{int}}$ is the reduced trace only over the internal degrees of freedom α.

An other important property of Weyl-Wigner calculus we need to introduce is that dealing with product of operators. If we define the *Moyal* $\star$*-product* of two symbols $A \star A'$ as the symbol of their operator $\hat{A} \circ \hat{A}'$, one can verify that such product can be written as

$$(A \star A')(x,k) = \int_{((\mathbb{R}^d)^4} dx'^d dx''^d \frac{dk'^d}{\pi^d} \frac{dk''^d}{\pi^d} A(x+x',k+k')\, A'(x+x'',k+k'') e^{i2(x'k''-x''k')}. \quad (27)$$

This formula can be proved by writing the formula of the symbol of $\hat{A} \circ \hat{A}'$ in function of the kernel $\langle x'| \hat{A} \circ \hat{A}' |x\rangle$. This kernel can then itself be expanded as $\langle x'| \hat{A} \circ \hat{A}' |x\rangle = \sum_{x''} \langle x'| \hat{A} |x''\rangle \langle x''| \hat{A}' |x\rangle$. Finally one uses the inversion formula for $\langle x'| \hat{A} |x''\rangle$ and $\langle x''| \hat{A}' |x\rangle$, to recover an equation which only includes symbols and which can be reduced to (27) up to some suitable changes of variables in x' ,x'', k', k''.

If the symbols $A(x+x',k+k')$ and $A'(x+x'',k+k'')$ are both smooth in x and k this expression can then be expanded in terms involving higher order derivatives. To do so, let us use the Taylor expansion

$$A(x+x',k+k') = \sum_{j,j'=0}^{j+j'=n} \partial_x^j \partial_k^{j'} A(x,k) \frac{x'^j}{j!} \frac{k'^{j'}}{j'!} + R(x,k) \quad (28)$$

where $R(x,k)$ decays faster than $\|(x,k)\|^n$ for x' and k' small. If we substitute this expansion into the Moyal product, we can write that $x'^k e^{i2x'k''} = \frac{1}{(2i)^j} \partial_{k''} e^{i2x'k''}$ or $k'^{j'} e^{-i2x''k'} = \frac{1}{(-2i)^{j'}} \partial_{x''} e^{-i2x''k'}$ and integrate by part. We then obtain an expansion of the Moyal product which is

$$(A \star A')_{\mathrm{sym}}(x,k) = \sum_{j,j'=0}^{j+j'=n} \frac{(-1)^j}{j!j'!(2i)^{j+j'}} \partial_x^j \partial_k^{j'} A(x,k) \partial_x^{j'} \partial_k^j A'(x,k) + \text{Error} \quad (29)$$

where the error term can be explicitly bounded using the derivatives in $n+1$ in x and $n'+1$ in k of both symbols. From this expansion, one can notice that if both symbols are constant in x, or in k, then the Moyal product is simplified a lot since it reduces to the simple product of the symbols $(A \star A')(x,k) = A(x)A'(x)$ or $(A \star A')(x,k) = A(k)A'(k)$.

Importantly, for slow-varying symbols, we can perform a semi-classical expansion of the Moyal product. For example, if we re-scale the symbols in one of the variables like $A_\epsilon(x,k) = A(\epsilon x,k)$ or $A_\epsilon(x,k) = A(x,\epsilon k)$ so that the symbols look like almost constant in that variable in the limit $\epsilon \to 0$, then the expansion (29) becomes a perturbative expansion in ϵ in that limit and we have

$$(A_\epsilon \star A'_\epsilon)_{\frac{1}{\epsilon}}(x,k) = \sum_{j,j'=0}^{j+j'=n} \frac{(-1)^j \epsilon^{j+j'}}{j!j'!(2i)^{j+j'}} \partial_x^j \partial_k^{j'} A(x,k) \partial_x^{j'} \partial_k^j A'(x,k) + O(\epsilon^{n+1}) \,. \quad (30)$$

In particular, we obtain that for slow-varying fields, the product of operators can be replaced by the product of their symbol at lowest (zeroth) order in ϵ

$$(A_\epsilon \star A'_\epsilon)_{\frac{1}{\epsilon}}(x,k) = A(x,k)A'(x,k) + O(\epsilon) \,. \quad (31)$$

Also, the symbol of a commutator of operators $[\hat{A}, \hat{A}']$ is given by the Moyal commutator $[A,B]_\star \equiv A \star A' - A' \star A$ of their symbols. A useful approximation is obtained in the same as above by keeping now the first order in ϵ in the expansion

$$\begin{aligned} [A_\epsilon, A'_\epsilon]_{\star,\frac{1}{\epsilon}}(x,k) =& [A(x,k), A'(x,k)] - \frac{\epsilon}{2i} \left([\partial_k A(x,k), \partial_x A'(x,k)]_+ \right. \\ & \left. - [\partial_x A(x,k), \partial_k A'(x,k)]_+ \right) + O(\epsilon^2) \\ \equiv& [A(x,k), A'(x,k)] + \epsilon i \{A, A'\}(x,k) + O(\epsilon^2) \end{aligned} \quad (32)$$

where $[B,C]_+ = BC + CB$ is just the usual symmetric sum (also called anti-commutator) and $\{A,B\}$ the Poisson bracket of the symbols. When $A(x,k)$ and $A'(x,k)$ commutes with each other (for example when $A(x,k)$ or $A'(x,k)$ is scalar, as it is often the case in the paper), one recovers the famous result that, at first order in ϵ, the symbol of the commutator is the Poisson bracket of the symbols.

Criteria for the semi-classical limit. In order to estimate how good the semi-classical approximation $A \star A' \sim AA'$ is for two symbols A and A', one needs to check how small the first order correction $(\partial_x A \partial_k A' - \partial_x A \partial_k A')(x,k)$ is compared to the product $(AA')(x,k)$. If we introduce the quantities $1/d_{x/k,A}(x,k) \equiv \|\partial_{x/k} A(x,k)\| \|A^{-1}(x,k)\|$, we can define the parameter $\epsilon \equiv 1/(d_{x,A}d_{k,A'}) + 1/(d_{k,A}d_{x,A'})$ which measures how small is the first order correction compared to the standard product. When ϵ is small ($\epsilon \ll 1$), we can expect the semi-classical approximation to be good, as higher order corrections (like terms $\partial_x^2 A \partial_k^2 A'$ with higher derivative) should be even smaller (here of order ϵ^2)[1]. Vice-versa when ϵ is not small, there is no reason to think that the semi-classical approximation is a good one.

In this paper, we deal with mainly two types of Moyal products: one involving the symbol of the Hamiltonian with the symbol of the cut-off operator $H \star \theta_\Gamma$, and one with only the symbol of the Hamiltonian $H \star H$ (in the computation of the flatten Hamiltonian H_F). θ_Γ can always be constructed to be slowly varying in the limit $\Gamma \to +\infty$ such that $1/d_{x/k,\theta_\Gamma} = O(1/\Gamma)$, so the semi-classical approxilation is always valid for the Moyal product $H \star \theta_\Gamma$ in that limit.

The problematic products that need to be verified are the $H \star H$ ones. There, the semi-classical criteria is $1/(d_{x,H}d_{k,H}) \ll 1$, which is the criteria given at the end of the section 1.1.5, using the fact that if $H(x,k)$ has a gap $\Delta(x,k)$, then $\|H^{-1}(x,k)\| = 1/\Delta(x,k)$.

B.2 The discrete version

For discrete systems, which are defined on a lattice $\mathbb{Z}^d$ rather than a continuous space $\mathbb{R}^d$, the usual Wigner-Weyl transform is not suitable and should instead be replaced by a discrete. If $\hat{A}$ is an operator acting on such a lattice, one can define its discrete symbol $A(n,k)$ as

$$A(x,k) = \sum_{n' \in \mathbb{Z}^d} \langle n + n' | \hat{A} | n \rangle e^{-ikn'} \tag{33}$$

where $n \in \mathbb{Z}^d$ is a discrete index, and $k \in [0, 2\pi]^d = \mathbb{T}^d$ is the equivalent of the Brillouin zone parameter.

When defining the discrete transform, one cannot choose a symmetric convention similar to the continuous one $\langle x + x'/n | \hat{A} | x - x'/2 \rangle$ mainly because if n and n' are sites of the lattice, their average $(n+n')/2$ is not guaranteed to be a site of the lattice. Therefore, every discrete conventions do not have all of the properties of the continuous ones. For example, having $\hat{A} = \hat{A}^\dagger$ does not imply $A^\dagger(x,k) = A(x,k)$.

However, the discrete transform still has good enough properties for the purpose of this article. The most important property is the fact that it is still a transform which maps, in a one to one correspondence, operators and symbols in phase space, with an inverse map given by

$$\langle n' | \hat{A} | n \rangle = \int_{\mathbb{T}^d} \frac{dk^d}{(2\pi)^d} A(n,k) e^{ik(n'-n)} \ . \tag{34}$$

[1] It is possible to fine-tune examples where in some points of phase space, the first order corrections are small but not the second order correction. However those examples are not really representative and our simple criteria is enough to understand why the semi-classical approximation is valid or not in all situations we encounter in this paper

We also have a trace property which is quite similar to that of the continuous case

$$\operatorname{Tr} \hat{A} = \sum_{n\in\mathbb{Z}^d} \operatorname{Tr}^{\text{int}} \langle n| \hat{A} |n\rangle = \sum_{n\in\mathbb{Z}^d} \int_{\mathbb{T}^d} \frac{dk^d}{(2\pi)^d} \operatorname{Tr}^{\text{int}} A(x,k) \ . \tag{35}$$

The Moyal product associated to this discrete Wigner-Weyl transform is a little bit different and can be expressed as

$$(A \star A')(n,k) = \sum_{n'\in\mathbb{Z}^d} \int_{(\mathbb{R}^d} \frac{dk'^d}{(2\pi)^d} A(n+n',k)\ A'(n,k+k') e^{in'k'} \tag{36}$$

from which we could also theoretically make a semi-classical expansion when the symbol is slowly varying in the n direction. Since the expressions become quickly more cumbersome than in the continuous case, we focus only on the zeroth and first orders of the expansion. For that purpose, we recall that if $\delta_n f(n) = f(n+1) - f(n)$, then for slowly varying function f, $f(n+n') \approx f(n) + \delta_n f(n) n' + \dots$. If we substitute that expression into the Moyal product we obtain

$$(A \star A')(n,k) \approx A(n,k)A'(n,k) + i\delta_n A(n,k)\partial_k A'(n,k) \ . \tag{37}$$

As a result, for slowly varying symbols, the leading coefficient of the symbol of a product of operators is just the product of symbols

$$AA'(n,k) \approx A(n,k)A'(n,k) \tag{38}$$

and the first order expansion of the symbol of a commutator is

$$\begin{aligned}[A,A']_\star(n,k) \approx& [A(n,k),A'(n,k)] + i\left(\delta_n A(n,k)\partial_k A'(n,k) - \partial_k A(n,k)\delta_n A'(n,k)\right) \\ \approx& [A(n,k),A'(n,k)] + i\{A,A'\}(n,k)\end{aligned} \tag{39}$$

which is again just a Poisson bracket when the symbols commute.

Since we only look at the leading coefficients of the semi-classical expansions, these properties are enough for the purpose of this paper. In particular, the semi-classical limit is the same as in the continuous case, up to the fact that the continuous derivatives ∂_x are replaced by discrete derivatives δ_n.

C Higher order insulators with hard boundary: Partial semi-classical limit and numerical programs

In this appendix we want to explain how we can partially simplify the computation of shell index (1.55) by doing a partial semi-classical expansion of the invariant and obtain the expression (1.78). First let us recall the general expression (1.55) we obtained for the shell index in the D-dimensional case without semi-classical hypothesis. This expression

$$\mathcal{I}_{\text{shell}} \underset{\text{lim}}{=} \frac{-1}{12}\left(\operatorname{Tr}\Big(\hat{C}\hat{H}_F[\hat{\alpha},\hat{H}_F]^3[\hat{\alpha},\hat{\theta}_\Gamma]\Big) + \frac{1}{2}\operatorname{Tr}\Big(\hat{C}\hat{H}_F[\hat{\alpha},\hat{H}_F]^4[\hat{\theta}_\Gamma,\hat{H}_F]\Big)\right) \tag{40}$$

where $\hat{\alpha} = T_x^\dagger n_x dx + -iT_x dk_x + T_y^\dagger n_y dy + -iT_y dk_y$ is a one form, and the whole expression is therefore an anti-symmetrised sum of all types of commutators.

Let's now try to simplify it assuming that the system is invariant by translation in both direction in the bulk and invariant in the tangent direction near the edges far away from the corners. In the above expression, one can first notice that the term $\operatorname{Tr}\Big(\hat{C}\hat{H}_F[d,\hat{H}_F]^4[\hat{\theta}_\Gamma,\hat{H}_F]\Big)$ is

always a product of three commutators $[T_x, \hat{H}_F]$ (non zero only near a vertical edge), $[T_y, \hat{H}_F]$ (non zero only near an horizontal edge) and $[\hat{\theta}_F, \hat{H}_F]$ (non zero only near the shell). This three terms are non zero in incompatible regions and the couplings are local, therefore this term decats to zero in the limit $\Gamma \to +\infty$ and we have that

$$\mathcal{I}_{\text{shell}} \underset{\text{lim}}{=} \frac{-1}{12} \text{Tr}\Big(\hat{C}\hat{H}_F[\hat{\alpha}, \hat{H}_F]^3[\hat{\alpha}, \hat{\theta}_\Gamma]\Big) \tag{41}$$

We can then simplify again the expression by noting that a commutator of the form $[T_x, \hat{H}_F]$ or $[T_y, \hat{H}_F]$ must always be present in the expression of $\mathcal{I}_{\text{shell}}$ which imply that the contribution to the expression are localised in the regions which are on the shell and near an edge (see figure 1.19). We can then simplifies partially the expression by using the invariance of translation of $\hat{H}_F$ in the direction tangent to each edge. Therefore the index can be written as the sum of two contributions $\mathcal{I}_{\text{shell}} = \mathcal{I}_{\text{edge},x} + \mathcal{I}_{\text{edge},y}$ with each contribution coming from a different edge where we are able use the Fourier transform in the tangent direction. For example we have that

$$\mathcal{I}_{\text{edge},x} = \frac{-1}{24\pi} \int_0^{2\pi} dk_x \tilde{\text{Tr}} \left(\tilde{C}\tilde{H}_F[\tilde{\alpha}, \tilde{H}_F]^3\right) \tag{42}$$

where the $\sim$ notation denotes here the fact that we do the Wigner-Weyl transform only in one direction. $\tilde{d}$ can for example be written as $\tilde{\alpha} = \partial_x dk_x + T_y^\dagger n_y dy + T_y dk_y$ now. This is indeed the expression (1.78) claimed in the main text.

We then present the numerical programs which compute the invariant. The first one using the expression of the mode index (1.8), the second one using the semi-classical limit of the shell index.

Computation of the index of the model (1.76) using the formula (1.8) of the mode index

```
from scipy import linalg
import numpy as np
#Function computing the operator func(H) for a given operator H
def funm_herm(H, func):
    w, v = linalg.eigh(H)
    w = func(w)
    return (v * w).dot(v.T.conj())

#function which is 0 for negative number and 1 for positive number
def step(x):
    return (np.sign(x)+1)/2

#the tanh serve as the smooth transition function in energy
def smoothstep(x):
    k=20
    return np.tanh(k*x)

#Lenght in site of the lattice
L = 13
#Coupling constants, topological when |t1|>|t|
t=0.6
t1 = 1

#C is the chiral operator, theta the cut-off operator,
#Id the identity and H the Hamiltonian
Id = np.eye(L*L*4)
H = np.zeros((L*L*4,L*L*4))
```

```
C = np.zeros((L*L*4,L*L*4))
theta = np.zeros((L*L*4,L*L*4))

#The degree of freedom which is situated on the i-th site in the x direction,
#the j-th site in the y direction
#and which correspond to the k-th degrees of freedom of tha site
#is encoded by the single number i+j*L+k*L**2
for i in range(L):
    for j in range(L):
        H[i+j*L+0*L**2,i+j*L+1*L**2]=t
        H[i+j*L+0*L**2,i+j*L+2*L**2]=t
        H[i+j*L+1*L**2,i+j*L+0*L**2]=t
        H[i+j*L+1*L**2,i+j*L+3*L**2]=t

        H[i+j*L+2*L**2,i+j*L+0*L**2]=t
        H[i+j*L+2*L**2,i+j*L+3*L**2]=-t
        H[i+j*L+3*L**2,i+j*L+1*L**2]=t
        H[i+j*L+3*L**2,i+j*L+2*L**2]=-t

        C[i+j*L+0*L**2,i+j*L+0*L**2]=1
        C[i+j*L+1*L**2,i+j*L+1*L**2]=-1
        C[i+j*L+2*L**2,i+j*L+2*L**2]=-1
        C[i+j*L+3*L**2,i+j*L+3*L**2]=1

        for k in range(4):
            theta[i+j*L+k*L**2,i+j*L+k*L**2] = step(i-L//2)* step(j-L//2)
        if i < L-1:
            H[(i+1)+j*L+0*L**2,i+j*L+2*L**2]=t1
            H[(i+1)+j*L+1*L**2,i+j*L+3*L**2]=t1
            H[i+j*L+2*L**2,(i+1)+j*L+0*L**2]=t1
            H[i+j*L+3*L**2,(i+1)+j*L+1*L**2]=t1
        if j < L-1:
            H[i+(j+1)*L+0*L**2,i+j*L+1*L**2]=t1
            H[i+j*L+1*L**2,i+(j+1)*L+0*L**2]=t1
            H[i+(j+1)*L+2*L**2,i+j*L+3*L**2]=-t1
            H[i+j*L+3*L**2,i+(j+1)*L+2*L**2]=-t1

#computation of the flatten Hamiltonian H_F
HF = funm_herm(H, smoothstep)

#computation of the index
I = np.trace(C.dot(Id-HF.dot(HF)).dot(theta)).real
```

Computation of the index of the model (1.76) using the partial semi-classical limit (1.78) of the shell index

```
from scipy import linalg
import numpy as np
from math import pi
#Function computing the operator func(H) for a given operator H
def funm_herm(H, func):
    w, v = linalg.eigh(H)
    w = func(w)
    return (v * w).dot(v.T.conj())

#function which is 0 for negative number and 1 for positive number
def step(x):
    return (np.sign(x)+1)/2
```

```
#the tanh serve as the smooth transition function in energy
def smoothstep(x):
    k=20
    return np.tanh(k*x)

#Commutator of two matrices AB-BA
def com(A,B):
    return A.dot(B)-B.dot(A)

#Sum of all antisimetrised combination of A,B,C
#which are ABC+BCA+CAB-ACB-CBA-BAC
def tricom(A,B,C):
    return A.dot(com(B,C))+B.dot(com(C,A))+C.dot(com(A,B))

#computation of the flatten Hamiltonian for a given transverse momentum k
#The degree of freedom which is situated on the i-th site in the normal
    direction,
#and which correspond to the k-th degrees of freedom of tha site
#is encoded by the single number i+k*L
def HF(k):
    H = np.zeros((L*4,L*4), dtype= np.complex128)
    for i in range(L):
        H[i+0*L,i+1*L]=t+t1*np.exp(-1j*k)
        H[i+0*L,i+2*L]=t
        H[i+1*L,i+0*L]=t+t1*np.exp(1j*k)
        H[i+1*L,i+3*L]=t

        H[i+2*L,i+0*L]=t
        H[i+2*L,i+3*L]=-(t+t1*np.exp(-1j*k))
        H[i+3*L,i+1*L]=t
        H[i+3*L,i+2*L]=-(t+t1*np.exp(1j*k))
        if i < L-1:
            H[(i+1)+0*L,i+2*L]=t1
            H[(i+1)+1*L,i+3*L]=t1
            H[i+2*L,(i+1)+0*L]=t1
            H[i+3*L,(i+1)+1*L]=t1
    return funm_herm(H, smoothstep)


#Lenght in site of the lattice
L = 13
#Coupling constants, topological when |t1|>|t|
t=0.6
t1 = 1

#C is the chiral operator, theta the cut-off operator,
#Id the identity, H the Hamiltonian
#ni is the diagonal position operator equal to i on the i-th site
#T is the tranlation operator of one unit cell in the normal direction
H = np.zeros((L*4,L*4))
C = np.zeros((L*4,L*4))
theta = np.zeros((L*4,L*4))
T = np.zeros((L*4,L*4))
ni = np.zeros((L*4,L*4))

for i in range(L):

        C[i+0*L,i+0*L]=1
        C[i+1*L,i+1*L]=-1
        C[i+2*L,i+2*L]=-1
        C[i+3*L,i+3*L]=1
```

```
        for k in range(4):
            theta[i+k*L,i+k*L] = step(L//2-i)
            ni[i+k*L,i+k*L] = i
        if i < L-1:
            for k in range(4):
                T[i+1+k*L,i+k*L] = 1
#operator T^\dagger*n_i
T1 = T.T.dot(ni)

#number of point in the discretisation of the tranverse wavenumber
n=50

listek = np.linspace(0,2*pi,n+1)
ListeI = np.zeros((n), dtype= np.complex128)

HF1 = HF(listek[0])
for i in range(n):
    HF0 = HF1
    HF1 = HF(listek[i+1])
    #discretisation of the discrete derivative in k
    dHF1 = (HF1-HF0)*n
    dHF2 = com(T1,HF0)
    dHF3 = com(T,HF0)
    #Computation of the density to integrate
    Z = C.dot(HF0).dot(tricom(dHF1,dHF2,dHF3)).dot(theta)
    #Integration in the transverse wavenumber k
    ListeI[i] = np.trace(Z*1j).real/n
I = -np.sum(ListeI)/(2*pi)/6
```

D Proof of the general mode-shell correspondence

In this appendix, the goal is to prove the mode-shell correspondence of the general mode index defined in section 3.1 and in particular the expressions (3.3). We separate the proof of the chiral and non chiral case. We start by the chiral case.

D.1 Chiral case

We start with the first equation of 3.2 which reads

$$\mathcal{C}_{2D}(\hat{H}') = b_{2D} \int \mathrm{Tr}\Big(\hat{\sigma}_z \hat{H}' (d\hat{H}')^{2D} \hat{\theta}_\Gamma\Big) \tag{43}$$

with $2D = \mathrm{D_M}$.

If we introduce the path $\hat{H}'_t = -\hat{C}e^{-t\hat{C}\hat{H}_F}$, we can differentiate such expression and obtain

$$\mathcal{C}_{2D}(\hat{H}')/b_D = \int_0^\pi dt \int \mathrm{Tr}\Big(\partial_t \hat{H}' (d\hat{H}')^{2D} \hat{\theta}_\Gamma\Big) + \sum_{i=0}^{D-1} \mathrm{Tr}\Big(\hat{H}' (d\hat{H}')^i \partial_t (d\hat{H}') (d\hat{H}')^{2D-i-1} \hat{\theta}_\Gamma\Big). \tag{44}$$

If we then integrate by part (in the derivative d) the second term, we obtain

$$\begin{aligned}\mathcal{C}_{2D}(\hat{H}')/b_D =& \int_0^\pi dt \int \mathrm{Tr}\Big(\partial_t \hat{H}'(d\hat{H}')^{2D}\hat{\theta}_\Gamma\Big) - \sum_{i=0}^{D-1}(-1)^i \mathrm{Tr}\Big((d\hat{H}')^{i+1}\partial_t\hat{H}'(d\hat{H}')^{2D-i-1}\hat{\theta}_\Gamma\Big)\\ &+ \sum_{i=0}^{D-1}(-1)^i \mathrm{Tr}\Big(\hat{H}'(d\hat{H}')^{i}\partial_t\hat{H}'(d\hat{H}')^{2D-i-1}(d\hat{\theta}_\Gamma)\Big)\\ =& \int_0^\pi dt \int \sum_{i=0}^{D}(-1)^i \mathrm{Tr}\Big((d\hat{H}')^{i}\partial_t\hat{H}'(d\hat{H}')^{2D-i}\hat{\theta}_\Gamma\Big))\\ &+ \sum_{i=0}^{D-1}(-1)^i \mathrm{Tr}\Big(\hat{H}'(d\hat{H}')^{i}\partial_t\hat{H}'(d\hat{H}')^{2D-i-1}(d\hat{\theta}_\Gamma)\Big)\end{aligned} \tag{45}$$

Because $(\hat{H}')^2 = \mathbb{1}$ we can insert it in the first term. Using the fact the anti-commutation relations $d(\hat{H}')^2 = 0 = \{\hat{H}', d\hat{H}'\}$ as well as $\partial_t(\hat{H}')^2 = 0 = \{\hat{H}', \partial_t\hat{H}'\}$, we can show that

$$\begin{aligned}\mathcal{C}_{2D}(\hat{H}')/b_D =& \int_0^\pi dt \int \sum_{i=0}^{D}\frac{1}{2} \mathrm{Tr}\Big((d\hat{H}')^{i}\hat{H}'\partial_t\hat{H}'(d\hat{H}')^{2D-i}[\hat{\theta}_\Gamma, \hat{H}']\Big))\\ &+ \sum_{i=0}^{D-1} \mathrm{Tr}\Big((d\hat{H}')^{i}\hat{H}'\partial_t\hat{H}'(d\hat{H}')^{2D-i-1}(d\hat{\theta}_\Gamma)\Big)\end{aligned} \tag{46}$$

Because in this formulation we have terms with either commutator of the cut-off or differential of it, the index is localised on the shell and we can use that $\hat{H}_F^2 = \mathbb{1}$ in this region and so $\hat{H}'_t = \sin(t)\hat{H}_F - \hat{C}\cos t$. This lead to

$$\begin{aligned}\mathcal{C}_{2D}(\hat{H}')/b_D =& -\int_0^\pi dt \int \sin(t)^{2D+1}\frac{2D+1}{2} \mathrm{Tr}\Big(\hat{C}\hat{H}_F(d\hat{H}_F)^{2D}[\hat{\theta}_\Gamma, \hat{H}']\Big))\\ &+ \sin(t)^{2D-1}2D \,\mathrm{Tr}\Big(\hat{C}\hat{H}_F(d\hat{H}_F)^{2D-1}(d\hat{\theta}_\Gamma)\Big)\end{aligned} \tag{47}$$

If we now use the that $\int_0^\pi \sin(t)^{2D-1} = \frac{2^{2D}(D-1)!^2}{2(2D-1)!}$ and $b_{2D} = \frac{1}{2^{2D+1}D!(-2i\pi)^D}$, we obtain

$$\begin{aligned}\mathcal{C}_{2D} =& -\int \frac{b_D 2^{2D}(D-1)!^2 D}{(2D-1)!}\left(\mathrm{Tr}\Big(\hat{C}\hat{H}_F(d\hat{H}_F)^{2D-1}(d\hat{\theta}_\Gamma)\Big) + \frac{1}{2}\mathrm{Tr}\Big(\hat{C}\hat{H}_F(d\hat{H}_F)^{2D}[\hat{\theta}_\Gamma, \hat{H}']\Big)\right)\\ &- \int \frac{D!}{(2D)!(-2i\pi)^D}\left(\mathrm{Tr}\Big(\hat{C}\hat{H}_F(d\hat{H}_F)^{2D-1}(d\hat{\theta}_\Gamma)\Big) + \frac{1}{2}\mathrm{Tr}\Big(\hat{C}\hat{H}_F(d\hat{H}_F)^{2D}[\hat{\theta}_\Gamma, \hat{H}']\Big)\right)\end{aligned} \tag{48}$$

which is the wanted result (3.3).

D.2 Non chiral case

We start with the first equation of 3.2 which reads

$$\mathcal{W}_{2D-1}(\hat{H}') = \frac{D!}{(2D)!(-2i\pi)^D}\int \mathrm{Tr}\Big(\hat{\sigma}_z\hat{H}'(d\hat{H}')^{2D-1}\hat{\theta}_\Gamma\Big) \tag{49}$$

with $\mathrm{D_M} = 2D-1$

If we introduce the path $\hat{H}'_t = -\sigma_x e^{-it\sigma_z\hat{H}_F}$, we can differentiate such expression and obtain

$$\begin{aligned}\mathcal{W}_{2D-1}(\hat{H}')/a_D =& \int_0^\pi dt \int \mathrm{Tr}\Big(\sigma_z\partial_t\hat{H}'(d\hat{H}')^{2D-1}\hat{\theta}_\Gamma\Big)\\ &+ \sum_{j=0}^{2D-2}\mathrm{Tr}\Big(\sigma_z\hat{H}'(d\hat{H}')^{j}\partial_t(d\hat{H}')(d\hat{H}')^{2D-j-2}\hat{\theta}_\Gamma\Big)\end{aligned} \tag{50}$$

if we then integrate by part (in the derivative d) the second term, we obtain

$$\begin{aligned}\mathcal{W}_{2D-1}(\hat{H}')/a_D =& \int_0^\pi dt \int \mathrm{Tr}\Big(\sigma_z \partial_t \hat{H}' (d\hat{H}')^{2D-1} \hat{\theta}_\Gamma\Big) \\ &- \sum_{j=0}^{2D-2} (-1)^j \,\mathrm{Tr}\Big(\sigma_z (d\hat{H}')^{j+1} \partial_t \hat{H}' (d\hat{H}')^{2D-j-2} \hat{\theta}_\Gamma\Big) \\ &- \sum_{j=0}^{2D-2} (-1)^j \,\mathrm{Tr}\Big(\sigma_z \hat{H}' (d\hat{H}')^{j} \partial_t \hat{H}' (d\hat{H}')^{2D-j-2} (d\hat{\theta}_\Gamma)\Big) \\ =& \int_0^\pi dt \int \sum_{j=0}^{2D-1} (-1)^j \,\mathrm{Tr}\Big(\sigma_z (d\hat{H}')^{j} \partial_t \hat{H}' (d\hat{H}')^{2D-1-j} \hat{\theta}_\Gamma\Big)) \\ &- \sum_{j=0}^{2D-2} (-1)^j \,\mathrm{Tr}\Big(\sigma_z \hat{H}' (d\hat{H}')^{j} \partial_t \hat{H}' (d\hat{H}')^{2D-j-2} (d\hat{\theta}_\Gamma)\Big).\end{aligned} \tag{51}$$

Because $(\hat{H}')^2 = \mathbb{1}$ we can insert it in the first term. Using the fact the anti-commutation relations $d(\hat{H}')^2 = 0 = \{\hat{H}', d\hat{H}'\}$ as well as $\partial_t(\hat{H}')^2 = 0 = \{\hat{H}', \partial_t \hat{H}'\}$, we can show that

$$\begin{aligned}\mathcal{W}_{2D-1}(\hat{H}')/a_D =& \int_0^\pi dt \int \sum_{j=0}^{2D-1} -\frac{1}{2} \,\mathrm{Tr}\Big(\sigma_z (d\hat{H}')^{j} \hat{H}' \partial_t \hat{H}' (d\hat{H}')^{2D-1-j} [\hat{\theta}_\Gamma, \hat{H}']\Big)) \\ &- \sum_{j=0}^{2D-2} \mathrm{Tr}\Big(\sigma_z (d\hat{H}')^{j} \hat{H}' \partial_t \hat{H}' (d\hat{H}')^{2D-j-2} (d\hat{\theta}_\Gamma)\Big)\end{aligned} \tag{52}$$

Because in this formulation we have terms with either commutator of the cut-off or differential of it, the index is localised on the shell and we can use that $\hat{H}_F^2 = \mathbb{1}$ in this region and so $\hat{H}_t' = -\sin(t)\sigma_y \hat{H}_F - \sigma_x \cos t$. This lead to

$$\begin{aligned}\mathcal{W}_{2D-1}(\hat{H}')/a_D =& -2i \int_0^\pi dt \int \sin(t)^{2D} D \,\mathrm{Tr}\Big(\hat{H}_F (d\hat{H}_F)^{2D-1} [\hat{\theta}_\Gamma, \hat{H}']\Big)) \\ &+ \sin(t)^{2D-2} (2D-1) \,\mathrm{Tr}\Big(\hat{H}_F (d\hat{H}_F)^{2D-2} (d\hat{\theta}_\Gamma)\Big)\end{aligned} \tag{53}$$

If we now use that $\int_0^\pi \sin(t)^{2D} = \pi \frac{(2D)!}{2^{2D} D!^2}$ and $a_{2D-1} = \frac{D!}{(2D)!(-2i\pi)^D}$ we obtain that

$$\begin{aligned}\mathcal{W}_{2D-1} =& \frac{-2i\pi a_D 2D(2D)!}{2^{2D} D!^2} \int \left(\mathrm{Tr}\Big(\hat{H}_F (d\hat{H}_F)^{2D-2} (d\hat{\theta}_\Gamma)\Big) + \frac{1}{2} \,\mathrm{Tr}\Big(\hat{H}_F (d\hat{H}_F)^{2D-1} [\hat{\theta}_\Gamma, \hat{H}']\Big)\right) \\ =& \frac{2D}{2^{2D} D! (-2i\pi)^{D-1}} \int \left(\mathrm{Tr}\Big(\hat{H}_F (d\hat{H}_F)^{2D-2} (d\hat{\theta}_\Gamma)\Big) + \frac{1}{2} \,\mathrm{Tr}\Big(\hat{H}_F (d\hat{H}_F)^{2D-1} [\hat{\theta}_\Gamma, \hat{H}']\Big)\right)\end{aligned} \tag{54}$$

which is the wanted result (3.3).